Study on Energy Saving in Electrical Drive System

電動機駆動システムの省エネルギー化に関する研究

March, 2003

Applied Electromagnetics Laboratory
Graduate School of Science and Engineering
Major in Electrical Engineering
Waseda University

Feri Yusivar

Dedicated to

my parents

and

my wife Vitri

Acknowledgements

I would like to thank my supervisor, Associate Professor Shinji Wakao, for accepting me to the Applied Electromagnetic Laboratory of Waseda University as a foreign student, and for guiding me and fully supporting throughout my researches.

I would like to give my deep appreciation to Professor Emeritus Takashi Onuki, my master course supervisor, for giving me a chance to study in Japan and supporting during research. I would also like to thank Dr. Keiichiro Kondo from the Railway Technical Research Institute (RTRI) Japan for advising and helping me to solve every research problem patiently.

I would like to thank Professor Seiji Kobayashi, Professor Shinichi Iwamoto, Professor Kenko Uchida, and Professor Atsushi Ishiyama for their advices and suggestions to my research work, especially during the examination in the Graduate School of Science and Engineering, Waseda University.

I will always remember everyday life and work together with everybody at the laboratory. Thanks to Kenji Uchida, Hiroyuki Haratsu, Takahiro Kihara, Mitsuhiro Sato, Taketoshi Kusakabe, Hirofumi Horii, Yasushi Fujishima, Takashi Yoneyama, and Koichiro Yano for helping me in facing Japanese language difficulties and research problems.

This work would have not realized without the financial supports from The Hitachi Scholarship Foundation (HSF). In this respect, I would like to acknowledge Mr. Tohru Fukui, Mr. Tsutomu Gomibuchi, Mr. Hirotsugu Sugai, Mr. Mikio Homma, Mr. Ichiro Shimizu, Ms. Maki Nunokami, and other staffs for all supports and warm friendship during my staying in Japan.

I feel thankful to all staffs of Electrical Engineering Department, University of Indonesia. Thanks to Dr. Rudy Setiabudy, A. A. P. Ratna M.Eng., Dr. Dadang Gunawan, Dr. Wahidin Wahab, Dr. Harry Sudibyo S. and Dr. Eko Tjipto Rahardjo for the encouragement to take research in Waseda University.

I wish to show a special gratitude to my wife, Tri Yulianti Savitri, for her permanent support in my everyday life and apology to her for the too little time I can spend with her.

Ohkubo Campus, Tokyo **Feri Yusivar**

March, 2003

Abstract

Electrical drive system, a major power electronics area, play a very important role in the energy saving effort as an action for global environmental protection. Electric vehicle is one of its application for such purpose. Electrical drive system interfaces the electrical supply with the vehicle wheels, transferring energy in either direction as required, with high efficiency, under control of the driver at all times. Most electric vehicles have a regenerative braking system. During braking, the motor acts as generator and converts the energy caused by the movement of the vehicle back into electricity and saved in battery or other storage system for further reuse.

Some problems occur in attempting the energy saving in electrical drive system. In one case, the motor is operated in high-speed area. High-speed motor operation capability can provide high kinetic energy to be recovered by the regenerative control system. This high-speed operation is limited by the output voltage of the inverter. In another case, the energy is saved by driving the vehicle in coasting operation, the motor should can be restarted from coasting operation. However, in the motor restarting under the speed sensorless control, the initial speed estimation problem occurs. And then, when the regenerative braking control is applied to the PMSM drive system of electric railway vehicle with the light-load energy consumption, the electrical oscillation occurs. Furthermore, the accurate system model is necessary for the high-performance control design to obtain the efficient energy maintenance system in electric vehicle. However, grasping the characteristic of large-scale combinational batteries is difficult. The works described in this thesis addresses the investigation of these problems with each solution as a result.

A simple novel field-weakening is proposed, which combines the saturation voltage strategy to improve the DC voltage utility for high-speed motor operation. In this scheme, the PMW mode is not changed, as a result, the control system construction is simple (cost reduction). The performance analysis is presented, and then, the control gain selection is decided.

The motor restarting capability after coasting operation is investigated. The result gives a consideration for a successful motor restarting after coasting operation under speed sensorless

control using a speed adaptive observer. The investigation is carried out through experiments and simulations, due to the system object is highly non-linear system. The minimizing convergent time strategy of speed estimation, using gain scheduling based on the gradient slope of estimated speed, is proposed.

The oscillation phenomenon of the light-load regenerative control is confirmed through the experiment and the simulation. The mathematical model of investigated system, which divided into four operation conditions, is derived. The cause of the oscillation phenomenon is then clarified. Based on the analytical results, a new regenerative braking control method in purpose to eliminate the oscillation is proposed.

The equivalent circuit of battery is estimated from the obtained admittance value decided using the transfer function concept. The series and parallel batteries model is calculated mathematically from a single battery model. It is verified that the battery modeling can be done easily by using a proposal technique.

Contents

List of Tables

List of Figures

Chapter 1

Introduction

1.1 Background of the thesis

Electrical drive systems as one of the basic technology has been put to the practical use to support the modern technology. The electrical drive system in electric vehicle is one of the representative objects. In present time when the environmental energy problem becomes serious, the electrical power regenerative becomes the large strong point of the electrical drive system to be paid attention. Especially, a large contribution on energy saving can be expected from the electrical drive system of the electric vehicle with relatively big inertia load by adopting the electrical power regenerative brake system. Based on this background, in this thesis the energy saving in electrical drive system for electric vehicle application is studied with a focus on the alternating-current (AC) motor that has advantage of less maintenance than the direct-current (DC) motor.

From the viewpoint of electric power source, electric vehicle can be classified to electric car (EC) and electric railway vehicle (ER). The electric power source of EC is stored in batteries those are carried onboard, while the electric power source of ER is provided by substation via a transmission cable along the railway path. The capacity of storage batteries of EC is limited with the restriction of the loading space and mass. This limitation results in a limit driving range of EC with the once charged storage batteries. On the other hand, although there is no problem with the driving range of ER, a method to save energy in a battery that is mounted on the vehicle onboard or placed at the power substation is considered for energy conservation purpose. For example, reusing the regenerative power in a DC supplied ER. Thus similar to the EC system, it is believed that in the future the capacity problem of storage battery becomes obvious existence in the ER system. From now on, it is thought that the importance of storing electricity rises further in addition to machine loss cutting down when it aims at the energy

saving in the electric vehicle drive system.

Refer to aforementioned background, the energy saving efforts in electrical drive system are attempted. First, increasing the regenerative braking power with a high-speed operation as to recover the kinetic energy as much as possible, and decreasing the total energy consumption are important to enhance the effectiveness of the regenerative brake control system. Then, to make the regenerative energy effectively, the regenerative electric power should be adjusted corresponding to the condition of the storage battery. Therefore, a proper grasping of the charging condition of the storage battery becomes indispensable too. Furthermore, in order to save the energy, it is also important to decrease the energy loss in the drive system. Concretely, by turning off the electricity while the vehicle is moving promptly for coasting operation after it reaches a speed, the occurrences of inverter switching loss and magnetic excitation loss (in case of induction motor) are prevented. It can be concluded that energy can be saved through the reuse of regenerative energy and the efficiency on consuming energy.

1.2 Statement of Problems

Based on the above background, the research-works of this thesis, in the area of electrical drive system, includes:

1. The investigation of a combination of the maximizing DC voltage utility strategy in the asynchronous PWM inverter and a novel field weakening scheme as to aim the increase of the regenerative electric power in the high-speed operation,

2. The investigation of the restarting capability of the induction motor under the speed sensorless control condition,

3. The proposal of the elucidation and solution of the electrical oscillation phenomenon in the permanent magnet synchronous motor drive system with a light load energy consumption, and

4. The investigation of the modeling technique for a lead-acid storage battery characteristic expression.

Through the investigation and verification of the above research-works, this thesis contributes to energy saving in the electric vehicle drive system. The summaries of problems statement and contributions of this thesis are illustrated in Fig. 1.1.

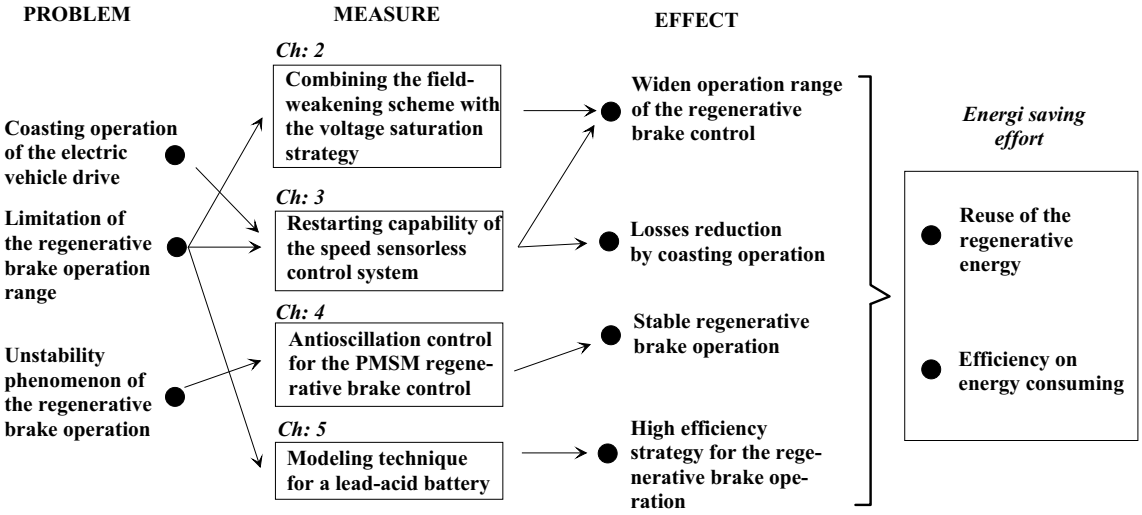

Figure 1.1: Statement of problems and contributions.

1.3 Overview on Electrical Drive System

1.3.1 Topology of Electrical Drive System

In the electrical drive system, energy conversion occurs between electrical energy and mechanical energy. In the motoring operation the electrical energy is converted to mechanical energy. In the generating operation the opposite conversion occurs. The electrical drive topology consists of electrical power source, power semiconductor converter, electrical machine (motor), load machine, and control unit. A block diagram representation of an electrical drive system is shown in Fig. 1.2.

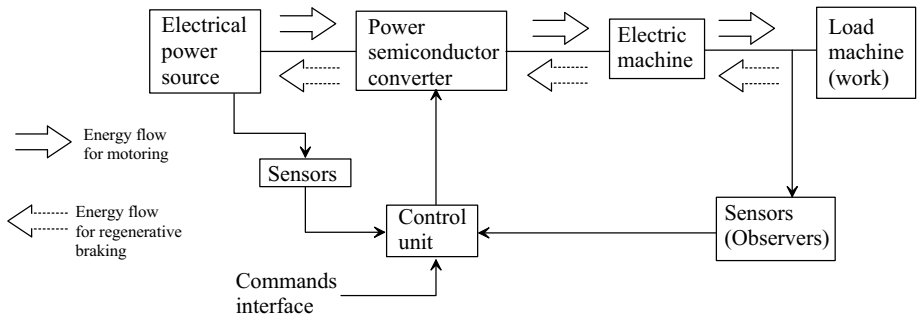

Figure 1.2: Block diagram of an electrical drive system.

The power semiconductor converter controls the flow of electrical power between the motor and the power source such that the motor matches the load requirements. The converter is an electrical power conditioner and acts as a voltage and frequency changer. The control of the converter is built in the low-voltage, low-power control unit. The command interfaces the inputs to the control unit which, in order to adjust the operating point (torque, speed or position) of the drive, makes use of direct feedback sensors, or indirect observers of some of the state variables such as voltages, fluxes, currents, torque, speed, and position.

Electrical drive system has been established for a long time. It evolutes from direct current (DC) drives to various forms of alternating current (AC) drives. Fig. 1.3 shows drive evolution as a basic four-step process.

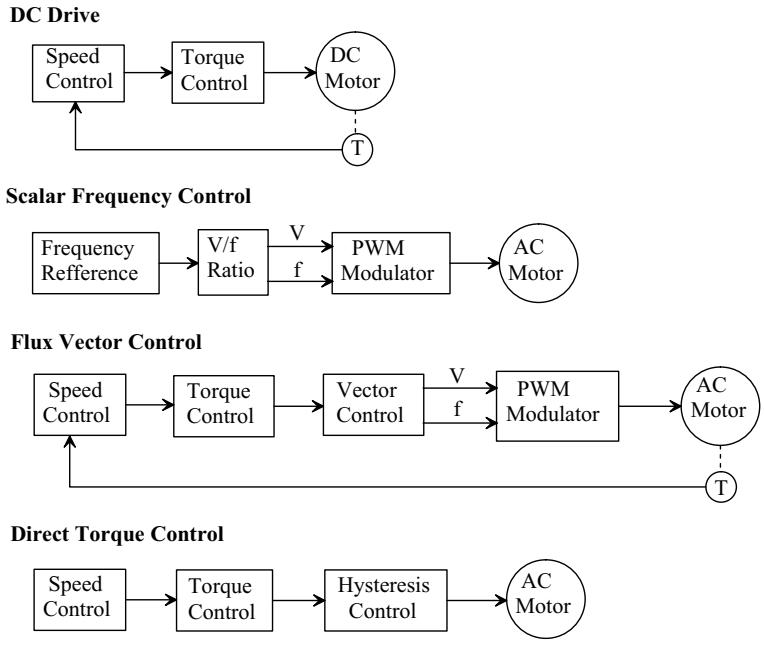

Figure 1.3: Evolution of drive control techniques.

DC Drive

Torque is directly proportional to armature current in the dc motor. By using an inner-current control loop, the dc drive can directly control torque. Likewise, the constant magnetic-field orientation, which is achieved mechanically through commutator action, makes direct flux control a given. Thus, two primary factors toward insuring responsive control (i.e., direct torque control and direct flux control) are both present in the dc drive. The relatively simple electronics

required to implement the dc drive represents another advantage. On the negative side, both the initial and maintenance costs of dc motors are high, and high performance speed accuracy can only be achieved if an encoder is included for feedback.

Scalar Frequency Control

All of the ac drives compared here allow the use of economical, robust ac induction motors. Scalar frequency control also offers the advantage of operation without an encoder. On the negative side, torque and flux are neither directly nor indirectly controlled. Control is instead provided by a frequency and voltage reference generator with constant volts per hertz output, which then drives a pulsewidth modulated (PWM) modulator. Although simple, this arrangement provides limited speed accuracy and poor torque response. Flux and torque levels are dictated by the response of the motor to the applied frequency and voltage and are not under the control of the drive.

Flux Vector Control

Flux vector control reestablishes one of advantages of the dc drive through implementation of direct flux control. In this case, field orientation is controlled electronically. The spatial angular position of rotor flux is calculated and controlled by the drive, based on a relative comparison of the known stator field motor to feedback of rotor angular position and speed. The motor's electrical characteristics are mathematically modeled with microprocessor techniques to enable processing of the data. Torque control is indirect because of its position in the control algorithm prior to the vector control process, however good torque response is achieved nonetheless. Inclusion of the pulse encoder insures high-performance speed and torque accuracy.

The biggest disadvantage of flux vector control is the mandated inclusion of the pulse encoder. Another minor disadvantage is that torque is indirectly, rather than directly, controlled. Finally, the inclusion of the PWM modulator, which processes the voltage and frequency reference outputs of the vector control stage, creates a signal delay between the input references and the resulting stator voltage vector produced. These last two factors limit the ultimate ability of flux vector control to achieve very rapid flux and torque control.

Direct Torque Control

Direct torque control also reestablishes direct flux control. In addition, direct torque control is implemented. Both flux and torque are controlled by a hysteresis controller. The delays asso-

ciated with the PWM modulator stage are removed, since the PWM modulator is replaced by optimal switching logic. The original benefits associated with the dc drive of direct torque control, direct flux control, and high responsiveness are, thus, all reestablished. Torque response is better than that available with either dc or flux vector control. In addition, assuming moderate speed accuracy is acceptable (typically 0.1%-0.3%, or 10% of motor slip) the need for a pulse encoder is eliminated.

Table 1.1 provides a summary comparison of the four drives described above.

Table 1.1: Comparisons of control types

Control Type	*Torque Control*	*Flux Control*	*Response*	*Advantages*	*Disadvantages*
DC Drive	Direct	Direct	High	High accuracy Good torque response Simple	Motor maintenance Motor Cost Encoder required for high accuracy
Scalar Frequency Control	None	None	Low	No encoder Simple	Low accuracy Poor torque response
Flux Vector Control	Indirect	Direct	High	High accuracy Good torque response	Encoder always required
Direct Torque Control	Direct	Direct	High	No encoder Moderate accuracy Excellent torque response	Encoder required for high accuracy

1.3.2 Energy Sources in Electrical Drive System

Basically, there are five energy sources to power the electrical drive system. These are (1) the electrical utility, (2) a fuel cell, (3) a battery bank, (4) super capacitor, (5) flywheel storage. Fig. 1.4 shows the block diagram of the energy sources in electrical drive system. To achieve the desired power transfer between the energy sources and the common DC bus, a DC-to-DC power converters are utilized. The fuel cell always supplies the DC bus, and hence, the corresponding converter is uni-directional. On the other hand, the converter associated with the super capacitor is bi-directional so that during deceleration, part of energy released by the motor can be fed into the super capacitor. As well as the converter of the super capacitor, the inverter of the flywheel system is be-directional. A high rotational flywheel is used to store kinetic energy. This energy can be maintained by minimizing the friction losses. The coupling of this flywheel with a high efficiency motor-generator allows to store-restore the kinetic energy in electrical form. The batteries are connected directly to the DC bus.

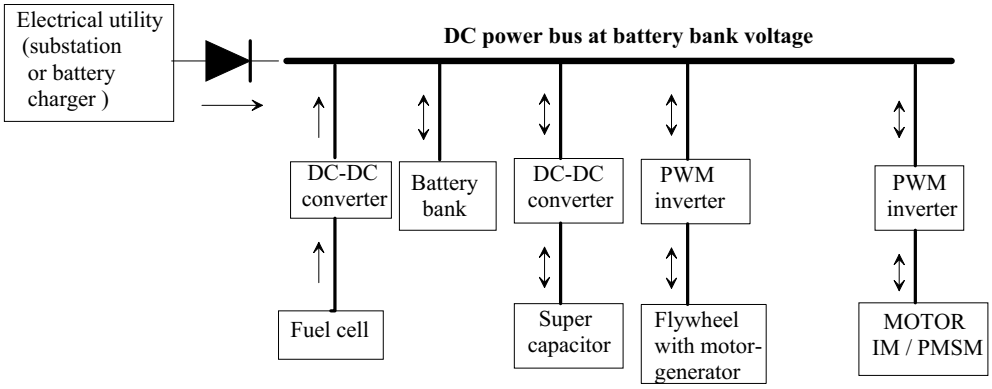

Figure 1.4: Energy sources in electrical drive system.

1.4 Outline of the Thesis

This thesis consist of six chapters, and topics of each chapter are briefly describe as follows:

Chapter 1: Introduction Chapter 1 outlines some backgrounds that motivate the works in this thesis. The problems related to energy saving in electrical drive system are formulated. The solutions to these problems are also briefly described. Outlining the topics of each chapters ends this chapter.

Chapter 2: Field-weakening scheme in combine with saturated voltage control strategy If the DC voltage utility can be improved as to improve the output power in the high speed motor operation, a larger kinetic energy can also be recover. In this chapter, to combine the maximizing DC voltage utility of the asynchronous PWM inverter using a saturation voltage strategy, a novel field-weakening scheme corresponding to the torque improvement is proposed. It is difficult to do so in the previous field-weakening scheme, since a Proportional-Integral (PI) controller controls the motor voltage not to exceed its limit. Instead using PI controller, to be able to implement a voltage saturation technique, the proposed scheme uses only a Proportional controller with low-pass filter. With using the proposed scheme, the control system construction is simple, since the changing in PWM mode is not necessary. Experimental results and performance comparisons are presented to show the proposed scheme has an improved torque capability over the previous one.

Chapter 3: Motor restarting capability of speed sensorless drive As for an energy saving effort, the energy loss decrease due to the electricity of the inverter is turned off

in the motor coasting operation. Then the motor should be restarted when the acceleration or the regenerative braking is needed. Therefore, the restarting capability is one of essential technology for energy saving in electrical drive system. For this research purpose, chapter 3 deals with the preliminary investigation of the induction motor restarting capability under the speed sensorless control condition. The speed sensorless scheme in this chapter utilizes a reduced order observer. The initial value problem of speed estimation that occurs when restarting the motor after coasting is emphasized. The initial estimated speed selection for a successful motor restarting operation is studied further.

Chapter 4: Anti oscillation strategy for the regenerative braking control In this chapter the analysis of the oscillation phenomenon, when the regenerative braking control is applied into the PMSM drive system with a light-load energy consumption, is presented and an anti oscillation strategy is proposed to overcome this stability problem. First, the oscillation phenomenon, which occurred in the actual electric vehicle, is confirmed through the experiment and the simulation. The mathematical model of investigated system, which divided into four operation conditions, is derived. The cause of the oscillation phenomenon is then clarified by solving each steady state solution and pole analyzing. Based on the analytical results, a new regenerative braking control method in purpose to eliminate the oscillation is proposed. Finally, the validity of the effectiveness of the proposed control technique is verified through the experiment according to the mini model of the investigated system.

Chapter 5: Storage battery modeling In this chapter, the new technique to model the transient characteristic of the lead-acid storage battery is proposed. First, the frequency-response of battery in the discharge state is measured. The concept of transfer function to decide the admittance value of battery is introduced. Then the equivalent circuit of battery is estimated from the obtained admittance value. The variation of circuit-constant values with the battery residual capacity is investigated. The series and parallel batteries model, which provides high voltage and power capacity, is calculated mathematically from a single battery model. This mathematical model is confirmed by comparing its frequency characteristic with the measured one from the experimental system. It is verified that the battery modeling can be done easily by using a proposal technique. The storage battery modeling contributes to the optimization of the regenerative energy usage.

Chapter 6: Conclusions and Recommendations Chapter 6 gives a summary of the overall results from the former chapters, identifies the main conclusions of this research works, and provides some directions to continue and to extend the research works in the future.

Chapter 2

Field-weakening scheme in combine with saturated voltage control strategy

In this chapter, a novel field-weakening scheme which is combined with a saturated voltage control strategy is proposed and its performance comparison with the previous scheme (without implementing the saturation strategy) is presented. Though the proposed scheme is quite simple, it is effective to provide a higher torque capability then the previous scheme does. The maximum torque is produced by increasing the flux-producing current as much as possible while the stator voltage reference is saturated. The voltage saturation condition is stimulated by adding the torque-producing current into the flux-producing current reference. Since the DC voltage utility can be improved, that hence, improve the output power in the high speed motor operation, a larger kinetic energy can also be recover. Experiments were carried out to verify the proposed scheme. The experimental results of the previous scheme are also presented for comparison purposes. Furthermore, the performance comparison analysis is presented and from the analysis results the gain parameters for a satisfied performance are selected.

2.1 Introduction

The high-speed operation of the field oriented induction motor control requires a flux decreasing to counteract the back electromotor force (EMF) increasing that will approach the available inverter voltage. Decreasing the flux causes the available torque is reduced. However, the available torque is still can be improved by implementing the voltage saturation strategy to maximize the dc-bus voltage utilization. The field weakening can be performed automatically using a voltage controller without utilizing any motor parameter. Unfortunately, in this field

weakening scheme the saturation strategy is not easy to be implemented.

In a torque-controlled induction motor drive, the maximum output torque and output power besides depend on the motor power rating, also depend on the inverter current rating and the maximum voltage that the inverter can supply to the machine. When the inverter power capability is higher than the machine power, it should be limited to keep operating the machine safely. To operate the machine at very high speed as required in many applications, such as the traction and spindle drives, field-weakening scheme should be adopted, but available torque is reduced. A control strategy, which considers current and voltage limitations, should be implemented so that a maximum torque can be obtained in the whole speed range.

Many papers have proposed new control strategies to provide a maximum torque capability in the field weakening area with taking into account the current and voltage limits [1]∼[4]. The approaches have superior torque capability compare to the conventional $1/\omega_r$ method. To achieve a maximum torque, the flux reference is calculated by examining the relation of the output torque capability with the leakage inductance of the machine [1]. A different approach in determining the flux reference is using a voltage controller [2, 3]. Then, a voltage-margin controller is developed that rejects dc-link and load disturbances [4]. However, all field-weakening schemes [1]∼[4] are applied only in the linear region of the PWM inverter.

Since the space vector pulse width modulation (SVPWM) becomes popular used in motor drive system, the study of the SPWM capability, especially for the field-weakening application, is left behind. Although many papers have been dealt with the maximizing voltage utility of PWM inverter through an overmodulation operation [5]∼[12], their implementation with the field-weakening scheme in the induction motor drive has been not studied intensively. Only few studies on it were found [13, 14]. An over modulation strategy by tracking the voltage vector along hexagon sides of SVPWM was incorporated with the field-weakening scheme to give a better voltage utilization [13]. However, here the field-weakening scheme that was adopted [1] still uses motor parameters to set the flux reference. It was not mentioned a possibility the use of the voltage control strategy as the authors proposed [3]. In another reference, a voltage saturation technique was used for maximizing dc-bus utilization in current regulator [14]. Here, a form of field weakening is provided intrinsically by using a complex vector synchronous frame PI current regulator. Unfortunately, the current limitation is not considered in this technique. And also a scheme for determining the flux reference is still required.

This chapter proposes a different approach of field-weakening control for providing a maximum torque capability considering voltage saturation and current limitation. The voltage

saturation performs a voltage limitation with maximum dc-bus utilization. In present time, the proposed scheme is implemented to the rotor-flux oriented control of a SPWM VSI-fed induction motor. The first part of the chapter describes the currents control with decoupling system. Then followed by describing the voltage saturation strategy and the field-weakening scheme in detail. Then the experimental results of the proposed scheme including comparisons with the previous scheme are presented. Finally the performance analysis is presented, and based on the analysis results the gain parameters for the satisfied performance are selected.

2.2 Currents control with decoupling system

The dynamics of an induction motor in the synchronous frame are given by

$$\dot{x} \;=\; Ax + Bu \tag{2.1}$$

where: $x = \left[\; i_{sd} \quad i_{sq} \quad \phi_{rd} \quad \phi_{rq} \;\right]^T$, $u = \left[\; v_{sd} \quad v_{sq} \;\right]^T$,

$$A = \begin{bmatrix} a_{11} & a_{12} & a_{13} & a_{14} \\ -a_{12} & a_{11} & -a_{14} & a_{13} \\ a_{31} & 0 & a_{33} & a_{34} \\ 0 & a_{31} & -a_{34} & a_{33} \end{bmatrix}, \qquad B = \begin{bmatrix} b_1 & 0 \\ 0 & b_1 \\ 0 & 0 \\ 0 & 0 \end{bmatrix},$$

$$a_{11} = -R_s/(\sigma L_s) - L_m^2/(\sigma L_s L_r T_r)\ , \qquad a_{12} = \omega_e\ ,$$
$$a_{13} = L_m/(\sigma L_s L_r T_r)\ , \qquad a_{14} = \omega_r L_m/(\sigma L_s L_r)\ ,$$
$$a_{33} = -1/T_r\ , \qquad a_{34} = \omega_{sl}\ ,$$
$$b_1 = 1/(\sigma L_s)\ , \qquad \sigma = 1 - L_m^2/(L_s L_r)\ ,$$

i_{sd}, i_{sq}	d-q axes stator currents in the synchronous frame;
ϕ_{rd}, ϕ_{rq}	d-q axes rotor fluxes in the synchronous frame;
v_{sd}, v_{sq}	d-q axes stator voltage in the synchronous frame;
L_s, L_r, L_m	stator, rotor, and mutual inductances;
R_s, R_r	stator and rotor resistances;
ω_e, ω_r	electrical and rotor angular frequency;
ω_{sl}	slip frequency $(\omega_e - \omega_r)$;
T_r	rotor time constant (L_r/R_r).

The rotor-flux-oriented control is achieved by letting $\phi_{rq} = 0$ and $\phi_{rd} = \phi_r =$ constant. Then, the current dynamic Eq. (2.1) yield

$$\sigma L_s(\frac{d}{dt}i_{sd}) = -R_s i_{sd} + \omega_e \sigma L_s i_{sq} + v_{sd} \tag{2.2}$$

$$\sigma L_s(\frac{d}{dt}i_{sq}) = -R_s i_{sq} - \omega_e \sigma L_s i_{sd} - \frac{\omega_e L_m}{L_r}\phi_{rd} + v_{sq} \tag{2.3}$$

The feed forward decoupling control method is to choose inverter output voltages such that

$$v^*_{sd} = (K_p + \frac{K_i}{s})(i^*_{sd} - i_{sd}) - \sigma L_s \omega_e i_{sq} \tag{2.4}$$

$$v^*_{sq} = (K_p + \frac{K_i}{s})(i^*_{sq} - i_{sq}) + \sigma L_s \omega_e i_{sd} + \frac{(1-\sigma)L_s}{L_m}\omega_e \phi_{rd} \tag{2.5}$$

where the proportional and integral gains are set to $K_p = \frac{\sigma L_s}{T_d}$ and $K_i = \frac{R_s}{T_d}$ respectively, as for the stator currents to have a first order delay response of their references with time constant of T_d . Then, to minimize loop feedback systems, the currents feedback used for decoupling system including the back EMF compensation can be estimated using

$$i^*_{sd1} = \frac{1}{1 + T_d s} i^*_{sd} \tag{2.6}$$

$$i^*_{sq1} = \frac{1}{1 + T_d s} i^*_{sq} \tag{2.7}$$

$$i^*_{sd2} = \frac{1}{1 + T_r s} i^*_{sd1} \tag{2.8}$$

and then

$$\omega_e = \omega_r + \frac{R_r}{L_r}\frac{i^*_{sq1}}{i^*_{sd2}} \tag{2.9}$$

$$\phi_{rd} = L_m i^*_{sd2} \tag{2.10}$$

The block diagram of the currents control with decoupling system is shown in Fig. 2.1. This configuration will be used in this chapter as a standard currents control system, so that only the field-weakening scheme of the proposed strategy will be different compared with one of the previous strategy.

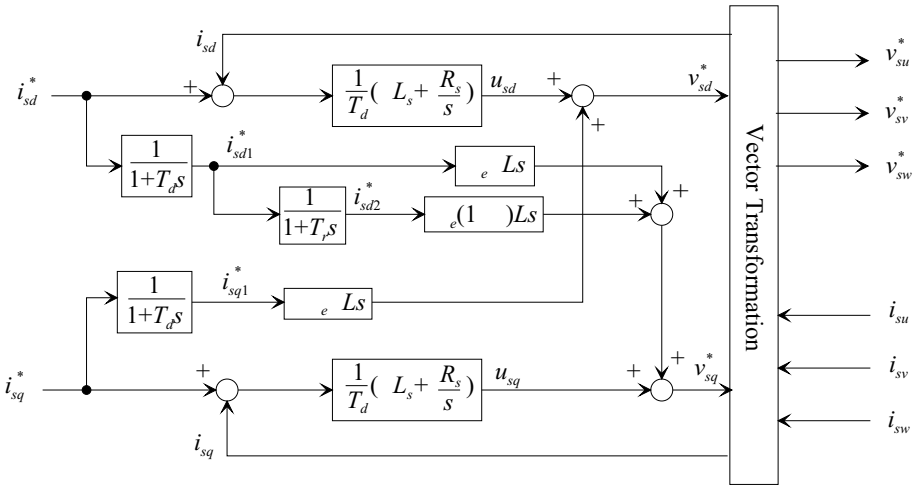

Figure 2.1: Currents control with decoupling system.

2.3 Voltage Saturation Technique

The SPWM signal is constructed by comparing a high-frequency triangular carrier with three reference signals. It can be easily implemented as an analog or a digital solution; hence it makes high flexibility in practical use.

With index modulation $m = 1$, SPWM provides voltage utility about 78% of the value that would be reached by square-wave (six step) operation. The dc-bus utilization can be increased through the use of zero-sequence harmonics addition [7], square wave addition [9], or reshaping the modulation command [11]. However, it is preferred to use the saturation technique instead, due to its simplicity, especially when it implemented with the field-weakening scheme. The saturation technique can be realized quite simple by limiting the phase voltage reference to the value of $\frac{V_{dc}}{2}$ as shown in Fig. 2.2.

In this way, the need to over-modulate in the pulse-dropping region is eliminated. Fig. 2.2 shows the half period SPWM construction of the saturated and unsaturated voltage reference. For the saturated voltage reference case, the amplitude is enlarged and then is limited to not exceed the triangle carrier amplitude. As a result the effective output voltage is boosted.

As well as the current control system described in previous section, the saturation technique illustrated in Fig. 2.2 will be used in this chapter as a standard of voltage limiter. In the previous field-weakening scheme that will be described later, the voltage limiter is still necessary to anticipate an overshoot phenomenon of the voltage controller in transient.

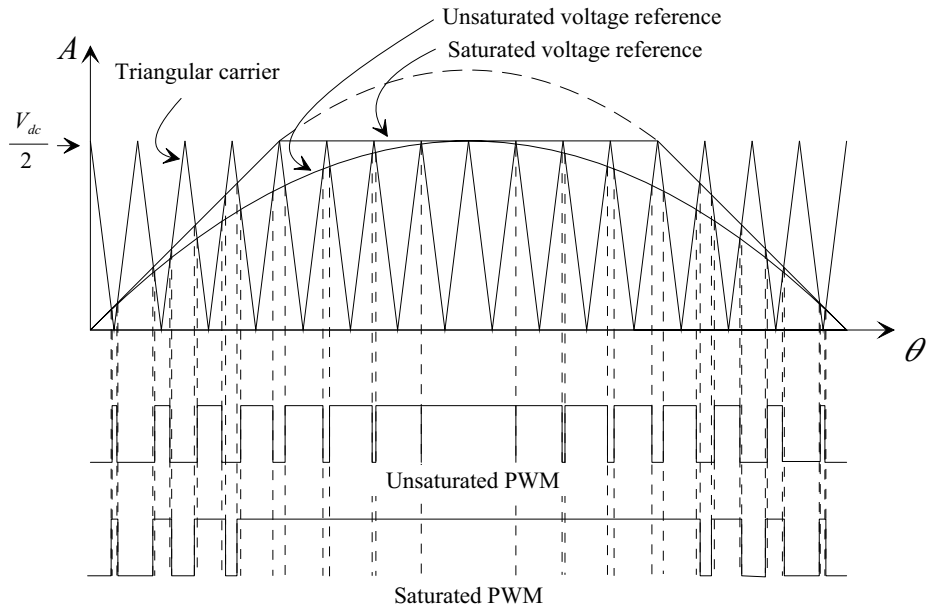

Figure 2.2: Sinusoidal pulse width modulation.

2.4 Field-Weakening Scheme

2.4.1 Constraints in Operating Conditions

Induction motor can operate in one of three operating modes: torque constant mode, power constant mode, and voltage constant mode. Below the rated speed (torque constant mode) the motor operation is current-limited. In power constant mode the motor operation is both current-limited and voltage-limited as the back-EMF approaches the maximum inverter voltage while the current is still limited. In voltage constant mode the speed becomes so high that the current cannot exceed the maximum inverter current anymore.

Current and voltage limitations are available in inverter by means of over-current and over-voltage protections. However, we still have to limit the motor operation below those over current and over voltage values. Otherwise the protection system will shut down the inverter. Thus it is useful to limit the motor operation in the controller system.

The machine current operation is limited to a maximum stator current $i_{s\max}$ that is the minimum of inverter maximum current and motor maximum current. This current limitation is provided by limiting q-axis current reference i_{sq}^{*} , which the priority is given to d-axis current reference i_{sd}^{*} , and follows the equation expressed in Eq. (2.11). The field weakening technique

determines the d-axis current reference i^*_{sd} which is limited to its rated value.

$$i^{*2}_{sd} + i^{*2}_{sq} \leq i^2_{s\,\max} \tag{2.11}$$

The voltage applied to the motor is limited to $v_{s\,\max}$ that depends on the available dc-bus voltage V_{dc} and pulse-width modulation (PWM) strategy. The motor voltage input follows the following equation.

$$v^{*2}_{sd} + v^{*2}_{sq} \leq v^2_{s\,\max} \tag{2.12}$$

The steady-state voltage equations of the induction motor in the synchronously rotating reference frame are given by

$$v^*_{sd} = R_s i^*_{sd} - \omega_e \sigma L_s i^*_{sq} \tag{2.13}$$

$$v^*_{sq} = R_s i^*_{sq} + \omega_e L_s i^*_{sd} \tag{2.14}$$

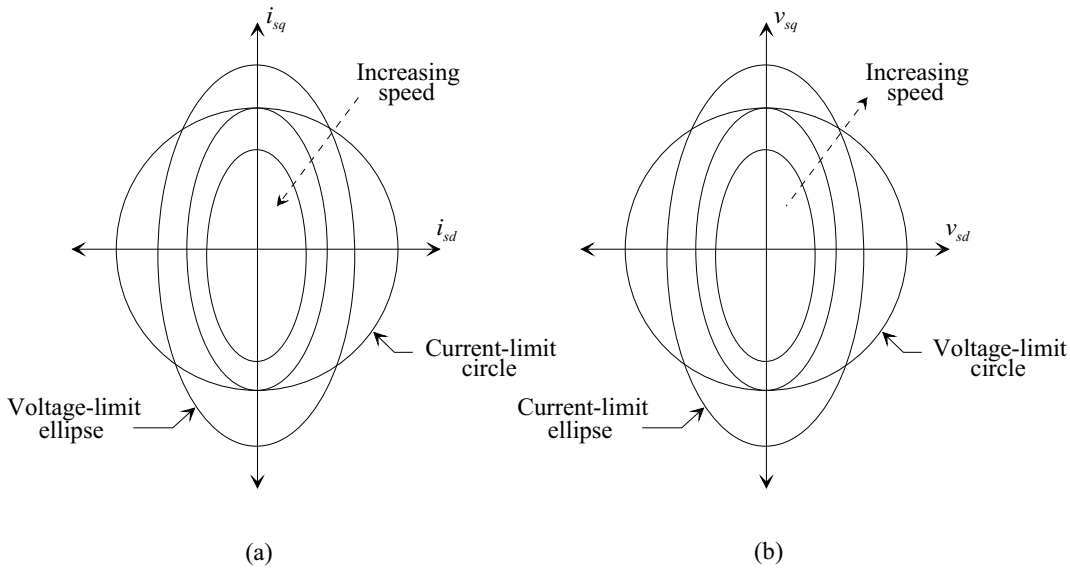

Figure 2.3: Voltage and current limits: (a) Current boundary (b) Voltage boundary.

In high-speed operation, the stator resistance effect is negligible in Eqs. (2.13) and (2.14). Then the current-limit constraint of Eq. (2.11) and the voltage-limit constraint of Eq. (2.12) can be rewritten as the following equations.

$$(i^*_{sd}\omega_e L_s)^2 + (i^*_{sq}\omega_e \sigma L_s)^2 \leq v^2_{s\,\max} \tag{2.15}$$

$$\left(\frac{v_{sd}^*}{\omega_e \sigma L_s}\right)^2 + \left(\frac{v_{sq}^*}{\omega_e L_s}\right)^2 \leq i_{s\max}^2 \tag{2.16}$$

Eqs. (2.11) and (2.12) mean the circle equations, while Eqs. (2.15) and (2.16) mean the ellipse equations. Fig. 2.3 shows the current-limit and voltage-limit boundaries in the qe-de current and voltage planes.

2.4.2 Maximum Torque Capability

The maximum torque provided by the field-weakening scheme based on voltage control strategy, which considering the current limit and voltage limit, was described clearly by Kim and Sul [3]. The whole field-weakening region can be divided into two sub regions: region I ($\omega_{base} < \omega_e \leq \omega_1$) and region II ($\omega_e > \omega_1$). In the field-weakening region I, the maximum output torque is obtained by the locus of the optimal voltage vector which moves rightward along the boundary of the voltage-limit circle as the operating frequency increases (from point A to point B as shown in Fig. 2.4). In the field-weakening region II, the maximum output torque is obtained only by the voltage-limit constraint as

$$v_{sq}^* = |v_{sd}^*| = \frac{V_{s\max}}{\sqrt{2}} \tag{2.17}$$

regardless of the operating frequency (at point B; not point C as shown in Fig. 2.4).

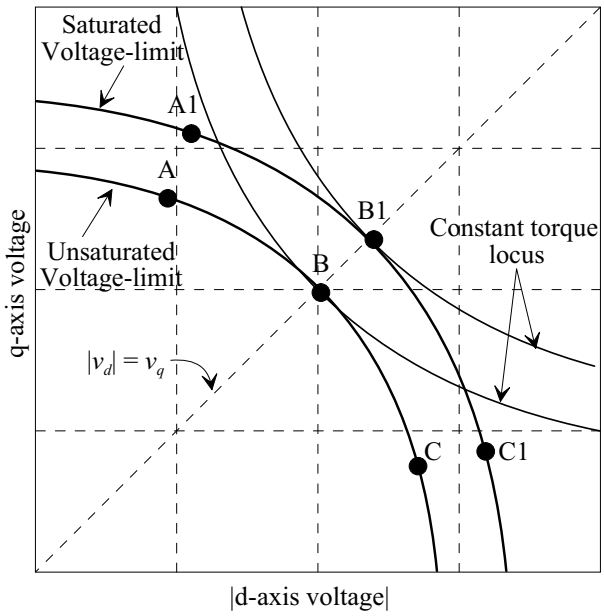

Figure 2.4: Voltage vector for producing maximum torque.

Now, if the voltage saturation strategy can be implemented with the field-weakening scheme, the voltage-limit boundary is enlarged as shown in Fig. 2.4. As the results, the base frequency ω_e becomes higher and the field-weakening area is widened. Without voltage saturation, the field-weakening operation starts at point A. Since the voltage limit $V_{s\max}$ become larger when the saturation strategy is used, the field-weakening operation starts at point A1 with higher v_{sd}^* and v_{sq}^* compared the ones at point A. The higher voltage references the higher base frequency, according to Eqs. (2.13) and (2.14). Then, more voltage available more power will available. Hence, for the same required torque the higher maximum frequency can be reached, since the mechanical power is

$$P_{mech} = T_e \omega_r \tag{2.18}$$

It means the field-weakening area is widened. In general, the torque capability is improved by maximizing the dc-bus voltage utilization. For instance, as shown in Fig. 2.4, a higher torque can be achieved at point B1 with implementing the saturation strategy rather than at point B without implementing the saturation strategy.

2.4.3 The Previous Field-Weakening Scheme

The voltage control strategy for providing maximum torque in the field weakening operation is implemented using two Proportional-Integral (PI) controllers [3] as shown in Fig. 2.5. One (PI_1) controls the field-component current i_{sd}^* to adjust the machine input voltage not exceeding the maximum voltage $V_{s\max}$ and following Eq. (2.12). Since the SPWM is used, $V_{s\max}$ is $\sqrt{\frac{3}{2}}\left(m\frac{V_{dc}}{2}\right)$ or v_c^* is set to $\sqrt{\frac{3}{2}}\left(m\frac{V_{dc}}{2}\right)$, where m is index modulation and $\sqrt{\frac{3}{2}}$ is the vector transformation factor. PI_1 controller input is $V_{s\max}^2 - (v_{sd}^{**2} + v_{sq}^{**2})$ to avoid the square-root computation. The other (PI_2) controls the maximum value $I_{q\max}$ of the torque-component current i_{sq}^* to adjust v_{sd}^*, so that follows the current limit of Eq. (2.17), when the field-weakening region II is entered. PI_2 controller input is $\frac{1}{2}V_{s\max}^2 - v_{sd}^{**2}$ to avoid the square-root computation as in PI_1 controller. Besides i_{sd}^* is fed to the d-axis current controller, it is also used to perform the current limiter as in Eq. (2.11). Then the limit value of Limiter2 is the minimum of $\sqrt{I_{s\max}^2 - i_{sd}^{*2}}$ and the PI_2 output.

Before the three-phase voltage references are fed to the SPWM inverter, each phase voltage reference is limited to $\frac{V_{dc}}{2}$ to guarantee the voltage reference amplitude doesn't exceed the triangle carrier amplitude. Although the voltage has been limited by PI_1, the voltage limiter (Limiter3) is still necessary to anticipate an overshoot phenomenon of the voltage controller in

transient. The limited voltage references are then transformed to the synchronous frame again and become the voltages feedback for the voltage controllers (PI_1 and PI_2).

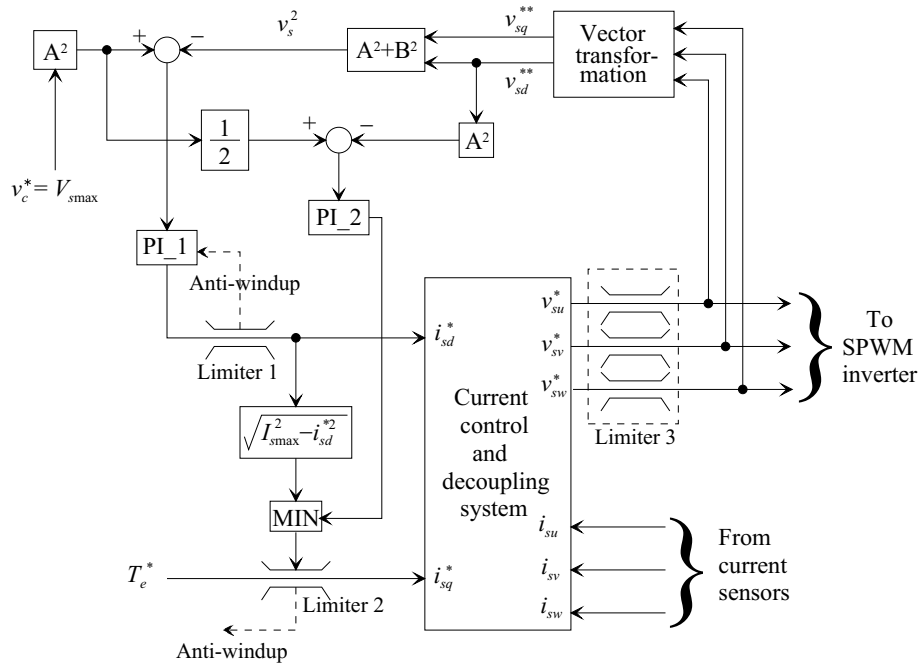

Figure 2.5: Field-weakening scheme based on voltage control strategy (previous scheme).

Voltage limitation will deteriorate the currents control performance since it causes an integrator windup phenomenon. To prevent integrator windup the "realizable references" [14] or "back-calculation" [15] method can be used. However, it is not needed in our proposed voltage limitation, since: first, the feedback voltages used by the field-weakening scheme (voltage controller) are the saturated voltage references and second, the phase voltage references are guaranteed not to exceed the triangle carrier amplitude. Therefore, the PWM outputs always linear with the input of the saturated voltage references.

The anti-windup strategy is applied in PI_1 since i^*_{sd} is limited to its rated value by Limiter1 (torque constant mode operation). However, a simpler way to prevent integrator windup can also be used instead. Here, when the control output reaches its limitation value, the integrator initial values of the controller for next iteration are reset to the initial values from previous iteration. This anti-windup strategy should also be applied in the speed controller if the torque reference T^*_e is provided by a speed controller, since the torque reference is limited by Limiter2.

2.4.4 The Proposed Field-Weakening Scheme

The problem that we are faced now, is how to combine the voltage control strategy [3] with the voltage saturation strategy as simple as possible. In the previous field-weakening scheme, the voltage saturation condition is difficult to be performed, since PI_1 controls the voltage to follow the voltage reference ($v_c^* = V_{s\max}$). The saturation condition occurs only when the voltage overshoot occurs. Although it is possible to enlarge the voltage reference ($v_c^* > V_{s\max}$), it is better if the voltage is only enlarged when a higher or maximum torque is required, not permanently. In another word, the available voltage should be varied proportional with the required torque. As an advantage, the voltage saturation condition only occurs when a high or maximum torque is required.

Field weakening control reduces the d-axis current reference in order to keep the voltage not exceed its maximum value. If it is seen in the opposite direction, the voltage will increase when the flux reference increase. Now if we assume a positive disturbance is added to the flux-producing current reference, the voltage controller (PI_1 in Fig. 2.5) will compensate it so that the voltage will be still kept constant and a saturated condition will be not achieved. In this case the flux will not increase and neither the torque. Then to achieve a saturated condition, a perfect controller like a PI controller should not be used. For this purpose a P (proportional) controller is used for the voltage controller instead of PI controller. As a result, a small steady state voltage error will occur and if a positive disturbance is added to the flux reference the voltage will be slightly increase proportional to the disturbance. If the voltage level greater than the limiter voltage, it will be saturated. Thus the effective voltage as seen by the motor is boosted.

In the steady state of field weakening area, the torque equation for the power-invariant form can be expressed as

$$T_e = N_p \frac{L_m^2}{L_r} i_{sd}^* . i_{sq}^* = k . v_{sd}^* . v_{sq}^* \tag{2.19}$$

where $k = -N_p L_m^2/(\sigma L_s^2 L_r \omega_e^2)$ and N_p is pole pairs number. As seen in Eq. (2.19), the torque is proportional to the product of i_{sd}^* and i_{sq}^*. It means the torque also depends on the flux. The higher flux is produced the higher torque is produced. Since i_{sq}^* is the torque producing current reference, the q-axis current i_{sq} will corresponds with the produced torque. Then if the i_{sq} is added to i_{sd}^* as disturbance, it will affect the flux, and then it will also affect the torque as a positive feedback signal. Since in the rotor flux oriented control the d-axis current i_{sd} is always positive value, the disturbance should be always positive value. It means the magnitude

of q-axis current i_{sq} only should be used as a disturbance. Fig. 2.6 shows block diagram of the proposed field-weakening scheme based on saturated voltage control strategy.

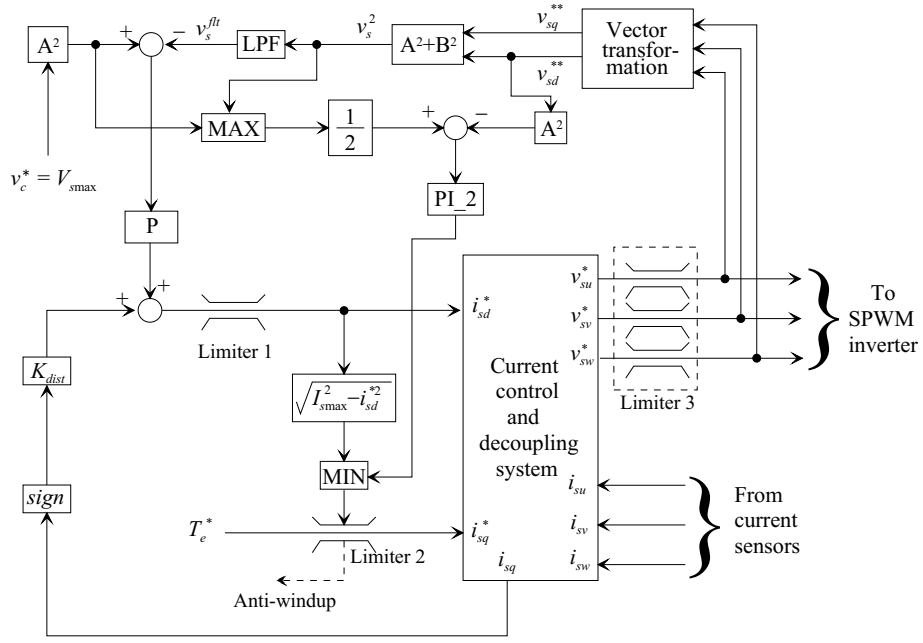

Figure 2.6: Field-weakening scheme based on saturated voltage control strategy (proposed scheme).

As seen in Fig. 2.6, a first order low-pass filter (LPF) with a cut-off frequency of 100 Hz filters the stator voltages firstly to improve the voltage control performance, since a P controller is used. The flux reference of the proposed strategy is expressed as

$$i_{sd}^{*} = K_{vp}(v_c^{*2} - v_s^{flt}) + sign.K_{dist}i_{sq} \tag{2.20}$$

where: $sign = 1$ if $i_{sq} > 0$ and $sign = -1$ if $i_{sq} < 0$. K_{vp} represents the proportional gain, v_s^{flt} is the filtered signal of the sum of squared d-axis and q-axis voltages, v_c^{*} is set to $V_{s\max}$, and K_{dist} is the disturbance gain.

Since the available voltage of the proposed field-weakening scheme is varied, the reference value for PI_2 should be modified as shown in Fig. 2.6. Here, the maximum of $V_{s\max}$ and $\sqrt{v_{sd}^{**2} + v_{sq}^{**2}}$ is chosen.

2.5 Experimental Results

2.5.1 Experimental setup

To validate the proposed scheme, experiments were carried out, and to verify it has an improved torque capability over the previous scheme, the comparison experimental results are also presented. Photograph of the experimental system is shown in Fig. 2.7. The test motor is a three-phase, four-poles, 750 W, 1410 rpm IM with the specifications listed in Table 2.1. All algorithms are implemented by the embedded 'C' code in a floating point DSP (Texas Instruments TMS320C32, operating speed 50MHz). An incremental encoder with 4096 ppr is mounted on the shaft for detecting the rotor position. The circle time (full control time) of whole experimental system is 0.1 milliseconds (sampling period is 0.1 milliseconds). The rotor speed and the speed control are sampled every 1 millisecond using an interrupt method.

Table 2.1: Induction motor parameters

750 W, 200 V, 4 poles, 1410 rpm		
R_s 2.76 Ω	R_r 2.9 Ω	Total inertia 0.0586 kg.m^2
L_s 234.9 mH	L_r 234.9 mH	L_m 227.9 mH

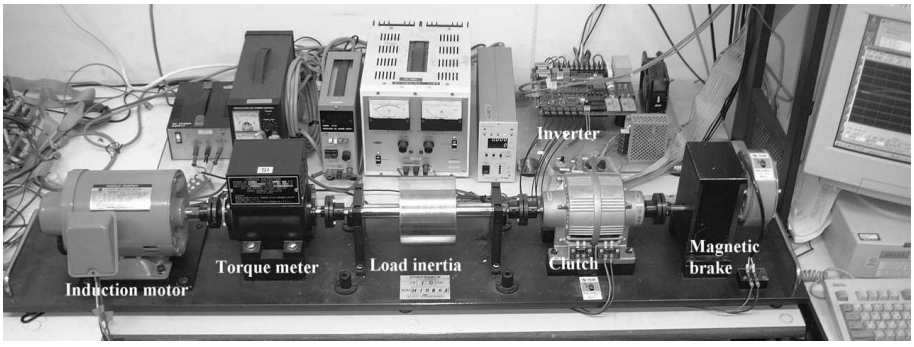

Figure 2.7: Induction motor laboratory experimental system.

2.5.2 Maximum torque test

The block diagram of experimental system is shown in Fig. 2.8. The motor is run from a standstill condition with the torque reference is set to its maximum (rated torque) for 15 seconds and then set to zero torque (see Fig. 2.9). This will forces the field-weakening scheme to provide a maximum torque in the whole motor operation.

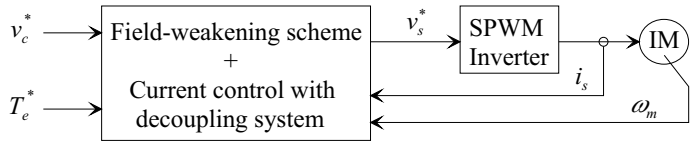

Figure 2.8: Block diagram of the experimental system.

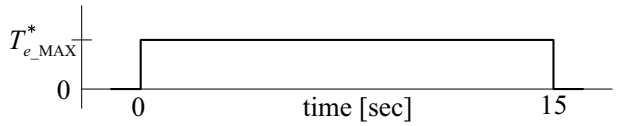

Figure 2.9: Torque reference for maximum torque test.

Figs. 2.10 and 2.11 show the experimental results of the maximum torque test operation of induction motor using the previous and proposed field-weakening scheme respectively. The base frequencies achieved by the previous and the proposed schemes are 1274.4 rpm and 1420.9 rpm, respectively. The maximum frequencies achieved by the previous and the proposed schemes are 6679.7 rpm and 7133.8 rpm. These results confirm that a higher base frequency and a widened field-weakening area are produced by the proposed scheme. This can be explained by comparing Fig. 2.10(d) with Fig. 2.11(d). The output voltages produced by the proposed scheme are larger than by the previous scheme. Fig. 2.10(e) and 2.11(e) show that the voltage locus of maximum torque moves along the voltage limit circle in region I and kept at the point of $v_{sq} = |v_{sd}|$ when the region II is entered.

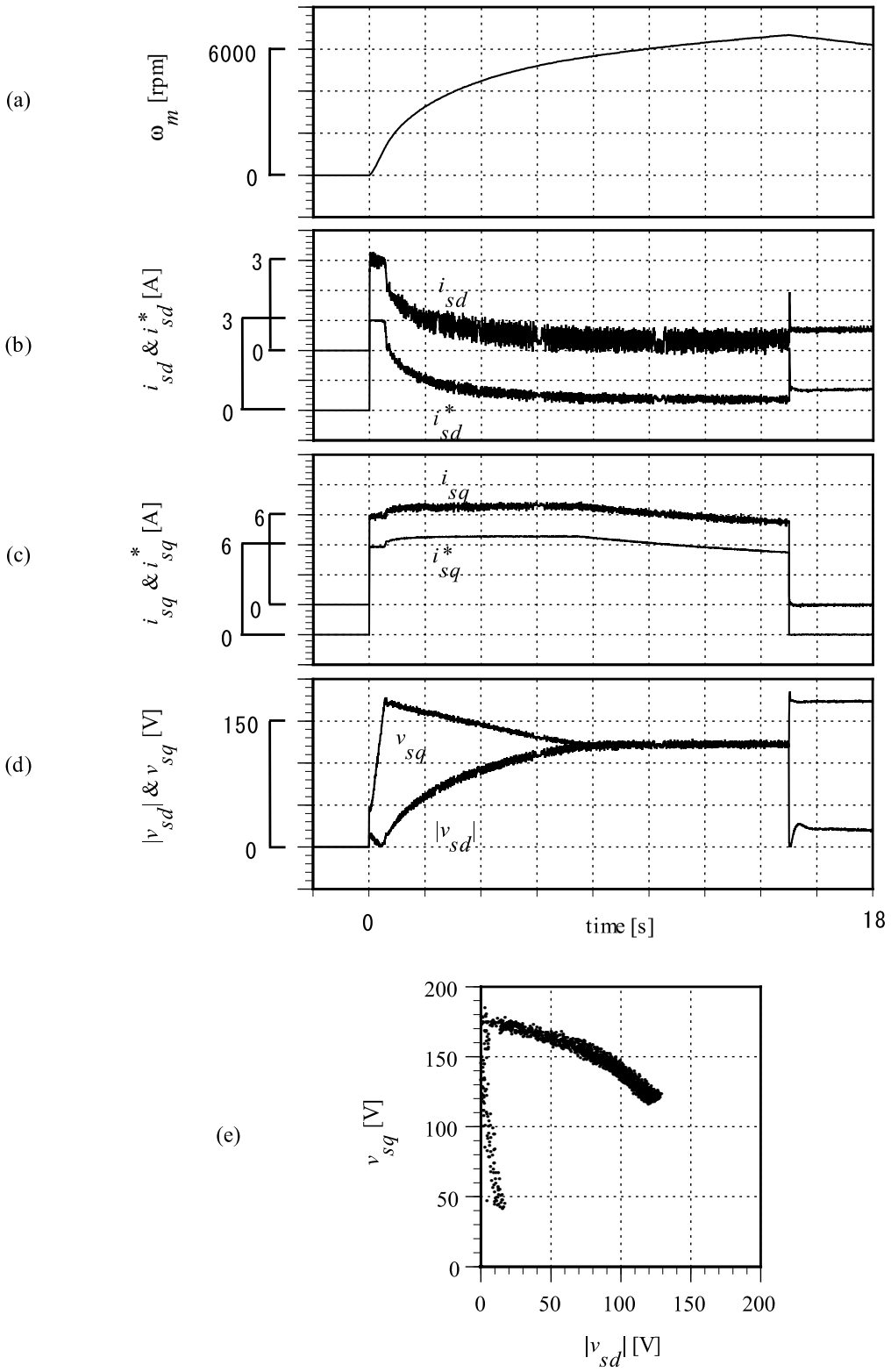

Figure 2.10: Experimental results of field-weakening operation based on unsaturated voltage control (previous scheme).

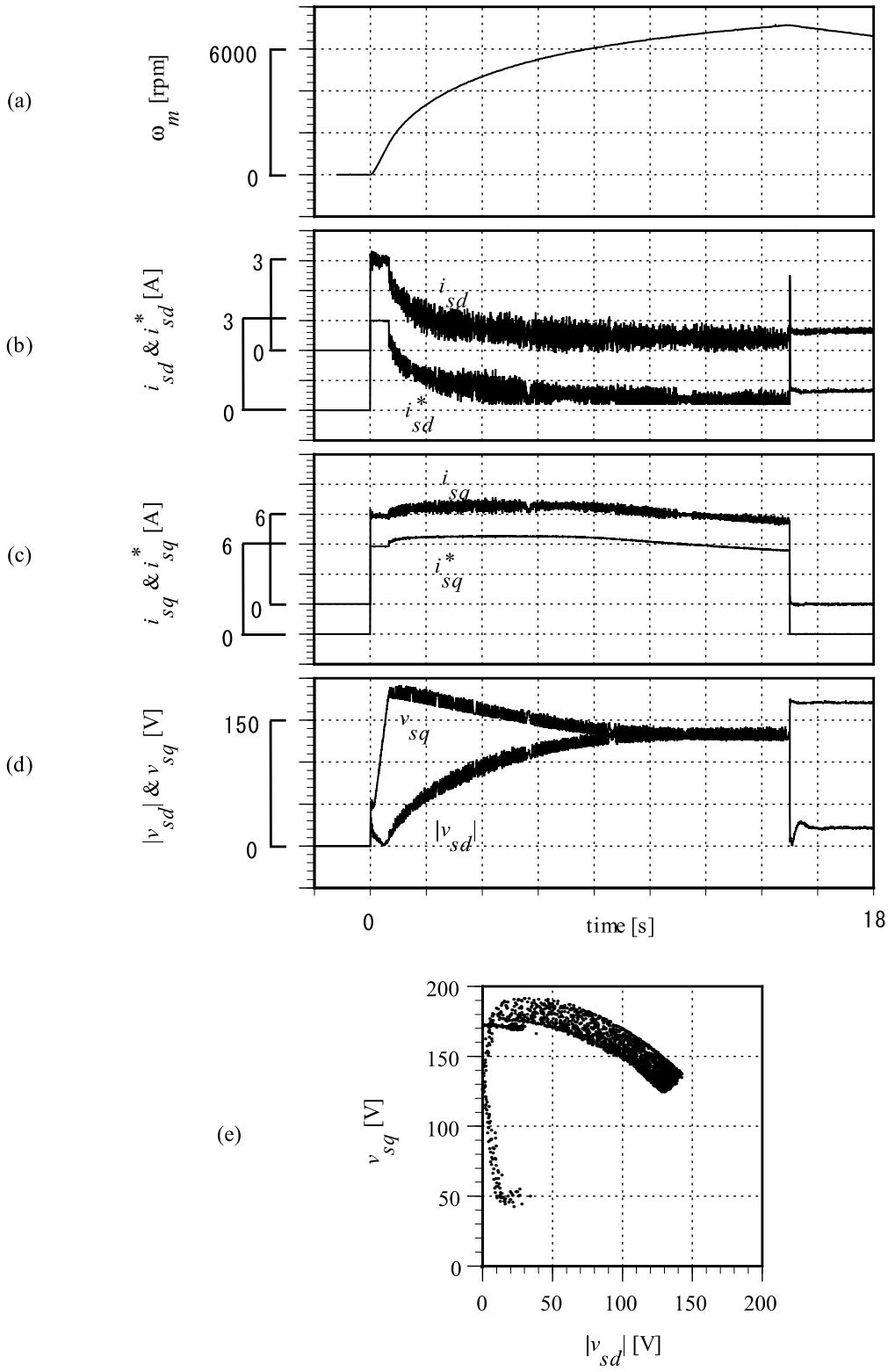

Figure 2.11: Experimental results of field-weakening operation based on saturated voltage control (proposed scheme).

2.5.3 Noise Effect

In the proposed field-weakening scheme, the saturation condition is stimulated by disturbing the flux current reference with the q-axis current i_{sq}. The performance of the flux current will be deteriorated by the current noise in i_{sq}. The noise effect in the field-weakening operation using the proposed scheme can be seen in Fig. 2.11(b) compared to Fig. 2.10(b). The ripple of i^*_{sd} by the proposed scheme was large. Although it did not really affect the d-axis current response (ripple of i_{sd} by proposed scheme was relatively same with one of i_{sd} by previous scheme), the same condition will be very difficult to be achieved if the motor power is large. Large motors have large leakage factor and currents. This situation affects noise conditions of the motor caused by the structure of the motor or by the electromagnetic interference (EMI). Large noise will cause the high performance of field-weakening operation very difficult to be achieved.

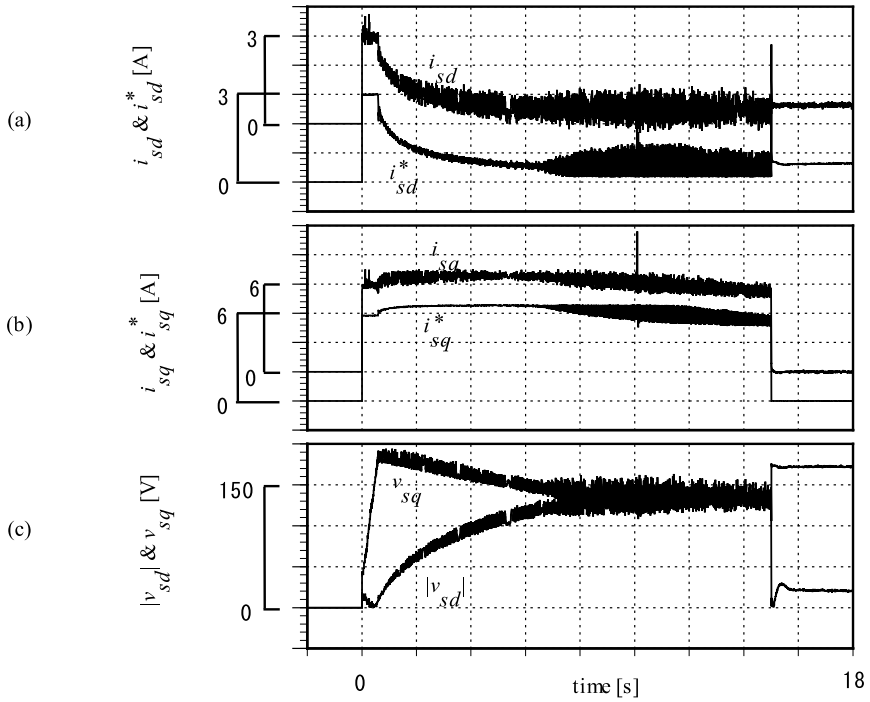

Figure 2.12: Noise effect investigating results when the voltage saturation condition is stimulated by i^*_{sq}.

To overcome the noise effect, the torque-producing current reference i^*_{sq} can be used to substitute i_{sq} as disturbance in stimulating a voltage saturation condition. Fig. 2.12 shows the

investigation results of the noise effect when the voltage saturation condition is stimulated by i^*_{sq}. As it is supposed, the ripple of i^*_{sd} can be eliminated in field-weakening region I, comparing i^*_{sd} of Fig. 2.12(a) with of Fig. 2.11(b). It is also less than the ripple of i^*_{sd} by previous scheme in Fig. 2.10(b). However, when region II is entered the ripple of i^*_{sd} in Fig. 2.12(a) becomes worse. This is because of the instability of the PI_2 controller. The control gains were not suitable anymore. It was found that the PI_2 control gain selection is critical, not only for the proposed scheme, but for the previous scheme too. For that reason we propose a new control strategy for the operation in region II.

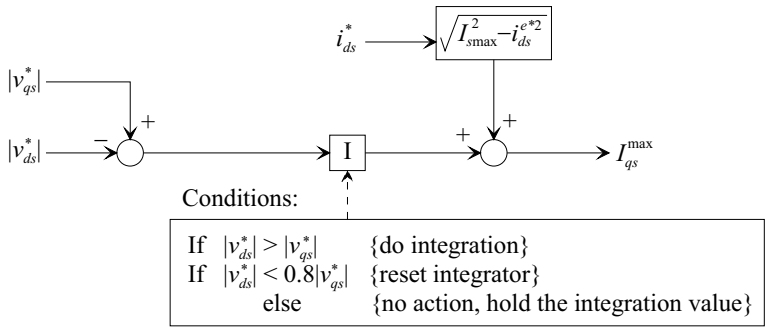

Figure 2.13: New control strategy for region II.

Fig. 2.13 shows the block diagram of the new control strategy for field-weakening operation in region II. The controller only uses an integrator with conditions. The input of integrator is $|v^*_{sq}| - |v^*_{sd}|$ and the output is used to adjust the maximum current, so that the voltages are kept to be $|v^*_{sq}| = |v^*_{sd}|$ when the field-weakening operation enters to region II. The integrator gain of 0.5 is selected. The selection of integrator gain is not critical. It can be used as it in all configurations in this chapter, including the configuration with the i_{sq} disturbance for stimulating the voltage saturation condition. The factor of 0.8 in the conditions of integrator is to provide a hysteresis band.

Fig. 2.14 shows the implementation results of the new control strategy for the field-weakening operation in region II. It is seen that the ripple of i^*_{sd} and i^*_{sq} occur when the region II is entered are eliminated by using the new control (comparing Fig. 2.14 with Fig. 2.12). These results are very important according to the application of the proposed field-weakening scheme with a large power motor.

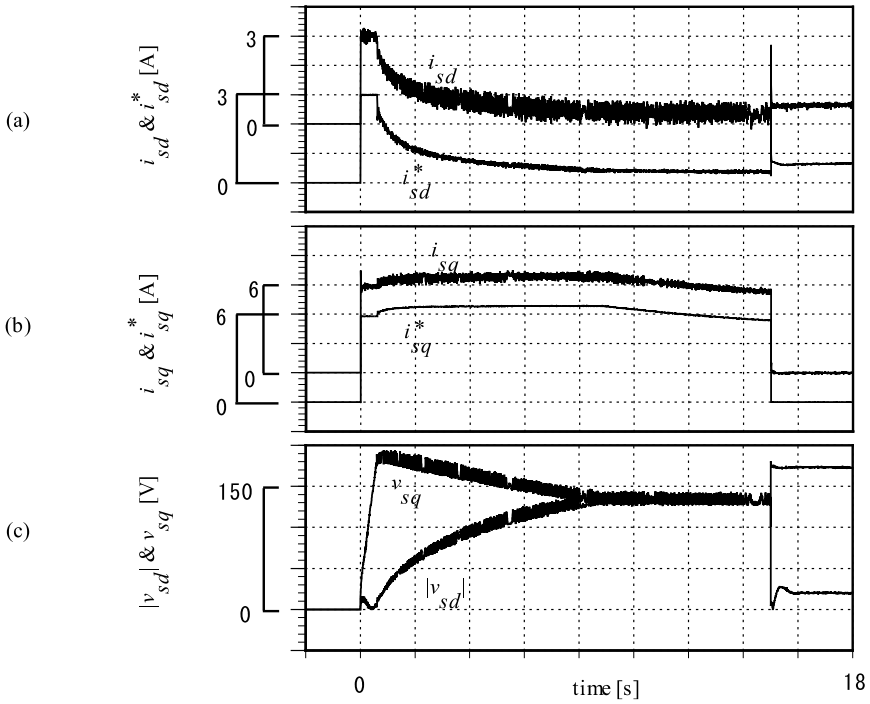

Figure 2.14: Experimental results of the new control strategy application for region II.

2.5.4 Behavior in Torque Requirement

As mentioned before, in the proposed field-weakening scheme, the voltage saturation condition only occurs when a higher or maximum torque is required. This statement is proven by looking to the locus of stationary voltages when the torque changed from maximum to zero torque condition as shown in Fig. 2.15. In the conventional scheme, the voltage saturation condition is not achieved. Therefore, the voltage locus always tracks the circle of voltage limit as shown in Fig. 2.15(a). When the proposed scheme is applied, in the maximum torque condition the voltage limit boundary becomes a hexagon (in case the disturbance gain $K_{dist} = 1$) and automatically returns to a circle when the maximum torque is not required anymore as shown in Fig. 2.15(b). The advantage of this situation, besides the torque capability is improved; the harmonic losses can be reduced in the high-speed operation when the maximum torque is not required (see the small ripple of experimental results in period time of 15 $\sim$ 18 seconds of Fig. 2.14). Fig. 2.15(c) shows the voltage locus in case the disturbance gain $K_{dist} = 2$. The voltage limit boundary becomes a 12-gon when the maximum torque is required and returns to a circle when the maximum torque is not required.

(a) Previous scheme

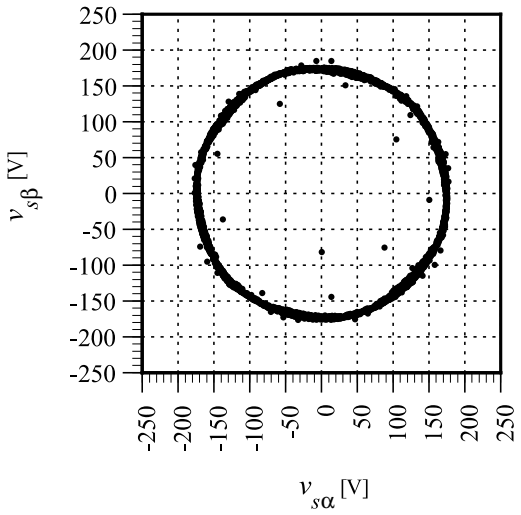

(b) Proposed scheme

($K_{dist} = 1$)

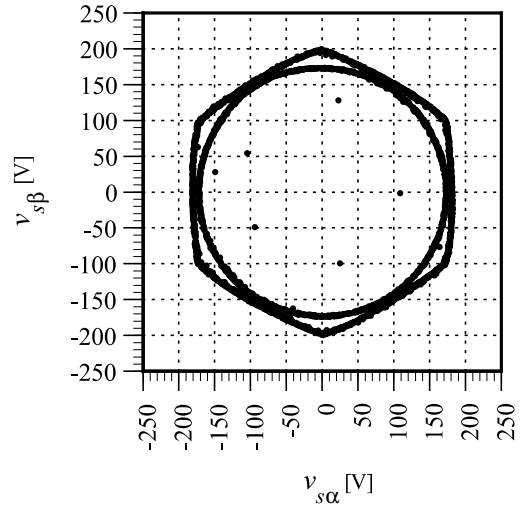

(c) Proposed scheme

($K_{dist} = 2$)

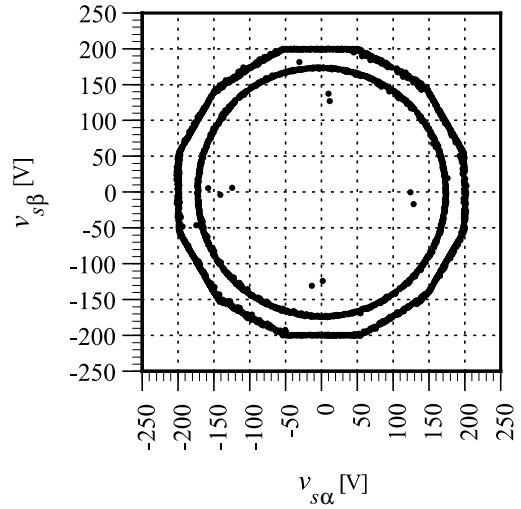

Figure 2.15: Locus of stationary voltages $v_{s\alpha}$ versus $v_{s\beta}$ when T_e changed from maximum torque to zero torque (Time: 13 Sec $\sim$ 16 Sec).

2.5.5 Speed Control Operation

Finally, the proposed scheme is tested with the speed control implementation. Fig. 2.16 shows the speed, torque, and flux comparisons of the speed control operation. The speed reference is changed from 500 rpm to 6500 rpm. It is proven that the proposed scheme provides a higher torque and flux as seen in Figs. 2.16(b) and 2.16(c) respectively. As a result, a higher speed response is achieved as shown in Fig. 2.16(a).

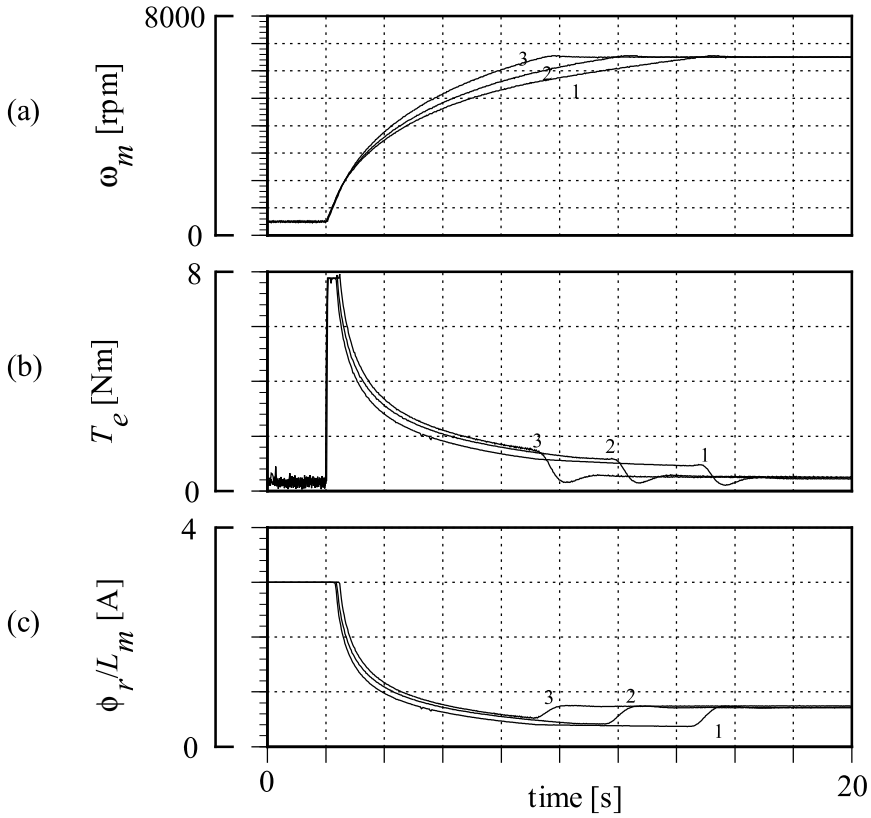

Figure 2.16: Speed, torque, and flux comparisons; 1: Conventional scheme 2: Proposed scheme ($K_{dist} = 1$) 3: Proposed scheme ($K_{dist} = 2$).

2.6 Performance Analysis

Performance analysis is carried out to give a recommendation for gain parameters selection of controller used in the field-weakening scheme. The classic Bode diagram method is used for the analysis purpose. Since Bode diagram method can only be applied to a linear system, the analysis model should be linearized around the equilibrium points.

2.6.1 Analysis model

As seen in Figs. 2.5 and 2.6, the overall configuration of the field-weakening scheme is very complex. It consists too many non-linear factors. Therefore, to reduce the burden of complexity some assumptions are established as follows:

1. The voltage source is a linear voltage source. So that the non-linear inverter is removed from the analysis model.

2. The current and voltage limitations are not applied. Since limiters are removed from the analysis model, the system gain is increased, which means the stability problem becomes worse than the system with limiters.

3. The control system for the field-weakening on region II is not included to the analysis model for simplicity purpose. Gain parameters selection of the new control for the field-weakening on region II (Fig. 2.13) is not critical.

With using the above assumptions, the analysis models for the previous and proposed field-weakening schemes are reconfigured as shown in Fig. 2.17. The analysis model of the proposed field-weakening scheme is configured into two configurations depends upon the disturbance which added to the d-axis current reference i^*_{sd} , i.e. i_{sq} and i^*_{sq} as shown Figs. 2.17(b) and 2.17(c) respectively. Then the linearized state equations for each configuration are derived using the Taylor series expansion method. These linearized state equations are expressed in appendix. The SISO (single input single output) systems those will be analyzed are the voltage control system and the q-axis current control system, which input and output of the systems are expressed in Eqs. (2.21) and (2.22) as indicated in Fig. 2.17.

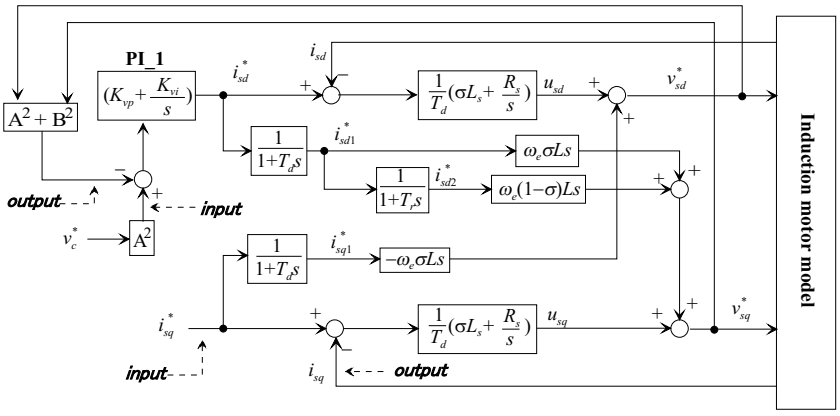

(a) Analysis model of the previous field-weakening scheme.

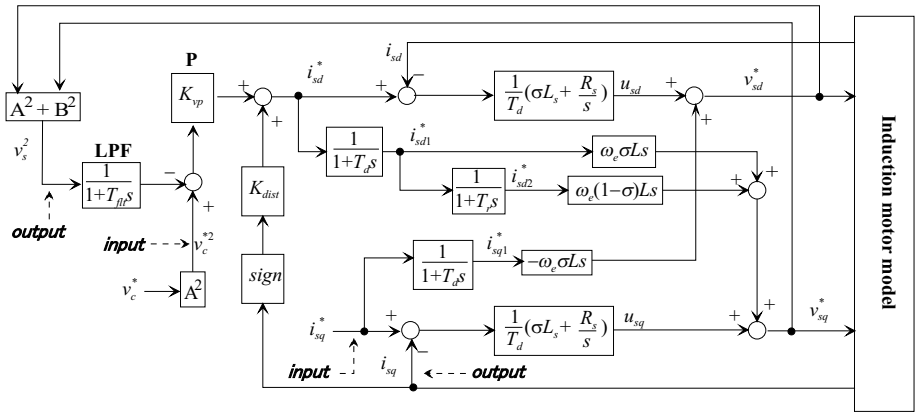

(b) Analysis model of the proposed field-weakening scheme (i_{sq} as disturbance).

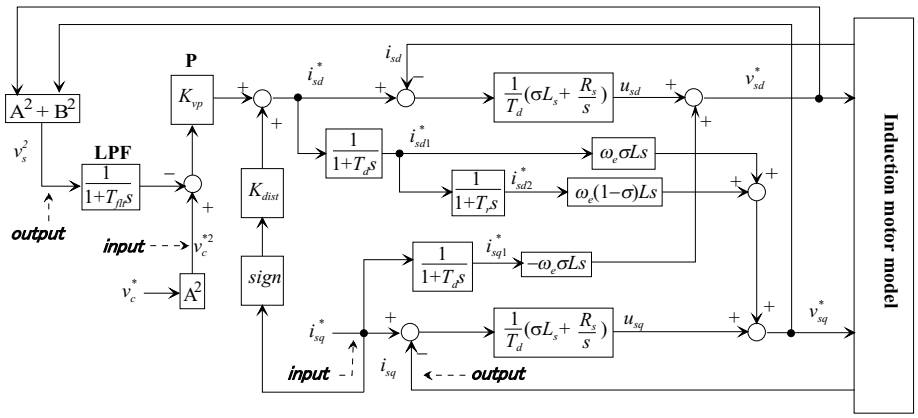

(c) Analysis model of the proposed field-weakening scheme (i^*_{sq} as disturbance).

Figure 2.17: Analysis model (Voltage control system $\frac{output}{input} = \frac{v_s^2}{v_c^{*2}}$, q-axis current control system $\frac{output}{input} = \frac{i_{sq}}{i^*_{sq}}$).

$$\frac{output}{input} = \frac{v_s^2}{v_c^{*2}} \tag{2.21}$$

$$\frac{output}{input} = \frac{i_{sq}}{i_{sq}^*} \tag{2.22}$$

The equilibrium points are determined by equating the derivation form of the non-linearized state equations of the system model to zero (the non-linearized state equations of the system model can be found in appendix). However, since it is difficult to make solution of these equations due to their complexity, some equilibrium points are taken from the experimental results as listed in Table 2.2. The experimental setup used here is the field-weakening system with implementing the speed control system. Data is collected in the steady-state condition, where the speed reference is set to 4000 rpm (418.88 rad/s). These experimental equilibrium points are then used to calculate the other equilibrium points as listed in Table 2.3.

Table 2.2: Equilibrium points taken from experimental results.

Equilibrium points	Previous	Proposed (i_{sq})	Proposed (i_{sq}^*)
ω_{r0}[rad/s]	418.88	418.92	418.89
i_{sd0}^*[A]	0.548	0.712	0.673
i_{sq0}^*[A]	1.127	1.141	1.138

2.6.2 Gain parameters setup

As mentioned in section 2.2, the currents control system is same for all system configurations. The proportional and integral gains of current controllers are set to $K_p = \frac{\sigma L_s}{T_d}$ and $K_i = \frac{R_s}{T_d}$ respectively, as for the stator currents to have a first order delay response of their references with time constant of T_d. Therefore, in the analysis system these gain parameters are not changed; only the gain parameters of the voltage controller are varied. As seen in Fig. 2.17, the

Table 2.3: The other equilibrium points.

Scheme item	Equilibrium points
Previous	$i_{sd0} = i^*_{sd10} = i^*_{sd20} = i^*_{sd0}; \quad i_{sq0} = i^*_{sq10} = i^*_{sq0}; \quad \phi_{dr0} = L_m i^*_{sd0}; \quad \phi_{qr0} = 0.0;$ $x_{sd0} = \frac{R_s i_{sd0}}{k_{idi}}; \quad x_{sq0} = \frac{R_s i_{sq0}}{k_{iqi}}; \quad x_{v0} = \frac{i_{sd0}}{k_{vi}};$ $v^*_{sd0} = v_{sd0} = R_s i_{sd0} - \sigma L_s N \omega_{m0} i_{sq0} - \frac{\sigma L_s R_r}{L_r} \frac{i^2_{sq0}}{i_{sd0}};$ $v^*_{sq0} = v_{sq0} = L_s N \omega_{m0} i_{sd0} + (R_s + \frac{L_s R_r}{L_r}) i_{sq0};$
Proposed, i_{sq} as disturbance	$i_{sd0} = i^*_{sd10} = i^*_{sd20} = i^*_{sd0}; \quad i_{sq0} = i^*_{sq10} = i^*_{sq0}; \quad \phi_{dr0} = L_m i^*_{sd0}; \quad \phi_{qr0} = 0.0;$ $x_{sd0} = \Big\{ [\frac{R_s + k_{idp}}{\sigma L_s} + \frac{R_r(1-\sigma)}{\sigma L_r}] i_{sd0} - [N\omega_{m0} + \frac{R_r i^*_{sq10}}{L_r i^*_{sd20}} + \frac{sign.k_{dist} k_{idp}}{\sigma L_s}] i_{sq0} - [\frac{MR_r}{\sigma L_s L_r^2}] \phi_{rd0}$ $- [\frac{N\omega_{m0} M}{\sigma L_s L_r}] \phi_{rq0} + [N\omega_{m0}] i^*_{sq10} + [\frac{R_r}{L_r}] \frac{i^{*2}_{sq10}}{i^*_{sd20}} + [\frac{k_{idp} k_{vp}}{\sigma L_s}] v^{flt}_{s0} - [\frac{k_{idp} k_{vp}}{\sigma L_s}] (v^{*2}_c) \Big\} \frac{\sigma L_s}{k_{idi}};$ $x_{sq0} = \Big\{ [N\omega_{m0} + \frac{R_r i^*_{sq10}}{L_r i^*_{sd20}}] i_{sd0} + [\frac{R_s + k_{iqp}}{\sigma L_s} + \frac{R_r(1-\sigma)}{\sigma L_r}] i_{sq0} + [\frac{NM\omega_{m0}}{\sigma L_s L_r}] \phi_{rd0} - [\frac{MR_r}{\sigma L_s L_r^2}] \phi_{rq0}$ $- [N\omega_{m0}] i^*_{sd10} - [\frac{(1-\sigma)R_r}{\sigma L_r}] i^*_{sq10} - [\frac{R_r}{L_r}] \frac{i^*_{sd10} i^*_{sq10}}{i^*_{sd20}} - [\frac{(1-\sigma)N\omega_{m0}}{\sigma}] i^*_{sd20} - [\frac{k_{iqp}}{\sigma L_s}] i^*_{sq0} \Big\} \frac{\sigma L_s}{k_{iqi}};$ $v^{flt}_{s0} = [-i_{sd0} + sign.k_{dist} i_{sq0} + k_{vp}(v^{*2}_c)] / k_{vp};$ $v_{sd0} = v^*_{sd0} = -k_{idp} i_{sd0} + k_{idp} sign.k_{dist} i_{sq0} + k_{idi} x_{sd0} - \sigma L_s N \omega_{m0} i^*_{sq10} - \sigma L_s \frac{R_r}{L_r} \frac{i^{*2}_{sq10}}{i^*_{sd20}}$ $- k_{idp} k_{vp} v^{flt}_{s0} + k_{idp} k_{vp} v^{*2}_c;$ $v_{sq0} = v^*_{sq0} = -k_{iqp} i_{sq0} + k_{iqi} x_{sq0} + \sigma L_s N \omega_m i^*_{sd10} + \frac{(1-\sigma) L_s R_r}{L_r} i^*_{sq10} + \frac{\sigma L_s R_r}{L_r} \frac{i^*_{sd10} i^*_{sq10}}{i^*_{sd20}}$ $+ (1-\sigma) L_s N \omega_m i^*_{sd20} + k_{iqp} i^*_{q0};$
Proposed, i^*_{sq} as disturbance	$i_{sd0} = i^*_{sd10} = i^*_{sd20} = i^*_{sd0}; \quad i_{sq0} = i^*_{sq10} = i^*_{sq0}; \quad \phi_{dr0} = L_m i^*_{sd0}; \quad \phi_{qr0} = 0.0;$ $x_{sd0} = \Big\{ [\frac{R_s + k_{idp}}{\sigma L_s} + \frac{R_r(1-\sigma)}{\sigma L_r}] i_{sd0} - [N\omega_{m0} + \frac{R_r i^*_{sq10}}{L_r i^*_{sd20}}] i_{sq0} - [\frac{sign.k_{dist} k_{idp}}{\sigma L_s}] i^*_{sq0} - [\frac{MR_r}{\sigma L_s L_r^2}] \phi_{dr0}$ $- [\frac{N\omega_{m0} M}{\sigma L_s L_r}] \phi_{qr0} + [N\omega_{m0}] i^*_{sq10} + [\frac{R_r}{L_r}] \frac{i^{*2}_{sq10}}{i^*_{sd20}} + [\frac{k_{idp} k_{vp}}{\sigma L_s}] v^{flt}_{s0} - [\frac{k_{idp} k_{vp}}{\sigma L_s}] (v^{*2}_c) \Big\} \frac{\sigma L_s}{k_{idi}};$ $x_{sq0} = \Big\{ [N\omega_{m0} + \frac{R_r i^*_{sq10}}{L_r i^*_{sd20}}] i_{sd0} + [\frac{R_s + k_{iqp}}{\sigma L_s} + \frac{R_r(1-\sigma)}{\sigma L_r}] i_{sq0} + [\frac{NM\omega_{m0}}{\sigma L_s L_r}] \phi_{dr0} - [\frac{MR_r}{\sigma L_s L_r^2}] \phi_{qr0}$ $- [N\omega_{m0}] i^*_{sd10} - [\frac{(1-\sigma)R_r}{\sigma L_r}] i^*_{sq10} - [\frac{R_r}{L_r}] \frac{i^*_{sd10} i^*_{sq10}}{i^*_{sd20}} - [\frac{(1-\sigma)N\omega_{m0}}{\sigma}] i^*_{sd20} - [\frac{k_{iqp}}{\sigma L_s}] i^*_{sq0} \Big\} \frac{\sigma L_s}{k_{iqi}};$ $v^{flt}_{s0} = [-i_{sd0} + sign.k_{dist} i^*_{sq0} + k_{vp}(v^{*2}_c)] / k_{vp};$ $v_{sd0} = v^*_{sd0} = -k_{idp} i_{sd0} + k_{idp} sign.k_{dist} i^*_{sq0} + k_{idi} x_{sd0} - \sigma L_s N \omega_m i^*_{sq10} - \sigma L_s \frac{R_r}{L_r} \frac{i^{*2}_{sq10}}{i^*_{sd20}}$ $- k_{idp} k_{vp} v^{flt}_{s0} + k_{idp} k_{vp} v^{*2}_c;$ $v_{sq0} = v^*_{sq0} = -k_{iqp} i_{sq0} + k_{iqi} x_{sq0} + \sigma L_s N \omega_{m0} i^*_{sd10} + \frac{(1-\sigma) L_s R_r}{L_r} i^*_{sq10} + \frac{\sigma L_s R_r}{L_r} \frac{i^*_{sd10} i^*_{sq10}}{i^*_{sd20}}$ $+ (1-\sigma) L_s N \omega_{m0} i^*_{sd20} + k_{iqp} i^*_{sq0};$

where: $k_{idp} = \frac{\sigma L_s}{T_d}$, $k_{idi} = \frac{R_s}{T_d}$, $k_{iqp} = \frac{\sigma L_s}{T_d}$, and $k_{iqi} = \frac{R_s}{T_d}$

previous field-weakening scheme has two gain parameters of PI_1 controller to be varied, i.e. K_{vp} and K_{vi}, and the proposed field-weakening scheme has three parameters to be varied, i.e. K_{vp} of the P controller, T_{flt} of the LPF, and K_{dist} of the disturbance gain. The gain parameters setting for performance analysis is listed in Table 2.4. The Fixed values in Table 2.4 means the initial parameter setting. When one of parameter is varied, the fixed value of this parameter is replaced by the corresponding varied values in Table 2.4.

Table 2.4: Gain parameters setting for performance analysis purpose.

Field-weakening scheme	Fixed values				Varied values			
	K_{vp}	K_{vi}	T_{flt}	K_{dist}	K_{vp}	K_{vi}	T_{flt}	K_{dist}
Previous	$1x10^{-4}$	0.05	–	–	$1x10^{-5}$ $5x10^{-5}$ $1x10^{-4}$ $5x10^{-4}$ $1x10^{-3}$	0.01 0.025 0.05 0.075 0.1	–	–
Proposed	$1x10^{-3}$	–	0.01	1.0	$1x10^{-4}$ $5x10^{-4}$ $1x10^{-3}$ $5x10^{-3}$ $1x10^{-2}$	–	0.001 0.005 0.01 0.05 0.1	0.0 0.5 1.0 1.5 2.0

2.6.3 Analysis results

Stability of the system can be determined by observing the gain margin (GM) and phase margin (PM) in the bode diagram of the open-loop system. If the gain margin and phase margin are positive the system is stable, and if they are negative the system is unstable. To achieve a satisfied performance, the phase margin should be in between 30^o and 60^o, and the gain margin should be larger than 6 dB [16]. With these values, the control system has a guarantee of its stability, even the open-loop gain and the time constant are changed until a certain value. The requirement of open-loop gain margin that should be in between 30^o and 60^o, corresponds with slope of the open-loop gain at gain crossover frequency that should be less than -40 dB/dekade. Practically, the slope of -20 dB/dekade is needed to maintain the system stability [16]. If the

slope is -40 dB/dekade, the system can be stable or unstable. If the slope is -60 dB/dekade or more then the system is unstable.

The close-loop and open-loop frequency responses and also the close-loop step responses of all performance analysis configurations are shown in Figs. 2.18∼2.25. The observation of analysis is concentrated to the open-loop frequency response of the voltage control system $Gol = \frac{v_s^2}{v_c^{*2}}$, which is shown in the sub-figure (c) of Figs. 2.18∼2.25. The close-loop frequency and step responses are observed to support or confirm the analysis of the open-loop frequency response. The frequency and step responses of the q-axis current control system are observed to see the coupling effect of the voltage control system.

First, we look to the performance of the previous field-weakening scheme when K_{vp} is varied (see Fig. 2.18(c)). The slopes of open-loop gain at gain crossover frequency for all cases of K_{vp} values are less than -40 dB/dekade. Gain margin for all cases of K_{vp} values are larger than 6 dB. Then if we observe the phase margin, the cases of $K_{vp} = 5\text{x}10^{-5}$ (PM$\approx 40^o$) and $K_{vp} = 1\text{x}10^{-4}$ (PM$\approx 55^o$) are acceptable for good performance. These are confirmed when we look to the step response in Fig. 2.18(e). The coupling effect of the voltage control system to the q-axis current system appears as shown in Fig. 2.18(d). However, it is still acceptable since the q-axis control system is still stable, and the effect to its close-loop system is small.

Figure 2.19 shows the performance of the previous field-weakening scheme when K_{vi} is varied. Almost for all cases (except for $K_{vi} = 0.01$), the performances are acceptable (GM > 6 dB, PM$\approx 55^o$). The selection of K_{vi} is not critical ($K_{vi} = 0.05 \sim 0.1$). And also the coupling effect of voltage control system to the q-axis current control system is negligible.

The purpose of the proposed field-weakening is to increase the voltage that is fed to the motor by combining the voltage saturation strategy. The saturation condition is stimulated by adding the q-axis current to the d-axis current reference, so that a higher stator voltage can be produced that is proportional to the required torque. If the saturation strategy (the voltage limiter) is not implemented as in the analysis model, the voltage control response of the proposed field-weakening scheme should has a higher over-shoot compare to one of the previous field-weakening scheme. However, the stability should still can be guaranteed.

Figure 2.20 shows the performance of the proposed field-weakening scheme with i_{sq} as disturbance when K_{vp} is varied. As it is supposed, a large over-shoot occurs as seen in the step response of Fig. 2.20(e). The voltages are oscillated for the cases of $K_{vp} = 5\text{x}10^{-3}$ and $K_{vp} = 1\text{x}10^{-2}$, because the phase margin are too small (PM $\approx 30^o$ and 20^o respectively as shown in Fig. 2.20(c)). For all cases the system is stable. The good performance is achieved for

the cases of $K_{vp} = 5\text{x}10^{-4}$ (GM≈ 35 dB and PM≈ 60°) and $K_{vp} = 1\text{x}10^{-3}$ (GM≈ 30 dB and PM≈ 55°). If we see to the close-loop response (Fig. 2.20(a)), around the resonant frequency the system is leading, so that its stability is better than the previous scheme has. And since the bandwidth frequency is wider, the rise time response of the proposed scheme is faster. The coupling effect of the voltage control system to the q-axis current control system can also be negligible here.

Figure 2.21 shows the performance of the proposed field-weakening scheme with i_{sq} as disturbance when T_{flt} is varied. The good performance is achieved for the cases of $T_{flt} = 0.005$ (GM≈ 25 dB and PM≈ 55°) and $T_{flt} = 0.01$ (GM≈ 30 dB and PM≈ 55°). If T_{flt} is too large, the over-shoot becomes larger and the convergent time becomes longer, which could lead to an unstable condition as seen in the step response of Fig. 2.21(e). This is because the gain margin is too large while the phase margin is relatively small; for case of $T_{flt} = 0.05$, GM≈ 45 dB and PM≈ 40° and for $T_{flt} = 0.1$, GM≈ 50 dB and PM≈ 30°.

Figure 2.22 shows the performance of the proposed field-weakening scheme with i_{sq} as disturbance when K_{dist} is varied. The variation on K_{dist} doesn't affect the performance of the system. This means the proposed field-weakening scheme is robust against the K_{dist} variation. K_{dist} has an effect to torque producing as shown in Fig. 2.16. The larger K_{dist} the higher torque is produced.

Figure 2.23 shows the performance of the proposed field-weakening scheme with i^*_{sq} as disturbance when K_{vp} is varied. As seen in Fig. 2.23(c), the system is stable for all cases of K_{vp}, since the phase response never reaches $-180°$. Here, the gain margin can't be determined, therefore, the satisfied performance is observed by looking to the close-loop step response of Fig. 2.23(e). The good performance is achieved for the cases of $K_{vp} = 5\text{x}10^{-4}$ and $K_{vp} = 1\text{x}10^{-3}$, which are same with the case of the proposed field-weakening scheme with i_{sq} as disturbance. The damping factor of the proposed field-weakening scheme with i^*_{sq} as disturbance is better than the one of the proposed field-weakening scheme with i_{sq} as disturbance (see Fig. 2.23(e) compared with Fig. 2.20(e)).

Figure 2.24 shows the performance of the proposed field-weakening scheme with i^*_{sq} as disturbance when T_{flt} is varied. As well as the proposed field-weakening scheme with i^*_{sq} as disturbance, here the good performance is achieved for the cases of $T_{flt} = 0.005$ and $T_{flt} = 0.01$ as shown in Fig. 2.24(e).

Figure 2.25 shows the performance of the proposed field-weakening scheme with i^*_{sq} as disturbance when K_{dist} is varied. Although the robustness against K_{dist} variation of proposed

field-weakening scheme with i_{sq}^{*} as disturbance isn't as good as the one with i_{sq} as disturbance, the system is stable for all cases of K_{dist}. The advantage of the proposed scheme with i_{sq}^{*} as disturbance over the one with with i_{sq} as disturbance is that the noise effect from the measured q-axis current i_{sq} can be avoided as proven by experimental results in Subsection 2.5.3.

Finally, Fig. 2.26 shows the comparison performance of all field-weakening schemes when the speed is varied from 100 rad/s until 500 rad/s where the gain parameters are set to the fixed values in Table 2.4. In general with these gain parameters all systems are stable. All field weakening systems have no stability problem with very high speed application, since the gain margin and phase margin are large enough. Especially, for the proposed field-weakening scheme with i_{sq}^{*} as disturbance; theoretically the system is always stable. The rise time response of the proposed field-weakening schemes are faster compared with the previous one.

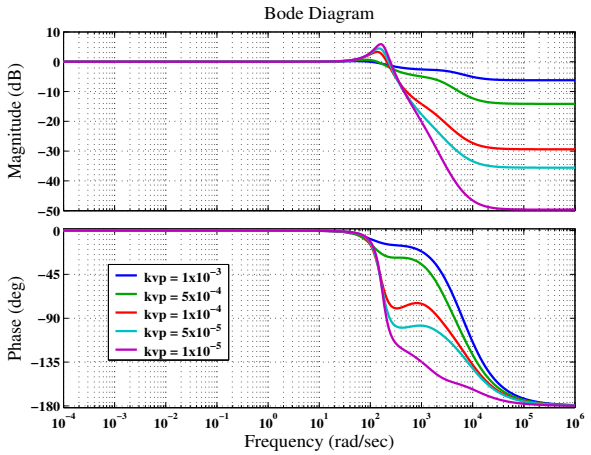

(a) Frequency response of close-loop system of $Gcl = \frac{v_s^2}{v_c^{*2}}$

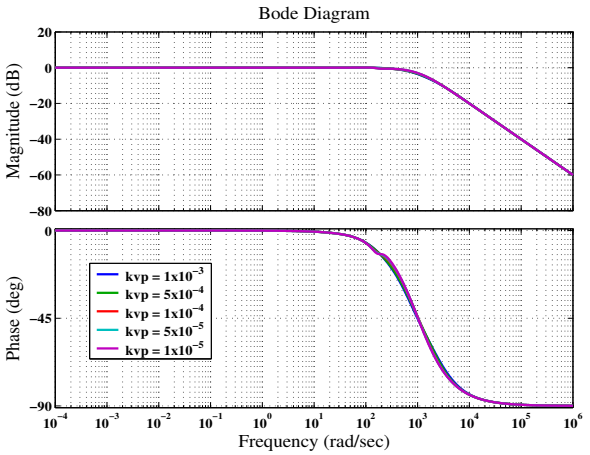

(b) Frequency response of close-loop system of $Gcl = \frac{i_{sq}}{i_{sq}^*}$

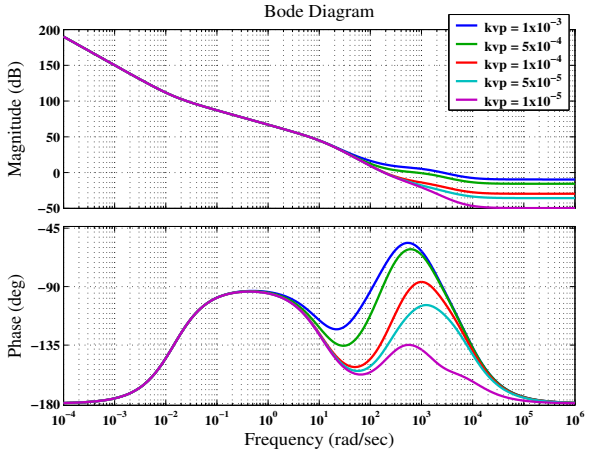

(c) Frequency response of open-loop system of $Gol = \frac{v_s^2}{v_c^{*2}}$

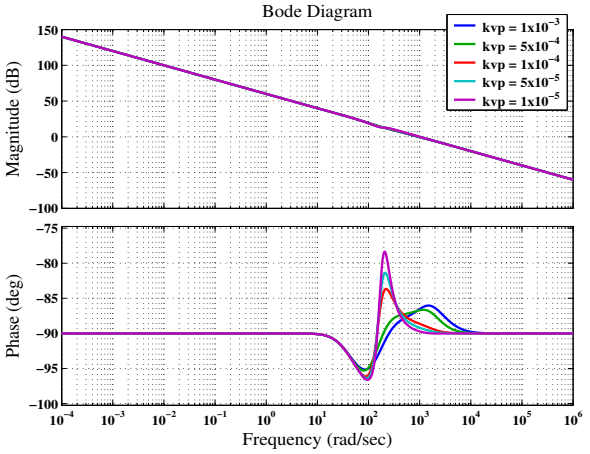

(d) Frequency response of open-loop system of $Gol = \frac{i_{sq}}{i_{sq}^*}$

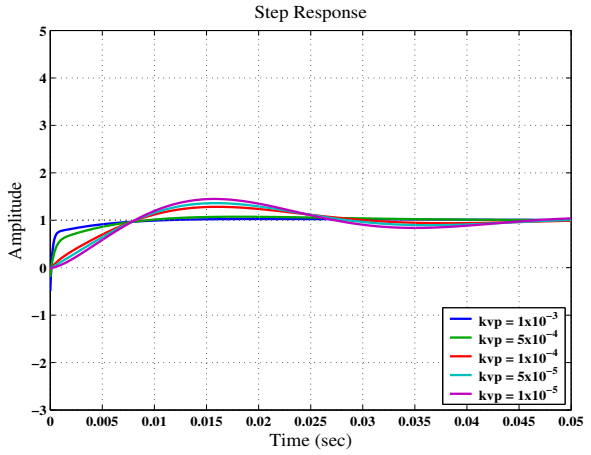

(e) Step response of close-loop system of $Gcl = \frac{v_s^2}{v_c^{*2}}$

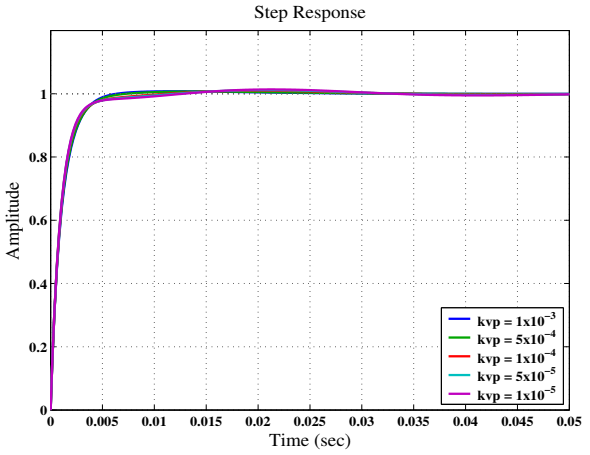

(f) Step response of close-loop system of $Gcl = \frac{i_{sq}}{i_{sq}^*}$

Figure 2.18: Performance of the previous filed-weakening scheme when K_{vp} is varied.

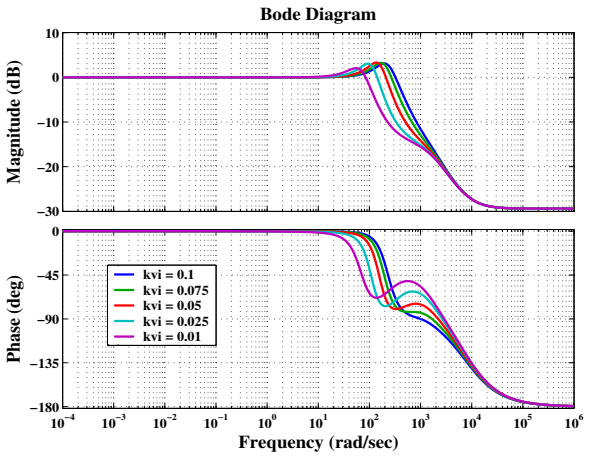

(a) Frequency response of close-loop system of $Gcl = \frac{v_s^2}{v_c^{*2}}$

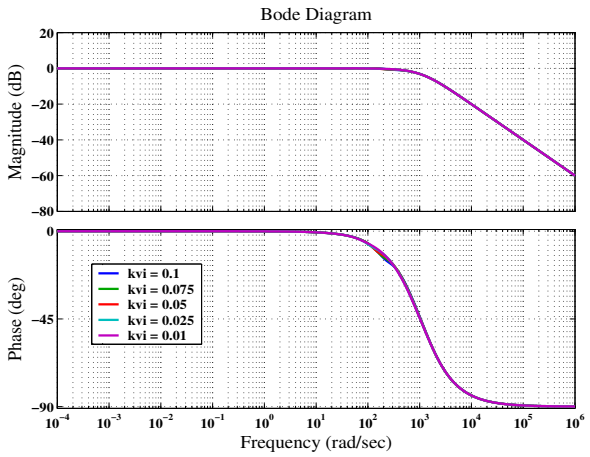

(b) Frequency response of close-loop system of $Gcl = \frac{i_{sq}}{i_{sq}^*}$

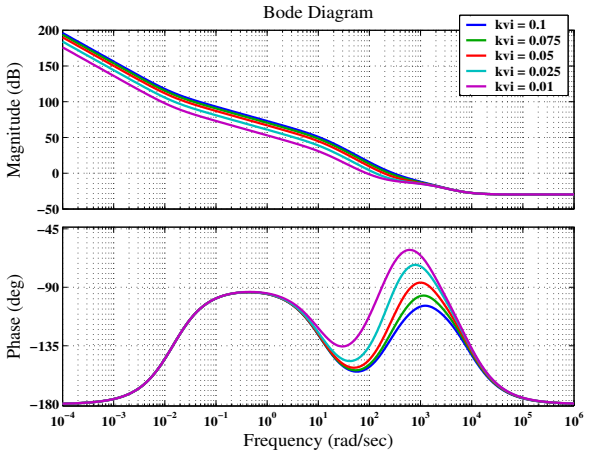

(c) Frequency response of open-loop system of $Gol = \frac{v_s^2}{v_c^{*2}}$

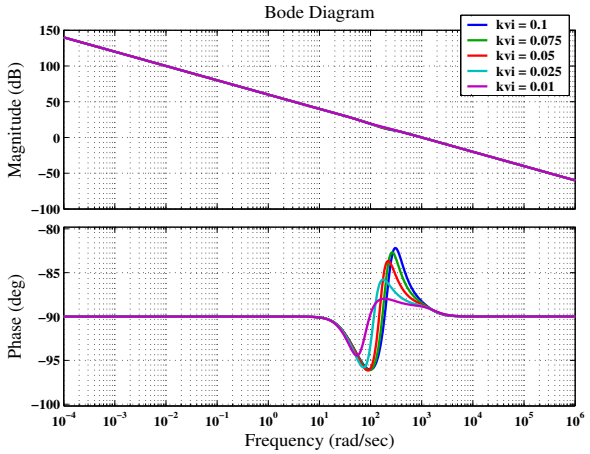

(d) Frequency response of open-loop system of $Gol = \frac{i_{sq}}{i_{sq}^*}$

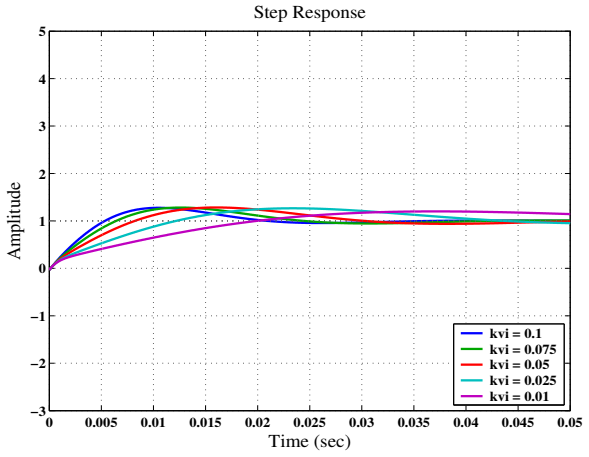

(e) Step response of close-loop system of $Gcl = \frac{v_s^2}{v_c^{*2}}$

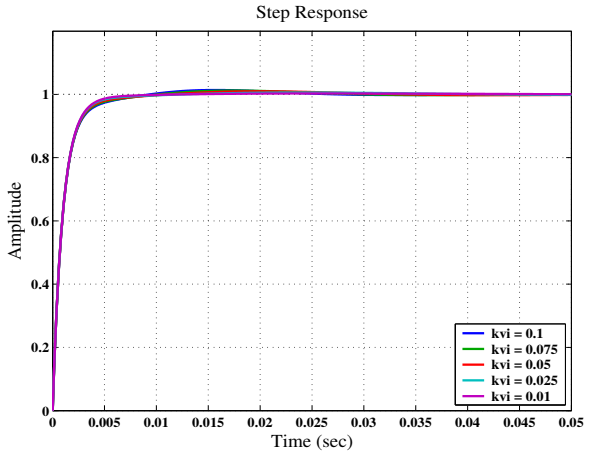

(f) Step response of close-loop system of $Gcl = \frac{i_{sq}}{i_{sq}^*}$

Figure 2.19: Performance of the previous filed-weakening scheme when K_{vi} is varied.

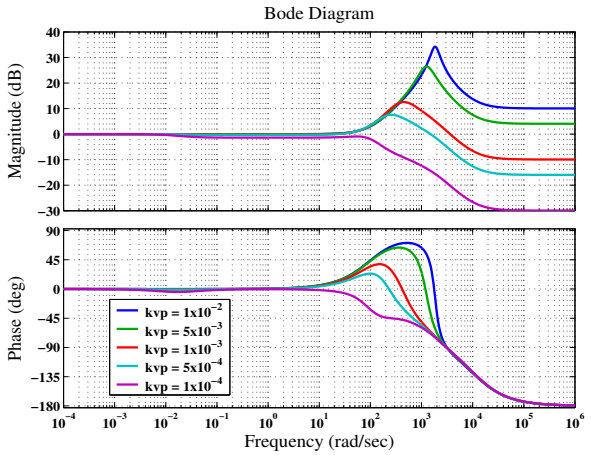

(a) Frequency response of close-loop system of $Gcl = \frac{v_s^2}{v_c^{*2}}$

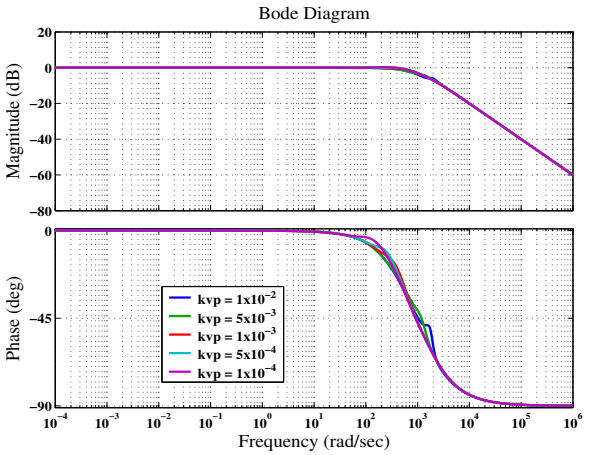

(b) Frequency response of close-loop system of $Gcl = \frac{i_{sq}}{i_{sq}^*}$

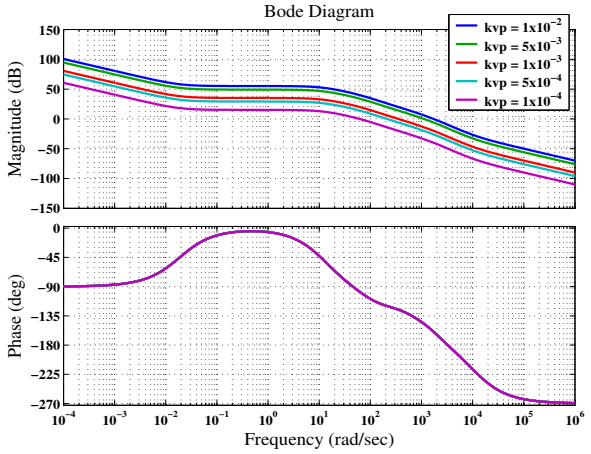

(c) Frequency response of open-loop system of $Gol = \frac{v_s^2}{v_c^{*2}}$

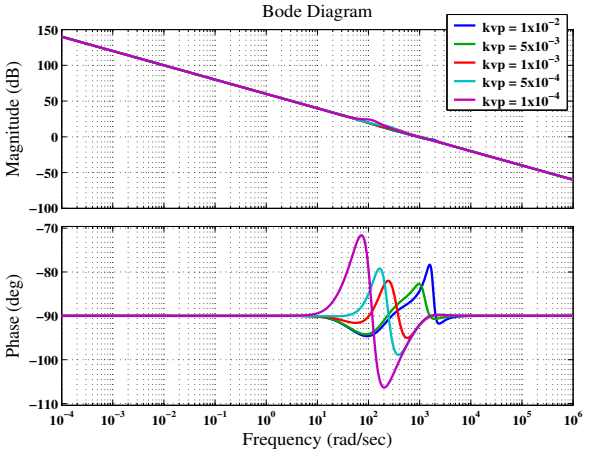

(d) Frequency response of open-loop system of $Gol = \frac{i_{sq}}{i_{sq}^*}$

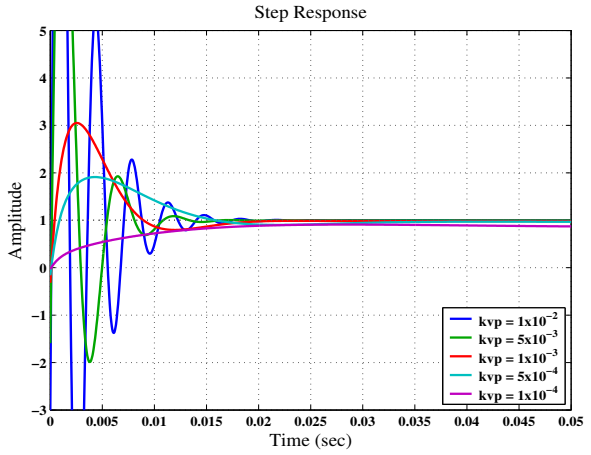

(e) Step response of close-loop system of $Gcl = \frac{v_s^2}{v_c^{*2}}$

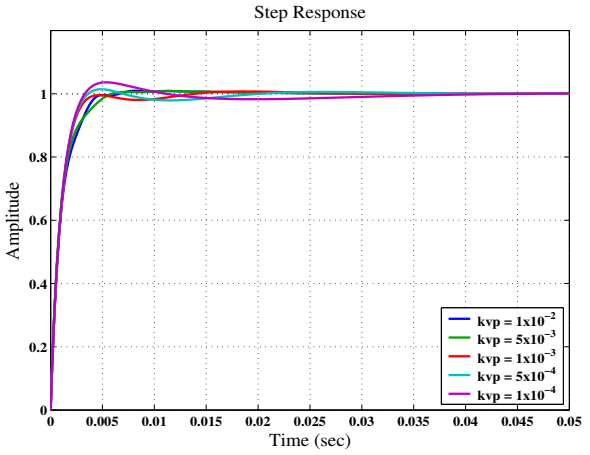

(f) Step response of close-loop system of $Gcl = \frac{i_{sq}}{i_{sq}^*}$

Figure 2.20: Performance of the proposed filed-weakening scheme when K_{vp} is varied (saturation condition is stimulated by i_{sq} as disturbance).

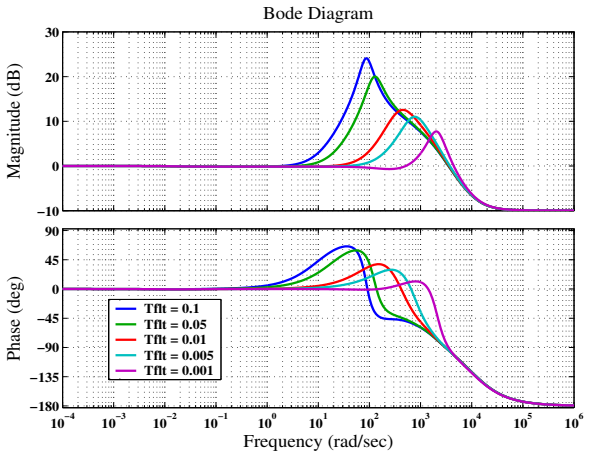

(a) Frequency response of close-loop system of $Gcl = \frac{v_s^2}{v_c^{*2}}$

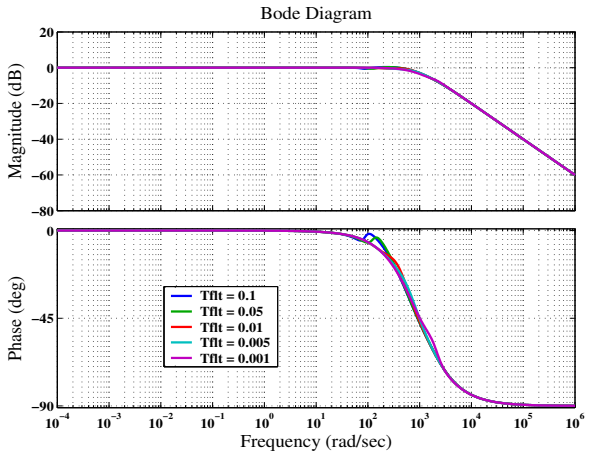

(b) Frequency response of close-loop system of $Gcl = \frac{i_{sq}}{i_{sq}^*}$

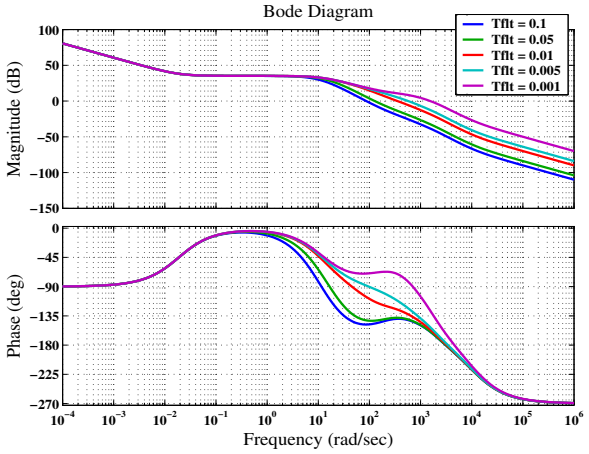

(c) Frequency response of open-loop system of $Gol = \frac{v_s^2}{v_c^{*2}}$

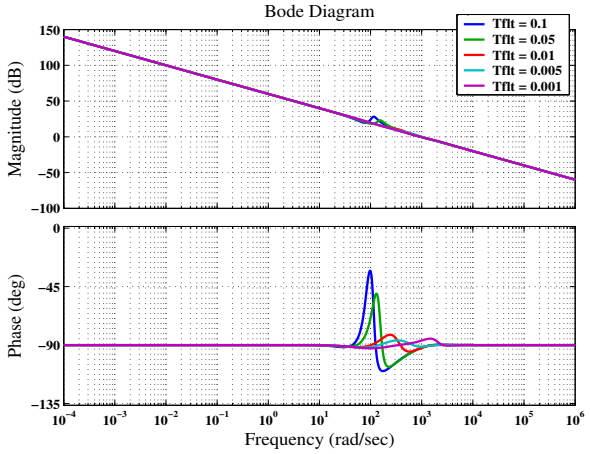

(d) Frequency response of open-loop system of $Gol = \frac{i_{sq}}{i_{sq}^*}$

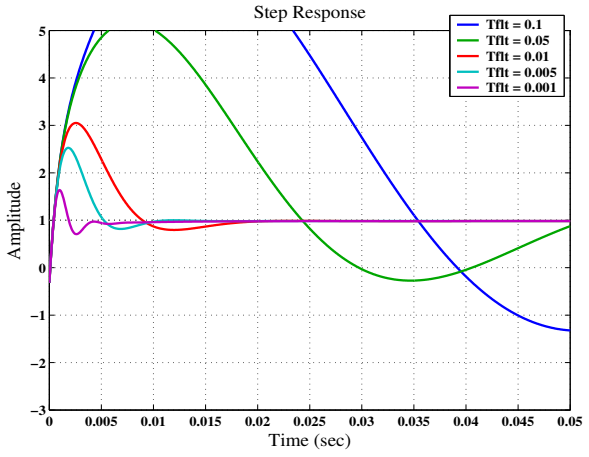

(e) Step response of close-loop system of $Gcl = \frac{v_s^2}{v_c^{*2}}$

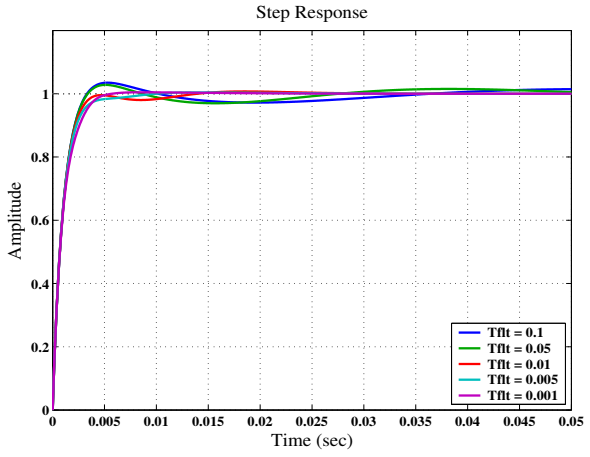

(f) Step response of close-loop system of $Gcl = \frac{i_{sq}}{i_{sq}^*}$

Figure 2.21: Performance of the proposed filed-weakening scheme when T_{flt} is varied (saturation condition is stimulated by i_{sq} as disturbance).

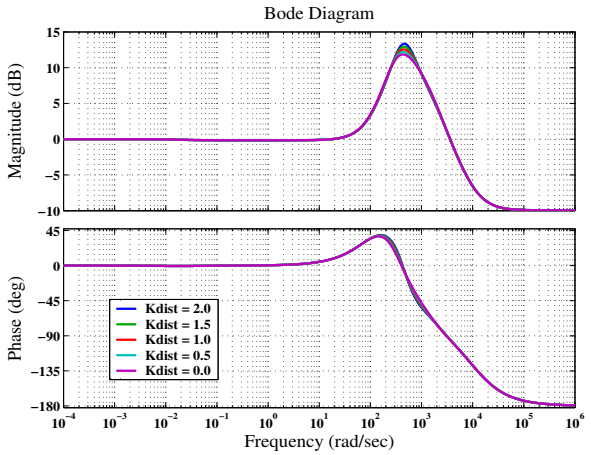

(a) Frequency response of close-loop system of $Gcl = \frac{v_s^2}{v_c^{*2}}$

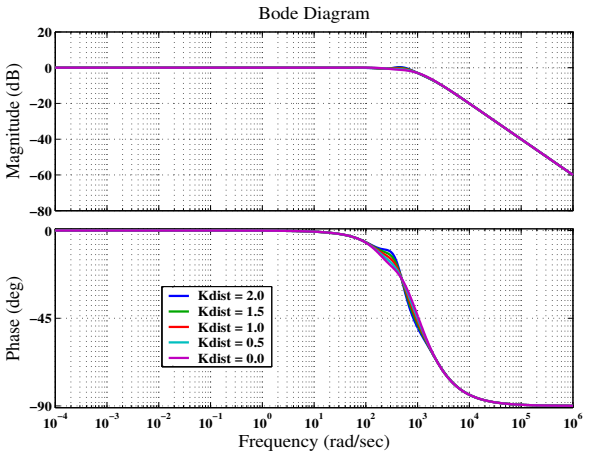

(b) Frequency response of close-loop system of $Gcl = \frac{i_{sq}}{i_{sq}^*}$

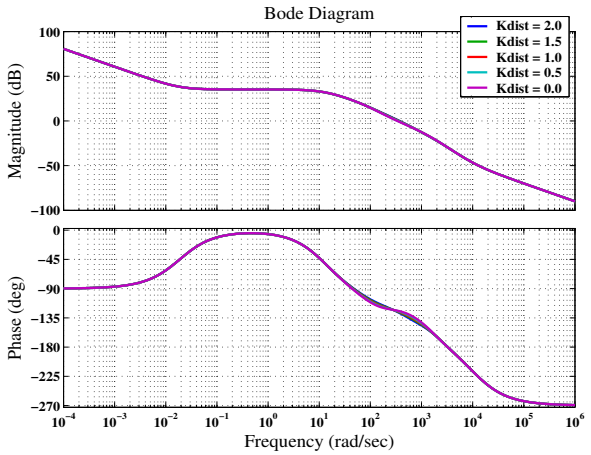

(c) Frequency response of open-loop system of $Gol = \frac{v_s^2}{v_c^{*2}}$

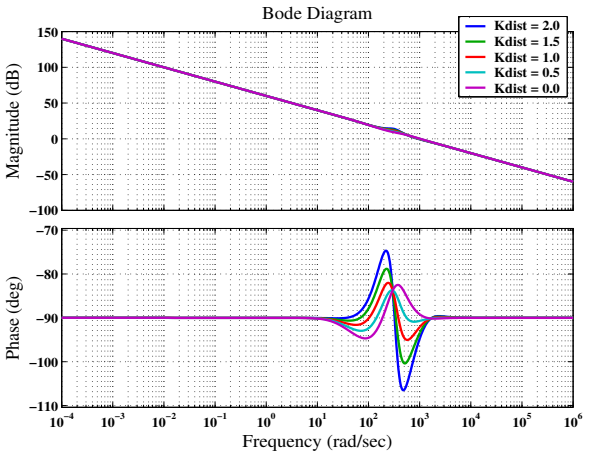

(d) Frequency response of open-loop system of $Gol = \frac{i_{sq}}{i_{sq}^*}$

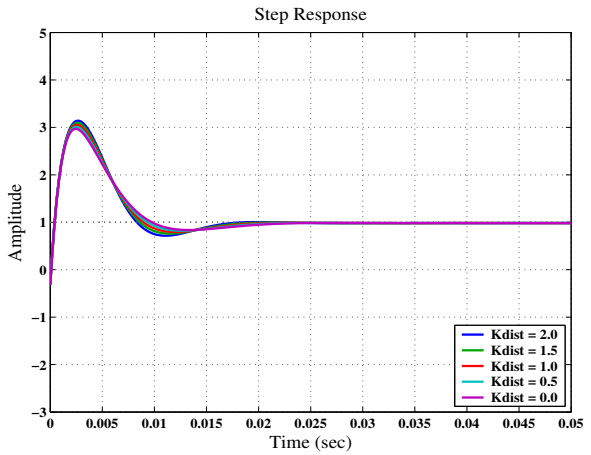

(e) Step response of close-loop system of $Gcl = \frac{v_s^2}{v_c^{*2}}$

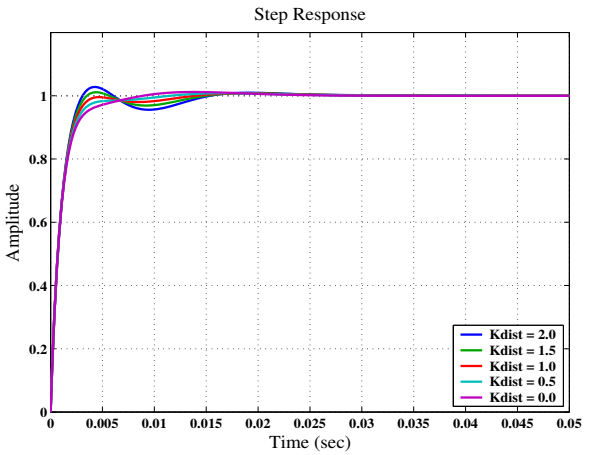

(f) Step response of close-loop system of $Gcl = \frac{i_{sq}}{i_{sq}^*}$

Figure 2.22: Performance of the proposed filed-weakening scheme when K_{dist} is varied (saturation condition is stimulated by i_{sq} as disturbance).

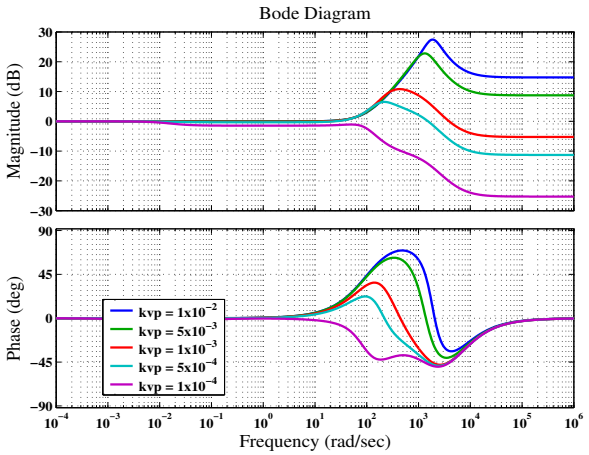

(a) Frequency response of close-loop system of $Gcl = \frac{v_s^2}{v_c^{*2}}$

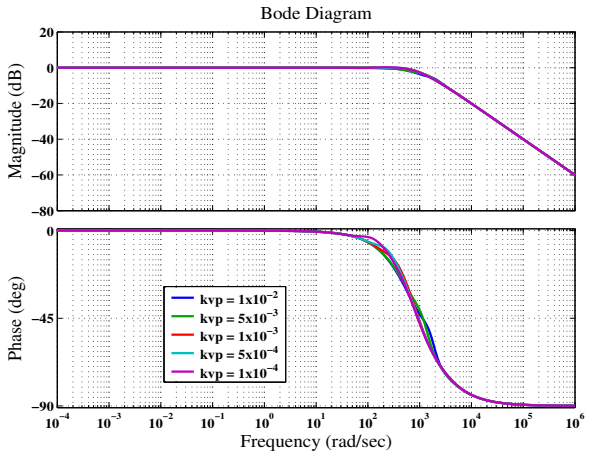

(b) Frequency response of close-loop system of $Gcl = \frac{i_{sq}}{i_{sq}^*}$

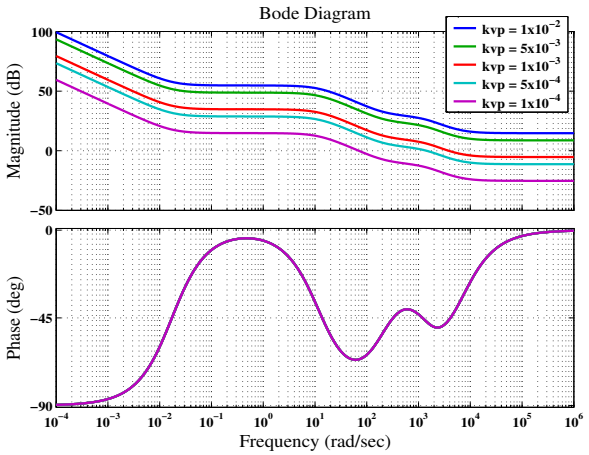

(c) Frequency response of open-loop system of $Gol = \frac{v_s^2}{v_c^{*2}}$

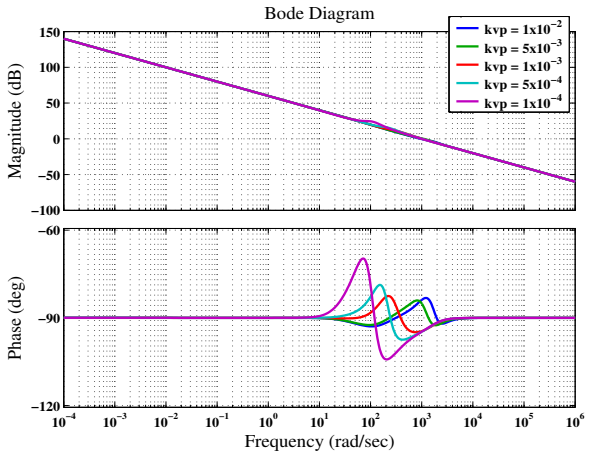

(d) Frequency response of open-loop system of $Gol = \frac{i_{sq}}{i_{sq}^*}$

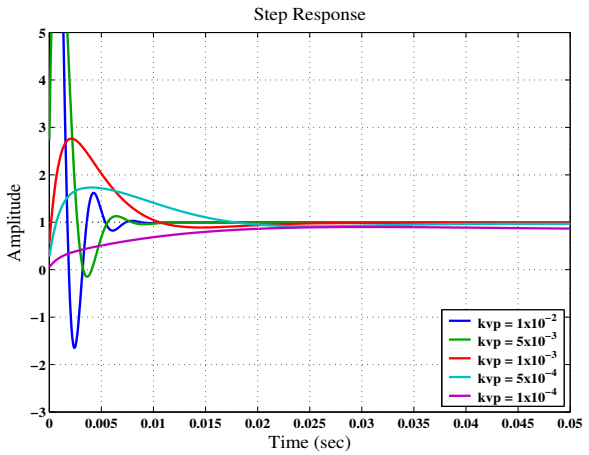

(e) Step response of close-loop system of $Gcl = \frac{v_s^2}{v_c^{*2}}$

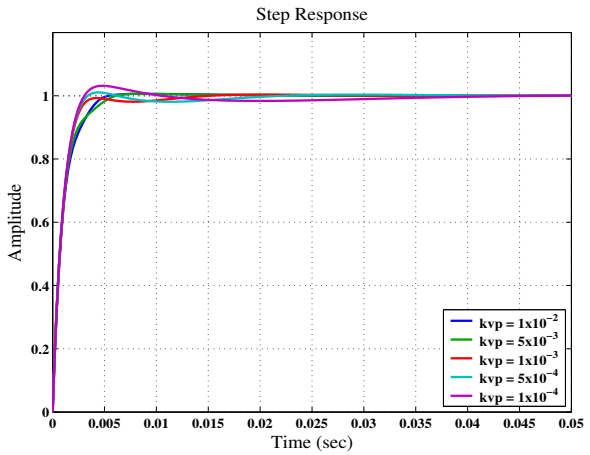

(f) Step response of close-loop system of $Gcl = \frac{i_{sq}}{i_{sq}^*}$

Figure 2.23: Performance of the proposed filed-weakening scheme when K_{vp} is varied (saturation condition is stimulated by i_{sq}^* as disturbance).

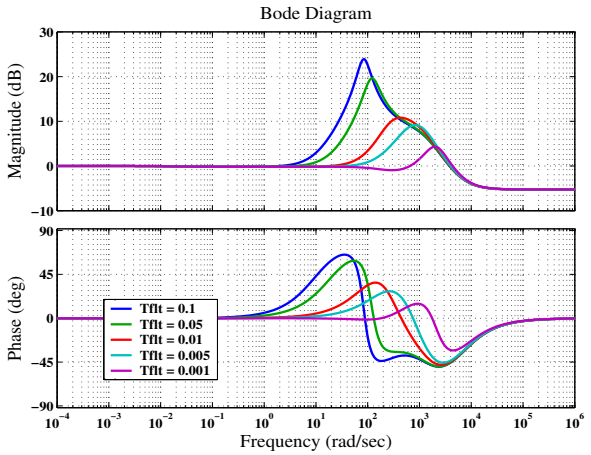

(a) Frequency response of close-loop system of $Gcl = \frac{v_s^2}{v_c^{*2}}$

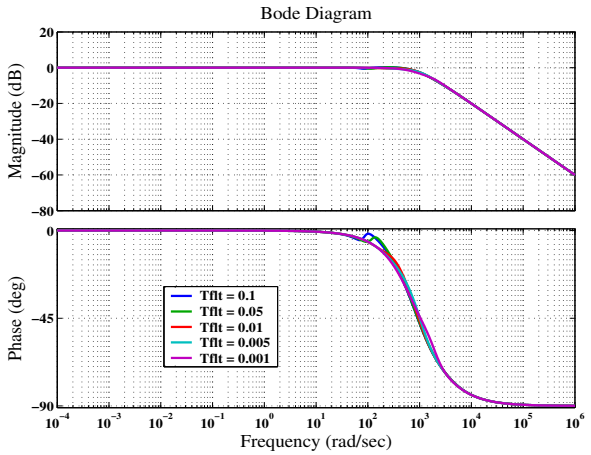

(b) Frequency response of close-loop system of $Gcl = \frac{i_{sq}}{i_{sq}^*}$

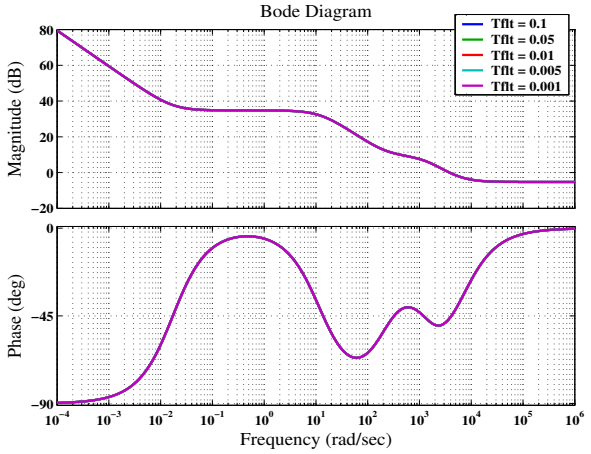

(c) Frequency response of open-loop system of $Gol = \frac{v_s^2}{v_c^{*2}}$

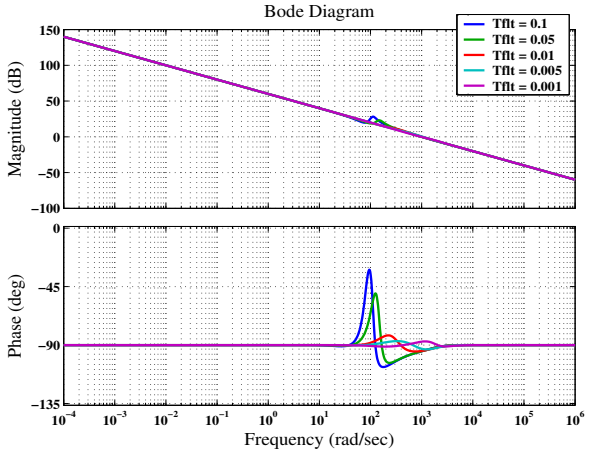

(d) Frequency response of open-loop system of $Gol = \frac{i_{sq}}{i_{sq}^*}$

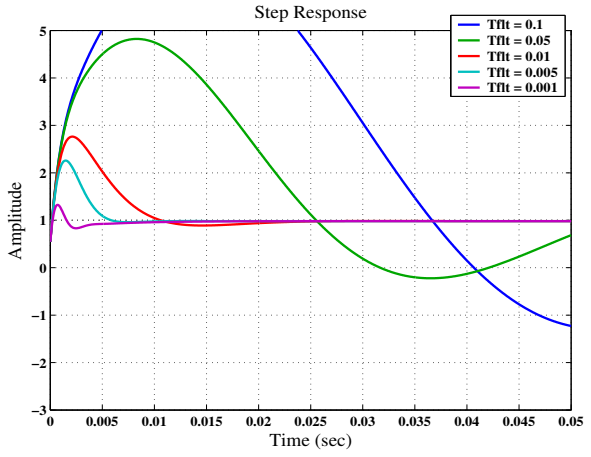

(e) Step response of close-loop system of $Gcl = \frac{v_s^2}{v_c^{*2}}$

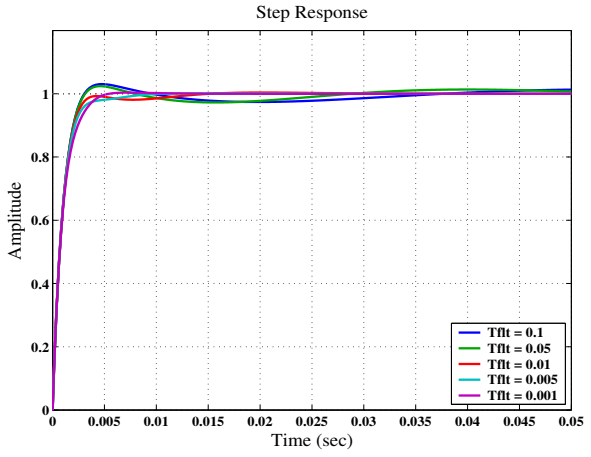

(f) Step response of close-loop system of $Gcl = \frac{i_{sq}}{i_{sq}^*}$

Figure 2.24: Performance of the proposed filed-weakening scheme when T_{flt} is varied (saturation condition is stimulated by i_{sq}^* as disturbance).

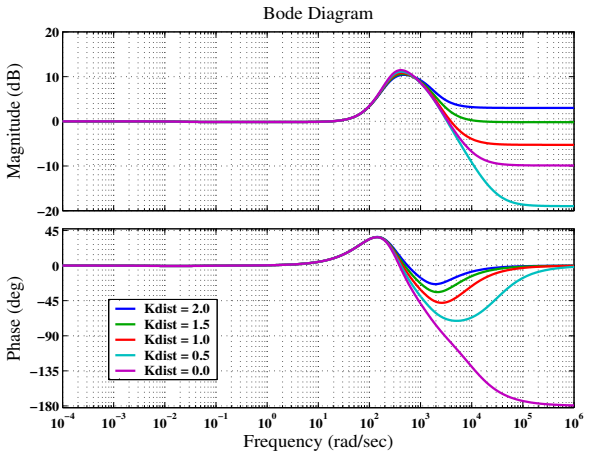

(a) Frequency response of close-loop system of $Gcl = \frac{v_s^2}{v_c^{*2}}$

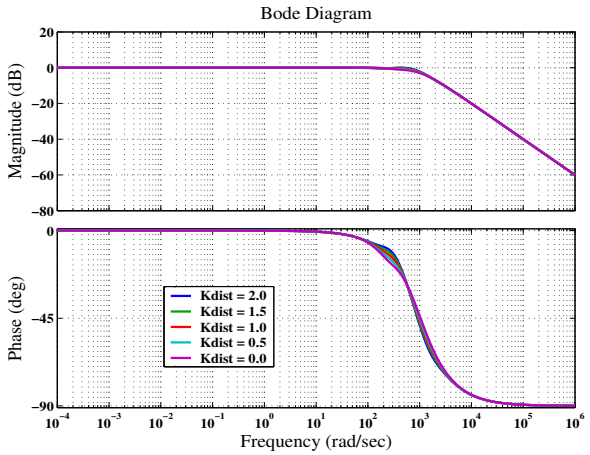

(b) Frequency response of close-loop system of $Gcl = \frac{i_{sq}}{i_{sq}^*}$

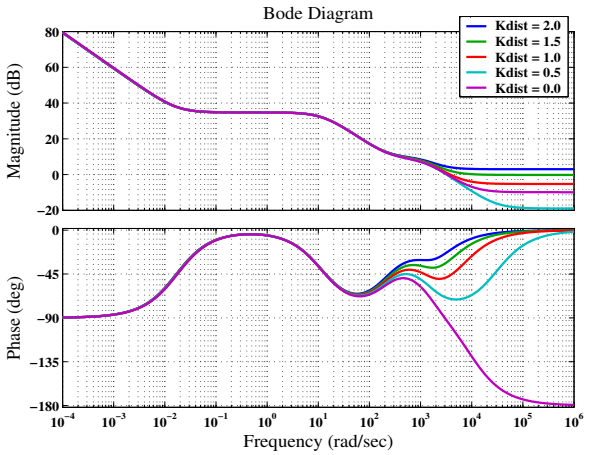

(c) Frequency response of open-loop system of $Gol = \frac{v_s^2}{v_c^{*2}}$

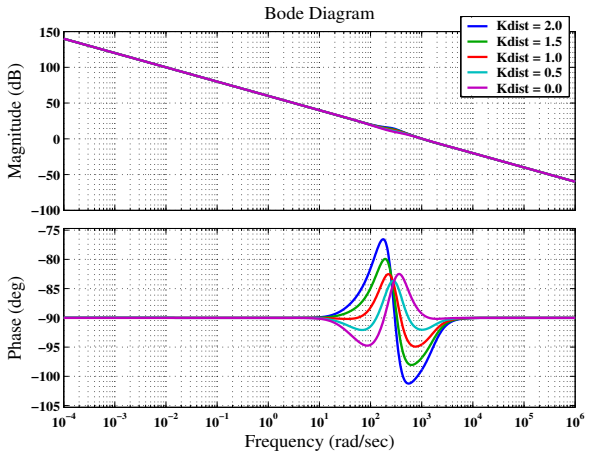

(d) Frequency response of open-loop system of $Gol = \frac{i_{sq}}{i_{sq}^*}$

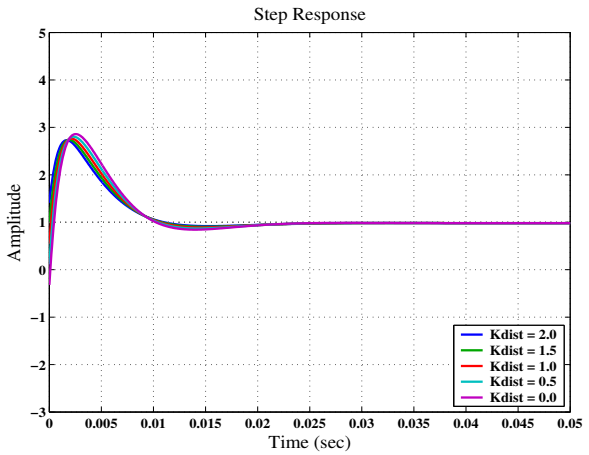

(e) Step response of close-loop system of $Gcl = \frac{v_s^2}{v_c^{*2}}$

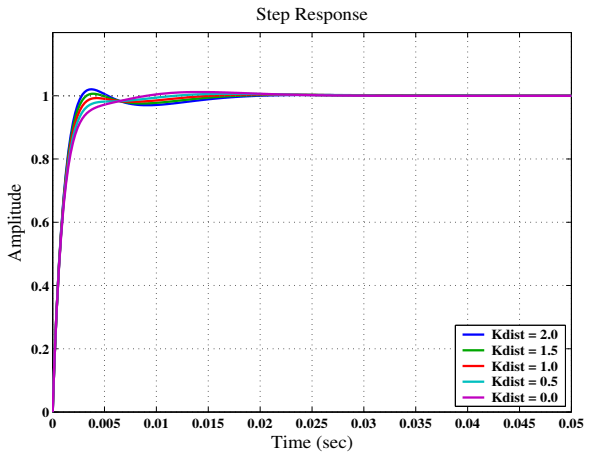

(f) Step response of close-loop system of $Gcl = \frac{i_{sq}}{i_{sq}^*}$

Figure 2.25: Performance of the proposed filed-weakening scheme when K_{dist} is varied (saturation condition is stimulated by i_{sq}^* as disturbance).

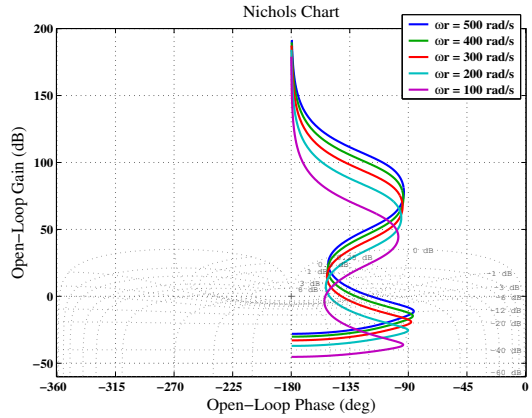

(a) Gain-phase response of open-loop system of $Gol = \frac{v_s^2}{v_c^{*2}}$ (conventional scheme).

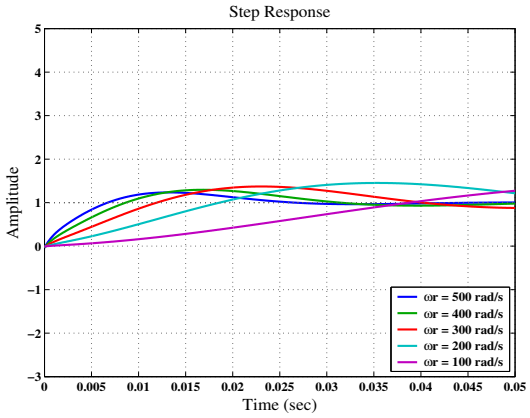

(b) Step response of close-loop system of $Gcl = \frac{v_s^2}{v_c^{*2}}$ (conventional scheme).

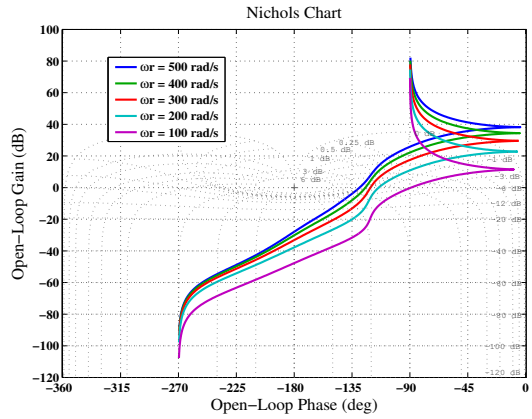

(c) Gain-phase response of open-loop system of $Gol = \frac{v_s^2}{v_c^{*2}}$ (proposed scheme with i_{sq} as disturbance).

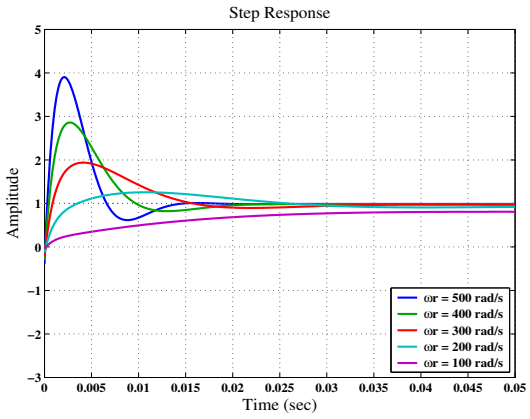

(d) Step response of close-loop system of $Gcl = \frac{v_s^2}{v_c^{*2}}$ (proposed scheme with i_{sq} as disturbance).

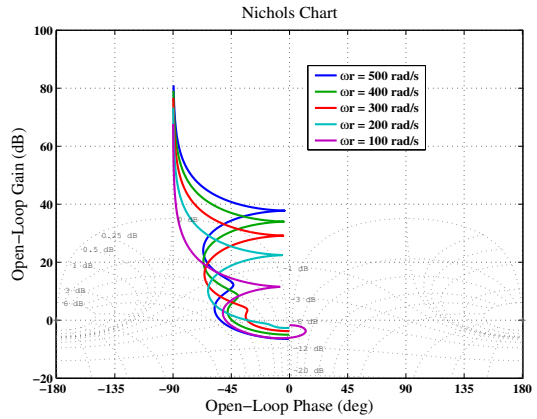

(e) Gain-phase response of open-loop system of $Gol = \frac{v_s^2}{v_c^{*2}}$ (proposed scheme with i_{sq}^* as disturbance).

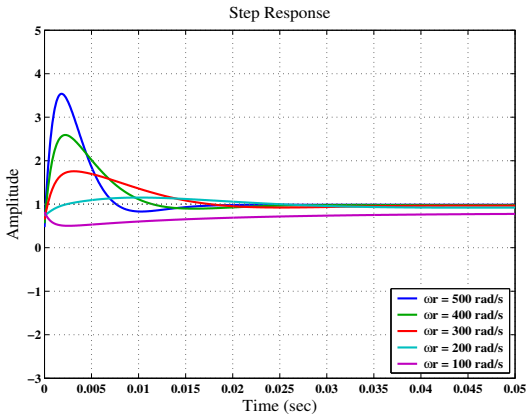

(f) Step response of close-loop system of $Gcl = \frac{v_s^2}{v_c^{*2}}$ (proposed scheme with i_{sq}^* as disturbance).

Figure 2.26: Voltage control performance comparison when ω_r is varied.

2.7 Summary

A novel and simple field-weakening scheme was proposed, which combining the voltage saturation strategy in order to improve the output power in the high-speed motor operation. Disturbing the flux-producing current reference with the torque-producing current reference while the stator voltage is limited or saturated, higher voltage availability can be provided, since the dc-bus voltage utilization is maximized. As a result, a higher torque is provided and the flux-weakening region is widened. Experimental results confirm the validity of the field-weakening scheme based on saturated voltage strategy. The voltage saturation condition only occurs when a higher or maximum torque is required. The maximum torque is produced by increasing the flux-producing current as much as possible.

The performance comparison analysis was presented to show the proposed field-weakening scheme has no stability problem due to a disturbance addition in order to stimulate the saturation condition. From the performance analysis results, the gain parameters for a satisfied performance of all field-weakening configurations are selected as listed in Table 2.5.

Table 2.5: Selected gain parameters for the satisfied performance.

Field-weakening scheme	K_{vp}	K_{vi}	T_{flt}	K_{dist}
Previous	$5\text{x}10^{-5} \sim 1\text{x}10^{-4}$	$0.05 \sim 0.1$	–	–
Proposed, i_{sq} as disturbance	$5\text{x}10^{-4} \sim 1\text{x}10^{-3}$	–	$0.005 \sim 0.01$	$1.0 \sim 2.0$
Proposed, i^*_{sq} as disturbance	$5\text{x}10^{-4} \sim 1\text{x}10^{-3}$	–	$0.005 \sim 0.01$	$1.0 \sim 2.0$

As the conclusion, the proposed scheme is verified to provide an improved torque capability over the previous field-weakening scheme using a voltage control strategy. Since the output power in the high speed motor operation was improved, a higher kinetic energy can be recover by the regenerative brake strategy.

The implementation of another method in maximizing the dc-bus utility for improving the torque capability in the field-weakening operation is still interesting to be investigated. Furthermore, its implementation with the speed sensorless system is still open to be studied.

Chapter 3

Motor restarting capability of speed sensorless drive

In this chapter, a preliminary investigation of the restarting capability of the speed sensorless induction motor drive is presented. First, the full-order observer is modified to reduce the order of the observer. The modified observer uses the rotor flux calculated by the flux model instead of estimating it, thus two of the four state equations can be removed. The experimental results of the modified observer are compared with the ones of the full-order observer, to confirm that the modified observer can work well. Then the restarting capability of the speed sensorless induction motor using the modified observer is investigated through experimental and simulation approaches. The restarting capability of speed sensorless drive makes the coasting operation of electric vehicle drive possible. The coasting operation is an effort to energy saving by reducing the electrical losses due to the electricity is shut off.

3.1 Introduction

Conventionally the speed of an electrical machine can be measured by tacho-generator. The rotor position can be measured by using electromagnetic resolvers or digitally by using incremental or absolute encoders. Optical encoders are one of the most widely used position sensors. Electromagnetic resolvers are popular for measuring the rotor position because of their rugged construction and higher operating temperature. In case the rotor position is monitored, the speed (which is the first derivative of the position) can be estimated directly from the position, but the speed resolution is limited by the resolution of the position transducer and also the sampling time. To reduce total hardware complexity and costs, to increase the mechanical robustness and reliability of the drive, and to obtain increased noise immunity, it is desirable

to eliminate the sensors in vector-controlled drive systems. Furthermore, an electromechanical sensor increases the maintenance requirements.

The squirrel-cage induction machines are still ideal candidates in motor drive systems. The high accuracy and good torque response are obtained by using the flux vector control, however the encoder is still required [17]. To eliminate speed and position sensors, various speed and position estimation algorithms have been proposed [18]∼[23]. These algorithms are generally based on machine parameters and the measurement of terminal voltages and currents of the motor. A full-order observer (speed adaptive flux observer) that high stability has been confirmed by experiments is proposed in [18]. Although advanced algorithms such as the ones making use of the Extended Kalman Filter [19] have been proposed, the full-order observer still has the advantage of requiring less intensive calculation.

3.2 Speed adaptive flux observer

3.2.1 Full-order speed adaptive flux observer

The speed adaptive observer [18] is based on the induction motor model which expressed in the stationary reference frame. The dynamics of induction motor in the stationary reference frame are given by

$$\dot{x} = Ax + Bu \tag{3.1}$$

where:

$$x = \begin{bmatrix} i_{s\alpha} & i_{s\beta} & \phi_{r\alpha} & \phi_{r\beta} \end{bmatrix}^T , \qquad u = \begin{bmatrix} v_{s\alpha} & v_{s\beta} \end{bmatrix}^T ,$$

$$A = \begin{bmatrix} a_{11} & 0 & a_{13} & a_{14} \\ 0 & a_{11} & -a_{14} & a_{13} \\ a_{31} & 0 & a_{33} & a_{34} \\ 0 & a_{31} & -a_{34} & a_{33} \end{bmatrix} , \qquad B = \begin{bmatrix} b_1 & 0 \\ 0 & b_1 \\ 0 & 0 \\ 0 & 0 \end{bmatrix} ,$$

$$a_{11} = -R_s/(\sigma L_s) - L_m^2/(\sigma L_s L_r T_r) , \qquad a_{13} = L_m/(\sigma L_s L_r T_r) ,$$
$$a_{14} = \omega_r L_m/(\sigma L_s L_r) , \qquad a_{31} = L_m/T_r ,$$
$$a_{33} = -1/T_r , \qquad a_{34} = -\omega_r ,$$
$$b_1 = 1/(\sigma L_s) , \qquad \sigma = 1 - L_m^2/(L_s L_r) .$$

with the output as

$$y = Cx \tag{3.2}$$

where:

$$y = \begin{bmatrix} i_{s\alpha} & i_{s\beta} \end{bmatrix}^T \quad \text{and} \quad C = \begin{bmatrix} 1 & 0 & 0 & 0 \\ 0 & 1 & 0 & 0 \end{bmatrix}$$

A state observer is a model-based state estimator, which can be used for the state estimation of a non-linear dynamic system in real time. As expressed in Eq. (3.1) the state variables of the motor model are the stator currents ($i_{s\alpha}$, $i_{s\beta}$) and the rotor flux ($\phi_{r\alpha}$, $\phi_{r\beta}$). Since the stator currents are the measurable state variables, they can be used for correcting the estimated states of the observer. Based on Eq. (3.1) the state observer of the induction motor can be written as follows:

$$\dot{\hat{x}} = \hat{A}\hat{x} + Bu + Ge_{is} \tag{3.3}$$

where:

$$\hat{x} = \begin{bmatrix} \hat{i}_{s\alpha} & \hat{i}_{s\beta} & \hat{\phi}_{r\alpha} & \hat{\phi}_{r\beta} \end{bmatrix}^T, \qquad u = \begin{bmatrix} v_{s\alpha} & v_{s\beta} \end{bmatrix}^T,$$

$$\hat{A} = \begin{bmatrix} a_{11} & 0 & a_{13} & a_{14} \\ 0 & a_{11} & -a_{14} & a_{13} \\ a_{31} & 0 & a_{33} & a_{34} \\ 0 & a_{31} & -a_{34} & a_{33} \end{bmatrix}, \qquad B = \begin{bmatrix} b_1 & 0 \\ 0 & b_1 \\ 0 & 0 \\ 0 & 0 \end{bmatrix},$$

$$a_{11} = -R_s/(\sigma L_s) - L_m^2/(\sigma L_s L_r T_r) \ , \qquad a_{13} = L_m/(\sigma L_s L_r T_r) \ ,$$
$$a_{14} = \hat{\omega}_r L_m/(\sigma L_s L_r) \ , \qquad a_{31} = L_m/T_r \ ,$$
$$a_{33} = -1/T_r \ , \qquad a_{34} = -\hat{\omega}_r \ ,$$
$$b_1 = 1/(\sigma L_s) \ , \qquad \sigma = 1 - L_m^2/(L_s L_r) \ ,$$

$$G = \begin{bmatrix} g_1 & g_2 & g_3 & g_4 \\ -g_2 & g_1 & -g_4 & g_3 \end{bmatrix}^T, \qquad e_{is} = \begin{bmatrix} e_{is\alpha} \\ e_{is\beta} \end{bmatrix},$$

$$g_1 = (1-k)(a_{11} + a_{33}) \ , \qquad e_{is\alpha} = i_{s\alpha} - \hat{i}_{s\alpha} \ ,$$
$$g_2 = (1-k)\hat{\omega}_r \ , \qquad e_{is\beta} = i_{s\beta} - \hat{i}_{s\beta} \ ,$$
$$g_3 = (1-k^2)(ha_{11} + a_{31}) - h(1-k)(a_{11} + a_{33}) \ ,$$
$$g_4 = h(1-k)\hat{\omega}_r \ ,$$
$$h = -\sigma L_s L_r / L_m \ .$$

with the output as

$$\hat{y} = \hat{C}\hat{x} \tag{3.4}$$

where:

$$\hat{y} = \begin{bmatrix} i_{s\alpha} & i_{s\beta} \end{bmatrix}^T \quad \text{and} \quad \hat{C} = \begin{bmatrix} 1 & 0 & 0 & 0 \\ 0 & 1 & 0 & 0 \end{bmatrix}$$

Here $\hat{}$ denotes estimated values. Matrixes $\hat{A}$, B, and u are the same as in Eq. (3.1) (the induction motor model in the stationary frame). However in the matrix $\hat{A}$ of Eq. (3.3), the

rotor speed ω_r is replaced by the estimated speed $\hat{\omega}_r$, since the drive system is the sensorless one. Instead of the rotor speed, all motor parameters used in the observer are assumed to be same with the actual ones. There is no motor's parameter error. G is the observer gain matrix and is selected by using the pole-placement technique so that the system will be stable. The selected observer gain matrix G in Eq. (3.3) is proposed by Kubota et.al. [24], where $k > 0$. An algorithm for the calculation of the motor speed estimation can be constructed using Lyapunov theory. The speed adaptation for estimating the speed is obtained by using the state-error equation of the system. To obtain the state-error equation, the Eq. (3.3) is subtracted from Eq. (3.1). Dynamic of the observer-error is expressed as follows:

$$\frac{de}{dt} = \frac{d}{dt}(x - \hat{x}) = (A - GC)(x - \hat{x}) + (A - \hat{A})\hat{x} = (A - GC)e - \Delta A\hat{x} \tag{3.5}$$

where:

$$\begin{aligned}
e &= (x - \hat{x}) \\
\Delta A &= (A - \hat{A}) = \begin{bmatrix} O_2 & -\Delta\omega_r J/h \\ O_2 & \Delta\omega_r J \end{bmatrix} \\
O_2 &= \begin{bmatrix} 0 & 0 \\ 0 & 0 \end{bmatrix} \\
J &= \begin{bmatrix} 0 & 1 \\ 1 & 0 \end{bmatrix} \\
\Delta\omega_r &= (\hat{\omega}_r - \omega_r) \\
h &= \sigma L_s L_r / L_m
\end{aligned}$$

In Eq. (3.5), $e = x - \hat{x}$ is the estimation-error vector of the stator currents and rotor fluxes. Then the Lyapunov function candidate is defined as follows:

$$V = e^T e + (\hat{\omega}_r - \omega_r)^2/\lambda \tag{3.6}$$

Here λ is a positive constant. This function is zero when the error e is zero and when the estimated speed $\hat{\omega}_r$ is equal to the actual speed ω_r. Since a sufficient condition for uniform asymptotic stability is that the derivative Lyapunov function, $\frac{d}{dt}V$, is negative definite, the derivative of V is obtained. By using the chain differentiation rule, it follows from Eq. (3.6) that the time derivative of V becomes as follows:

$$\frac{d}{dt}V = e\left[\frac{d(e^T)}{dt}\right] + e^T\left[\frac{de}{dt}\right] + 2\frac{d\hat{\omega}_r}{dt}\frac{(\hat{\omega}_r - \omega_r)}{\lambda} \tag{3.7}$$

By substitution of $\frac{de}{dt}$ by its expression given by Eq. (3.5), Eq. (3.7) becomes

$$\frac{d}{dt}V = e^T[(A - GC)^T + (A - GC)]e - (\hat{x}^T\Delta A^T e + e^T\Delta A\hat{x}) + 2\frac{d\hat{\omega}_r}{dt}\frac{(\hat{\omega}_r - \omega_r)}{\lambda} \tag{3.8}$$

When $e = (x - \hat{x})$, $x = \begin{bmatrix} i_{s\alpha} & i_{s\beta} & \phi_{r\alpha} & \phi_{r\beta} \end{bmatrix}^T$, and $\hat{x} = \begin{bmatrix} \hat{i}_{s\alpha} & \hat{i}_{s\beta} & \hat{\phi}_{r\alpha} & \hat{\phi}_{r\beta} \end{bmatrix}^T$ are substituted into Eq. (3.8), finally the derivative of the Lyapunov function can be expressed as follows:

$$\frac{d}{dt}V = e^T[(A - GC)^T + (A - GC)]e - 2\frac{L_m}{L_r}(\hat{\omega}_r - \omega_r)\frac{(e_{is\alpha}\hat{\phi}_{r\beta} - e_{is\beta}\hat{\phi}_{r\alpha})}{\sigma L_s} + \frac{2}{\lambda}(\hat{\omega}_r - \omega_r)\frac{d\hat{\omega}_r}{dt} \tag{3.9}$$

Since a sufficient condition for uniform asymptotic stability is that the derivative Lyapunov function, $\frac{dV}{dt}$, is negative definite, e.g. V has to decrease when the error is not zero, this can be satisfied by ensuring that the sum of the last two terms in Eq. (3.9) is zero (the other terms on the right-hand side of Eq. (3.9) are always negative definite). Thus it follows that the adaptive scheme (adjustment law) for the speed estimation can be obtained as

$$\frac{d\hat{\omega}_r}{dt} = K_{\omega ri}(e_{is\alpha}\hat{\phi}_{r\beta} - e_{is\beta}\hat{\phi}_{r\alpha}) \tag{3.10}$$

where $K_{\omega ri} = \frac{\lambda L_m}{\sigma L_s L_r} = \frac{\lambda}{h}$ is the integral gain. From Eq. (3.10) the speed can be estimated as follows:

$$\hat{\omega}_r = K_{\omega ri}\int (e_{is\alpha}\hat{\phi}_{r\beta} - e_{is\beta}\hat{\phi}_{r\alpha})dt \tag{3.11}$$

To improve the response of the speed observer, Eq. (3.11) is modified to

$$\hat{\omega}_r = K_{\omega rp}(e_{is\alpha}\hat{\phi}_{r\beta} - e_{is\beta}\hat{\phi}_{r\alpha}) + K_{\omega ri}\int (e_{is\alpha}\hat{\phi}_{r\beta} - e_{is\beta}\hat{\phi}_{r\alpha})dt \tag{3.12}$$

Figure 3.1 shows the block diagram of the full-order speed adaptive observer. The estimated rotor flux-linkage and the stator-current error are used to obtain the error speed-tuning signal. The estimated speed is obtained from the speed-tuning signal by using a PI controller that is expressed in Eq. (3.12).

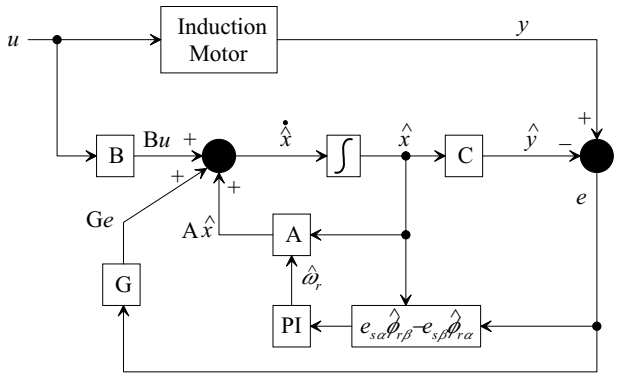

Figure 3.1: The full-order speed adaptive observer.

In order to observe the performance of the speed adaptive observer [18] when it is implemented with the rotor flux oriented IM control, we drive the motor using the configuration shown in Fig. 3.2. The flux model block in Fig. 3.2 calculates the torque T_e, the rotor magnetizing current i_{mr} ($i_{mr} = \frac{\phi_r}{L_m}$), the electrical frequency ω_e, and the flux angle θ_e, which are expressed as follows:

$$T_e = N_p(1-\sigma)L_s i_{sq} i_{mr} \tag{3.13}$$

$$\frac{d}{dt} i_{mr} = \frac{R_r}{L_r}(i_{sd} - i_{mr}) \tag{3.14}$$

$$\omega_e = \omega_r + \frac{R_r}{L_r}\frac{i_{sq}}{i_{mr}} \tag{3.15}$$

$$\frac{d}{dt}\theta_e = \omega_e \tag{3.16}$$

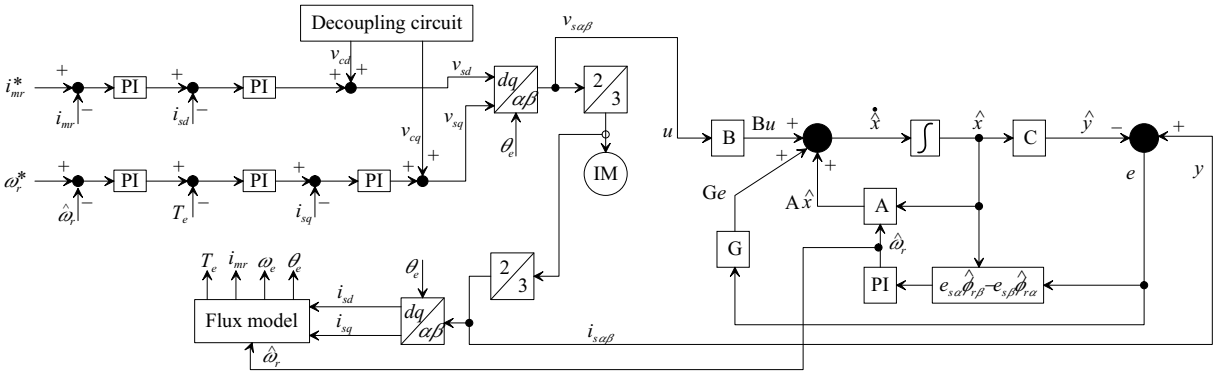

Figure 3.2: Sensorless induction motor control using full-order speed adaptive observer.

The controller uses the rotor magnetizing current calculated in the flux model using Eq. (3.14) as a feedback to control the flux. The observer estimates the flux and uses it to estimate the rotor speed. Therefore, there are two values of the flux in this configuration. The former is calculated in the flux model and the later is estimated in the observer.

The dynamic performance of the drive system using this observer is shown in Fig. 3.3. As seen in Figs. 3.3 (c) and (d), the estimated rotor flux of the observer changes rapidly during the speed change transition period. The estimated rotor flux goes far away from its presupposed constant value even though it is controlled by the vector controller. The d-axis current that corresponds to the flux is not really changed, but the estimated rotor flux of the observer (called

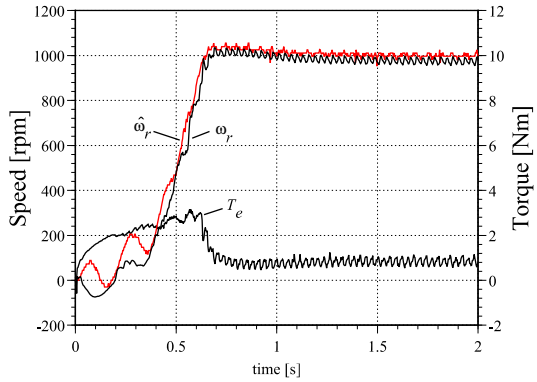

(a) Forward Rotor speed responses

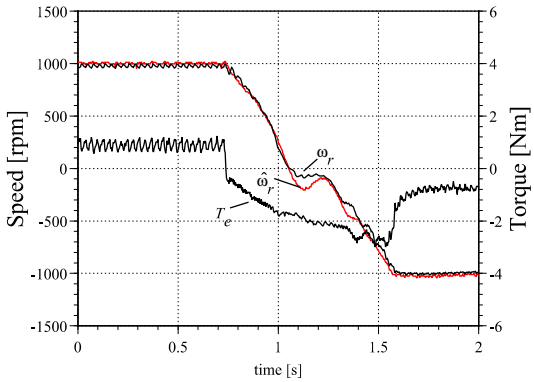

(b) Reverse Rotor speed responses

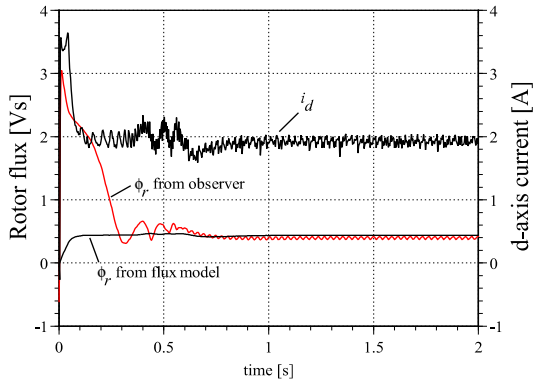

(c) Flux dynamic of the forward speed responses

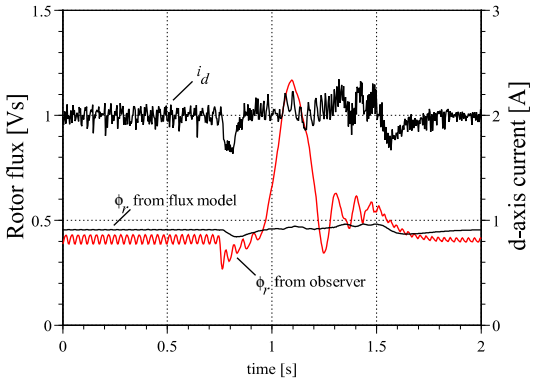

(d) Flux dynamic of the reverse speed responses

Figure 3.3: Flux dynamics of the full-order observer with the calculated flux as the flux control feedback.

"estimated flux") is changed significantly. The change of the flux causes a poor performance of the speed response in transients, especially around the low speed area (see Figs. 3.3 (a) and (b)). On the contrary, the rotor flux calculated in the flux model of the controller (called "calculated flux") is much more stable. We can state that the calculated flux is more reliable than the estimated flux for speed estimation. It can be supposed that if the observer uses the calculated flux instead of estimating the flux for the speed estimation purpose, we can improve the performance of the sensorless drive system. Based on this observation, we propose a modification of the full-order observer by using combined reference frames for the performance improvement of the sensorless induction motor drive.

3.2.2 Modified speed adaptive flux observer

The observer can use the calculated flux by transforming ϕ_r to $\hat{\phi}''_{r\alpha}$ and $\hat{\phi}''_{r\beta}$, as expressed in Eqs. (3.17) and (3.18). Here $\phi_r = L_m i_{mr}$. The flux transformation is shown diagrammatically in Fig. 3.4. Since the observer already makes use of the calculated flux to palliate the lack of flux dynamics found in the speed change transition region we don't need to estimate the flux again. And since the induction motor is stable by itself, the observer gain matrix can be removed from the state equation for simplification. In this case, the poles of the observer coincide with the induction motor poles. This simplified state observer is expressed in Eq. (3.19), and the block diagram of the modified observer implemented with the rotor flux oriented induction motor control is shown in Fig. 3.5.

$$\hat{\phi}''_{r\alpha} = \phi_r \cos\theta_e \tag{3.17}$$

$$\hat{\phi}''_{r\beta} = \phi_r \sin\theta_e \tag{3.18}$$

$$\frac{d}{dt}\begin{bmatrix} \hat{i}_{s\alpha} \\ \hat{i}_{s\beta} \end{bmatrix} = \begin{bmatrix} a_{11} & 0 & a_{13} & a_{14} \\ 0 & a_{11} & -a_{14} & a_{13} \end{bmatrix} \begin{bmatrix} \hat{i}_{s\alpha} \\ \hat{i}_{s\beta} \\ \hat{\phi}''_{r\alpha} \\ \hat{\phi}''_{r\beta} \end{bmatrix} + \begin{bmatrix} b_1 & 0 \\ 0 & b_1 \end{bmatrix} \tag{3.19}$$

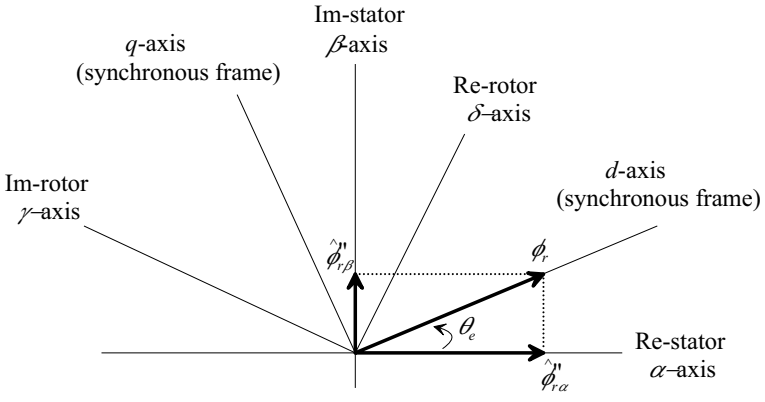

Figure 3.4: Reference frame transformation of the rotor flux.

Figure 3.6(a) shows the actual and estimated speeds and the torque when the motor runs from the stand still condition with a constant speed reference and a constant flux reference. As

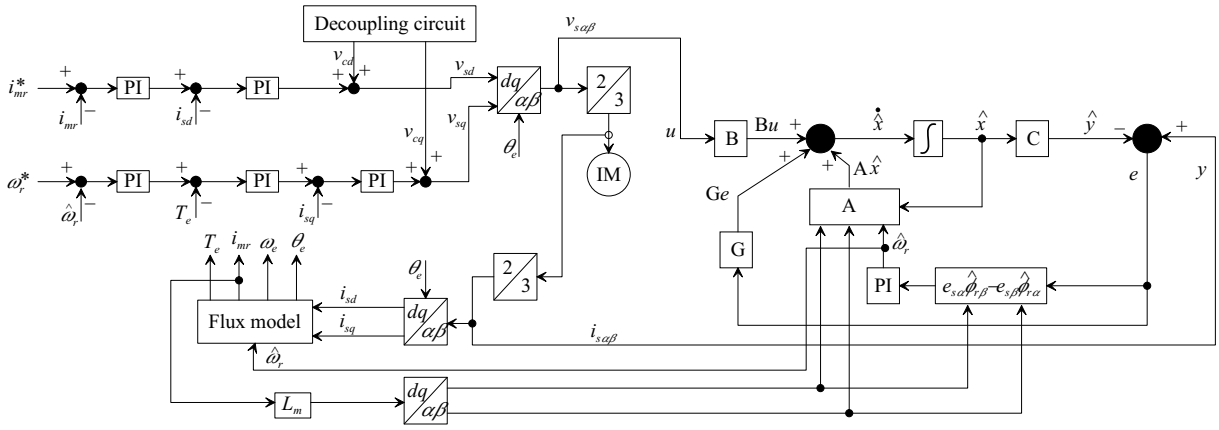

Figure 3.5: Implementation of the modified observer.

seen in Fig. 3.6(a) compared to Fig. 3.3(a), the sensorless field oriented control of the modified observer gives a better performance. The modified observer can estimate the speed properly and the speed response becomes faster. By using the modified observer the drive system can produce a higher torque while the torque ripple is minimized. Fig. 3.6(c) that is in the same condition as Fig. 3.6(a), shows the rotor flux and the d-axis current in order to observe the flux behavior. The d-axis current that corresponds to the flux is much more stable and faster compared to the one shown in Fig. 3.3(c). Fig. 3.6(b) shows the reversal response of the drive system that uses the modified observer. In this experiment, the speed reference is changed from +1000 rpm to -1000 rpm and the flux reference is constant. The flux behavior is shown in Fig. 3.6(d). From these figures compared with Figs. 3.3(b) and (d), the modified observer implemented with the rotor flux oriented control is also proved to improve the performance of the sensorless induction motor drive system. A higher torque is produced and there is almost no influence to the d-axis current when the speed reference is changed.

As expressed in Eq. (3.13) there is a coupling between the torque-producing component of the q-axis stator current and the rotor magnetizing current. As a consequence, any change in the q-axis stator current without changing the d-axis stator current accordingly will cause a transient in the rotor flux. In order to overcome the disadvantage, a feed-forward decoupling scheme is added to compensate the coupling effect. Unfortunately, according to Figs. 3.6(a)∼(d), in the sensorless drive system using the full-order observer the compensation of the coupling effect becomes ineffective since the observer estimates the rotor flux and uses it for the rotor speed estimation, even though the estimated flux is not fed to the flux controller. To make a

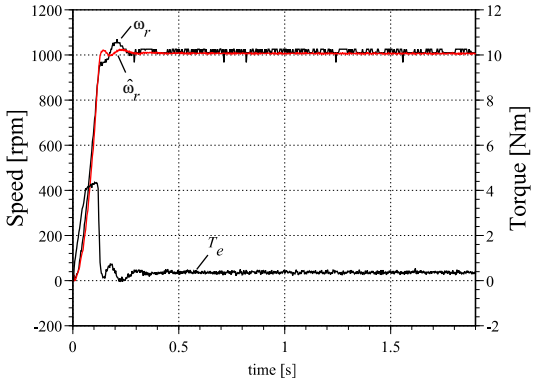

(a) Forward Rotor speed responses

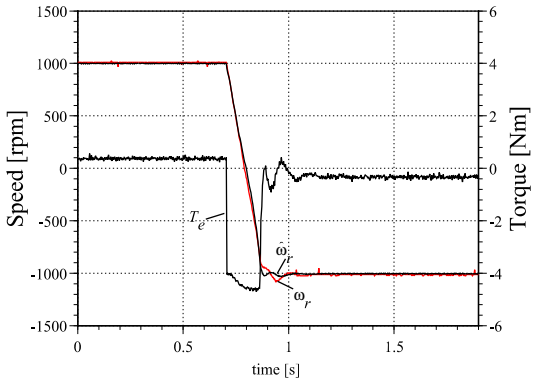

(b) Reverse Rotor speed responses

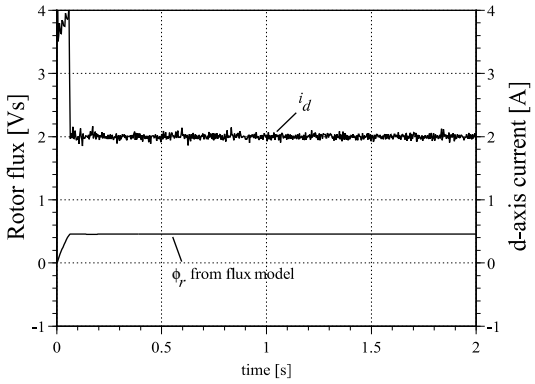

(c) Flux dynamic of the forward speed responses

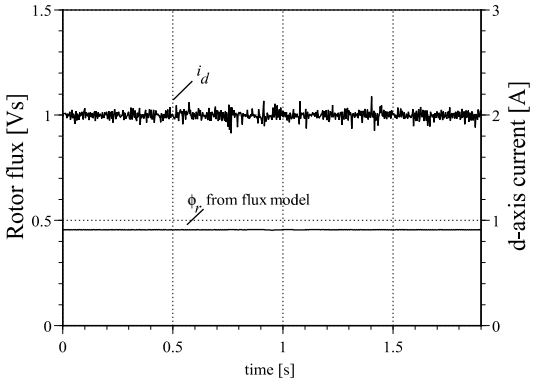

(d) Flux dynamic of the reverse speed responses

Figure 3.6: Flux dynamics of the modified observer with the calculated flux as the flux control feedback.

confirmation of this behavior, the motor is run again with the configuration shown in Fig. 3.2, but with the use of the estimated flux as a flux control feedback from the full-order observer. The results are shown in Figs. 3.7(a)∼(d). As seen in these figures compared to Figs. 3.3(a)∼(d), the performance of the present experiment becomes worse. Besides the speed response becomes slower, the d-axis current behavior becomes very rough. As seen in Figs. 3.7(c) and (d) , in the transients, the estimated flux is disturbed a little, but the d-axis current goes far away from the presupposed constant value. This behavior is the opposite to the one shown in Figs. 3.3(c) and (d). Furthermore, in the steady state the d-axis current is oscillated similarly to the torque. We suggest that there is a flux estimation problem in the full-order observer due to the coupling effect. Then, after we modify the observer and implement it to the sensorless rotor flux oriented induction motor drive system, the coupling effect disappears completely as seen in Figs. 3.6(c) and (d). Fig. 3.8 shows the speed estimation errors comparison. As seen in those figures,

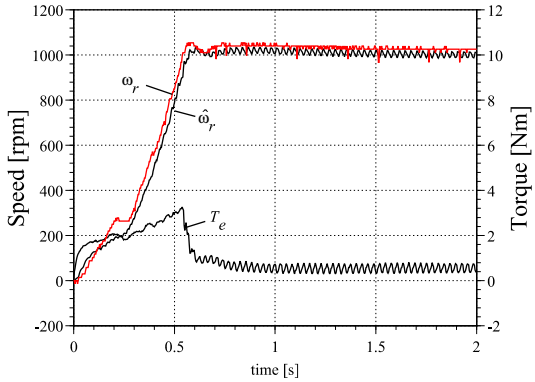

(a) Forward Rotor speed responses

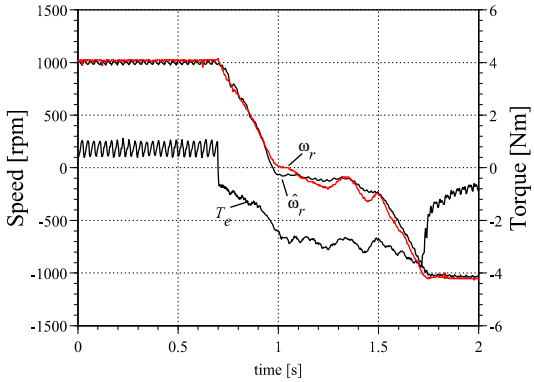

(b) Reverse Rotor speed responses

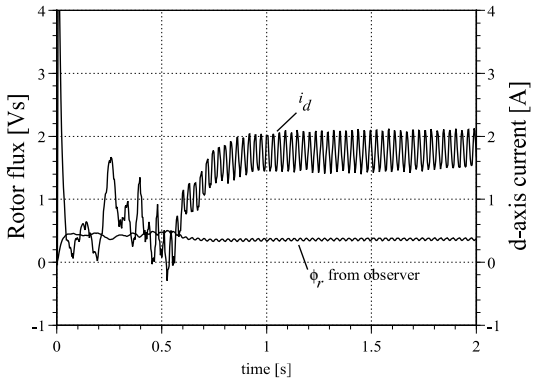

(c) Flux dynamic of the forward speed responses

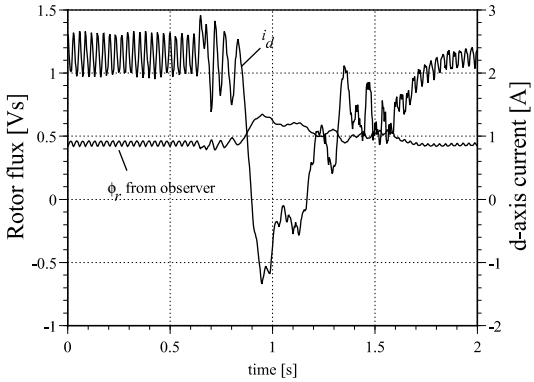

(d) Flux dynamic of the reverse speed responses

Figure 3.7: Flux dynamics of the full-order observer with the estimated flux as the flux control feedback.

the speed estimation error of the modified observer is relatively smaller than the others of the full-order observer.

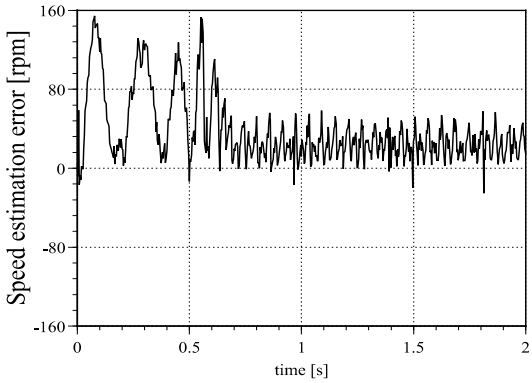

(a) Forward speed estimation error of the full-order observer with the calculated flux as the flux control feedback

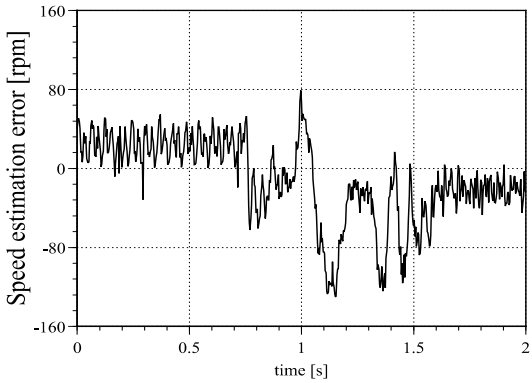

(b) Reverse speed estimation error of the full-order observer with the calculated flux as the flux control feedback

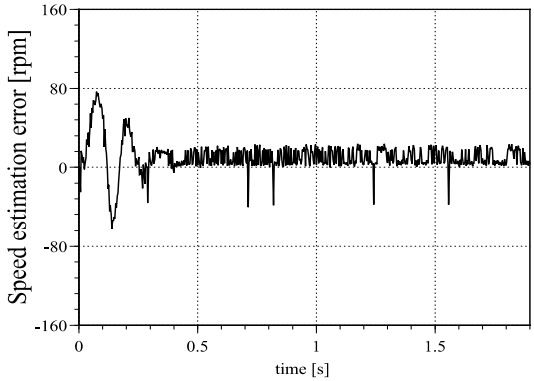

(c) Forward speed estimation error of the modified observer with the calculated flux as the flux control feedback

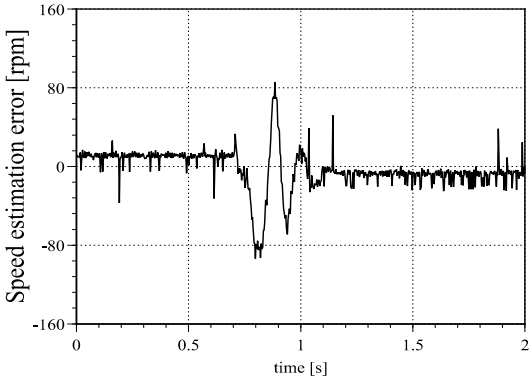

(d) Reverse speed estimation error of the modified observer with the calculated flux as the flux control feedback

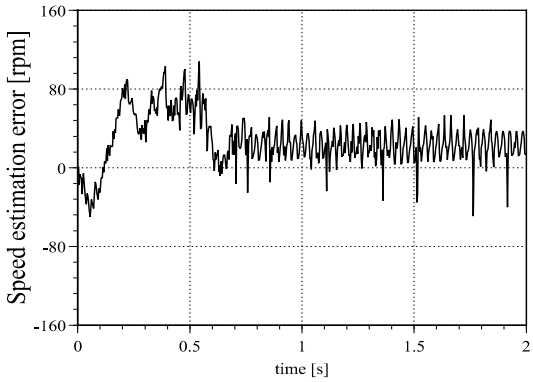

(e) Forward speed estimation error of the full-order observer with the estimated flux as the flux control feedback

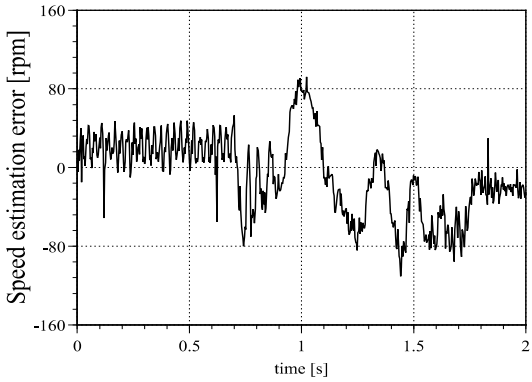

(f) Reverse speed estimation error of the full-order observer with the estimated flux as the flux control feedback

Figure 3.8: Speed estimation error comparison.

3.3 Preliminary investigation of the restarting capability

In this section, the preliminary investigation for motor restarting capability under speed sensorless drive system is presented through experiments and simulation confirmation. The speed estimation is provided by the modified speed adaptive flux observer that has been proposed in the previous section.

3.3.1 Experimental investigation with simulation confirmation

The motor restarting capability under speed sensorless drive system is very essential for coasting operation of an electric vehicle. The motor drive system should be restarted when the electric vehicle needs to be accelerated or decelerated. The initial conditions of the motor drive system when it is restarted after coasting operation are zero for electrical parameters (e.g. motor currents and voltages) and a certain value of actual rotor speed. In a speed sensorless motor drive system, the actual rotor speed is an unknown parameter, and it is estimated using an observer. Differ to the speed sensorless motor drive system that is started from the standstill condition, the initial value of actual speed becomes a problem when the motor is restarted after the coasting operation. Since the actual speed is the unknown parameter, we can't decide to determine what is the initial value (non-zero) for the speed estimation used by the observer. If the motor is started from the standstill condition, we can set the initial value of the speed estimation to zero, since we know exactly the initial value for the actual speed is zero without measuring it previously. Therefore, the initial speed problem is essential to be investigated for the motor restarting capability under speed sensorless drive system.

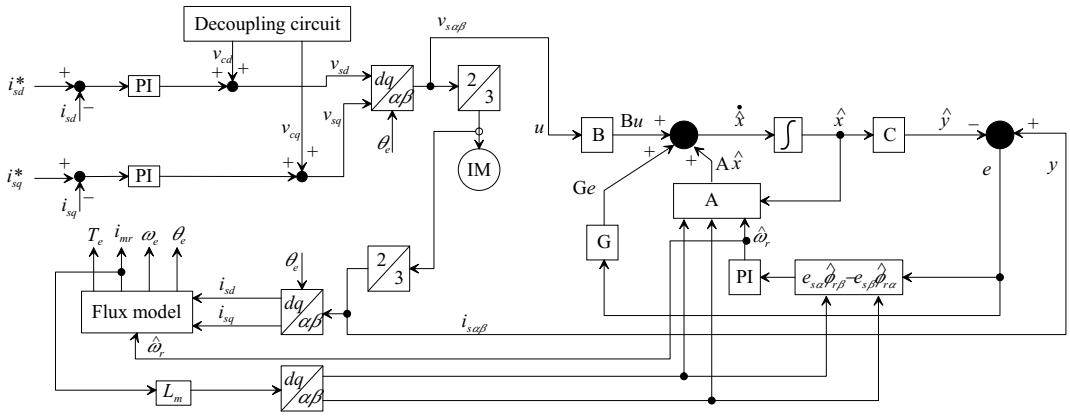

Figure 3.9: Investigating configuration of the motor restarting capability.

Configuration of the speed sensorless motor drive system used for the restarting capability investigation is shown in Fig. 3.9. As seen in this figure, the control system is only the current controller as for investigating the basic configuration. The d-axis current reference is set to be increased from 0 to 3 A during 0 to 0.5 s period and kept constant of 3 A for after 0.5 s period. The q-axis current reference is set to be increased from 0 to 2.5 A during 0 to 0.5 s period, then is kept constant of 2.5 A during 0.5 to 1 s period, then is decreased from 2.5 to -1 A during 1 to 1.2 s period, then is kept constant of -1 A during 1.2 to 3.5 s period, and finally is set to 0 A. These current references patterns are shown in Fig. 3.10. Initial values of actual speed ω_r, estimated speed $\hat{\omega}_r$, and rotor magnetizing current i_{mr} are set to 0 rpm and 1000 rpm (104.7198 rad/s) and 0 A respectively. The such initial setting values of the rotor speed is arranged in accordance to imitate the initial speed estimation error of the speed sensorless motor drive system. This arrangement makes the experimental setup easy to be realized in laboratory. The speed adaptive gains are set as $K_{\omega rp} = 6$ and $K_{\omega ri} = 420$.

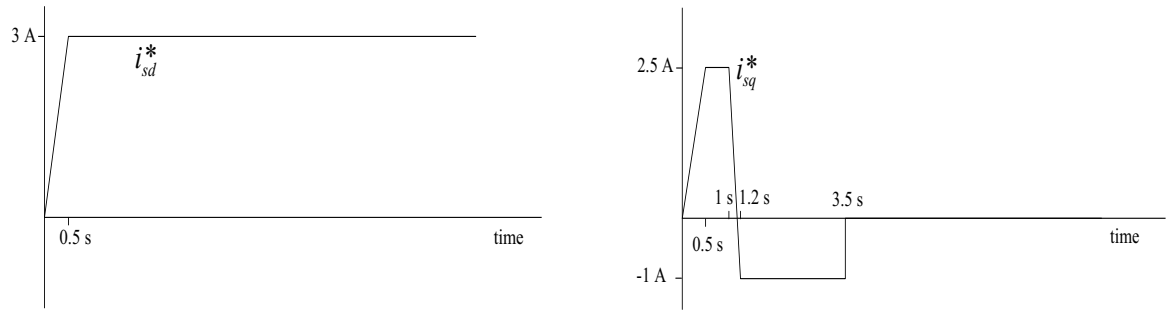

(a) d-axis current reference pattern

(b) q-axis current reference pattern

Figure 3.10: Current references patterns.

Figure 3.11 shows the preliminary experimental results of the restarting capability of the speed sensorless motor drive system. As seen in Fig. 3.11(a), the initial value of the estimated speed is about 100 rad/s, while the initial value of the actual speed is 0 rad/s. The estimated speed approaches toward the actual speed in about 0.5 second. In this period as seen in Figs. 3.11(b)∼(d), the motor currents are responded properly following their references, and the rotor magnetizing current, torque, and the d-axis and q-axis voltages are also responded as well. However, when the braking condition is entered (in period of 1∼2 seconds) the estimated speed fail to follow the actual speed. Here the speed adaptation is loss. The estimated speed drops to zero speed and remains zero until the actual speed becomes zero. After this, the estimated speed follows the actual speed again. This situation affects the responses of the other

electrical motor parameters, especially the q-axis voltage as seen in Fig. 3.11(d).

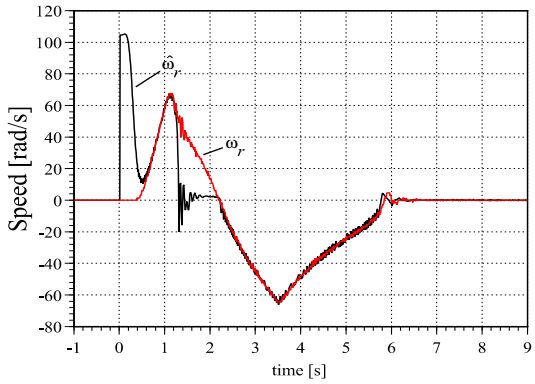

(a) Speed responses

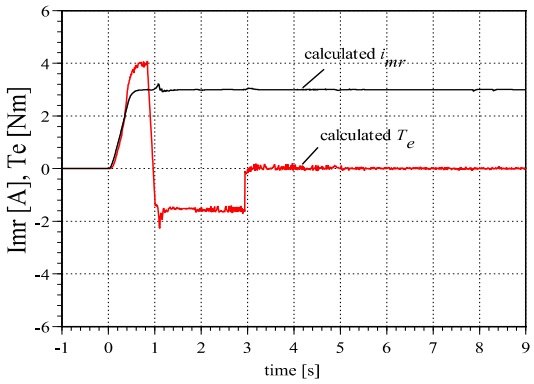

(b) Rotor magnetizing current and torque responses

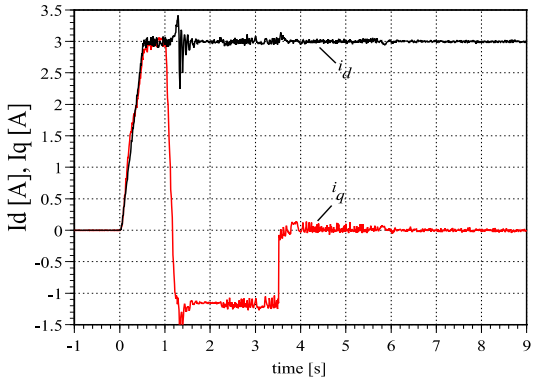

(c) d-axis and q-axis currents responses

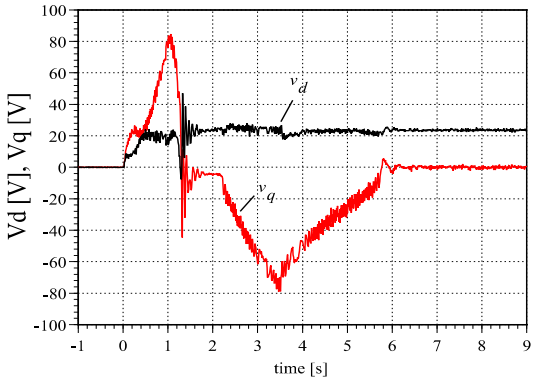

(d) d-axis and q-axis voltages responses

Figure 3.11: Experimental results of the speed sensorless motor drive system with initial speed estimation error.

To confirm the experimental results shown in Fig. 3.11, the simulation with same condition is carried out. Figure 3.12 shows the simulation results of the preliminary experimental results of the restarting capability of the speed sensorless motor drive system. In the simulation the actual rotor magnetizing current and the actual torque can be provided from the motor model as shown in Fig. 3.12(b). Generally, the simulation results of Fig. 3.12 confirm the experimental results of Fig. 3.11. Therefore, we believe that the actual values of rotor magnetizing current and torque, which couldn't be provided from the experiment, in Fig. 3.12(b) are valid. From this figure, we notice that the actual rotor magnetizing current goes far away from the constant value of the calculated one, even though the d-axis current (in Fig. 3.12(c)) is fast recovered. This is because the flux response is much slower than the current response. This situation

affects the actual torque response. The dynamics of the actual torque become worse and as a consequence the actual speed response will be also affected.

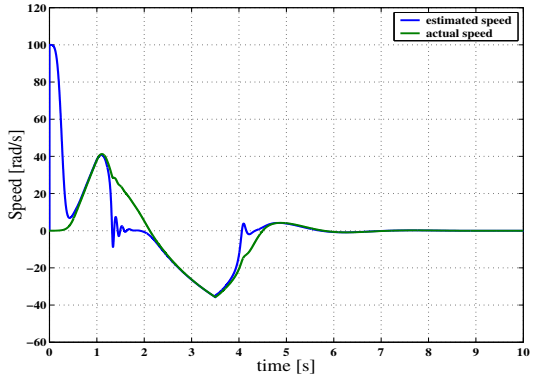

(a) Speed responses

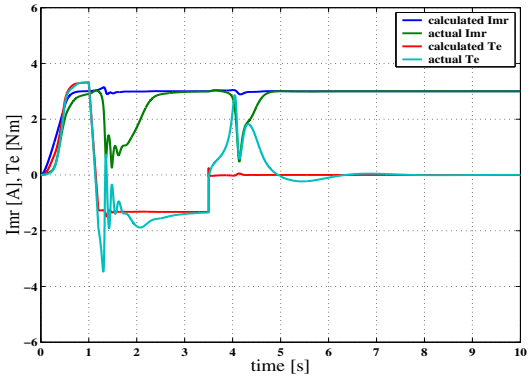

(b) Rotor magnetizing current and torque responses

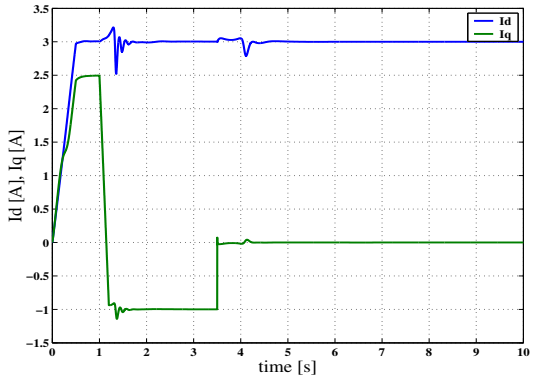

(c) d-axis and q-axis currents responses

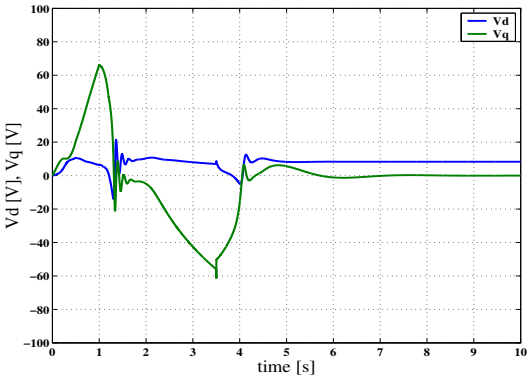

(d) d-axis and q-axis voltages responses

Figure 3.12: Simulation results of the speed sensorless motor drive system with initial speed estimation error.

3.3.2 Speed adaptive gain setting effect

We suppose that the setting values of speed adaptive gains ($K_{\omega rp} = 6$ and $K_{\omega ri} = 420$) are too large, and cause the lost adaptive capability of speed estimation. To this reason the simulation is one again carried out with the lower setting values of speed adaptive gains ($K_{\omega rp} = 1$ and $K_{\omega ri} = 72.5$), and the simulation results are shown in Fig. 3.13. As it was supposed, the problem of lost adaptive capability of speed estimation can be overcome. To confirm this simulation result, the experiment is also carried out in the same condition. The comparison

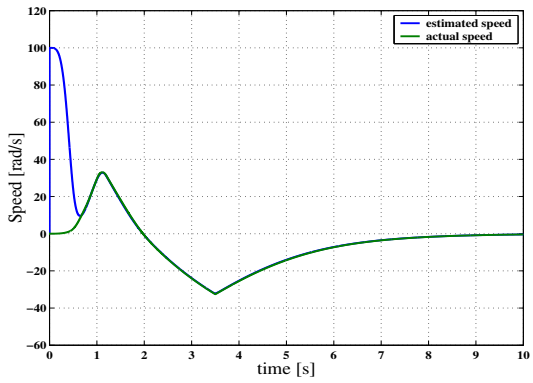

(a) Speed responses

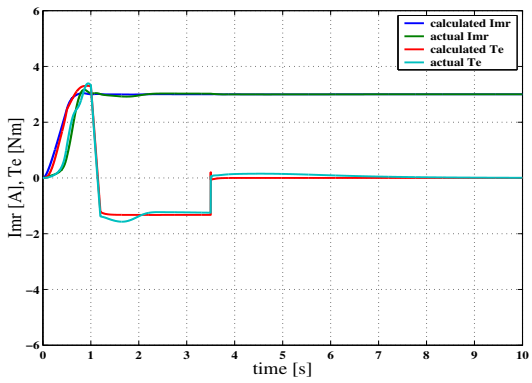

(b) Rotor magnetizing current and torque responses

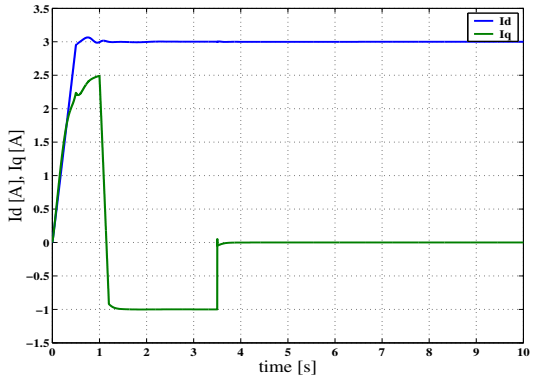

(c) d-axis and q-axis currents responses

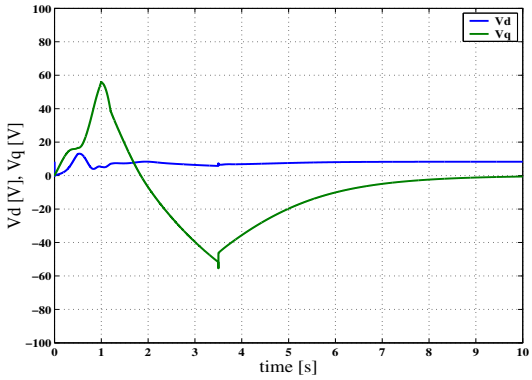

(d) d-axis and q-axis voltages responses

Figure 3.13: Simulation results of the speed sensorless motor drive system with initial speed estimation error and lower speed adaptive gains settings ($K_{\omega rp} = 1$ and $K_{\omega ri} = 72.5$).

of the experimental speed responses with the different speed adaptive gains settings are shown in Fig. 3.14. The experimental speed responses in Fig. 3.14(b), comparing with Fig. 3.13(a), confirm the validity of simulation results of Fig. 3.13.

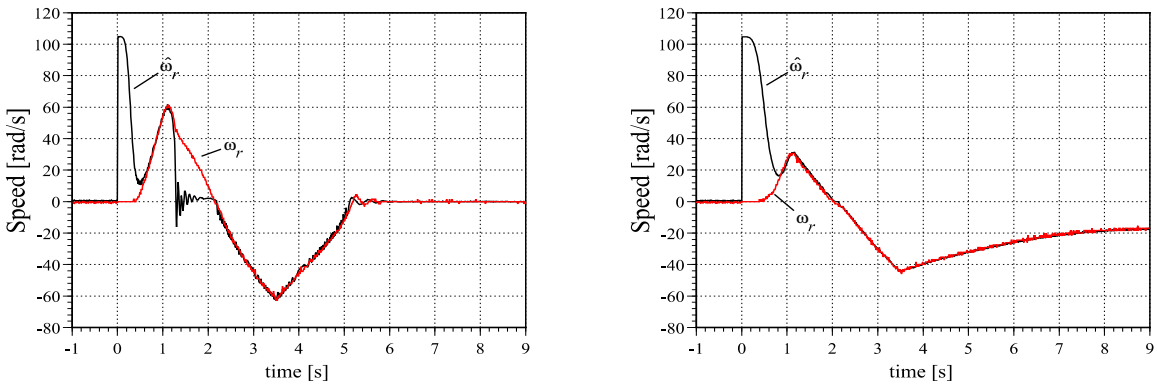

(a) ($K_{\omega rp} = 6$ and $K_{\omega ri} = 420$) (b) ($K_{\omega rp} = 1$ and $K_{\omega ri} = 72.5$)

Figure 3.14: Experimental results of speed adaptive gains effect of the speed sensorless motor drive system .

3.3.3 Initial estimated speed effect

All the investigation results in previous subsection are carried out with the initial estimated speed sets to $\hat{\omega}_{r0} = 100$ rad/s and the initial actual speed is $\omega_{r0} = 0$ rad/s. Now to observe the initial estimated speed effect, the simulation with $\hat{\omega}_{r0} = 0$ rad/s and $\omega_{r0} = 10$ rad/s is carried out, and the results are shown in Fig. 3.15. As seen in this figure, the speed adaptive flux observer works properly that the estimated speed can approach the actual speed.

For further confirmation that the motor can be still restarted even the initial value of the actual speed is far from the initial value of the estimated speed ($\hat{\omega}_{r0} = 0$ rad/s), the simulation is carried out with $\omega_{r0} = 50$ rad/s, and the results are shown in Fig. 3.16. Unfortunately, according to results in Fig. 3.16(a), the estimated speed couldn't approach the actual speed. It remains around the zero speed value. If we see to the rotor magnetizing current response in Fig. 3.16(b), the actual i_{mr} is very slow to approach the calculated i_{mr}. Furthermore, the actual torque dynamic is the opposite with the calculated one. This situation will cause the restarting capability fails.

Following the previous investigation of the initial speed effect, the simulation is carried out once again. Now, the initial estimated speed is set to $\hat{\omega}_{r0} = 100$ rad/s, while the initial actual speed is $\omega_{r0} = 50$ rad/s. The results are shown in Fig. 3.17. In this condition, the estimated speed can approach the actual speed properly. The simulation results as in Fig. 3.13 are reestablished. It is supposed with the condition that the initial estimated speed is set to be larger than the initial actual speed, the motor restarting operation under the speed sensorless

motor drive system using the modified observer will be successful. To confirm this supposition, the experiments are carried out. The motor is started from the standstill condition, then is shut down, and then is restarted repeatedly for the case of the initial estimated speed is set to $\hat{\omega}_{r0} = 100$ rad/s and for the case of the initial estimated speed is set to $\hat{\omega}_{r0} = 0$ rad/s. The comparison results are shown in Fig. 3.18. These results confirm the our supposition for the motor restarting capability under the speed sensorless motor drive system. In the first case, as seen in Fig. 3.18(a), the motor is always able to be restarted since the initial estimated speed is always larger then the initial actual speed. On the contrary, as seen in Fig. 3.18(b), the motor fails to be restarted when the initial actual speed is too larger then the initial estimated speed.

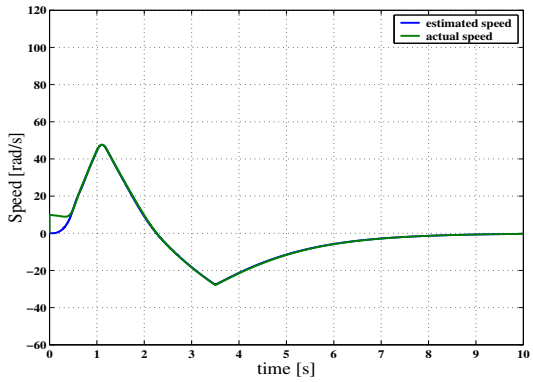

(a) Speed responses

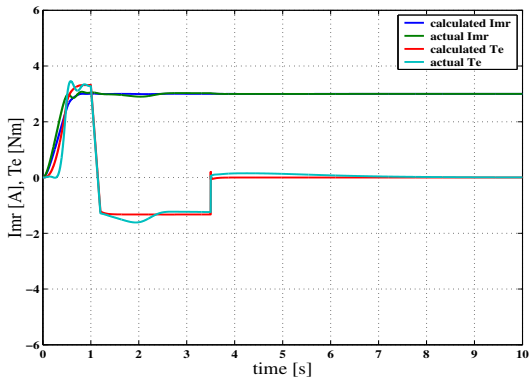

(b) Rotor magnetizing current and torque responses

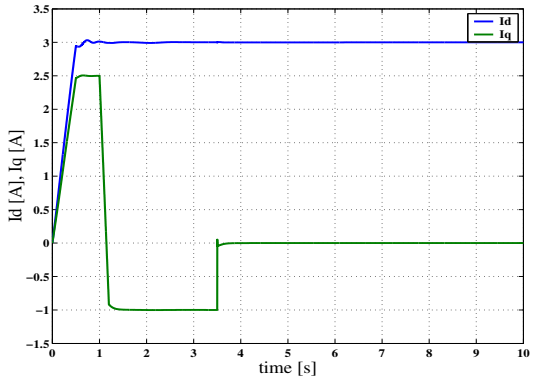

(c) d-axis and q-axis currents responses

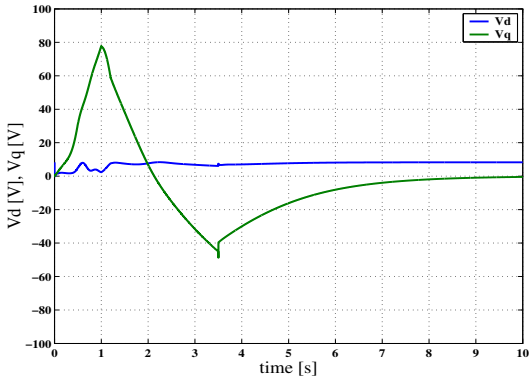

(d) d-axis and q-axis voltages responses

Figure 3.15: Simulation results of the speed sensorless motor drive system with initial speed as $\hat{\omega}_{r0} = 0$ rad/s and $\omega_{r0} = 10$ rad/s.

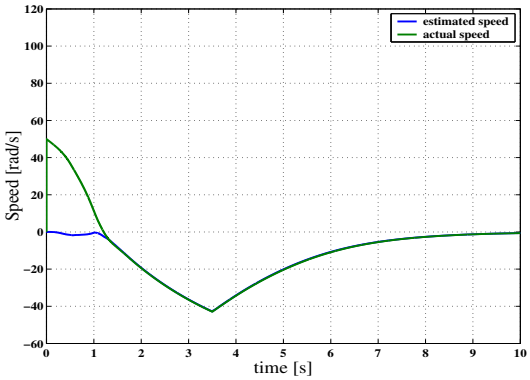

(a) Speed responses

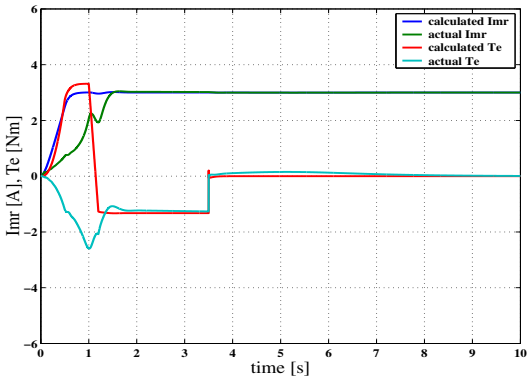

(b) Rotor magnetizing current and torque responses

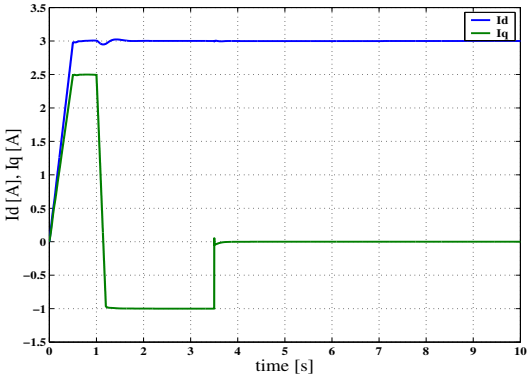

(c) d-axis and q-axis currents responses

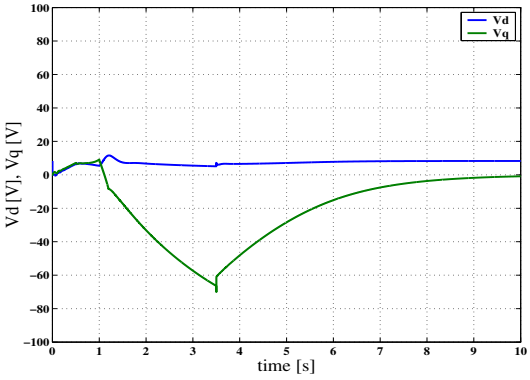

(d) d-axis and q-axis voltages responses

Figure 3.16: Simulation results of the speed sensorless motor drive system with initial speed as $\hat{\omega}_{r0} = 0$ rad/s and $\omega_{r0} = 50$ rad/s.

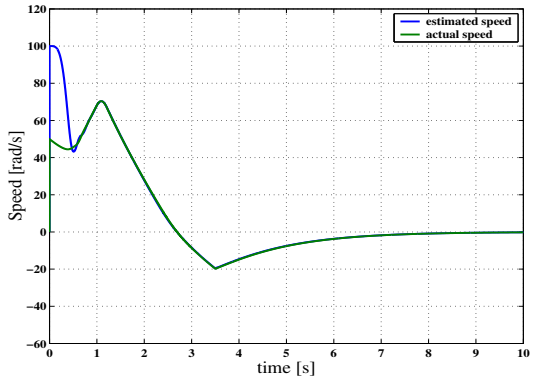

(a) Speed responses

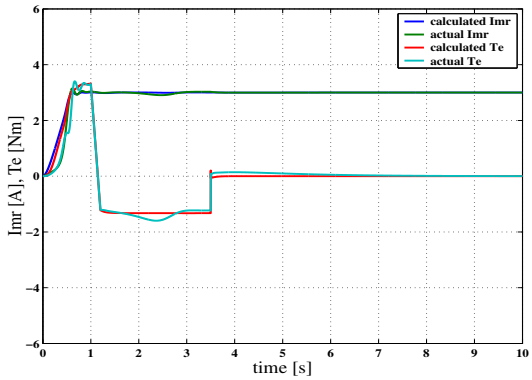

(b) Rotor magnetizing current and torque responses

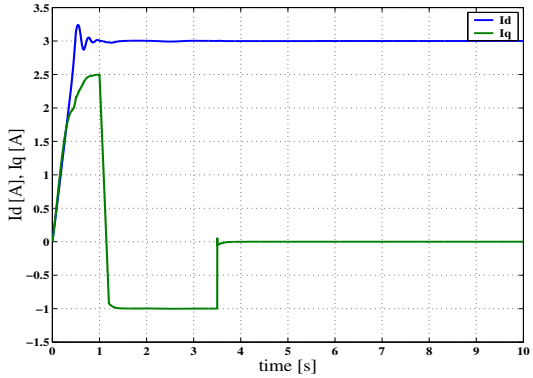

(c) d-axis and q-axis currents responses

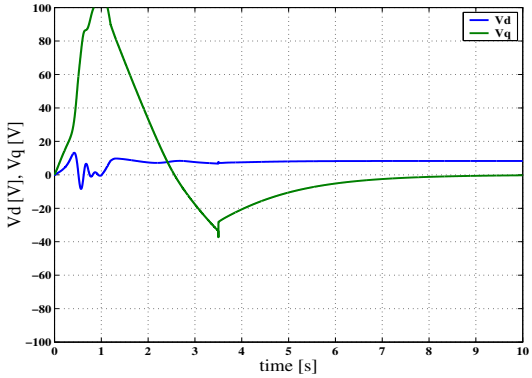

(d) d-axis and q-axis voltages responses

Figure 3.17: Simulation results of the speed sensorless motor drive system with initial speed as $\hat{\omega}_{r0} = 100$ rad/s and $\omega_{r0} = 50$ rad/s.

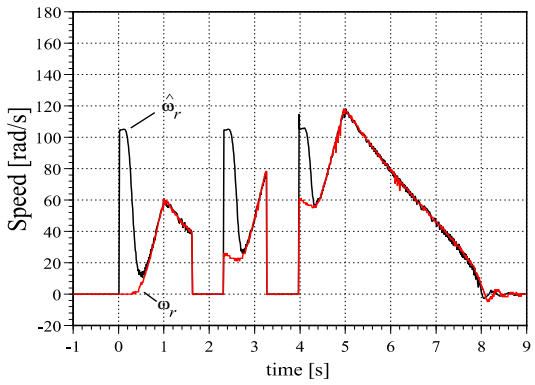

(a) the initial estimated speed is set to ($\hat{\omega}_{r0}$ = 100 rad/s)

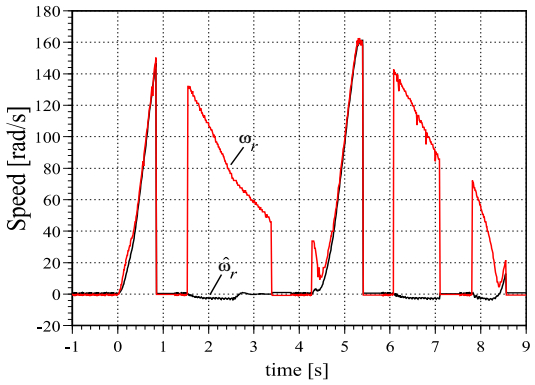

(b) the initial estimated speed is set to ($\hat{\omega}_{r0}$ = 0 rad/s)

Figure 3.18: Experimental results of initial estimated speed effect of the motor restarting capability.

3.3.4 Maximum speed of motor restarting capability

Finally, to investigate the maximum condition of the initial actual speed that the motor is still possible to be restarted, the motor is once again restarted repeatedly with the case of the initial estimated speed is set to $\hat{\omega}_{r0}$ = 100 rad/s and the case of the initial estimated speed is set to $\hat{\omega}_{r0}$ = 400 rad/s until the motor restarting operation fails. The comparison results are shown

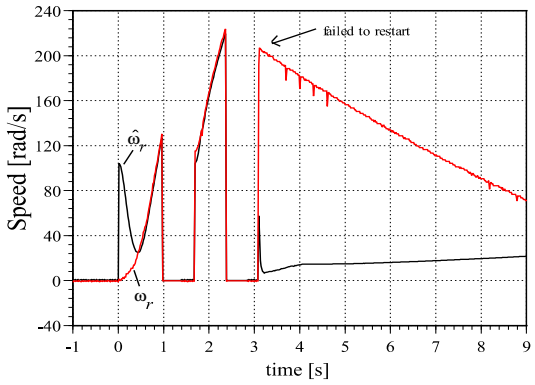

(a) the initial estimated speed is set to ($\hat{\omega}_{r0}$ = 100 rad/s)

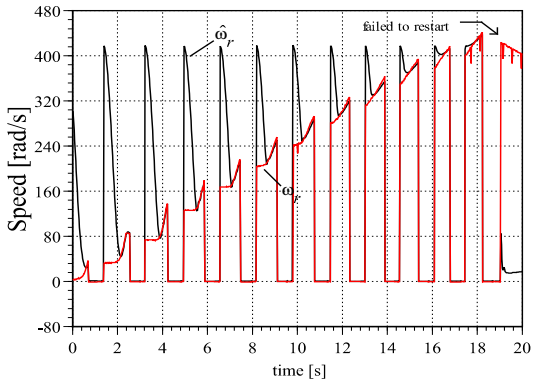

(b) the initial estimated speed is set to ($\hat{\omega}_{r0}$ = 400 rad/s)

Figure 3.19: Experimental results of the maximum speed of motor restarting capability.

in Fig. 3.19. From these results we notice that the maximum actual speed that the motor can be still restarted corresponds with the setting value of the initial estimated speed. If the initial actual speed is larger then the initial estimated speed, the motor fails to be restarted.

3.4 Minimizing Convergence Time Strategy

In previous section, we have investigated that to operate the motor restarting capability of the sensorless induction motor drive system using the modified speed adaptive flux observer, the following conditions should be considered.

1. Set the initial value of estimated speed greater than the initial value of actual speed (set to be equal to the maximum operating speed).

2. The speed adaptive gains should not too large to prevent the lost adaptive capability.

However by considering these conditions, the convergence time that the estimated speed approaches the actual speed is affected. The convergence time becomes slower due to the small speed adaptive gains and the high initial value of estimated speed (see Fig. 3.14). Therefore, it is necessary to minimize this convergence time in which to be able to control the motor immediately. In this section we propose a simple method to overcome the convergence time problem that occurs in the motor restarting of the sensorless induction motor drive system using the modified speed adaptive flux observer where the initial actual speed is an unknown. The proposed method is based on the characteristic of previous experimental results. This strategy is confirmed by experimental results.

3.4.1 Concept for minimizing the convergence time

The concept of the minimizing convergence time strategy is to accelerate the adaptive capability of speed observer with using a very high value of speed adaptive gain when the system is started. This acceleration is stop when the estimated speed becomes close enough to the actual speed. At this time the value of speed adaptive gain is switched to a low value. However, it is difficult to determine the time that the estimated speed is close enough to the actual speed and how close it is, since we can't use the value of actual speed for such purpose. Based on this background, we investigate the characteristic of some parameters from the previous experimental results and then use it to determine the gain switching time. Fig. 3.20 shows the currents and speeds

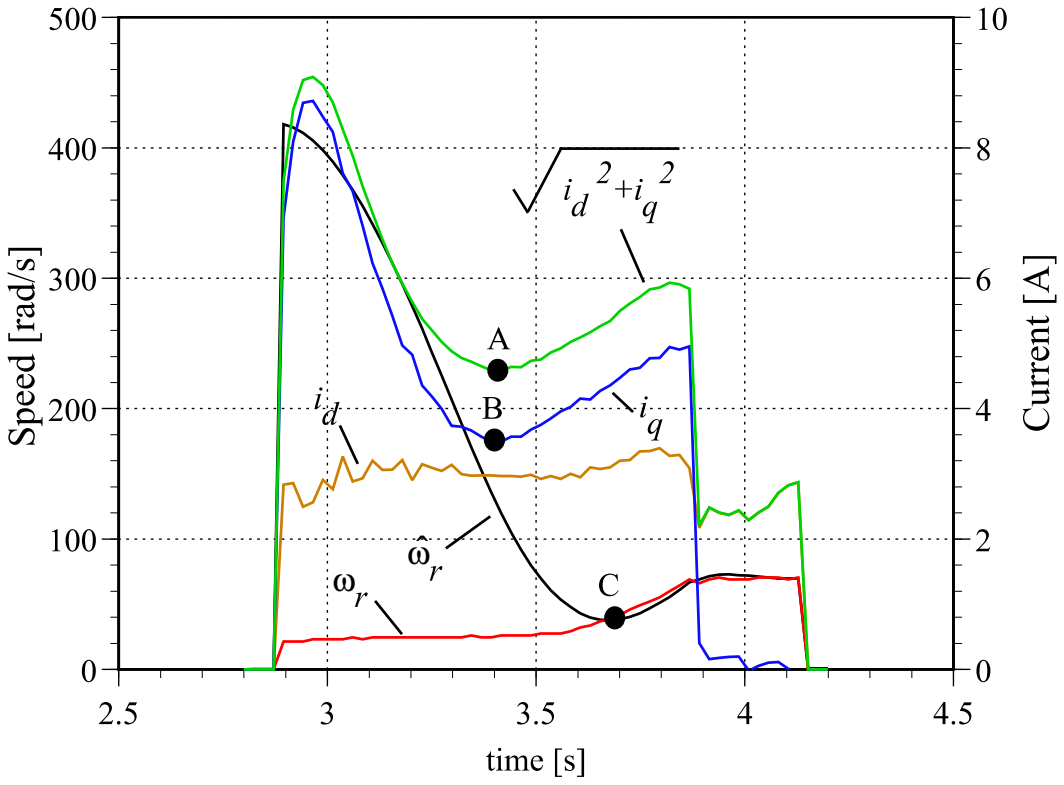

Figure 3.20: Currents and speeds responses of previous experimental results of the motor restarting operation.

responses of previous experimental results. This figure is a part of Fig. 3.19(b). The graph is enlarged for convenience. From this figure, we notice that the dq-axis current, q-axis current and estimated speed have relatively a same pattern. The pattern rises to a maximum value then goes down to a minimum value and then rises again as the actual speed is start to accelerate. We can determine when the value of the speed adaptive gain to be switched from the large value to the small value based on the time when the minimum point of the pattern is approached. Points A, B, and C, shown in Fig. 3.20, are the minimum points of the pattern of dq-axis current, q-axis current, and estimated speed respectively. Comparing these points, point C is the point that the estimated speed is very close to the actual speed. Therefore, we decided to use point C for determining the gain switching time.

The maximum or minimum value of a signal can be determined using the gradient slope of that signal. Mathematically the gradient slope can be found by differentiating the equation of that signal. Then in case of patterns in Fig. 3.20, the minimum point occurs when the gradient

slope changes from a negative value to a positive value. By using this way the minimum point determination is easy to realize in practice. Fortunately, the differential of estimated speed is available from the adaptive speed observer algorithm, which is expressed in Eq. (3.10). Therefore by choosing point C for determining the gain switching time we can save the time consuming of microprocessor calculation.

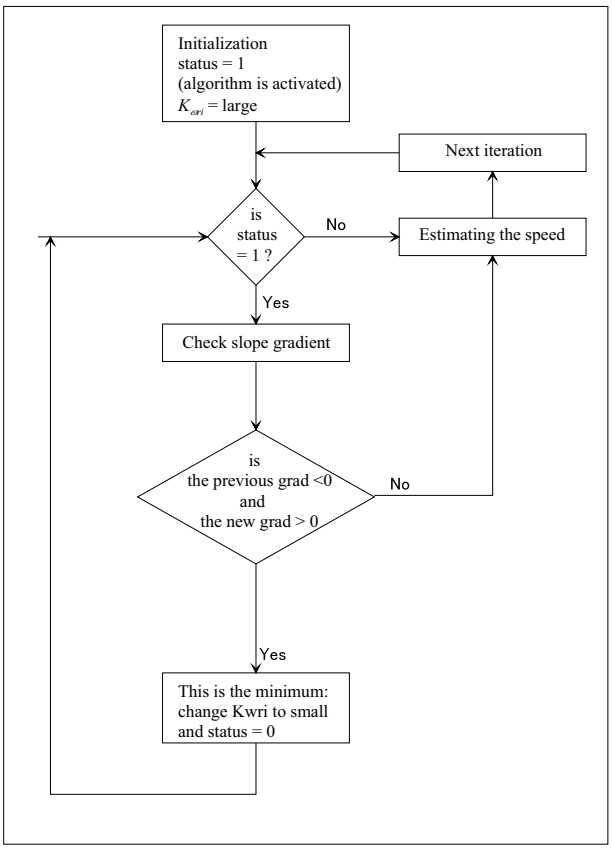

Figure 3.21: Flow chart of the minimizing convergence time strategy.

Now, let we define that

$$grad = (e_{is\alpha}\hat{\phi}_{r\beta} - e_{is\beta}\hat{\phi}_{r\alpha}) \tag{3.20}$$

where $grad$ is the slope gradient of the estimated speed. Then the speed estimation is expressed as follows:

$$\hat{\omega}_r = K_{\omega rp}(grad) + K_{\omega ri}\int (grad)dt \tag{3.21}$$

To determine the minimum value of estimated speed, $grad$ is always checked. When ever the sign of $grad$ changes from negative to positive the adaptive capability acceleration algorithm

is stop (speed adaptive gain is changed from the large value to small value). This algorithm is inactivated and only can be activated as an initial condition again when the motor is restarted. The initial status of the speed adaptive acceleration algorithm is active (operated). Fig. 3.21 shows a flow chart of the minimizing convergence time strategy.

3.4.2 Implementation of the minimizing convergence time strategy

To confirm the proposed method experiments are carried out. The field-weakening control using voltage controller is applied so that very high speed can be achieved. The motor is accelerated for 2.5 seconds by applying the q-axis current reference i^*_{sq} to its maximum value. After that it is set to zero. The initial estimated speed is set to 4000 rpm (418.9 rad/sec).

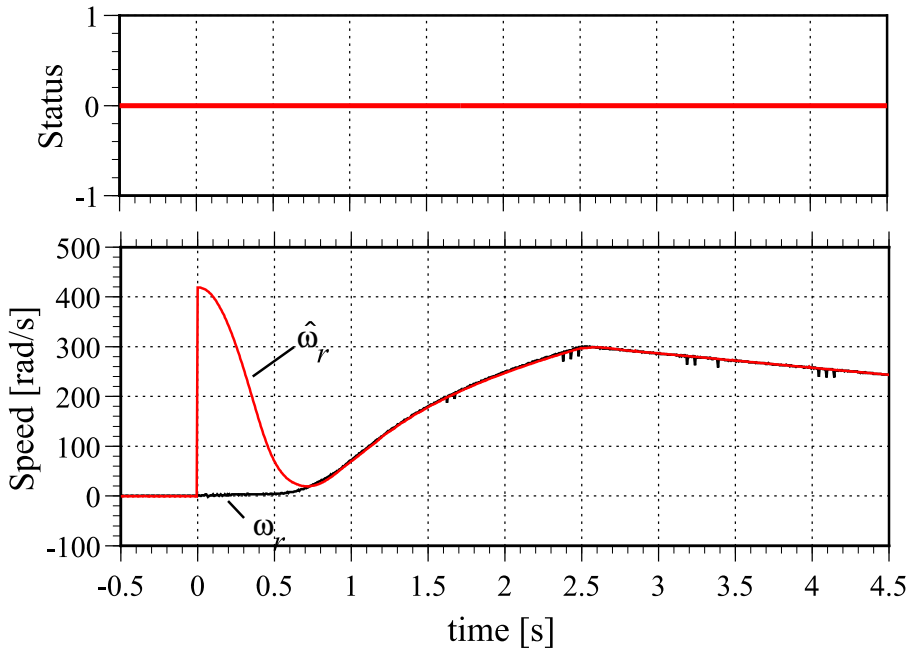

Figure 3.22: Experimental results of starting motor from the standstill condition without implementing the minimizing convergence time strategy.

Fig. 3.22 shows the experimental results of starting motor from the standstill condition without implementing the minimizing convergence time strategy (the acceleration status is always zero). From Fig. 3.22, one can see that the initial speed convergence time is about 0.7 second. In the next experimental results where the minimizing convergence time strategy is applied the initial speed convergence time is reduced becomes about 0.2 second (70 % reduced)

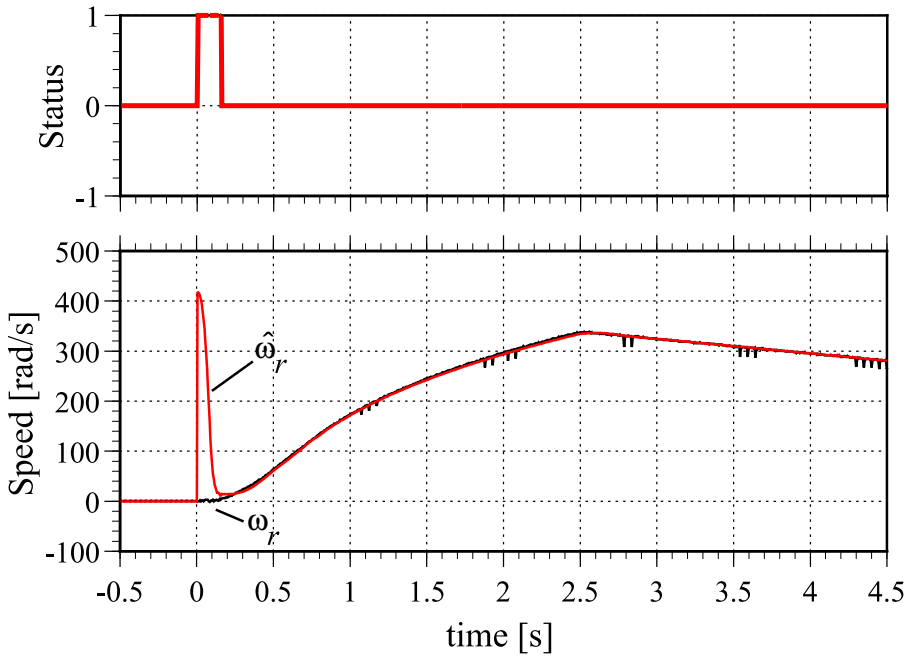

Figure 3.23: Experimental results of starting motor from the standstill condition with implementing the convergence time minimizing strategy.

as shown in Fig. 3.23. As seen in Fig. 3.23, the adaptive speed estimation is accelerated from the initial until the slope gradient of the estimated speed changes from a negative value to a positive value and the strategy is never active again, which is indicated by the acceleration status. These results confirm the effectiveness of the minimizing convergence time strategy. Finally, Fig. 3.24 shows speed responses of restarting capability of the sensorless induction motor drive system using the modified speed adaptive observer with applying the minimizing convergence time strategy. It is confirmed that the minimizing convergence time strategy can work properly.

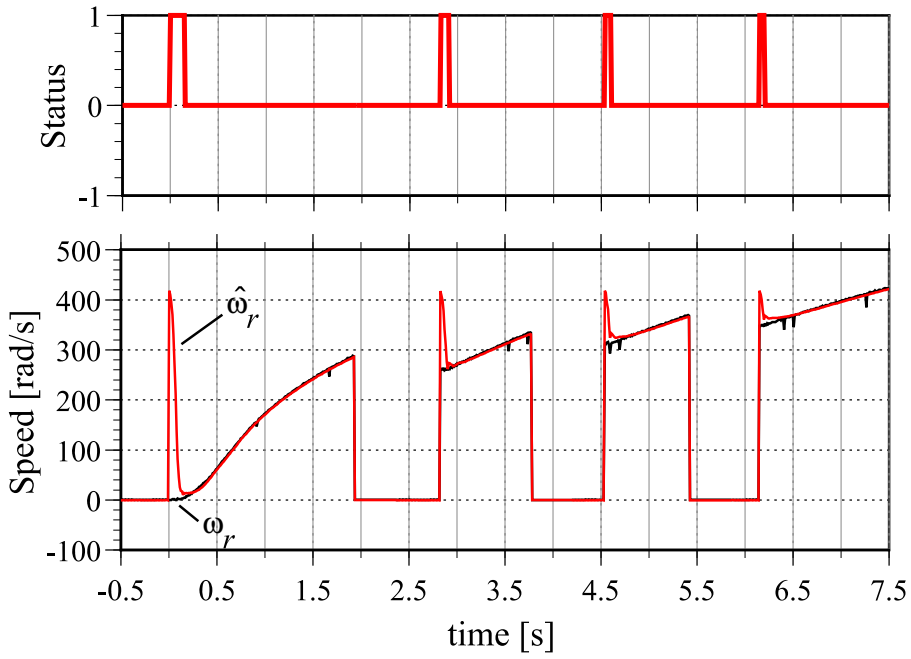

Figure 3.24: Experimental results of restarting motor with implementing the convergence time minimizing strategy.

3.5 Summary

The combine advantages of both, the established rotor-flux oriented induction motor control (high accuracy and good torque response) and the full-order observer (less intensive calculation) are achieved through a modification of the full-order observer that estimates the rotor speed for sensorless induction motor drive. Since the flux value is provided by the flux model that uses the rotor flux reference frame, the two equations in the state observer equation for flux estimating are removed. And since the observer uses the calculated flux, the lack of speed estimation due to the coupling effect was overcome. The modified observer has a better performance than the full-order observer has for each implementation to the sensorless rotor-flux oriented induction drive system.

The preliminary investigation of the motor restarting capability under the speed sensorless motor drive system using the modified speed adaptive observer has been carried out. The investigation includes:

1. Imitating the coasting operation of the electric vehicle by restarting the laboratory motor under the speed sensorless motor drive system with the speed estimation error as an initial

problem.

2. Speed adaptive gain setting effect. If the gain is too large, the lost speed adaptive capability occurs.

3. Initial estimated speed effect. If the initial estimated value is much smaller than the initial actual speed, the motor restarting operation will fail.

4. Maximum speed of motor restarting capability. The maximum initial actual speed corresponds with the initial estimated speed setting.

Therefore, in order to operate the motor restarting under the speed sensorless motor successfully, the following conditions should be considered.

1. Set the initial value of estimated speed greater than the initial value of actual speed (set to be equal to the maximum operating speed).

2. The speed adaptive gains should not too large to prevent the lost adaptive capability.

By considering these conditions, the convergence time that the estimated speed approaches the actual speed is affected. The convergence time becomes slower due to the small speed adaptive gains and the high initial value of estimated speed. To overcome this problem, a minimizing convergence time strategy for the restarting capability of the sensorless induction motor drive system with using speed adaptive observer has been proposed. By applying the minimizing convergence time strategy the convergence time can be reduced about 70%. The effectiveness of the proposed strategy is confirmed by experimental and simulation results.

This chapter has contribution to the energy saving effort by giving the preliminary investigation results of the motor restarting capability under speed sensorless drive system. Since the motor restarting can be operated successfully with considering some conditions, the motor coasting operation under speed sensorless drive system is possible.

To improve the performance of the motor restarting capability under the speed sensorless drive system, the stability analysis should be carried out for the next works. Based on the analysis results, a strategy for minimizing the speed, flux, and torque estimations errors should be studied.

Chapter 4

Anti-oscillation strategy for the regenerative braking control

In this chapter the analysis of the oscillation phenomenon, when the regenerative braking control is applied into the PMSM drive system with a light-load energy consumption, is presented and an anti oscillation strategy is proposed to overcome this stability problem. First, the oscillation phenomenon, which occurred in the actual electric vehicle, is confirmed through the experiment and the simulation. The mathematical model of investigated system, which divided into four operation conditions, is derived. The cause of the oscillation phenomenon is then clarified by solving each steady state solution and pole analyzing. Based on the analytical results, a new regenerative braking control strategy in purpose to eliminate the oscillation is proposed. This control strategy puts the operating point to a stable region when it moves to an unstable region. And then, when the last control pattern remains to be unchanged, the regenerative power is maintained to be constant even though the rotor speed is decreasing to provide a regenerative power as much as possible. Finally, the validity of the effectiveness of the proposed control technique is verified through the experiment according to the mini model of the investigated system. As a result, the stable regenerative braking control can be realized.

4.1 Introduction

Usually, electric vehicle uses a regenerative braking control system for energy conservation and the less maintenance purposes. In a DC-fed electric railway vehicle system the load power consumption of other railway vehicles as a main DC-voltage source's load of one railway vehicle always varies due to their operation conditions. Therefore, when the load power consumption is light in the power generating condition, the filter capacitor voltage v_f which corresponds to

the DC link voltage of the inverter rises because the load power consumption is insufficient. The inverter operation will be stopped by an over voltage protection mechanism included in the inverter circuit when the filter capacitor voltage v_f exceeds its permitted value, and the power generating condition is lost by which the regenerative braking is interrupted. The effect of this decreasing energy consumption is not only to bear all the desired brake power with a mechanical brake when the regenerative braking lapse occurs but also causes the demerit of the maintenance cost rise due to the use of the mechanical brake devices. In a conventional system, the DC link voltage is controlled using the regenerative method such as the thyristor control with a resistor load in substation. However, it increases the initial cost and the maintenance fee [25]. Then, a light-load regenerative braking control by which the use of regenerative braking is continued as much as possible has been adopted. This control strategy decreases the regenerative braking power so that the filter capacitor voltage v_f should not exceed a voltage permitted by the over voltage detection device [26]. When the light-load regenerative braking control is adopted in the investigated vehicle that has a PMSM drive system shown in Fig. 4.1, it turns to might cause a continuous oscillation of the electricity of system as shown in Fig. 4.2 (experimental data from an actual electric railway vehicle system provided by the Railway Technical Research Institute, Japan). Simulation is carried out to confirm this oscillation phenomenon. Then, in

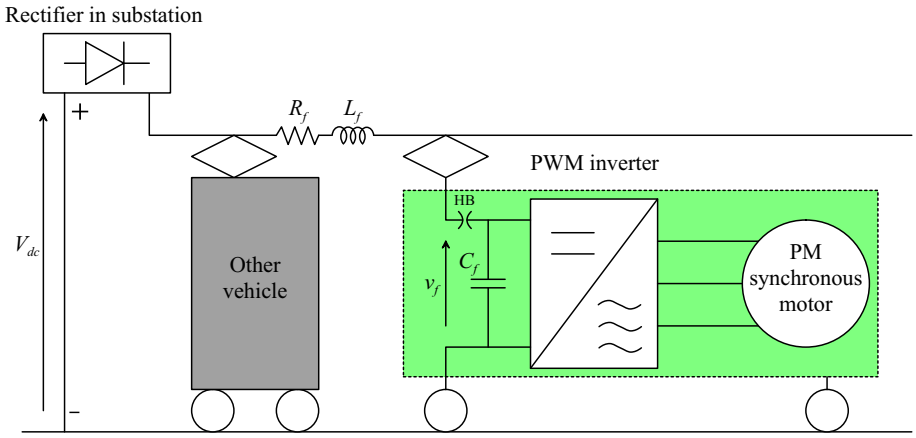

Figure 4.1: Investigated model.

this chapter we aim to contribute to the practical use of the PMSM drive system by elucidating this continuous oscillation phenomenon, and considering the countermeasures. Concretely, a nonlinear time-varying model of the investigated system that includes the main circuit from the substation to the vehicle is derived. This model is then analyzed separately into four operation

modes of linear time-invariant state equation models. Then, the cause of this continuous oscillation phenomenon is clarified by solving the steady state solution and pole analyzing. Based on this analytical result, a new light-load regenerative braking control method in purpose to eliminate the oscillation is proposed, and the validity of the analysis and the effectiveness of the proposed control technique are verified through the experiment according to the mini model of the investigated system.

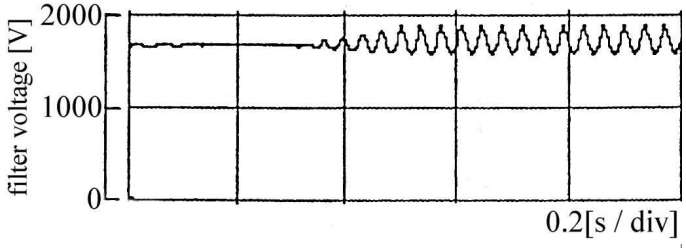

(a) Voltage oscillation phenomenon.

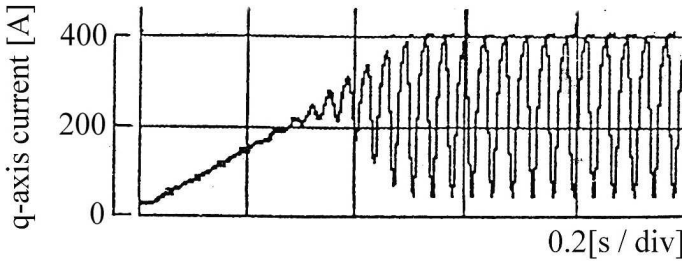

(b) Current oscillation phenomenon.

Figure 4.2: Electrical oscillation in the regenerative braking control with insufficient load power consumption.

4.2 Influence and necessity of the light-load regenerative braking control

It is supposed that the light-load regenerative braking control is an immediate cause of the oscillation phenomenon since this phenomenon has been occurred only when the regenerative current is regulated to prevent the over voltage condition. To confirm this oscillation phenomenon, simulations of the investigated system are carried out in the cases of light-load regenerative braking control is adopted and not adopted. As it was supposed, the influence of the light-load regenerative braking control on the oscillation phenomenon is actually confirmed according to

simulation results shown in Fig. 4.3. It is understood that the light-load regenerative braking

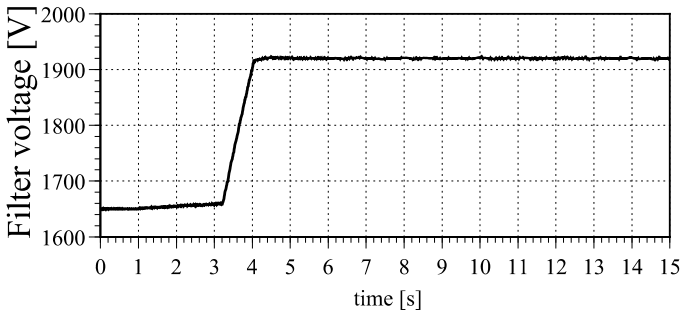

(a) Without implementing the regenerative braking control.

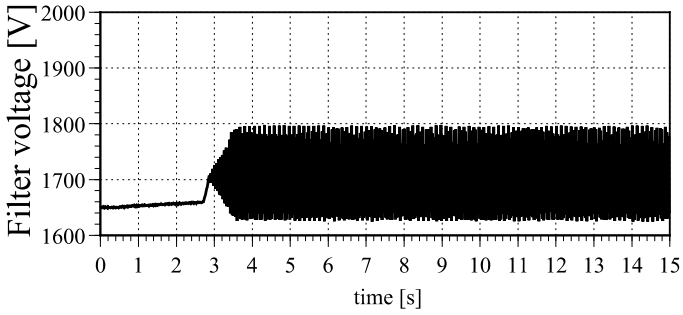

(b) With implementing the regenerative braking control.

Figure 4.3: Filter voltage oscillation phenomenon (simulation).

control is a cause of the oscillation phenomenon. In these simulations the over voltage protection mechanism is not imitated to show how high the voltage becomes. Therefore, this result does not show the necessity of the light-load regenerative braking control. However, when the voltage of the overhead wiring is 1650V, operating voltage of the over voltage protection of an electric railway vehicle is often set from 1800V to 1900V. It means if the over-voltage protection is operated or applied meanwhile the light-load regenerative braking control is not adopted the filter capacitor voltage v_f rises up to 1900V or more as shown in Fig. 4.3(a), then the over-voltage condition occurs and the inverter will be shut down. As a result, the regenerative braking lapse occurs. Therefore, the light-load regenerative braking control strategy that avoids the oscillation phenomenon is necessary and indispensable to prevent the over voltage condition occurs and the regenerative braking lapses.

4.3 Analytical model

4.3.1 System model

The investigated model shown in Fig. 4.1, can be expressed by the equivalent circuit of system model as shown in Fig. 4.4, which the control model is shown in Fig. 4.5. The system model is divided into two basic categories, i.e. the main circuit model and the control model. The

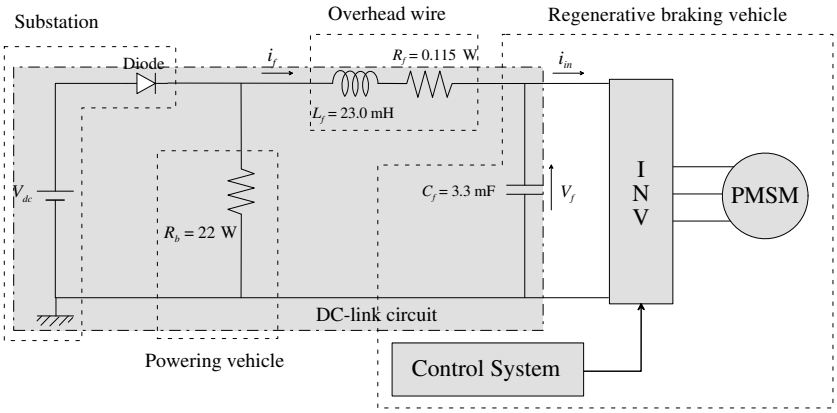

Figure 4.4: System model.

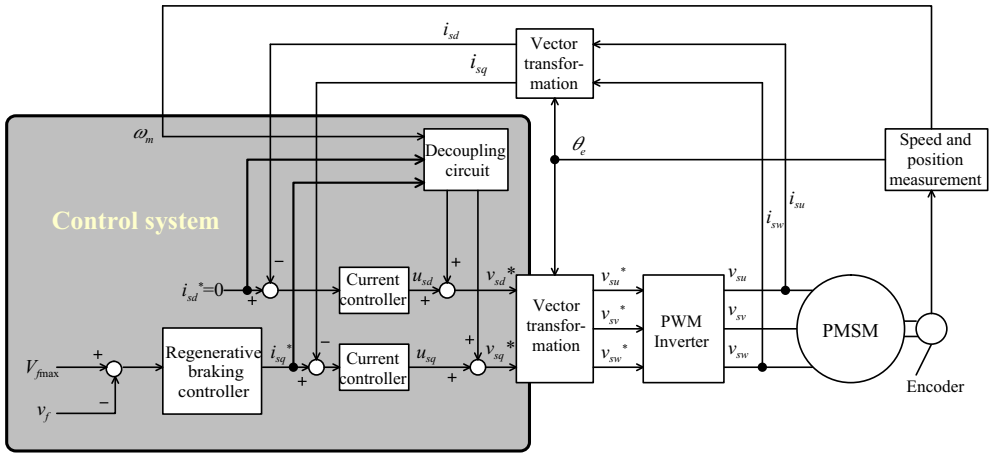

Figure 4.5: Control model.

main circuit model consists of the permanent magnet synchronous motor (PMSM) model, the asynchronous inverter model, and the DC-link circuit model. The control model consists of the current control model and the regenerative braking control model. The electrical power

source of the inverter is provided from the DC-link circuit. The operation of the motor is controlled through the switching pattern of the inverter, which the voltage reference provided by the current controller. When the motor is operated in the braking condition, the regenerative braking controller regulates the current reference pattern to the current controller. Since it is assumed that the digital current control loop in the inverter is very short in time, the analysis of the investigated phenomenon is carried out by treat all models as a continuous system. For analysis purpose the system model is divided into five sub-model as follows:

- Motor model
- Inverter model
- DC-link circuit model
- Current control model
- Regenerative braking control model

Motor model

The motor used for analysis model is an interior type of permanent magnet synchronous motor (PMSM). The inertia load is assumed to be a very large one, therefore, the rotor speed can be assumed to be a parameter constant that is used for analyzing the regenerative braking operation.The PMSM model including the mechanical model are expressed in Eqs. (4.1)∼(4.3) as follows:

$$\frac{di_{sd}}{dt} = -\frac{R_s}{L_{sd}} i_{sd} + N\omega_m \frac{L_{sq}}{L_{sd}} i_{sq} + \frac{1}{L_{sd}} v_{sd} \tag{4.1}$$

$$\frac{di_{sq}}{dt} = -N\omega_m \frac{L_{sd}}{L_{sq}} i_{sd} - \frac{R_s}{L_{sq}} i_{sq} - \frac{N\psi_F}{L_{sq}} \omega_m + \frac{1}{L_{sq}} v_{sq} \tag{4.2}$$

$$\frac{d\omega_m}{dt} = \frac{N\psi_F}{J} i_{sq} + \frac{N\left(L_{sd} - L_{sq}\right)}{J} i_{sd} i_{sq} - \frac{1}{J} t_L \tag{4.3}$$

Since the inertia load J is assumed very large, the right-hand part of Eq. (4.3) becomes very small ($\frac{d\omega_m}{dt} \approx 0$). Then the rotor speed ω_m in Eqs. (4.1) and (4.2) is substituted by the constant ω_{m0}. Therefore, the PMSM model can be simplified as follows:

$$\frac{di_{sd}}{dt} = -\frac{R_s}{L_{sd}} i_{sd} + \frac{N\omega_{m0} L_{sq}}{L_{sd}} i_{sq} + \frac{1}{L_{sd}} v_{sd} \tag{4.4}$$

$$\frac{di_{sq}}{dt} = -\frac{N\omega_{m0}L_{sd}}{L_{sq}}i_{sd} - \frac{R_s}{L_{sq}}i_{sq} - \frac{N\omega_{m0}\psi_F}{L_{sq}} + \frac{1}{L_{sq}}v_{sq} \tag{4.5}$$

Inverter model

The inverter used as a model is a two level voltage type asynchronous inverter. The inverter model used in the simulation includes two expressions. One is expressed by a switching function, and another one is expressed by a voltage conversion function.

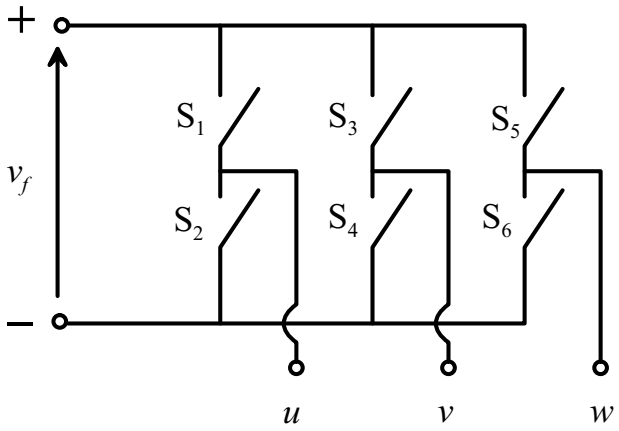

Figure 4.6: Inverter switching.

Table 4.1: Switching pattern

Switching function	Switching state	
$S_u = 1$	S_1ON	S_2OFF
$S_u = 0$	S_1OFF	S_2ON
$S_v = 1$	S_3ON	S_4OFF
$S_v = 0$	S_3OFF	S_4ON
$S_w = 1$	S_5ON	S_6OFF
$S_w = 0$	S_5OFF	S_6ON

In simulation, the uvw-axes voltages are determined by the switching arm position as shown in Fig. 4.6. The switching functions S_u, S_v, and S_w are decided to be equal 1 or 0 depend on the switching state as listed in Table 4.1. The switching state is controlled by the pulse width modulation (PWM) signal, which is produced by comparing the 3-phase voltage references

with a triangle carrier wave. Then the inverter output voltages are expressed in the following equations.

$$v_{su} = \frac{1}{3} v_f \left(2S_u - S_v - S_w\right) \tag{4.6}$$

$$v_{sv} = \frac{1}{3} v_f \left(-S_u + 2S_v - S_w\right) \tag{4.7}$$

$$v_{sw} = \frac{1}{3} v_f \left(-S_u - S_v + 2S_w\right) \tag{4.8}$$

Then, the detection value of DC voltage input (filter condenser voltage) $v_{f\,\mathrm{det}}$, which has a modulation factor, is expressed using laplace operator as

$$v_{f\,\mathrm{det}} = \frac{1}{sT_{DC} + 1} v_f \tag{4.9}$$

In the detection process v_f is filtered using the one-order delay filter with a time constant of T_{DC} to eliminate the noise or ripple. The modulation factors α_d^* and α_q^* are calculated using $v_{f\,\mathrm{det}}$ and dq-axes voltage references (v_d^* and v_q^*) as expressed in the following equations.

$$\alpha_d^* = 2\sqrt{\frac{2}{3}} \frac{v_{sd}^*}{v_{f\,\mathrm{det}}} \tag{4.10}$$

$$\alpha_q^* = 2\sqrt{\frac{2}{3}} \frac{v_{sq}^*}{v_{f\,\mathrm{det}}} \tag{4.11}$$

The dq-axes voltages are expressed using the modulation factor as

$$v_{sd} = \frac{1}{2}\sqrt{\frac{3}{2}} \alpha_d^* v_f \tag{4.12}$$

$$v_{sq} = \frac{1}{2}\sqrt{\frac{3}{2}} \alpha_q^* v_f \tag{4.13}$$

From Eqs. (4.9)∼(4.13), the inverter model is rewritten as expressed in Eqs. (4.14)∼(4.16).

$$\frac{dv_{f\,\mathrm{det}}}{dt} = -\frac{1}{T_{DC}} v_{f\,\mathrm{det}} + \frac{1}{T_{DC}} v_f \tag{4.14}$$

$$v_{sd} = \frac{v_f}{v_{f\,\mathrm{det}}} v_{sd}^* \tag{4.15}$$

$$v_{sq} = \frac{v_f}{v_{f\,\mathrm{det}}} v_{sq}^* \tag{4.16}$$

Since it becomes complicated if we use the switching function in the analysis, the inverter is assumed as an ideal power conversion machine with an efficiency factor η. The power conversion expression of inverter model for analysis purpose is expressed as

$$\eta v_f i_{in} = v_{sd} i_{sd} + v_{sq} i_{sq} \tag{4.17}$$

In the analysis the inverter is assumed to be ideally efficient, and then $\eta = 1.00$.

DC-link circuit model

The substation, which is included in the DC-link circuit model (see Fig. 4.4), is represented by a fixed voltage source and a diode. The directions of currents flow defined by the directions of the arrows in Fig. 4.4 are assigned as positive directions. Expressions of the DC-link inverter voltage v_f are separated into different circuit equations depended upon the turn-on and the turn-off times of the substation diode operations as expressed in Eqs. (4.18)∼(4.21) as follows:

(i) State of substation diode ON:

$$\frac{dv_f}{dt} = \frac{1}{C_f} i_f - \frac{1}{C_f} i_{in} \tag{4.18}$$

$$v_f - V_{dc} = -R_f i_f - L_f \frac{di_f}{dt} \tag{4.19}$$

(ii) State of substation diode OFF:

$$\frac{dv_f}{dt} = \frac{1}{C_f} i_f - \frac{1}{C_f} i_{in} \tag{4.20}$$

$$v_f = -\left(R_b + R_f\right) i_f - L_f \frac{di_f}{dt} \tag{4.21}$$

Current control model

The dq-axis stator voltage references, which are the output of the current controller is shown by using laplace transformation in Eqs. (4.22) and (4.23). The first and second terms of the right-hand side of Eqs. (4.22) and (4.23) are the PI current controllers, and the third terms are the current decoupling compensation element. The fourth term of the right-hand side of Eq. (4.23) is the compensation element of the voltage induced by rotor-flux linkage.

$$v_{sd}^* = K_{pd}\left(i_{sd}^* - i_{sd}\right) + \frac{K_{id}}{s}\left(i_{sd}^* - i_{sd}\right) - \frac{N\omega_m L_{sq} i_{sq}^*}{T_d s + 1} \tag{4.22}$$

$$v_{sq}^{*} = K_{pq}\left(i_{sq}^{*} - i_{sq}\right) + \frac{K_{iq}}{s}\left(i_{sq}^{*} - i_{sq}\right) + \frac{N\omega_m L_{sd} i_{sd}^{*}}{T_d s + 1} + N\omega_m \psi_F \tag{4.23}$$

where, K_{pd} and K_{pq} are the proportion gains, K_{id} and K_{iq} are the integral gains, which are decided by a time constant of T_d and the motor parameters. These gain parameters are expressed in Eq. (4.24) ,which are introduced in [27].

$$K_{pd} = \frac{L_{sd}}{T_d}, \quad K_{pq} = \frac{L_{sq}}{T_d}, \quad K_{id} = \frac{R_s}{T_d}, \quad K_{iq} = \frac{R_s}{T_d} \tag{4.24}$$

Now, the new state variables, i.e. x_{sd}, x_{sq}, i_{sd1}^{*}, and i_{sq1}^{*}, are defined as follows:

$$\frac{dx_{sd}}{dt} = i_{sd}^{*} - i_{sd} \tag{4.25}$$

$$\frac{dx_{sq}}{dt} = i_{sq}^{*} - i_{sq} \tag{4.26}$$

$$T_d \frac{di_{sd1}^{*}}{dt} + i_{sd1}^{*} = i_{sd}^{*} \tag{4.27}$$

$$T_d \frac{di_{sq1}^{*}}{dt} + i_{sq1}^{*} = i_{sq}^{*} \tag{4.28}$$

Then, Eqs. (4.22) and (4.23) are expressed using the new state variables as follows:

$$v_{sd}^{*} = K_{pd} i_{sd}^{*} - K_{pd} i_{sd} + K_{id} x_{sd} - N\omega_{m0} L_{sq} i_{sq1}^{*} \tag{4.29}$$

$$v_{sq}^{*} = K_{pq} i_{sq}^{*} - K_{pq} i_{sq} + K_{iq} x_{sq} + N\omega_{m0} L_{sd} i_{sd1}^{*} + N\omega_{m0} \psi_F \tag{4.30}$$

Here, the rotor speed ω_m is assumed to be constant and is substituted by ω_{m0}.

Regenerative braking control model

The torque t_e of a PMSM can be written in the synchronous frame (dq-axes) as follows:

$$t_e = N\psi_F i_{sq} + \left(L_{sd} - L_{sq}\right) i_{sd} i_{sq} \tag{4.31}$$

Since the d-axis current is following its reference current $i_{sd}^{*} = 0$ due to the current control operation, i_{sd} is assumed to be zero. Therefore, the regenerative torque can be controlled by control the q-axis current i_{sq}, which is proportional to its reference i_{sq}^{*}.

The light-load regenerative braking control is to control the reference value of q-axis current i_{sq} in such a way described by Eq. (4.32) and illustrated in Fig. 4.7. The magnitude of q-axis

current reference value I_r is narrowed according to the rise of the filter capacitor voltage as shown in Fig. 4.7. In Eq. (4.32), I_r is a current reference value when the current narrowing is not done, $V_{f\,\mathrm{lim}}$ is a voltage when the current narrowing is begins, and $V_{f\,\mathrm{max}}$ is a voltage when the current narrowing is end.

$$i_{sq}^{*} = \begin{cases} -I_r & (v_f \leq V_{f\,\mathrm{lim}}) \\ \frac{I_r}{V_{f\,\mathrm{max}} - V_{f\,\mathrm{lim}}} (v_f - V_{f\,\mathrm{max}}) & (V_{f\,\mathrm{lim}} \leq v_f \leq V_{f\,\mathrm{max}}) \\ 0 & (V_{f\,\mathrm{max}} \leq v_f) \end{cases} \tag{4.32}$$

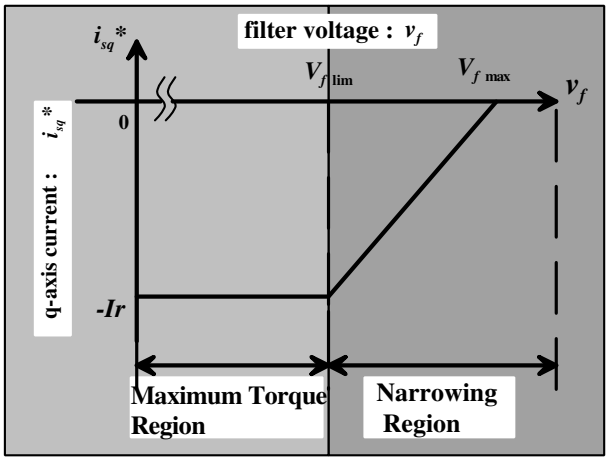

Figure 4.7: Light-load regenerative current control pattern for the insufficient load power consuming condition.

In the analysis, it is assumed that the contribution of the control scheme when $v_f > V_{f\,\mathrm{max}}$ to the oscillation phenomenon is small, so that only the conditions of $v_f < V_{f\,\mathrm{lim}}$ and $V_{f\,\mathrm{lim}} < v_f < V_{f\,\mathrm{max}}$ are considered to be investigated. Therefore, these conditions are designated into two operation regions as follows: $v_f < V_{f\,\mathrm{lim}}$ condition as Maximum torque region and $v_f > V_{f\,\mathrm{lim}}$ condition as Narrowing region.

4.3.2 The linearized system model

Since the analysis is carried out using the classic analysis method for linear system, such as the system pole analysis, the system model, which is described in Subsection 4.3.1 previously, should be linearized around the equilibrium points. The equilibrium points are determined by equating the differential part of the system model equations in Subsection 4.3.1 to zero

($\frac{d}{dt}x = 0$). Then by using the chain differentiation rule, the system model is linearized around the equilibrium points as follows: (the linearized state variable is denoted by Δx)

Linearized motor model

From Eqs. (4.4)∼(4.5) by substituting $\frac{d}{dt}x = 0$, the equilibrium points are:

$$0 = -R_s i_{sd0} + N\omega_{m0} L_{sq} i_{sq0} + v_{sd0} \tag{4.33}$$

$$0 = -N\omega_{m0} L_{sd} i_{sd0} - R_s i_{sq0} - N\omega_{m0}\psi_F + v_{sq0} \tag{4.34}$$

The linearized equations are:

$$\frac{d}{dt}\Delta i_{sd} = -\frac{R_s}{L_{sd}}\Delta i_{sd} + \frac{N\omega_{m0} L_{sq}}{L_{sd}}\Delta i_{sq} + \frac{1}{L_{sd}}\Delta v_{sd} \tag{4.35}$$

$$\frac{d}{dt}\Delta i_{sq} = -\frac{N\omega_{m0} L_{sd}}{L_{sq}}\Delta i_{sd} - \frac{R_s}{L_{sq}}\Delta i_{sq} + \frac{1}{L_{sq}}\Delta v_{sq} \tag{4.36}$$

Linearized inverter model

From Eqs. (4.14)∼(4.16) by substituting $\frac{d}{dt}x = 0$, the equilibrium points are:

$$v_{f\,\mathrm{det}\,0} = v_{f0} \tag{4.37}$$

$$v_{sd0} = v^*_{sd0} \tag{4.38}$$

$$v_{sq0} = v^*_{sq0} \tag{4.39}$$

and from Eq. (4.17), the equilibrium point is:

$$\eta v_{f0} i_{in0} = v_{sd0} i_{sd0} + v_{sq0} i_{sq0} \tag{4.40}$$

The linearized equations are:

$$\frac{d}{dt}\Delta v_{f\,\mathrm{det}} = -\frac{1}{T_{DC}}\Delta v_{f\,\mathrm{det}} + \frac{1}{T_{DC}}\Delta v_f \tag{4.41}$$

$$\Delta v_{sd} = \frac{v_{sd0}}{v_{f0}}\Delta v_f - \frac{v_{sd0}}{v_{f0}}\Delta v_{f\,\mathrm{det}} + \Delta v^*_{sd} \tag{4.42}$$

$$\Delta v_{sq} = \frac{v_{sq0}}{v_{f0}}\Delta v_f - \frac{v_{sq0}}{v_{f0}}\Delta v_{f\,\mathrm{det}} + \Delta v_{sq}^{*} \tag{4.43}$$

$$\eta i_{in0}\Delta v_f + \eta v_{f0}\Delta i_{in} = i_{sd0}\Delta v_{sd} + v_{sd0}\Delta i_{sd} + i_{sq0}\Delta v_{sq} + v_{sq0}\Delta i_{sq} \tag{4.44}$$

Then Eq. (4.44) is rearranged as follow:

$$\Delta i_{in} = \frac{1}{\eta v_{f0}}\left(-\eta i_{in0}\Delta v_f + i_{sd0}\Delta v_{sd} + v_{sd0}\Delta i_{sd} + i_{sq0}\Delta v_{sq} + v_{sq0}\Delta i_{sq}\right) \tag{4.45}$$

Linearized DC-link circuit model

(i) State of substation diode ON:

From Eqs. (4.18) and (4.19), the equilibrium points are:

$$i_{f0} = i_{in0} \tag{4.46}$$

$$v_{f0} - V_{dc} = -R_f i_{f0} \tag{4.47}$$

And the linearized equations are:

$$\frac{d}{dt}\Delta v_f = \frac{1}{C_f}\Delta i_f - \frac{1}{C_f}\Delta i_{in} \tag{4.48}$$

$$\frac{d}{dt}\Delta i_f = -\frac{R_f}{L_f}\Delta i_f - \frac{1}{L_f}\Delta v_f \tag{4.49}$$

(ii) State of substation diode OFF:

From Eqs. (4.20) and (4.21), the equilibrium points are:

$$i_{f0} = i_{in0} \tag{4.50}$$

$$v_{f0} = -\left(R_b + R_f\right) i_{f0} \tag{4.51}$$

And the linearized equations are:

$$\frac{d}{dt}\Delta v_f = \frac{1}{C_f}\Delta i_f - \frac{1}{C_f}\Delta i_{in} \tag{4.52}$$

$$\frac{d}{dt}\Delta i_f = -\frac{R_b + R_f}{L_f}\Delta i_f - \frac{1}{L_f}\Delta v_f \tag{4.53}$$

Linearized current control model

From Eqs. (4.25)∼(4.30), the equilibrium points are:

$$i^*_{sd0} = i_{sd0} \tag{4.54}$$

$$i^*_{sq0} = i_{sq0} \tag{4.55}$$

$$i^*_{sd10} = i^*_{sd0} \tag{4.56}$$

$$i^*_{sq10} = i^*_{sq0} \tag{4.57}$$

$$v^*_{sd0} = K_{pd} i^*_{sd0} - K_{pd} i_{sd0} + K_{id} x^*_{sd0} - K_{id} x_{sd0} - N\omega_{m0} L_{sq} i^*_{sq10} \tag{4.58}$$

$$v^*_{sq0} = K_{pq} i^*_{sq0} - K_{pq} i_{sq0} + K_{iq} x^*_{sq0} - K_{iq} x_{sq0} + N\omega_{m0} L_{sd} i^*_{sd10} + N\omega_{m0}\psi_F \tag{4.59}$$

By substituting Eqs. (4.54)∼(4.57) into Eqs. (4.58) and (4.25), these equations become:

$$v^*_{sd0} = K_{id} x_{sd0} - N\omega_{m0} L_{sq} i_{sq0} \tag{4.60}$$

$$v^*_{sq0} = K_{iq} x_{sq0} + N\omega_{m0} L_{sd} i_{sd0} + N\omega_{m0}\psi_F \tag{4.61}$$

Then from Eqs. (4.33) and (4.34), we have:

$$v^*_{sd0} = R_s i_{sd0} - N\omega_{m0} L_{sq} i_{sq0} \tag{4.62}$$

$$v^*_{sq0} = R_s i_{sq0} + N\omega_{m0} L_{sd} i_{sd0} + N\omega_{m0}\psi_F \tag{4.63}$$

By equating Eqs. (4.60) and (4.61) with Eqs. (4.62) and (4.63) respectively, the others equilibrium points are determined as follows:

$$x_{sd0} = \frac{R_s i_{sd0}}{K_{id}} \tag{4.64}$$

$$x_{sq0} = \frac{R_s i_{sq0}}{K_{iq}} \tag{4.65}$$

And the linearized equations are:

$$\frac{d}{dt}\Delta x_{sd} = \Delta i^*_{sd} - \Delta i_{sd} \tag{4.66}$$

$$\frac{d}{dt}\Delta x_{sq} = \Delta i^*_{sq} - \Delta i_{sq} \tag{4.67}$$

$$\frac{d}{dt}\Delta i^*_{sd1} = \frac{1}{T_d}\Delta i^*_{sd} - \frac{1}{T_d}\Delta i^*_{sd1} \tag{4.68}$$

$$\frac{d}{dt}\Delta i^*_{sq1} = \frac{1}{T_d}\Delta i^*_{sq} - \frac{1}{T_d}\Delta i^*_{sd1} \tag{4.69}$$

$$\Delta v^*_{sd} = K_{pd}\Delta i^*_{sd} - K_{pd}\Delta i_{sd} + K_{id}\Delta x_{sd} - N\omega_{m0}L_{sq}\Delta i^*_{sq1} \tag{4.70}$$

$$\Delta v^*_{sq} = K_{pq}\Delta i^*_{sq} - K_{pq}\Delta i_{sq} + K_{iq}\Delta x_{sq} + N\omega_{m0}L_{sd}\Delta i^*_{sd1} \tag{4.71}$$

Linearized regenerative braking control model

From the d-axis current reference $i^*_{sd} = 0$ and the q-axis current reference in Eq. (4.7), the equilibrium points are:

$$i^*_{sd0} = 0 \tag{4.72}$$

$$i^*_{sq0} = \begin{cases} -I_r & (v_f \le V_{f\,\mathrm{lim}}) \\ \frac{I_r}{V_{f\,\max} - V_{f\,\mathrm{lim}}}\left(v_{f0} - V_{f\,\max}\right) & (V_{f\,\mathrm{lim}} \le v_f) \end{cases} \tag{4.73}$$

And the linearized equations are:

$$\Delta i^*_{sd} = 0 \tag{4.74}$$

$$\Delta i^*_{sq} = \begin{cases} 0 & (v_f \le V_{f\,\mathrm{lim}}) \\ \frac{I_r}{V_{f\,\max} - V_{f\,\mathrm{lim}}}\Delta v_f & (V_{f\,\mathrm{lim}} \le v_f) \end{cases} \tag{4.75}$$

4.4 Analytical result

4.4.1 Analysis method

Since the analytical object system contains a rectifier (see Fig. 4.4), which is a nonlinear element due to the ON-OFF operations of the substation diode, and the operation of the light-load regenerative control, handling it in the analysis is difficult. The ON-OFF operations of the substation diode, and the operation of the light-load regenerative control are illustrated in Fig. 4.8. Therefore, the model derived in the previous section is divided into four kinds of operation modes as follows:

- **Mode 1:** S_I&D_{ON} Narrowing region and substation diode ON
- **Mode 2:** S_I&D_{OFF} Narrowing region and substation diode OFF
- **Mode 3:** S_{II}&D_{ON} Maximum torque region and substation diode ON
- **Mode 4:** S_{II}&D_{OFF} Maximum torque region and substation diode OFF

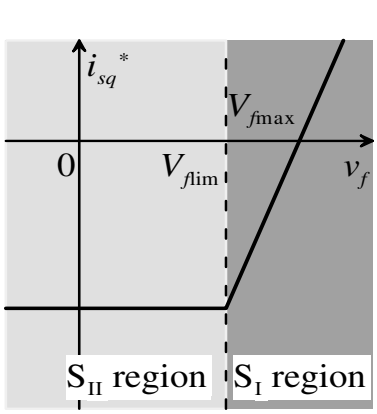

(a) The operation of the light-load regenerative control.

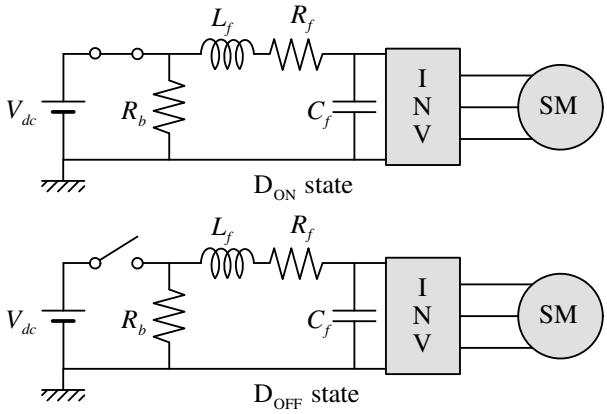

(b) The ON-OFF operations of the substation diode.

Figure 4.8: The operations mode of the regenerative braking control.

An analytical technique whereabouts the stability of the equilibrium point of the state equation is examined is arranged as follows: The state of the narrowing region or the maximum torque region depends on the filter capacitor voltage and the ON-OFF operation of the substation diode according to the end-to-end terminal voltage of equivalent load resistance R_b.

Therefore, the ON-OFF condition of the substation diode is defined according to the current that flows in the equivalent load resistance R_b.

4.4.2 Equilibrium points of each operation mode

(i) Substation diode ON state

First, a balance point when rectifier turns on is determined at the filter condenser voltage in the DC-link circuit side. When a system is supposed to reach a balance condition, the electric power supplied by the DC-link circuit side and the electric power consumed by a motor side are same, which is expressed as

$$-R_s i_{sq0}^2 - N\omega_{m0}\psi_F i_{sq0} = \frac{v_{f0}\left(v_{f0} - V_{dc}\right)}{R_f} \tag{4.76}$$

By substituting Eq. (4.73) into Eq. (4.76), the equilibrium points of Mode 1 and Mode 3 are expressed as follows:

$$\text{Mode 1}: \quad R_s A_r^2 \left(v_{f0} - V_{f\max}\right)^2 + N\omega_{m0}\psi_F A_r \left(v_{f0} - V_{f\max}\right) + \frac{v_{f0}\left(v_{f0} - V_{dc}\right)}{R_f} = 0 \tag{4.77}$$

$$\text{Mode 3}: \quad R_s I_r^2 - N\omega_{m0}\psi_F I_r + \frac{v_{f0}\left(v_{f0} - V_{dc}\right)}{R_f} = 0 \tag{4.78}$$

where $A_r = \frac{I_r}{V_{f\max} - V_{f\lim}}$.

(ii) Substation diode OFF state

The electric power balance condition when the substation diode turns off is expressed as

$$-R_s i_{sq0}^2 - N\omega_{m0}\psi_F i_{sq0} = \frac{v_{f0}^2}{R_b + R_f} \tag{4.79}$$

By substituting Eq. (4.73) into Eq. (4.79), the equilibrium points of Mode 2 and Mode 4 are expressed as follows:

$$\text{Mode 2}: \quad R_s A_r^2 \left(v_{f0} - V_{f\max}\right)^2 + N\omega_{m0}\psi_F A_r \left(v_{f0} - V_{f\max}\right) + \frac{v_{f0}^2}{R_b + R_f} = 0 \tag{4.80}$$

$$\text{Mode 4}: \quad R_s I_r^2 - N\omega_{m0}\psi_F I_r + \frac{v_{f0}^2}{R_b + R_f} = 0 \tag{4.81}$$

By using the model parameters listed in Table 4.2, the equilibrium points of each operation mode are calculated and listed in Table 4.3.

Table 4.2: Model parameters

Item	Symbol	Value	Item	Symbol	Value
Stator resistant	R_s	0.1[Ω]	Rotor speed	ω_{m0}	250[rpm]
d-axis inductance	L_{sd}	15[mH]	Wheel diameter	d_m	820[mm]
q-axis inductance	L_{sq}	10[mH]	Maximum regenerative current	I_r	415.7[A]
Permanent magnet flux	ψ_F	4.23[Wb]	Current control time constant	T_d	10[ms]
Rotor inertia	J	10^5[kgm^2]	Voltage detection time constant	T_{DC}	100[ms]
Poles number	N	4	Narrowing start voltage	$V_{f\,\mathrm{lim}}$	1700[V]
Load torque	T_L	0	Narrowing end voltage	$V_{f\,\max}$	1800[V]
Source voltage	V_{dc}	1650[V]	Over voltage limit	V_{fOVD}	1900[V]
Powering vehicle load	R_b	22[Ω]	Inverter carrier frequency	f_c	5[kHz]
Filter inductance	L_f	23[mH]	Maximum index modulation	$M_{\max}$	1
Filter resistance	R_f	0.115[Ω]	Current control sampling time	dT	250[μs]
Filter condenser	C_f	3.3[mF]	Simulation time base	Δt	2[μs]

Table 4.3: Equilibrium of each operation mode

Equilibrium point	Symbol	Narrowing region		Max torque region	
		Diode ON	Diode OFF	Diode ON	Diode OFF
		Mode 1	Mode 2	Mode 3	Mode 4
Filter condenser voltage [V]	v_{f0}	1664.995	1721.4389	1661.5488	1920.964
Detected filter condenser voltage [V]	$v_{f\mathrm{det}0}$	1664.995	1721.4389	1661.5488	1920.964
Filter inductance current [A]	i_{f0}	-130.3921	-77.840329	-100.4242	-86.862492
d-axis current [A]	i_{sd0}	0	0	0	0
q-axis current [A]	i_{sq0}	-561.2154	-326.57855	-415.7	-415.7
d-axis current control integral variable [C]	x_{sd0}	0	0	0	0
q-axis current control integral variable [C]	x_{sq0}	-5.612154	-3.2657855	-4.157	-4.157
One-order delayed d-axis current reference [A]	i^*_{sd10}	0	0	0	0
One-order delayed q-axis current reference [A]	i^*_{sq10}	-561.2154	-326.57855	-415.7	-415.7
d-axis voltage [V]	v_{sd0}	587.70338	341.99226	435.32002	435.32002
q-axis voltage [V]	v_{sq0}	386.84303	410.30671	401.39456	401.39456
Inverter input current [A]	i_{in0}	-130.3921	-77.840329	-100.4242	-86.862492

xxx ...the equilibrium point is out of its mode operation area

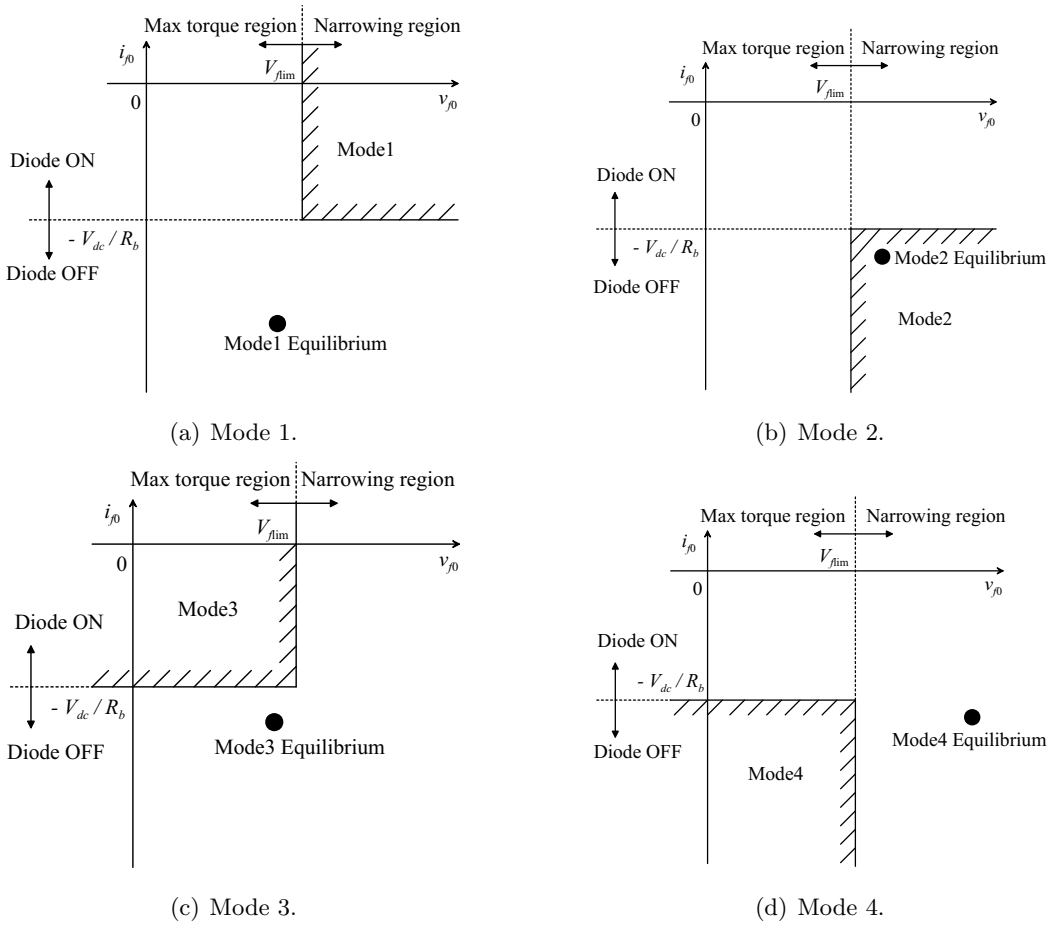

(a) Mode 1. (b) Mode 2.

(c) Mode 3. (d) Mode 4.

Figure 4.9: The equilibrium points mapping into its operation mode.

Then, the equilibrium points of the filter capacitor voltage v_{f0} and the current of the overhead wiring i_{f0}, which relates to the operation mode, are mapped in the current-voltage plane as shown in Fig. 4.9.

4.4.3 Poles of each operation mode

The four operation modes are described by four linearized state equations those are expressed in Eqs. (4.83)∼(4.86), where $A_r = \frac{I_r}{V_{f\max} - V_{f\lim}}$, and the state variables as follow:

$$x = \left[\begin{array}{cccccccc} \Delta v_f & \Delta v_{f\,\mathrm{det}} & \Delta i_f & \Delta i_{sd} & \Delta i_{sq} & \Delta x_{sd} & \Delta x_{sq} & \Delta i^*_{sd1} & \Delta i^*_{sq1} \end{array} \right]^T \tag{4.82}$$

The poles of the linearized system model for each operating mode are shown in Fig. 4.10 and listed in Table 4.4.

Mode 1:

$$\frac{d}{dt}\begin{bmatrix}\Delta v_f\\ \Delta v_{f\,\mathrm{det}}\\ \Delta i_f\\ \Delta i_{sd}\\ \Delta i_{sq}\\ \Delta x_{sd}\\ \Delta x_{sq}\\ \Delta i^*_{sd1}\\ \Delta i^*_{sq1}\end{bmatrix} = \begin{bmatrix} -\frac{A_r i_{sq0} K_{pq}}{\eta C_f v_{f0}} & \frac{i_{in0}}{C_f v_{f0}} & \frac{1}{C_f} & \frac{-v_{sd0}+i_{sd0}K_{pd}}{\eta C_f v_{f0}} & \frac{-v_{sq0}+i_{sq0}K_{pq}}{\eta C_f v_{f0}} \\ \frac{1}{T_{DC}} & -\frac{1}{T_{DC}} & 0 & 0 & 0 \\ -\frac{1}{L_f} & 0 & -\frac{R_f}{L_f} & 0 & 0 \\ \frac{v_{sd0}}{L_{sd}v_{f0}} & -\frac{v_{sd0}}{L_{sd}v_{f0}} & 0 & -\frac{R_s+K_{pd}}{L_{sd}} & \frac{N\omega_{m0}L_{sq}}{L_{sd}} \\ \frac{v_{sq0}}{L_{sq}v_{f0}}+\frac{A_r K_{pq}}{L_{sq}} & -\frac{v_{sq0}}{L_{sq}v_{f0}} & 0 & -\frac{N\omega_{m0}L_{sd}}{L_{sq}} & -\frac{R_s+K_{pq}}{L_{sq}} \\ 0 & 0 & 0 & -1 & 0 \\ A_r & 0 & 0 & 0 & -1 \\ 0 & 0 & 0 & 0 & 0 \\ \frac{A_r}{T_d} & 0 & 0 & 0 & 0 \end{bmatrix}$$

$$\begin{bmatrix} -\frac{i_{sd0}K_{id}}{\eta C_f v_{f0}} & -\frac{i_{sq0}K_{iq}}{\eta C_f v_{f0}} & -\frac{i_{sq0}N\omega_{m0}L_{sd}}{\eta C_f v_{f0}} & \frac{i_{sd0}N\omega_{m0}L_{sq}}{\eta C_f v_{f0}} \\ 0 & 0 & 0 & 0 \\ 0 & 0 & 0 & 0 \\ \frac{K_{id}}{L_{sd}} & 0 & 0 & -\frac{N\omega_{m0}L_{sq}}{L_{sd}} \\ 0 & \frac{K_{iq}}{L_{sq}} & \frac{N\omega_{m0}L_{sd}}{L_{sq}} & 0 \\ 0 & 0 & 0 & 0 \\ 0 & 0 & 0 & 0 \\ 0 & 0 & -\frac{1}{T_d} & 0 \\ 0 & 0 & 0 & -\frac{1}{T_d} \end{bmatrix} \begin{bmatrix}\Delta v_f\\ \Delta v_{f\,\mathrm{det}}\\ \Delta i_f\\ \Delta i_{sd}\\ \Delta i_{sq}\\ \Delta x_{sd}\\ \Delta x_{sq}\\ \Delta i^*_{sd1}\\ \Delta i^*_{sq1}\end{bmatrix} \tag{4.83}$$

Mode 2:

$$\frac{d}{dt}\begin{bmatrix}\Delta v_f\\ \Delta v_{f\,\mathrm{det}}\\ \Delta i_f\\ \Delta i_{sd}\\ \Delta i_{sq}\\ \Delta x_{sd}\\ \Delta x_{sq}\\ \Delta i^*_{sd1}\\ \Delta i^*_{sq1}\end{bmatrix} = \begin{bmatrix} -\frac{A_r i_{sq0} K_{pq}}{\eta C_f v_{f0}} & \frac{i_{in0}}{C_f v_{f0}} & \frac{1}{C_f} & \frac{-v_{sd0}+i_{sd0}K_{pd}}{\eta C_f v_{f0}} & \frac{-v_{sq0}+i_{sq0}K_{pq}}{\eta C_f v_{f0}} \\ \frac{1}{T_{DC}} & -\frac{1}{T_{DC}} & 0 & 0 & 0 \\ -\frac{1}{L_f} & 0 & -\frac{R_b+R_f}{L_f} & 0 & 0 \\ \frac{v_{sd0}}{L_{sd}v_{f0}} & -\frac{v_{sd0}}{L_{sd}v_{f0}} & 0 & -\frac{R_s+K_{pd}}{L_{sd}} & \frac{N\omega_{m0}L_{sq}}{L_{sd}} \\ \frac{v_{sq0}}{L_{sq}v_{f0}}+\frac{A_r K_{pq}}{L_{sq}} & -\frac{v_{sq0}}{L_{sq}v_{f0}} & 0 & -\frac{N\omega_{m0}L_{sd}}{L_{sq}} & -\frac{R_s+K_{pq}}{L_{sq}} \\ 0 & 0 & 0 & -1 & 0 \\ A_r & 0 & 0 & 0 & -1 \\ 0 & 0 & 0 & 0 & 0 \\ \frac{A_r}{T_d} & 0 & 0 & 0 & 0 \end{bmatrix}$$

$$\begin{bmatrix} -\frac{i_{sd0}K_{id}}{\eta C_f v_{f0}} & -\frac{i_{sq0}K_{iq}}{\eta C_f v_{f0}} & -\frac{i_{sq0}N\omega_{m0}L_{sd}}{\eta C_f v_{f0}} & \frac{i_{sd0}N\omega_{m0}L_{sq}}{\eta C_f v_{f0}} \\ 0 & 0 & 0 & 0 \\ 0 & 0 & 0 & 0 \\ \frac{K_{id}}{L_{sd}} & 0 & 0 & -\frac{N\omega_{m0}L_{sq}}{L_{sd}} \\ 0 & \frac{K_{iq}}{L_{sq}} & \frac{N\omega_{m0}L_{sd}}{L_{sq}} & 0 \\ 0 & 0 & 0 & 0 \\ 0 & 0 & 0 & 0 \\ 0 & 0 & -\frac{1}{T_d} & 0 \\ 0 & 0 & 0 & -\frac{1}{T_d} \end{bmatrix} \begin{bmatrix}\Delta v_f\\ \Delta v_{f\,\mathrm{det}}\\ \Delta i_f\\ \Delta i_{sd}\\ \Delta i_{sq}\\ \Delta x_{sd}\\ \Delta x_{sq}\\ \Delta i^*_{sd1}\\ \Delta i^*_{sq1}\end{bmatrix} \tag{4.84}$$

Mode 3:

$$\frac{d}{dt}\begin{bmatrix}\Delta v_f\\ \Delta v_{f\,\mathrm{det}}\\ \Delta i_f\\ \Delta i_{sd}\\ \Delta i_{sq}\\ \Delta x_{sd}\\ \Delta x_{sq}\\ \Delta i^*_{sd1}\\ \Delta i^*_{sq1}\end{bmatrix} = \begin{bmatrix} 0 & \frac{i_{in0}}{C_f v_{f0}} & \frac{1}{C_f} & \frac{-v_{sd0}+i_{sd0}K_{pd}}{\eta C_f v_{f0}} & \frac{-v_{sq0}+i_{sq0}K_{pq}}{\eta C_f v_{f0}}\\ \frac{1}{T_{DC}} & -\frac{1}{T_{DC}} & 0 & 0 & 0\\ -\frac{1}{L_f} & 0 & -\frac{R_f}{L_f} & 0 & 0\\ \frac{v_{sd0}}{L_{sd}v_{f0}} & -\frac{v_{sd0}}{L_{sd}v_{f0}} & 0 & -\frac{R_s+K_{pd}}{L_{sd}} & \frac{N\omega_{m0}L_{sq}}{L_{sd}}\\ \frac{v_{sq0}}{L_{sq}v_{f0}} & -\frac{v_{sq0}}{L_{sq}v_{f0}} & 0 & -\frac{N\omega_{m0}L_{sd}}{L_{sq}} & -\frac{R_s+K_{pq}}{L_{sq}}\\ 0 & 0 & 0 & -1 & 0\\ 0 & 0 & 0 & 0 & -1\\ 0 & 0 & 0 & 0 & 0\\ 0 & 0 & 0 & 0 & 0 \end{bmatrix}$$

$$\begin{bmatrix} -\frac{i_{sd0}K_{id}}{\eta C_f v_{f0}} & -\frac{i_{sq0}K_{iq}}{\eta C_f v_{f0}} & -\frac{i_{sq0}N\omega_{m0}L_{sd}}{\eta C_f v_{f0}} & \frac{i_{sd0}N\omega_{m0}L_{sq}}{\eta C_f v_{f0}}\\ 0 & 0 & 0 & 0\\ 0 & 0 & 0 & 0\\ \frac{K_{id}}{L_{sd}} & 0 & 0 & -\frac{N\omega_{m0}L_{sq}}{L_{sd}}\\ 0 & \frac{K_{iq}}{L_{sq}} & \frac{N\omega_{m0}L_{sd}}{L_{sq}} & 0\\ 0 & 0 & 0 & 0\\ 0 & 0 & 0 & 0\\ 0 & 0 & -\frac{1}{T_d} & 0\\ 0 & 0 & 0 & -\frac{1}{T_d} \end{bmatrix}\begin{bmatrix}\Delta v_f\\ \Delta v_{f\,\mathrm{det}}\\ \Delta i_f\\ \Delta i_{sd}\\ \Delta i_{sq}\\ \Delta x_{sd}\\ \Delta x_{sq}\\ \Delta i^*_{sd1}\\ \Delta i^*_{sq1}\end{bmatrix} \tag{4.85}$$

Mode 4:

$$\frac{d}{dt}\begin{bmatrix}\Delta v_f\\ \Delta v_{f\,\mathrm{det}}\\ \Delta i_f\\ \Delta i_{sd}\\ \Delta i_{sq}\\ \Delta x_{sd}\\ \Delta x_{sq}\\ \Delta i^*_{sd1}\\ \Delta i^*_{sq1}\end{bmatrix} = \begin{bmatrix} 0 & \frac{i_{in0}}{C_f v_{f0}} & \frac{1}{C_f} & \frac{-v_{sd0}+i_{sd0}K_{pd}}{\eta C_f v_{f0}} & \frac{-v_{sq0}+i_{sq0}K_{pq}}{\eta C_f v_{f0}}\\ \frac{1}{T_{DC}} & -\frac{1}{T_{DC}} & 0 & 0 & 0\\ -\frac{1}{L_f} & 0 & -\frac{R_b+R_f}{L_f} & 0 & 0\\ \frac{v_{sd0}}{L_{sd}v_{f0}} & -\frac{v_{sd0}}{L_{sd}v_{f0}} & 0 & -\frac{R_s+K_{pd}}{L_{sd}} & \frac{N\omega_{m0}L_{sq}}{L_{sd}}\\ \frac{v_{sq0}}{L_{sq}v_{f0}} & -\frac{v_{sq0}}{L_{sq}v_{f0}} & 0 & -\frac{N\omega_{m0}L_{sd}}{L_{sq}} & -\frac{R_s+K_{pq}}{L_{sq}}\\ 0 & 0 & 0 & -1 & 0\\ 0 & 0 & 0 & 0 & -1\\ 0 & 0 & 0 & 0 & 0\\ 0 & 0 & 0 & 0 & 0 \end{bmatrix}$$

$$\begin{bmatrix} -\frac{i_{sd0}K_{id}}{\eta C_f v_{f0}} & -\frac{i_{sq0}K_{iq}}{\eta C_f v_{f0}} & -\frac{i_{sq0}N\omega_{m0}L_{sd}}{\eta C_f v_{f0}} & \frac{i_{sd0}N\omega_{m0}L_{sq}}{\eta C_f v_{f0}}\\ 0 & 0 & 0 & 0\\ 0 & 0 & 0 & 0\\ \frac{K_{id}}{L_{sd}} & 0 & 0 & -\frac{N\omega_{m0}L_{sq}}{L_{sd}}\\ 0 & \frac{K_{iq}}{L_{sq}} & \frac{N\omega_{m0}L_{sd}}{L_{sq}} & 0\\ 0 & 0 & 0 & 0\\ 0 & 0 & 0 & 0\\ 0 & 0 & -\frac{1}{T_d} & 0\\ 0 & 0 & 0 & -\frac{1}{T_d} \end{bmatrix}\begin{bmatrix}\Delta v_f\\ \Delta v_{f\,\mathrm{det}}\\ \Delta i_f\\ \Delta i_{sd}\\ \Delta i_{sq}\\ \Delta x_{sd}\\ \Delta x_{sq}\\ \Delta i^*_{sd1}\\ \Delta i^*_{sq1}\end{bmatrix} \tag{4.86}$$

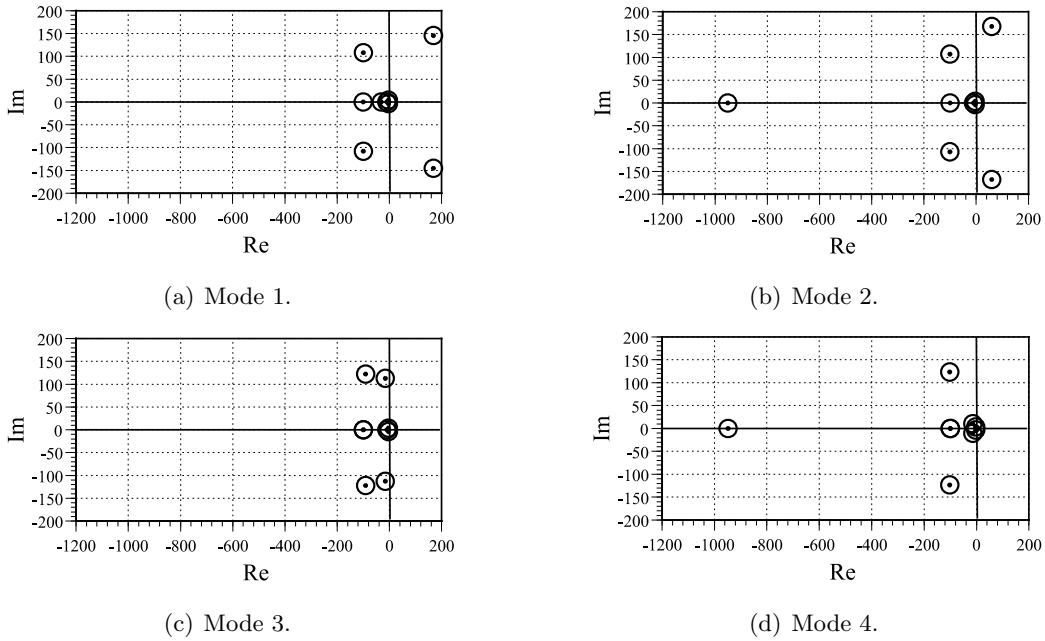

(a) Mode 1.

(b) Mode 2.

(c) Mode 3.

(d) Mode 4.

Figure 4.10: Poles of each operation mode.

Table 4.4: Poles of each operation mode

Region	Narrowing region				Maximum torque region			
Diode state	Diode ON		Diode OFF		Diode ON		Diode OFF	
Mode	Mode 1		Mode 2		Mode 3		Mode 4	
	Re	Im	Re	Im	Re	Im	Re	Im
Poles	168.575	145.477	-951.100	0	-91.368	122.249	-947.816	0
	168.575	-145.477	59.393	167.888	-91.368	-122.249	-102.357	123.384
	-99.744	108.032	59.393	-167.888	-15.687	112.738	-102.357	-123.384
	-99.744	-108.032	-100.554	107.032	-15.687	-112.738	-14.346	10.460
	-31.040	0	-100.554	-107.032	-9.927	0	-14.346	-10.460
	-9.886	0	-10.390	0	-3.815	3.835	-3.483	3.246
	-3.813	3.830	-3.775	3.781	-3.815	-3.835	-3.483	-3.246
	-3.813	-3.830	-3.775	-3.781	-100	0	-100	0
	-100	0	-100	0	-100	0	-100	0

xxx ...the positive real pole (unstable pole)

4.4.4 Stability analysis of each operation mode

From the steady state solutions of the state equations, the equilibrium points of each operation mode are found out as presented in subsection 4.4.2. If paying attention to the filter capacitor voltage v_{f0} and the current of the overhead wiring i_{f0} of these steady state solutions which relates to the operation mode, it is noticed that the steady state solution reaches a value outside

the area corresponding to each its operation mode except of Mode 2 as shown in Fig. 4.9. Therefore, according to this matter, to achieve a stable condition when the light-load regenerative breaking control is active the operating point should be in Mode 2 (narrowing region and diode is turned off). Furthermore, from the pole of the linearized state equation of each operation mode as shown in Fig. 4.10, it is noticed that Modes 1 and 2 are unstable by presence in a positive real part of poles, and Modes 3 and 4 are stable. Table 4.5 shows the relation between the stability and the existence equilibrium point (steady state solution) of each operating mode. It is understood that no one of four operation modes can meet the requirement to settle the operating point in the area corresponding to the operation mode and to guarantee the stability. As a result, the operating point of the system becomes not to settle to any operation mode, but to move between each mode. Therefore, the oscillation phenomenon of the electricity system, occurs in the PMSM drive system when the light-load regenerative braking control is applied, can be explained.

Table 4.5: Equilibrium point position and stability at each "Operation Mode"

Operation mode	Equilibrium point position	. Stability
Mode 1	OUT	Unstable
Mode 2	IN	Unstable
Mode 3	OUT	Stable
Mode 4	OUT	Stable

xxx ...undesired condition

4.5 Proposed anti-oscillation Strategy

From the examination in the preceding section, the dynamical stability is achieved only in the maximum torque region (Modes 3 and 4). However, a corresponding position of steady state solution does not exist in the operation mode of the maximum torque region. Then, we suggest controlling the oscillation by changing the control pattern so that a corresponding position of the steady state solution may exist in the maximum torque region. Furthermore, the change in the regenerative electric power due to the decrease at the rotor speed is considered in the proposed anti-oscillation control, even though the rotor speed has been being examined constantly in the oscillation phenomenon analysis in the preceding section. In the proposed strategy, the

regenerative power is maintained to be constant when the insufficient load condition does not occur anymore to provide the regenerative power as much as possible. The proposed anti-oscillation control algorithm is described in two steps as follows:

- **Step 1:** Anti-oscillation control strategy
- **Step 2:** Constant regenerative power maintenance control.

4.5.1 Anti-oscillation strategy

The purpose of the anti-oscillation control strategy is to put the operating point to a stable region when it moves to an unstable region. First, when the light-load regenerative control is active, and then the operating point moves to the narrowing region, the control pattern is changed as shown in Fig. 4.11 (values of I_r and $V_{f\,\mathrm{lim}}$ are changed), so that the maximum torque region is expanded. A ratio of α $(0 < \alpha < 1)$ is multiplied to the q-axis current reference initial value to realize the change of I_r. As a consequence, the q-axis current reference value is narrowed and the operating point is returned to the maximum torque area. In other words, the operating point in the narrowing region is avoided and the unstable condition is also avoided. This operation may be repeated and the steady state solution can be kept exist in the maximum torque area. As a result, the operating point is always settled to Mode 3 or Mode 4, and the oscillation is controlled.

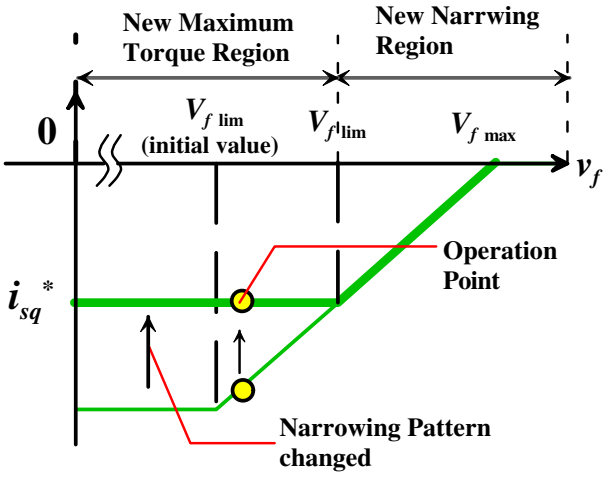

Figure 4.11: Anti-oscillation strategy.

4.5.2 Constant regenerative power maintenance control

After controlling the oscillation, when the last control pattern remains to be unchanged in step 1 since the light-load regenerative condition doesn't occur anymore, the regenerative electric power is decreasing according to the decrease at the rotor speed. This regenerative power's decreasing indicates the filter capacitor voltage decreasing. The actual regenerative electric power becomes smaller than the maximum dissipation that could be anticipated by the load of R_b. Therefore, to provide a regenerative power as much as possible the q-axis current reference value in the maximum torque area is changed while the regenerative power is maintained to be constant ($P_{constant} = i_{sq}^{*} v_f$) as illustrated in Fig. 4.12. Furthermore, the anti-oscillation control in step 1 will be active again when the operating point deviates from the maximum torque region. Then, it is possible to regenerate a large electric power as much as possible and control the oscillation by repeating these two steps.

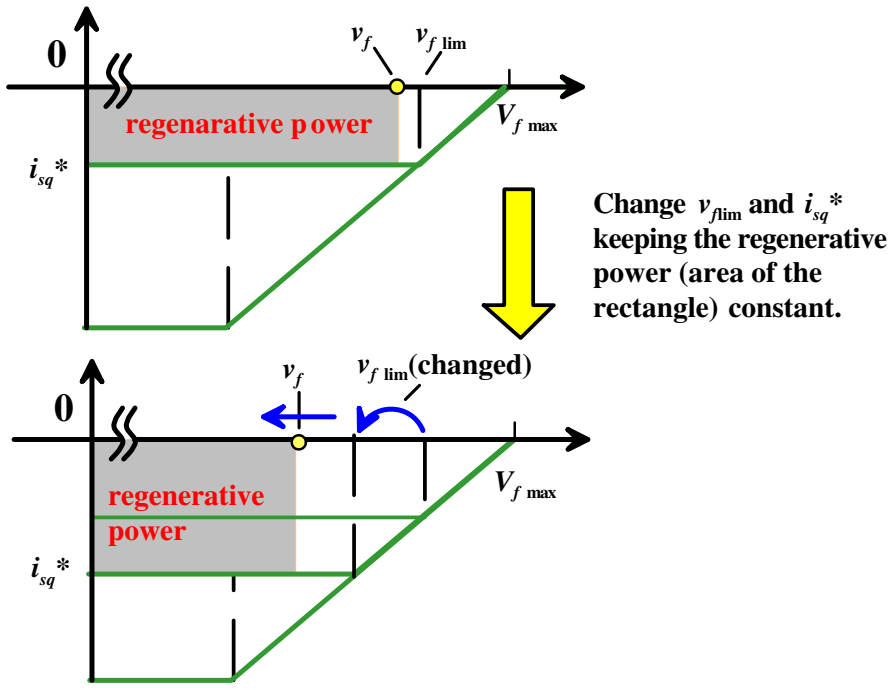

Figure 4.12: Constant regenerative power maintenance control.

4.6 Experimental results

In order to verify the validation of the proposed anti-oscillation strategy, the proposed anti-oscillation strategy is applied to a mini model of the experimental system shown in Fig. 4.13, which imitates the oscillation phenomenon as in the experiment result of a real railway vehicle when the light-load regenerative braking control is adopted. A PMSM with an inertia load imitates the regenerative power of vehicle, and then a load resistance imitates a load power consuming by other vehicles according to the equivalent circuit shown in Fig. 4.4. Parameters of the mini-model experimental system are listed in Table 4.6.

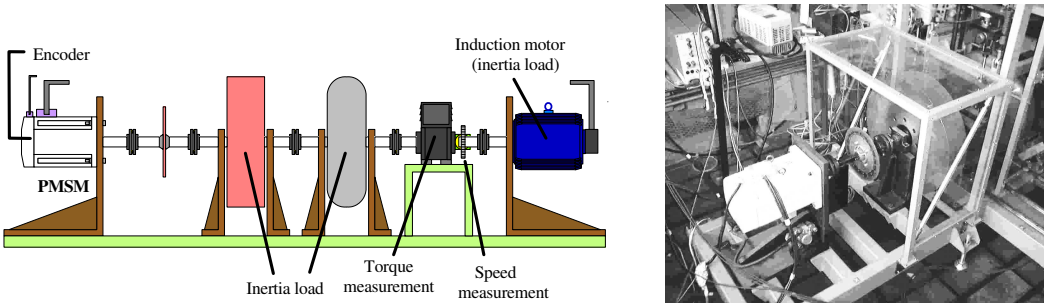

(a) Mechanical system configuration.

(b) Experimental system photograph.

Figure 4.13: Mini model of the experimental system.

Table 4.6: Mini model system parameters

Item	Symbol	Value	Item	Symbol	Value
Stator resistant	R_s	0.1[Ω]	Rotor speed	ω_{m0}	1000[rpm]
d-axis inductance	L_{sd}	1[mH]	Rise time	T_r	3[s]
q-axis inductance	L_{sq}	1[mH]	Maximum regenerative current	I_r	10[A]
Permanent magnet flux	ψ_F	0.153[Wb]	Current control time constant	T_d	1[ms]
Rotor inertia	J	10[kgm^2]	Voltage detection time constant	T_{DC}	100[ms]
Poles number	N	4	Narrowing start voltage	$V_{f\,\mathrm{lim}}$	145[V]
Load torque	T_L	0	Narrowing end voltage	$V_{f\,\mathrm{max}}$	150[V]
Source voltage	V_{dc}	140[V]	Over voltage limit	V_{fOVD}	160[V]
Powering vehicle load	R_b	50[Ω]	Inverter carrier frequency	f_c	5[kHz]
Filter inductance	L_f	100[mH]	Maximum index modulation	M_{max}	0.9
Filter resistance	R_f	1[Ω]	Current control sampling time	dT_c	200[ms]
Filter condenser	C_f	68[μF]	Speed calculation sampling time	dT_s	2[ms]

Fig. 11 shows the experimental results of the light-load regenerative braking control with and without the proposed anti-oscillation control. From the comparison of the system with and

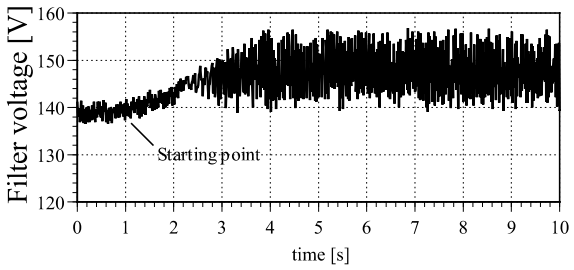

(a) voltage response of system without anti-oscillation control.

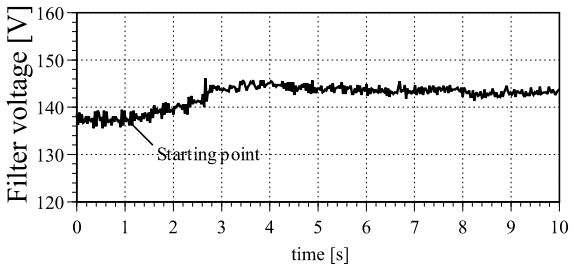

(b) voltage response of system with anti-oscillation control.

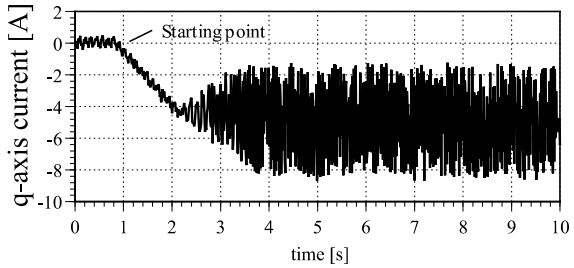

(c) current response of system without anti-oscillation control.

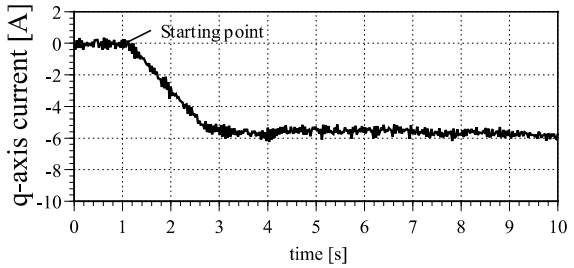

(d) current response of system with anti-oscillation control.

Figure 4.14: Experimental results of the downsized experimental system.

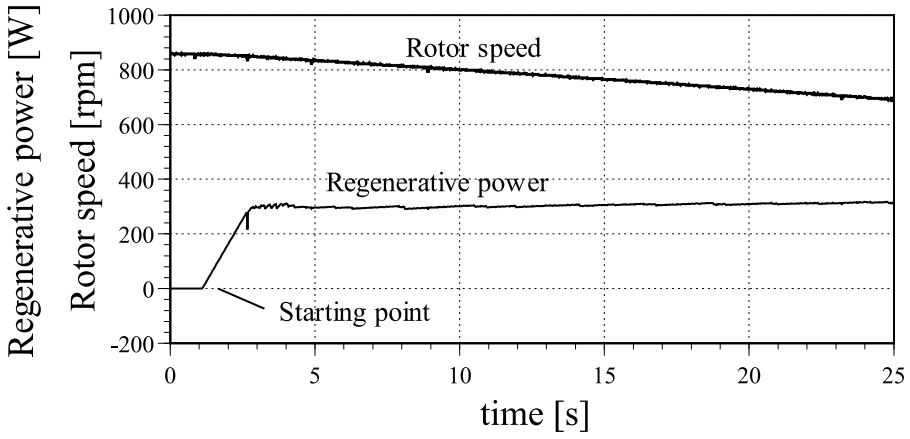

Figure 4.15: Rotor Speed and Regenerative Power response of downsized experimental system with anti-oscillation control.

without the proposed anti-oscillation control, it is understood that the oscillation phenomenon is controlled by the proposed anti-oscillation control method. Fig. 12 shows rotor speed and regenerative power responses of downsized experimental system with suggested anti-oscillation

control. Even though the rotor speed decreases the regenerative electric power is kept constant, and moreover, the maximum dissipation that can be anticipated by R_b (other vehicles) is provided anytime. The effectiveness of the anti-oscillation control proposed above is confirmed.

4.7 Summary

From analysis and experimental results we can summarize the conclusion as follows: It was pointed out that the oscillation of the electric system occurs in the PMSM drive railway vehicle traction system when the light-load regenerative braking control is adopted. To elucidate the oscillation phenomenon, the main circuit that contains a nonlinear system is modeled by the nonlinear time-varying state equations. A treated analytical approach that the state equation of a nonlinear time varying main circuit model is divided into four appropriate operation modes (linear system) using the Taylor series expansion was proposed. And, from the location of the steady state solution (the equilibrium points) of each 'Operating Mode' and the stability analysis results, the existence of the oscillation phenomenon when a light-load regenerative braking control is adopted is clarified. Based on the above-mentioned analytical results the control technique by which the oscillation phenomenon is controlled is proposed and verified according to the mini model. As a result, since the proposed control method is confirmed to be effective and appropriate to control the oscillation when a light-load regenerative braking control is adopted, the analytical result is also proven.

Chapter 5

Storage battery modeling

In this chapter, a novel method to model the transient response of battery in view of the control engineering is proposed. The frequency-response of battery is measured and the concept of transfer function to decide the admittance value of battery is introduced. Finally, the equivalent circuit of battery from the obtained admittance value is estimated. Furthermore, the variation of electrical circuit parameter with the battery residual capacity is investigated.

5.1 Introduction

Recently, a storage battery is used very much for the portable machine from the small system, like the uninterruptible power supply system, to the large system, like the electric vehicle. Even it is used in very large-scale application, the storage battery used for the electric vehicle has a special condition that is rapid charged-discharged repeatedly. Especially, when the electric vehicle is run in the city area that the speed acceleration and deceleration are very often. The storage battery is discharged in the acceleration condition (motoring) and is charged in the deceleration condition (regenerative braking). In the storage battery system that the electrical charge-discharge is done frequently, a more high efficiency drive system should be designed. Therefore, the character of storage battery is modeled and it is very important to grasp the whole character of the system precisely.

Up to this time, the technique that the character of the storage battery is modeled from the viewpoint of the electrical engineering is examined. For example the equivalent circuit of the storage battery is estimated by calculating the circuit parameters from some points of the frequency response. However, by using this method to calculate a circuit parameter from few data, there is a problem that the dispersion of data influences the computation results. On the other hand, the equivalent circuit of the storage battery is estimated using the Cole-Cole plot

that is made from the frequency response of the experiment result. Here, the circuit parameter is decided by treating the data graphically. There is a problem that inductance element of the storage battery isn't being taken into consideration in the equivalent circuit so far. From these reasons, even if the above modeling technique can grasp the characteristic of the storage battery, it can be said that it can't be grasped precisely.

In this chapter, the new modeling technique of the storage battery characteristic from the viewpoint of control engineering is proposed. The general concept of the transfer function is introduced. From the treatment of the frequency response characteristic of the storage battery, which is provided by experiment, the system admittance is decided. Since the graphical treatment is carried out under the sufficient number of data, which the inductance was taken into consideration, this technique has the strong point that the influence of the dispersion of data measurement can be restrained low. Then, based on the admittance obtained from this technique, the equivalent circuit of the storage battery is estimated and the circuit parameter can be calculated. As it was mentioned previously, with the obtained transfer function that the influence of the data dispersion is restrained low, the stable technique for obtaining the electrical circuit parameters are obtained. From the examination of battery charging condition, which is changed from 100%, 80%, ... to 0% charging capacity, the investigation of circuit parameters for each condition are also considered. Furthermore, by using the concept of transfer function, the characteristic of the combinational batteries can be obtained easily that is calculated mathematically from the characteristic of a single battery. This technique is verified by comparing the frequency response of this calculated model (the combinational batteries characteristic obtained mathematically from the single battery characteristic) with the frequency response of the actual combinational batteries from experiment. This technique can be applied to the large-scale storage battery power supply system, such as electric vehicle, solar cell generating electricity system, and uninterruptible power supply system.

5.2 The measurement of the storage battery frequency characteristic

To model the character in electric charge-discharge of the storage battery, the frequency response of storage battery admittance is measured by experiment. To add an ideal proper sinusoidal wave to the storage battery, the laboratory power amplifier that is combined with the laboratory function generator is used as a power supply. The configuration of the measurement circuit

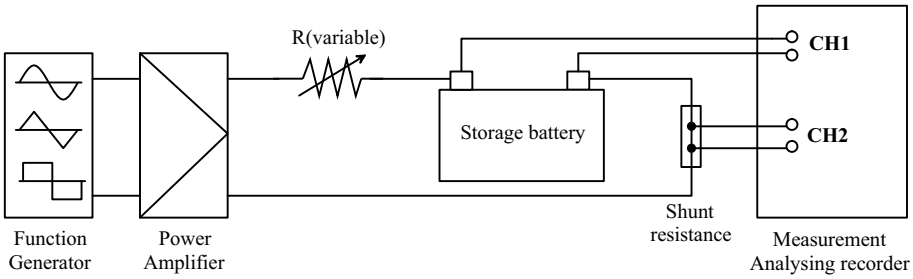

Figure 5.1: Schematic circuit diagram of frequency response measurement equipment.

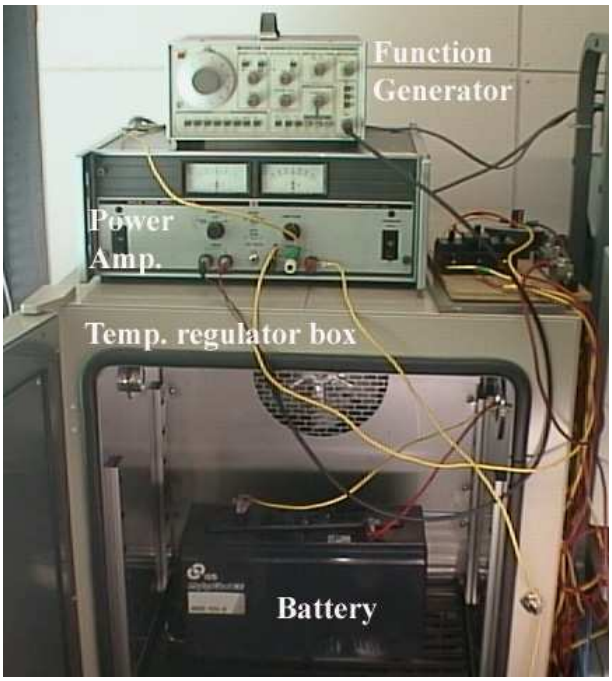

Figure 5.2: Photograph of frequency response measurement equipment.

Table 5.1: Battery specifications

Type	Lead-acid storage battery
Capacity	100 Ah (10 hours average)
Series number	MSE-100Ah
Nominal voltage	6 V

and appearance of the experiment device are shown in Figs. 5.1 and 5.2 respectively. And, the specifications of the storage battery are listed in Table 5.1. The measurement of the storage battery frequency characteristic is carried out as follows: the storage battery is put into an isothermal regulator box where the storage battery itself was kept in 25^o, and its charging capacity is made to change with 100%, 80%, 60%, 40%, 20%, and 0%.

Here, charging capacity is calculated from the product of the electric discharge current and the discharge time starting from a full-charging condition. The full-charging condition is defined from the release terminal voltage (2.23V/ cell) by considering the rated current and voltage charges [29]. First, the frequency response is measured in the full-charging condition, and after it is finished, the discharging electricity with the current of 10 A is started continuously for 2 hours. After it lapses for about 30 minutes, this is considered 80% of the charging capacity condition, and then the frequency response is measured again. The measurement is repeated every time of the charging capacity is decrease for 20%, until the charging capacity becomes 0% (100%, 80%, 60%, 40%, 20%, and 0% charging conditions). In this time, the sinusoidal signal with frequency stage of 10Hz-1000 Hz is put on the main object. The gain and phase of the system are calculated from the wave shape of the electrical voltage and current for each charging capacity condition. The FFT (Fast Fourier Transformation) analytic [30] is being used for reading of the data, since the ripple is seen in the voltage wave shape due to the resolution problem of the analyzing recorder. The experiment was carried out with the electric current of 5 A, which was the rated current value of the power amplifier used this time. The gain plot and the phase plot of the storage battery admittance, which are obtained from these experiment results, are shown in Fig. 5.3.

5.3 The transfer function expression of the storage battery

Here, to obtain the approximated transfer function the storage battery admittance, the whole frequency characteristic of the storage battery from the experiment result is compared with the bode diagram of the various typical reference model. And then, the method to decide each parameter inside the storage battery transfer function is described.

5.3.1 The frequency characteristic of the approximated model

The transfer function and bode diagram of the reference models [31] (phase-lead system, one-order delay system, and phase-lead + one-order delay system) are shown in Table 5.2. Com-

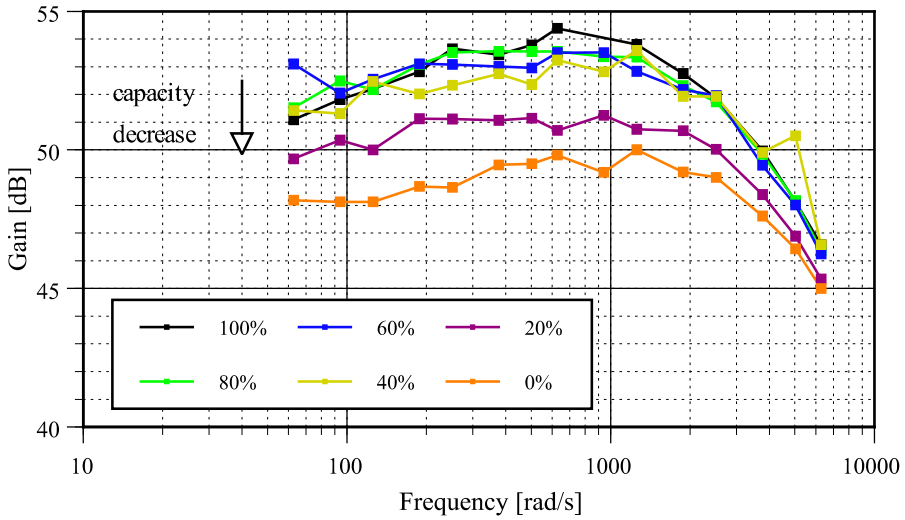

(a) Gain response.

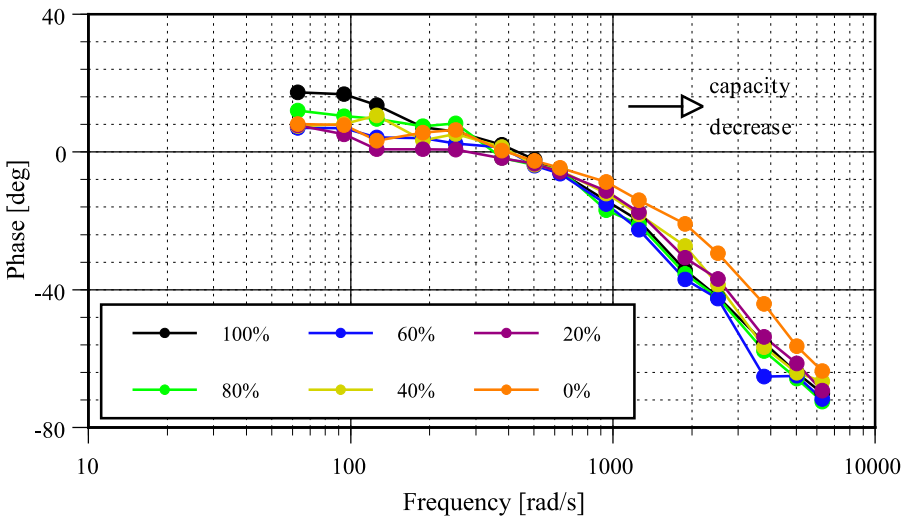

(b) Phase response.

Figure 5.3: Frequency response of lead-acid battery admittance.

paring Table 5.2 with the frequency response from the experiment result shown in Fig. 5.3, the transfer function $\frac{I}{V}(\omega)$ of the storage battery is decided to be approximated by a "phase-lead + one-order delay system". Then the storage battery model is expressed in Eq. (5.1).

$$G(s) = K_0 \frac{1+T_1 s}{1+T_2 s} \frac{1}{1+T_0 s} \qquad T_1 < T_2 < T_0 \tag{5.1}$$

Table 5.2: Frequency responses of transfer function (Bode diagram)

Transfer function	Gain plot	Phase plot
Phase-lead $\frac{1+T_1 s}{1+T_2 s}$ $(T_1 > T_2)$	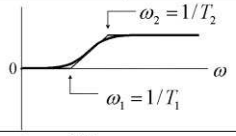	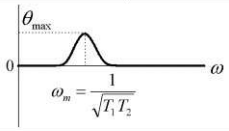
One-order delay $\frac{1}{1+T_0 s}$	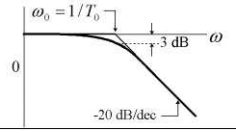	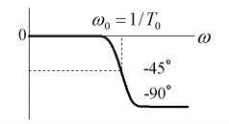
Phase-lead + one-order delay $\frac{1+T_1 s}{1+T_2 s} \frac{1}{1+T_0 s}$ $(T_1 > T_2 > T_0)$	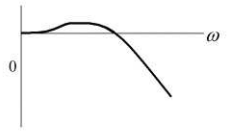	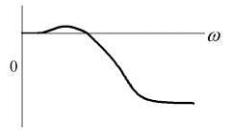

5.3.2 Technique for obtaining the parameter constants

To obtain the parameter constants of T_1, T_2, T_0, and K_0 in Eq. (5.1), the use of least-square method is decided. By using the least- square method under the sufficient number of data, the influence of the dispersion of the experiment data is restrained low, and a valid transfer function can be found. Then it is decided to assume that the system model can be analyzed separately as a phase-lead system only and as a one-order delay system only, so that the model parameters can be calculated as follows:

1. **T_1 and T_2 determination**
   From the experiment result data, the expressions $(T_1 T_2)$ and (T_1/T_2) are calculated in four steps as described in the following passages. This calculation process is illustrated in Fig. 5.4. Then, parameter constants of T_1 and T_2 are decided.

   - **Step 1.** $\theta_{\max}$ and ω_m are determined graphically from the phase curve. (see Fig. 5.5)

- **Step 2.** By mapping $\theta_{\max}$, which is obtained from step 1, into the $\theta_{\max}$ versus (T_1/T_2) correlation in the phase characteristic curve of the phase-lead system, the value of (T_1/T_2) is obtained. (see Fig. 5.6)
- **Step 3.** By substituting ω_m that is obtained from step 1 into expression $\omega_m = \frac{1}{\sqrt{T_1 T_2}}$, the value of $(T_1 T_2)$ is obtained.
- **Step 4.** Since from steps 2 and 3 the value of expressions $(T_1 T_2))$ and $((T_1/T_2)$ are obtained, the parameter constants of T_1 and T_2 can be calculated.

2. K_0 **determination**

   By using the current I and the voltage descent ΔV in discharge condition, the gain parameter constant is calculated by $K_0 = \frac{I}{\Delta V}$.

3. T_0 **determination**

   By obtaining the frequency ω_0 when phase is -45^o in the phase curve, the parameter constant T_0 is calculated by $T_0 = \frac{1}{\omega_0}$.

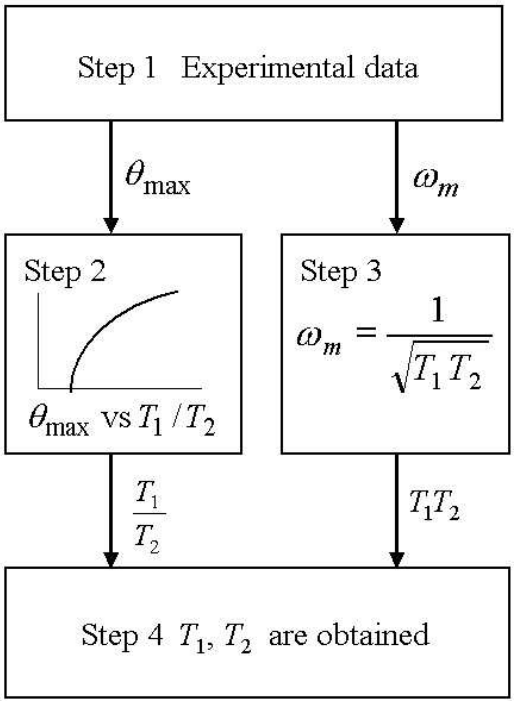

Figure 5.4: Flowchart for estimating T_1 and T_2.

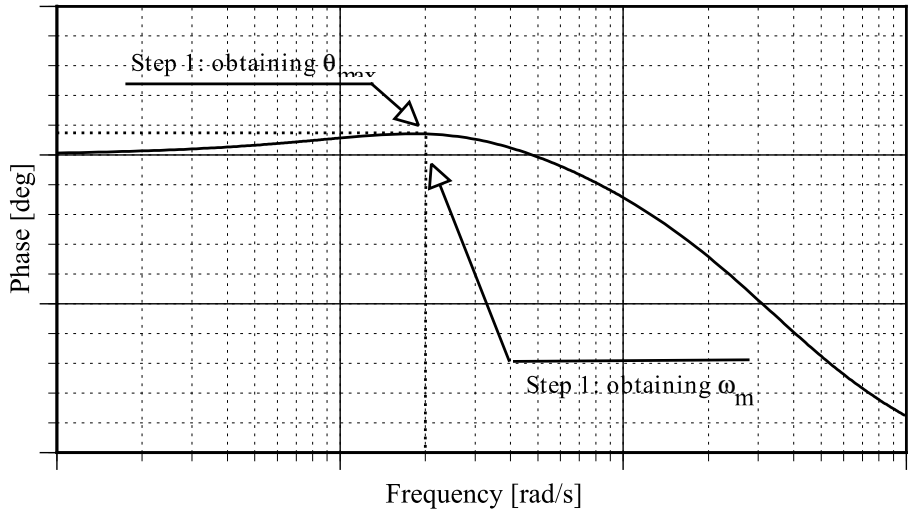

Figure 5.5: Phase curve of the phase-lead system.

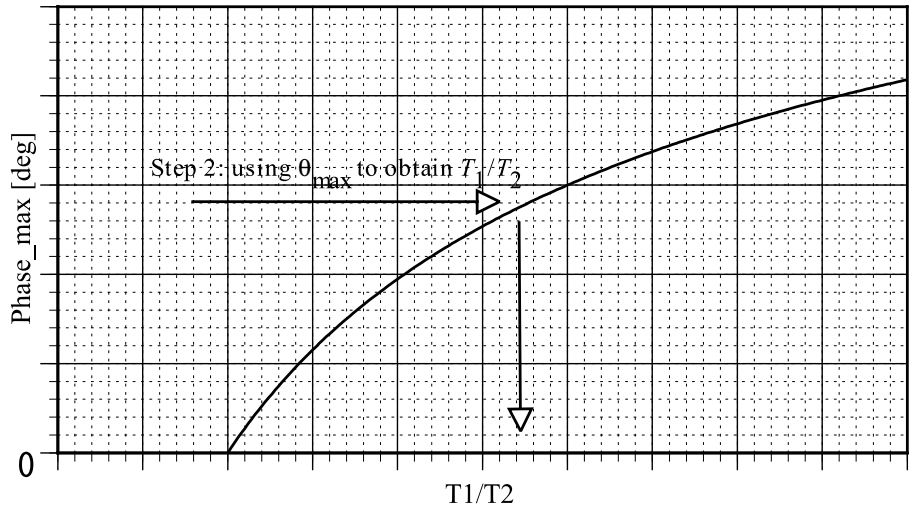

Figure 5.6: $\theta_{\max}$ versus T_1/T_2 .

Description 1: Expression of $\omega_m = \frac{1}{\sqrt{T_1 T_2}}$

The transfer function of the phase-lead system $G1(s)$ is expressed as follows:

$$G_1(s) = \frac{1 + T_1 s}{1 + T_2 s} \tag{5.2}$$

$$G_1(j\omega) = \frac{1 + j\omega T_1}{1 + j\omega T_2} \tag{5.3}$$

$$\theta = \angle G_1(j\omega) = \tan^{-1}(\omega T_1) - \tan^{-1}(\omega T_2) \tag{5.4}$$

Here, since when $\omega = \omega_m$, the value of θ becomes maximum, yields:

$$\frac{d}{d\omega}\angle G_1(j\omega_m) = \frac{T_1}{1+(\omega_m T_1)^2} - \frac{T_2}{1+(\omega_m T_2)^2} = 0 \tag{5.5}$$

Therefore, ω_m becomes:

$$\omega_m = \frac{1}{\sqrt{T_1 T_2}} \tag{5.6}$$

Description 2: The curve characteristic of $\theta_{\max}$ versus T_1/T_2

From the transfer function of the phase-lead system, the $\theta_{\max}$ vs. T_1/T_2 characteristic can be expressed as follows:

$$G_1(s) = \frac{1+T_1 s}{1+T_2 s} \tag{5.7}$$

$$G_1(j\omega) = \frac{1+j\omega T_1}{1+j\omega T_2} \tag{5.8}$$

$$\angle G_1(j\omega) = \tan^{-1}(\omega T_1) - \tan^{-1}(\omega T_2) \tag{5.9}$$

Here since when $\omega_m = \frac{1}{\sqrt{T_1 T_2}}$, $\angle G_1(j\omega) = \theta_{\max}$, $\theta_{\max}$ can be expressed as a function of $\frac{T_1}{T_2}$ in the following equation.

$$\theta_{\max} = \tan^{-1}\left(\sqrt{\frac{T_1}{T_2}}\right) - \tan^{-1}\left(\sqrt{\frac{T_2}{T_1}}\right) \tag{5.10}$$

Table 5.3: T_1, T_2, T_0, and K_0 determined by the least square method

State of charge	T_1	T_2	T_0	K_0
100 %	$1.08\text{x}10^{-2}$	$7.20\text{x}10^{-3}$	$3.98\text{x}10^{-4}$	$3.54\text{x}10^{2}$
80 %	$1.06\text{x}10^{-2}$	$7.52\text{x}10^{-3}$	$3.99\text{x}10^{-4}$	$3.48\text{x}10^{2}$
60 %	$9.42\text{x}10^{-2}$	$7.88\text{x}10^{-3}$	$3.58\text{x}10^{-4}$	$3.46\text{x}10^{2}$
40 %	$7.54\text{x}10^{-3}$	$5.89\text{x}10^{-3}$	$3.03\text{x}10^{-4}$	$3.47\text{x}10^{2}$
20 %	$1.09\text{x}10^{-2}$	$9.16\text{x}10^{-3}$	$2.86\text{x}10^{-4}$	$3.09\text{x}10^{2}$
0 %	$4.52\text{x}10^{-3}$	$3.27\text{x}10^{-3}$	$2.86\text{x}10^{-4}$	$2.43\text{x}10^{2}$

The values of each parameter constants, which are obtained from the experimental results, are listed in Table 5.3. Then, by using the parameter constants listed in Table 5.3, the transfer

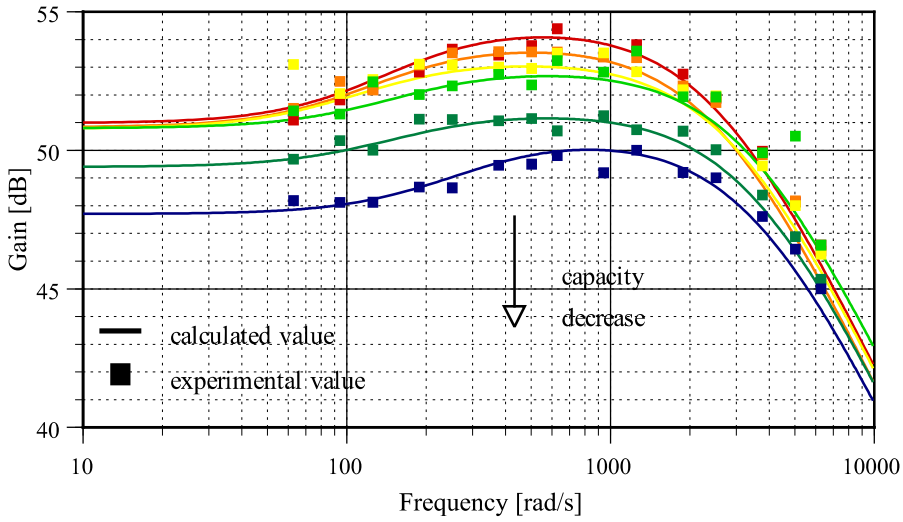

(a) Gain response.

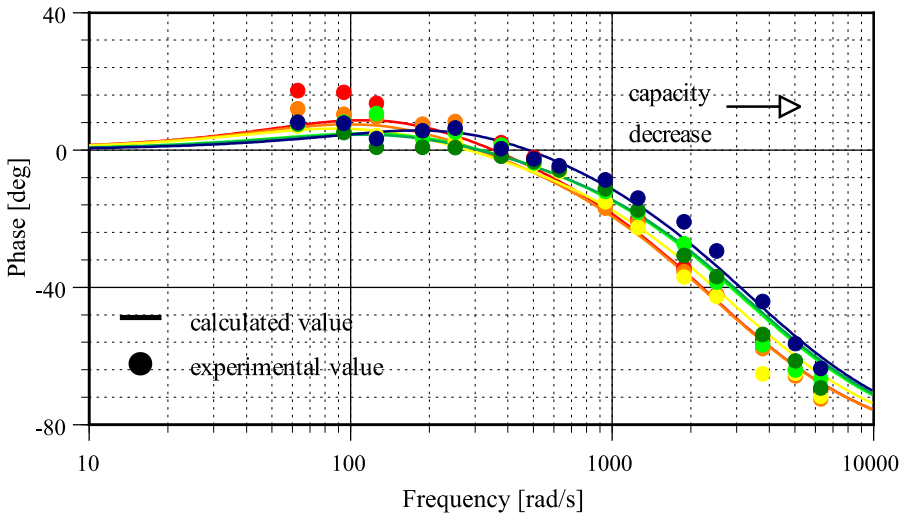

(b) Phase response.

Figure 5.7: Frequency response of lead-acid battery model.

functions of the storage battery model of each charging capacity condition are constructed. The bode diagram of these transfer functions are compared with the experimental values as shown in Fig. 5.7. Since the frequency characteristic of the obtained admittance reflected well the frequency characteristic of the experimental system as shown in Fig. 5.7, the validity of the transfer function obtaining process in this technique can be confirmed.

5.4 The equivalent circuit expression of a storage battery model

By considering the transfer function expression of the storage battery, which is obtained in the previous section, we presume the equivalent electrical circuit that shows a same characteristic. Generally, the equivalent electrical circuit with same characteristic is not unique, here, we adopt the general equivalent electrical circuit from [29] which is shown in Fig. 5.8. This equiv-

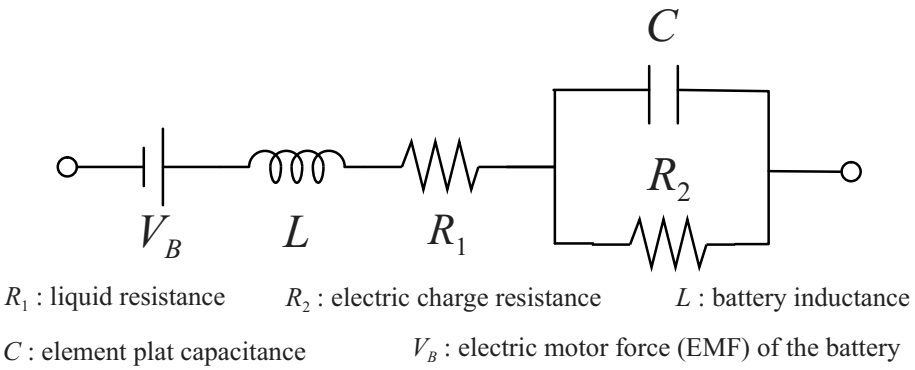

Figure 5.8: Equivalent circuit of battery.

alent circuit is the so-called Randles equivalent circuit with an additional inductance. Usually the equivalent circuit for battery uses only the Randles equivalent circuit. Theoretically, the equivalent circuit of Fig. 5.8 is fitted to the transfer function of Eq. (5.1). Here, inductance of the storage battery can be said as the form of the energizing part of the storage battery. The inductance occurs due to the existence of the wiring straps between cell element and battery terminal/pole, and also between one cell element and the other cell element inside the battery.

5.4.1 The calculation of each electrical parameter

The terminal voltage V of the storage battery is expressed as $V = V_B + I \times R$ (where R is the storage battery internal resistance, and I is the charge-discharge current). The different voltage

value V_B, which is from the electric motor force, is shown. According to the range of battery utility, the proportion relation between the charging capacity and voltage is difference for each state, since the resistance R changes corresponding to the charging capacity in the non-linear shape. The terminal voltage V and the charging capacity disappear by this proportion relation. Therefore, it is important to verify the internal resistance R at the beginning, in such case of grasping each parameter of the storage battery equivalent circuit precisely. The internal admittance of the equivalent circuit, which shows it in the Fig. 5.8, is expressed in the following equation.

$$G(s) = \frac{1 + CR_2 s}{LCR_2 s^2 + (L + CR_1 R_2)\, s + R_1 + R_2} \tag{5.11}$$

Table 5.4: Electric circuit parameter at each state of charge

State of Charge	R_1[mΩ]	R_1[mΩ]	C[F]	L[μH]
100 %	1.92	0.90	12.0	0.75
80 %	2.06	0.81	13.1	0.81
60 %	2.20	0.69	13.6	0.78
40 %	8.28	0.61	12.5	0.68
20 %	2.72	0.67	11.1	0.79
0 %	3.06	1.06	4.25	0.85

By equating the time constants in Eq. (5.1) with the corresponding equivalent circuit parameter in Eq. (5.11), each electrical parameters of the storage battery (R_1, R_2, L, C) can be found. The result that each electrical circuit parameter was calculated from the Table 5.3 is shown in the Table 5.4. And, it is illustrated in Fig. 5.9.

It is possible to calculate the four-electrical circuit parameter of the proposed equivalent circuit, by using two point of frequency response that is shown in Fig. 5.3. However, since the dispersion of the data measurement of the lead storage battery for a certain degree couldn't be avoided, it is not a suitable technique to obtain the precision results. Different to this classical technique, in the proposed technique, the transfer function of battery model is obtained under the sufficient number of data and it cope with an equivalent circuit based on the graphical treatment, so that the influence of the dispersion is restrained low. As a result, the stable technique and precision electrical circuit parameter of the storage battery model can be found.

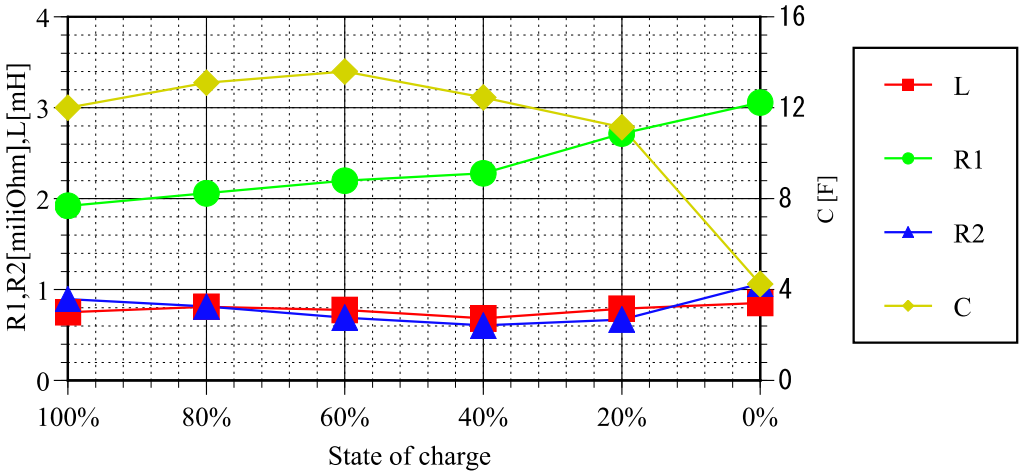

Figure 5.9: Variations of electrical circuit parameters in discharging.

5.4.2 A consideration about the change in the equivalent circuit parameter caused by the electric discharge

Here, the physics phenomenon, which happens inside the storage battery, due to the change in the equivalent circuit parameter caused by the electric discharge is examined. When the electric discharge process occurs the chemical formation of the cell material is changed that the electrolytic liquid decreases. This causes the electrodes of cell inert and then the resistances R_1 and R_2 increase. This can be confirmed by the result of the Fig. 5.9. The inductance L hardly changes when the charging capacity of battery changes. It is understood since L is

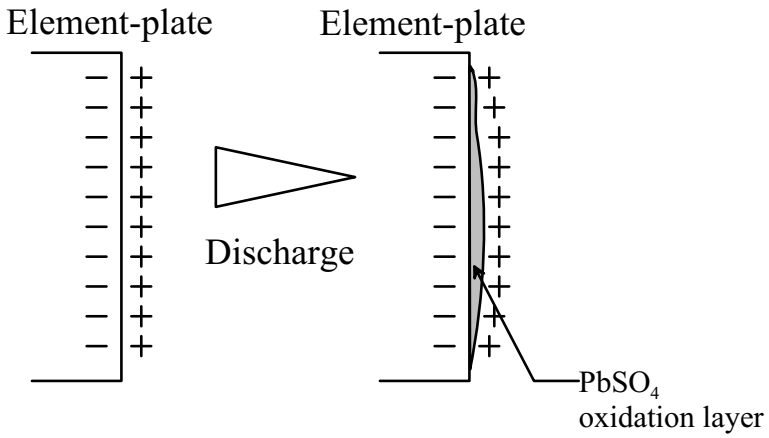

Figure 5.10: Chemical change at plate in discharging.

constructed based on the structure of the main circuit of the battery (straps wiring between cells and terminal pole). And, the structure doesn't vary according to the electric discharge. The capacitance C occurs due to the two-plate electrode place side by side in the electrolyte solution. When the electric discharge process occurs the oxidant of $PbSO_4$ occurs in the electrolyte solution. This oxidant may be formed also in the electrode plate, which causes the effective area of the electrode plate becomes narrow as illustrated in Fig. 5.10. As a result, the electric discharge causes the capacitance C of battery decreases.

5.5 Characteristic of the combinational batteries

Since up to this time, we have examined the storage battery characteristic as a single battery, to grasp the characteristic of large power supply system such as in electric vehicle, the characteristic of the combinational batteries should be examined as well. In this section, the frequency response characteristic when a storage battery is connected to a series and parallel arrangement is measured, and a comparison with the single storage battery is presented. Since the difference deterioration condition of each battery influences the whole characteristic of the combinational batteries greatly, the same new storage batteries were purchased for the investigation of the combinational batteries experimentally.

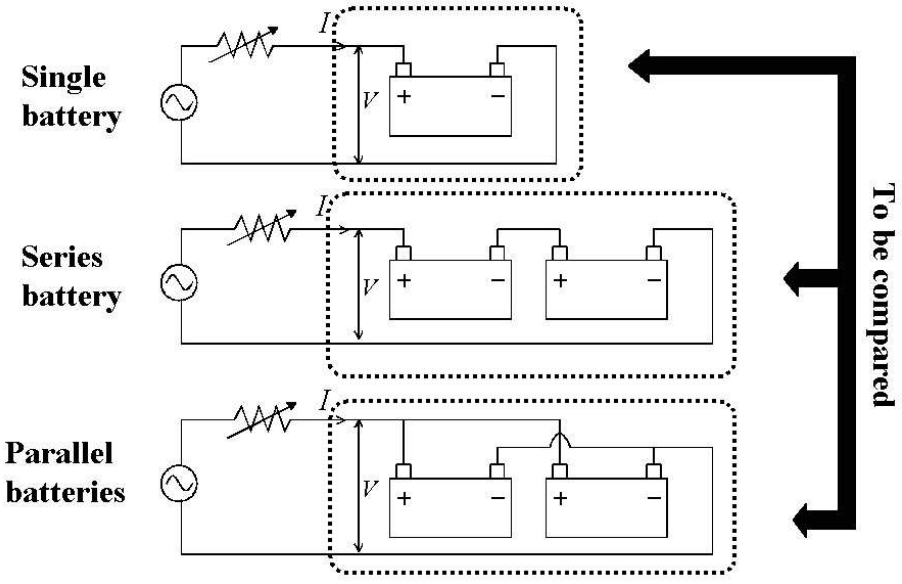

Figure 5.11: Experiment configuration.

5.5.1 Experiment configuration

As shown in Fig. 5.11, an alternating voltage is applied to the following storage battery configurations: a single battery, series batteries, and parallel batteries configurations, and then the electrical frequency response of each configuration is measured. From the frequency response characteristic of combinational batteries obtained from experimental results it was verified that the characteristic is changed from the characteristic of a single battery. Here, the experiment was carried out under the condition that the charging condition of each storage battery is full-charged of 20Ah.

5.5.2 Experiment result and consideration

The appearance of the experimental system for measuring the frequency response characteristic of the combinational batteries is shown in the Figs. 5.12(a) and 5.12(b). The frequency response character of series and parallel combinational batteries obtained from experimental

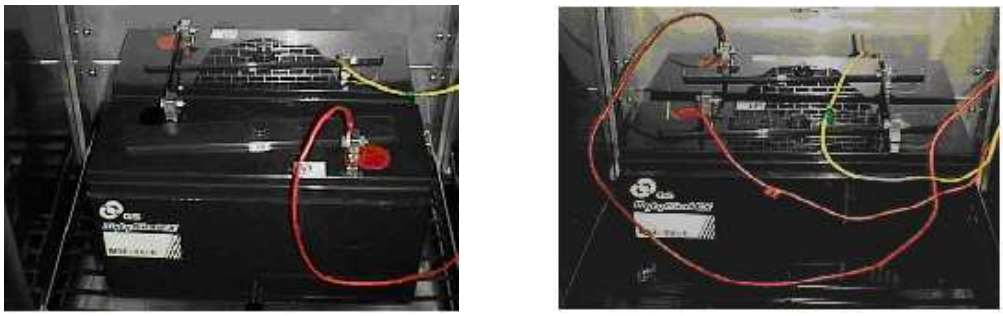

(a) Series connected batteries. (b) Parallel connected batteries.

Figure 5.12: Photograph of series and parallel connected batteries.

results are shown in Figs. 5.13 and 5.14 respectively. In Fig. 5.13, the frequency characteristic of the series combinational batteries obtained from experimental result is compared with the frequency characteristic of the series combinational batteries calculated from the characteristic of the single battery. In Fig. 5.14, the frequency characteristic of the parallel combinational batteries obtained from experimental results is compared with the frequency characteristic of the parallel combinational batteries calculated from the characteristic of the single battery. From these results, it is noticed that the frequency characteristic of the series-parallel combinational batteries obtained from the experimental results fit with the ones calculated from the single battery well. In other words, it can be said that the transfer function of the combinational

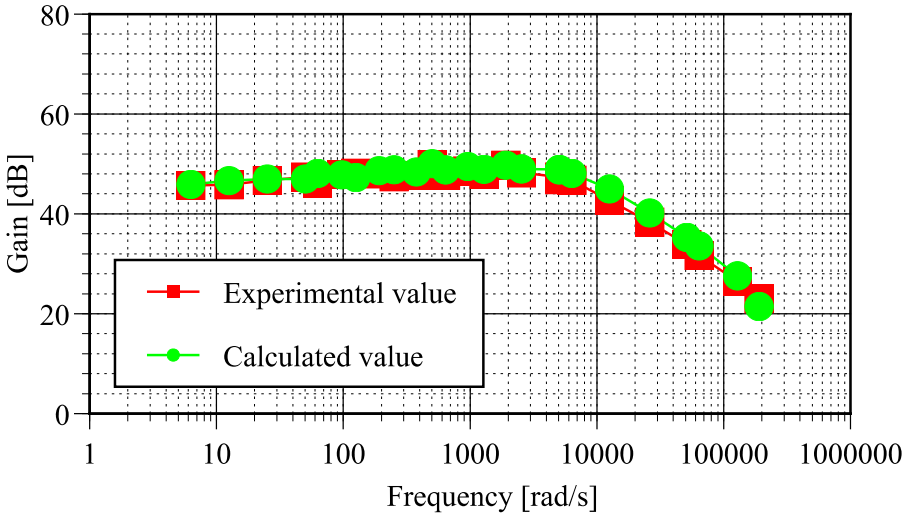

(a) Gain response.

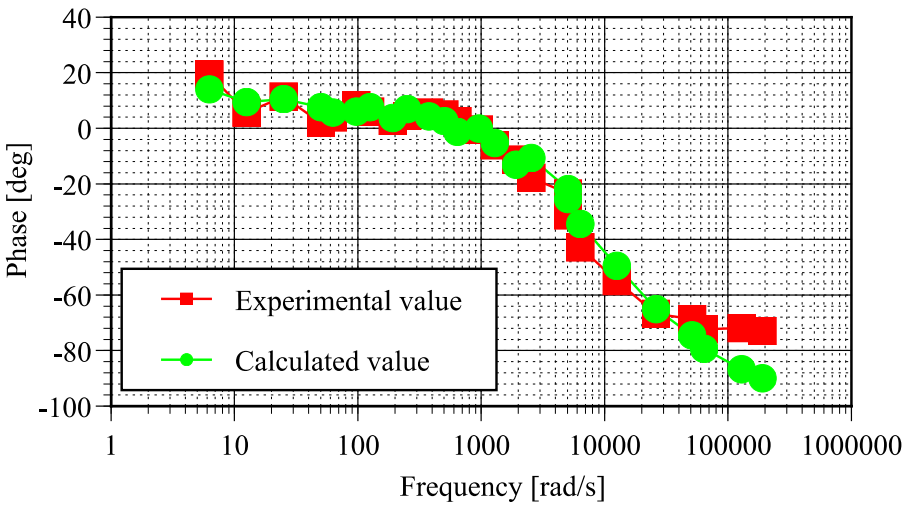

(b) Phase response.

Figure 5.13: Frequency response of series connected batteries.

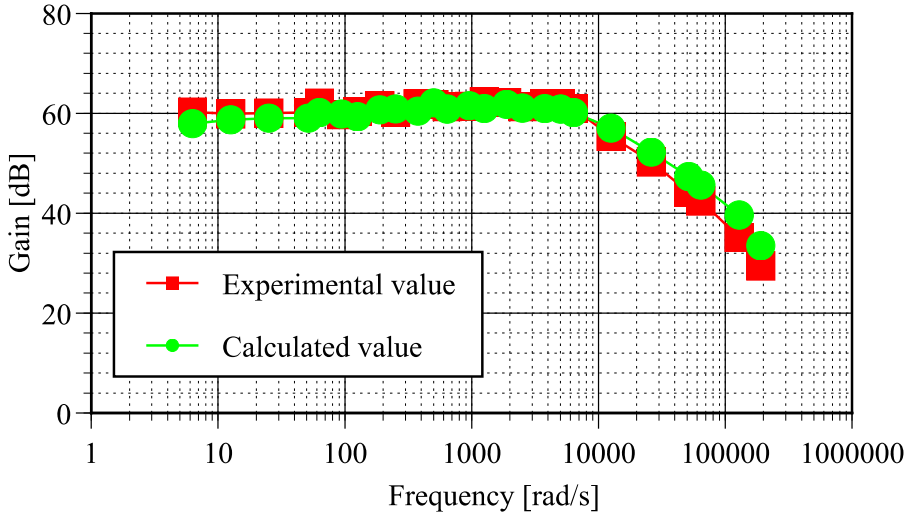

(a) Gain response.

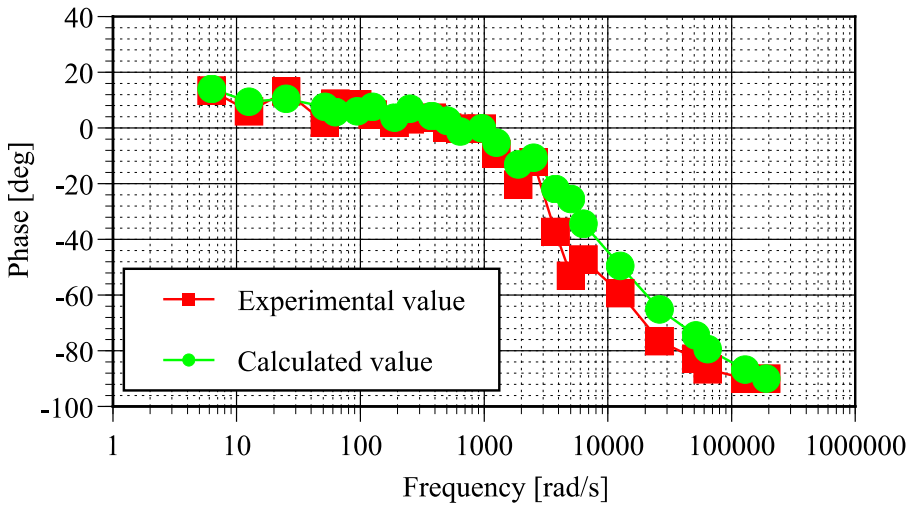

(b) Phase response.

Figure 5.14: Frequency response of parallel connected batteries.

batteries expression can be obtained easily by calculating mathematically from the transfer function of the single battery. From these results, it is confirmed that the proposed storage battery modeling technique can be applied to grasping the characteristic of the large-scale storage battery system easily.

5.6 Summary

In such case of the use of the storage battery power supply system in the electric vehicle, which the electrical charge-discharge process occurs frequently, to design a more high efficiency drive system, the suitable model of the storage battery is necessary. Therefore, it is very important to grasp the whole characteristic of the system precisely. In this chapter, based on the general concept of the transfer function, the new modeling technique of the storage battery that using the frequency response characteristic was proposed. Concretely, a storage battery is considered to consist of starting electrical power and internal admittance. From the frequency character of the experiment result, the admittance was decided to be expressed by the "one-order delay + phase-lead" transfer function. The approximated time constant parameter of the storage battery admittance was calculated using least square method from the whole frequency response obtained from the experiment results.

Then, based on the admittance, which was obtained from this technique, the equivalent circuit that has the same frequency characteristic was presumed, and the electrical circuit parameter was calculated. Since the transfer function is obtained under the sufficient number of data, based on the graphical treatment, the influence of the dispersion of the data can be restrained low. As a result, the stable technique for obtaining the electrical circuit parameters can be provided. Furthermore, to consider the change in the electrical circuit parameter caused by the electric discharge, the approximated electrical circuit parameters under each charging capacity of the storage battery (100%, 80%, ..., 0%) are calculated. It confirmed that the resistance element and capacity element expressed in the equivalent circuit are influenced by the change in the charging capacity, but the inductance element isn't influenced very much.

Finally, the characteristic of the combinational batteries was examined. By using the proposed technique with the general concept of the transfer function, it is possible to calculate easily the characteristic of the combinational batteries. The electrical circuit parameter of the combinational batteries, which are connected in series or parallel configurations, is easy to be calculated mathematically from the character of the single battery. From now on, the effective-

ness of the proposed model, which can be applied to the large power supply system such as an electric vehicle, was confirmed.

The subject for future works:

- Verifying the proposed modeling technique by applying a step response and various transient responses.
- Developing the proposal modeling technique for the storage battery with the combinational cases of different charging capacity and deterioration condition
- Investigating and generalizing the model of the storage battery against the deterioration and the change in the temperature condition

Chapter 6

Conclusions and Recommendations

This thesis studied the energy saving in electrical drive system for electric vehicle application with a focus on the alternating-current (AC) motor that has advantage of less maintenance than the direct-current (DC) motor. Some problems occur in attempting the energy saving in electrical drive system are pointed out. From the results of this works, we can summary the conclusions and some recommendations as follows:

Chapter 2

- In order to improve the output power in the high-speed motor, so that a higher kinetic energy can be recovered by the regenerative control, a novel and simple field-weakening scheme has been proposed.

- Disturbing the flux-producing current reference with the torque-producing current reference while the stator voltage is limited or saturated, higher voltage availability can be provided, since the dc-bus voltage utilization is maximized (10.27% voltage boost when $K_{dist} = 1$ and 36.47% voltage boost when $K_{dist} = 2$). To prevent the noise effect, especially for a high-power motor application, the q-axis current reference i_{sq}^{*} is used as disturbance instead of the q-axis current i_{sq} and a new control for field-weakening region II has been proposed.

- The voltage saturation condition only occurs when a higher or maximum torque is required. The maximum torque is produced by increasing the flux-producing current as much as possible.

- Since the PWM mode changing is not necessary, the control system construction is simple that effects on cost reduction.

- From the performance analysis results, the proposed field-weakening scheme was confirmed to guarantee its stability and the control gain selection was decided that is listed in Table 2.5.

  The implementation of another method in maximizing the dc-bus utility for improving the torque capability in the field-weakening operation is still interesting to be investigated. Furthermore, its implementation with the speed sensorless system is still open to be studied.

Chapter 3

- A modification of the full-order observer was introduced. The two equations in the state observer equation for flux estimating are removed, since the flux value is provided by the flux model that uses the rotor flux reference frame. And since the observer uses the calculated flux, the lack of speed estimation due to the coupling effect was overcome.

- The preliminary investigation of the motor restarting capability under the speed sensorless motor drive system using the modified speed adaptive observer has been carried out.

- In order to operate the motor restarting after coasting under the speed sensorless motor successfully, which is the essential technology for energy saving in electrical drive system, the following conditions should be considered.

  1. Set the initial value of estimated speed greater than the initial value of actual speed (set to be equal to the maximum operating speed).
  2. The speed adaptive gains should not too large to prevent the lost adaptive capability.

- The convergence time becomes slower due to the small speed adaptive gains and the high initial value of estimated speed. To overcome this problem, a minimizing convergence time strategy of speed estimation has been proposed. This strategy uses the gain scheduling method based on the gradient slope of the estimated speed.

  To improve the performance of the motor restarting capability under the speed sensorless drive system, the stability analysis should be carried out for the next works. Based on the analysis results, a strategy for minimizing the speed, flux, and torque estimations errors should be studied.

Chapter 4

- It is pointed out that the oscillation of the electric system occurs in the PMSM drive railway vehicle traction system when the light-load regenerative braking control is adopted.
- To elucidate the oscillation phenomenon, the main circuit that contains a nonlinear system is modelled by the nonlinear time-varying state equations. For analysis purpose the state equation of a nonlinear time varying main circuit model is divided into four appropriate operation modes (linear system).
- From the location of the steady state solution (equilibrium points) of each 'Operating Mode' and the stability analysis results, the existence of the oscillation phenomenon when a light-load regenerative braking control is adopted is clarified.
- Based on the above-mentioned analytical results the control technique by which the oscillation phenomenon is controlled is proposed and verified according to the mini model.

Chapter 5

- Based on the of the transfer function concept, the new modeling technique of the storage battery that using the frequency response characteristic was proposed.
- From the frequency character of the experiment result, the admittance was decided to be expressed by the "one-order delay + phase-lead" transfer function.
- The approximated time constant parameter of the storage battery admittance was calculated using least square method from the whole frequency response obtained from the experiment results.
- Since the transfer function is obtained under the sufficient number of data, based on the graphical treatment, the influence of the dispersion of the data can be restrained low. As a result, the stable technique for obtaining the electrical circuit parameters can be provided.
- It confirmed that the resistance element and capacity element expressed in the equivalent circuit are influenced by the change in the charging capacity, but the inductance element isn't influenced very much.

- By using the proposed technique with the general concept of the transfer function, it is possible to calculate easily the characteristic of the combinational batteries. The electrical circuit parameter of the combinational batteries, which are connected in series or parallel configurations, is easy to be calculated mathematically from the character of the single battery.

  Verifying the proposed modeling technique by applying a step response and various transient responses, developing the proposal modeling technique for the storage battery with the combinational cases of different charging capacity and deterioration condition, and investigating and generalizing the model of the storage battery against the deterioration and the change in the temperature condition are the challenges for the future works.

.

Bibliography

[1] S.-H. Kim, S. K. Sul, and M. H. Park, "Maximum torque control of an induction machine in the field weakening region," *IEEE Trans. Ind. Appl.*, vol. 31, no. 4, pp. 787-794, 1995. 10

[2] H. Grotstollen and J. Wiesing, "Torque capability and control of a saturated induction motor over a wide range of flux weakening," *IEEE Trans. Ind. Electron.*, vol. 42, no. 4, pp. 374-381, 1995. 10

[3] S-H. Kim and S-K Sul, "Voltage Control Strategy for Maximum Torque Operation of an Induction Machine in the Field-Weakening Region," *IEEE Trans. Ind. Electron.*, vol. 44, no. 4, pp. 512-518, 1997. 10, 16, 17, 19

[4] B.J. Seibel, T.M. Rowan, and R.J. Kerkman, "Field-Oriented Control of an Induction Machine in the Field-Weakening Region with DC-Link an Load Disturbance Rejection," *IEEE Trans. Ind. Appicat.*, vol. 33, no. 6, pp. 1578-1584, 1997. 10

[5] R.J. Kerkman, D. Leggate, B.J. Seibel, and T.M. Rowan, "An Overmodulation Strategy for PWM Voltage Inverters," in *IECON'93, 19th Int. Conf. Ind. Electron., Contr. Instrumentation*, Maui, Hawaii, Nov. 15-19, pp. 1215-1221, 1993. 10

[6] J. Holtz, W. Lotzkat, and A.M. Khambdkone, "On Continuous Control of PWM Inverters in the Overmodulation Range Including the Six-Step Mode," *IEEE Trans. On Power Elec.*, vol. 8, no. 4, pp. 546-553, 1993.

[7] S. Halasz, G. Csonka, A.A.M. Hassan, "Sinusoidal PWM Techniques With Additional Zero-Sequence Harmonics," in *IECON'94, 20th Int. Conf. Ind. Electron., Contr. Instrumentation*, pp. 85-90, 1994. 13

[8] R.J. Kerkman, T.M. Rowan, D. Leggate, and B.J. Seibel, "Control of PWM Voltage Inverters in the Pulse Dropping Region," *IEEE Trans. on Power Elec.*, vol. 10, no. 5, pp. 559-565, 1995.

[9] V. Kaura and V. Blasko, "A New Method to Extend Linearity of a Sinusoidal PWM in the Overmodulation Region," *IEEE Trans. on Ind. Applicat.*, vol. 32, no. 5, pp. 1115-1121, 1996. 13

[10] S. Bolognani and M. Zigliotto, "Novel Digital Continuous Control of SVM Inverters in the Overmodulation Range," *IEEE Trans. on Ind. Applicat.*, vol. 33, no. 2, pp. 525-530, 1997.

[11] V. Kaura, "A New Method to Linearize Any Triangle-Comparison-Based PWM by Reshaping the Modulation Command," *IEEE Trans. on Ind. Applicat.*, vol. 33, no. 5, pp. 1254-1259, 1997. 13

[12] D.C. Lee and G.M. Lee, "A Novel Overmodulation Technique for Space-Vector PWM Inverter," *IEEE Trans. on Power Elec.*, vol. 13, no. 6, pp. 1144-1151, 1998. 10

[13] B.H. Bae, S.H. Kim, and S.K. Sul, "A New Overmodulation Strategy for Traction Drive," in *IECON'99, 25th Int. Conf. Ind. Electron., Contr. Instrumentation*, pp. 437-442, 1999. 10

[14] F. Briz, A. Diez, M.W. Degner, and R.D. Lorenz, "Current and Flux Regulation in Field-Weakening Operation," *IEEE Trans. on Ind. Applicat.*, vol. 37, no. 1, pp. 42-50, 2001. 10, 18

[15] L. Harnefors, and H.P. Nee, "Model-based current control of ac machines using the internal model control method," *IEEE Trans. on Ind. Applicat.*, vol. 34, no. 1, pp. 133-141, 1998. 18

[16] K. Ogata, **Modern Control Engineering**, Prentice-Hall, Inc., Englewood Cliffs, N.J., 1970. 34

[17] J. N. Nash, "Direct Torque Control, Induction Motor Vector Control Without an Encoder," *IEEE Trans. Ind. Applicat.*, vol. 33, no. 2, pp. 333-341, 1997. 50

[18] H. Kubota, K. Matsuse, and T. Nakano, "DSP-Based Speed Adaptive Flux Observer of Induction Motor," *IEEE Trans. Ind. Applicat.*, vol. 29, no. 2, pp. 344-348, 1993. 50, 54

[19] Y. R. Kim, S. K. Sul, and M. H. Park, "Speed Sensorless Vector Control of Induction Motor Using an Extended Kalman Filter," I*EEE Trans. Ind. Applicat.*, vol. 30, no. 5, pp. 1225-1233, 1994. 50

[20] L. Ben-Brahim and A. Kawamura, "A Fully Digitized Field-Oriented Controlled Induction Motor Drive Using Only Current Sensors," *IEEE Trans. Ind. Electron.*, vol. 39, no. 3, pp. 241-249, 1992.

[21] T. Ohtani, N. Takada, and K. Tanaka, "Vector Control of Induction Motor without Shaft Encoder," *IEEE Trans. Ind. Applicat.*, vol. 28, no. 1, pp. 157-164, 1992.

[22] K. D. Hurst, T. G. Habetler, G. Griva, F. Profumo, and P. L. Jansen, "A Self-Tuning Closed-Loop Flux Observer for Sensorless Torque Control of Standard Induction Machines," *IEEE Trans. Power Electron.*, vol. 12, no. 5, pp. 807-815, 1997.

[23] M. Marchesoni, P. Segarich, and E. Soressi, "A Simple Approach to Flux and Speed Observation in Induction Motor Drives," *IEEE Trans. Ind. Electron.*, vol. 44, no. 4, pp. 528-535, 1997. 50

[24] H. Kubota, K. Matsuse, and T. Nakano, "New adaptive flux observer for induction motor drives," *IEEE IECON'90*, pp. 921-926, 1990. 52

[25] The Railway Electrical Engineering Association of Japan, **Power Electronics for Electric Railway Systems**, pp. 92-93, March 1998. 80

[26] S. Arai, M. Sugaya, M. Edane, M. Iwahori, and H. Tamura, "New Regenerative Power Control for EMUs in Light Load," *1997 National Convention Record I.E.E. Japan Industry Applications Society*, No. 180, pp 259-262, 1997. 80

[27] K. Kondo, K. Matsuoka, and Y. Nakazawa, "A Designing Method in Current Control System of Permanent Magnet Synchronous Motor for Railway Vehicle Traction," *The Transactions of The Institute of Electrical Engineers of Japan, A Publication of Industry Applications Society*, Vol.118-D, 7/8, pp.900-907, 1998. 88

[28] Fujishima, Aizawa, and Inoue, **The electrochemistry measurement method**, Gihodo.

[29] Japan storage battery Co., Ltd, **The latest utility secondary battery**, Nikkan Kogyo Shinbun. 110, 117

[30] IEE Japan, **Denki kogaku pocket book**, Ohm. 110

[31] Akashi and Imai, **Detail description of practice control engineering**, Kyouritsu Shuppan. 110

Appendix A

General AC motor model

A.1 Transformation from three-phase model to two-phase model

Modelling motor is the most important subject to be understood in vector control theory since the control strategy is derived from motor model. The motor model used in the present work is the space vector model, which dynamic motor equations are expressed into two axes: the real and imaginary axes. Therefore, the three-phase motor is transformed into its equivalent two-phase motor. The space vector model is very closely related to the *dq*-model. The real and imaginary axes of the space vector model can be considered to be the same as the *dq* axes. The simplicity and compactness of the space-phasor equations make an easy understanding of space vector model. For an example the transformation of stator-currents from the three-phase currents into their two-phase equivalents is explained using phasor theory. Figure A.1 shows the projections of the stator-current space phasor. The space phasor of the stator currents can be defined as a phasor whose real part is equal to the instantaneous value of the d-axis stator component, $i_\alpha(t)$, and whose imaginary part is equal to the q-axis stator current component, $i_\beta(t)$. Thus, the stator-current space vector in the stationary reference frame fixed to the stator can be expressed as

$$\bar{i}_s = i_\alpha(t) + \mathrm{j}i_\beta(t) \tag{A.1}$$

Then, the real part of stator-current is also equal to the sum of real parts of i_u, i_v, and i_w, and the imaginary part of stator-current is also equal to the sum of imaginary parts of i_u, i_v, and i_w those are expressed as follows:

$$\mathrm{Re}(\bar{i}_s) = i_\alpha = K[\mathrm{Re}(I_u\angle\theta_u) + \mathrm{Re}(I_v\angle\theta_v) + \mathrm{Re}(I_w\angle\theta_w) = K[i_u - \frac{1}{2}i_v - \frac{1}{2}i_w] \tag{A.2}$$

$$\mathrm{Im}(\bar{i}_s) = i_\beta = K[\mathrm{Im}(I_u\angle\theta_u) + \mathrm{Im}(I_v\angle\theta_v) + \mathrm{Im}(I_w\angle\theta_w) = K[\frac{\sqrt{3}}{2}i_v - \frac{\sqrt{3}}{2}i_w] \tag{A.3}$$

K is the transformation constant, which for the power-invariant form $K = \sqrt{\frac{2}{3}}$ and for the non-power-invariant form $K = \frac{2}{3}$. The transformation of stator-currents from the 3-phase frame into the 2-phase frame is expressed in the matrix form as follows:

$$\begin{bmatrix} i_\alpha \\ i_\beta \end{bmatrix} = K \begin{bmatrix} 1 & -\frac{1}{2} & -\frac{1}{2} \\ 0 & \frac{\sqrt{3}}{2} & \frac{\sqrt{3}}{2} \end{bmatrix} \begin{bmatrix} i_u \\ i_v \\ i_w \end{bmatrix} \tag{A.4}$$

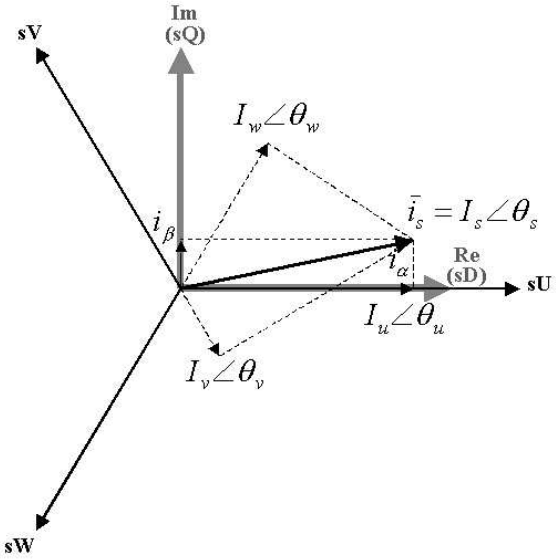

Figure A.1: Projections of the stator-current space phasor.

A.2 The AC motor Model in the General Reference Frame

The motor model can be represented in any reference frame that can be fixed to stator winding, rotor winding, stator flux, rotor flux, and magnetizing flux. Here, the motor model is derived, which is given by voltage equations expressed in the general reference frame (xy-axis). The generalization of reference frame makes easy to express the motor model in any reference frame. The stator and rotor voltage equations of a symmetrical three-phase motor can be expressed in the stationary reference frame as follows:

$$\bar{v}_s = R_s\bar{i}_s + \frac{d}{dt}\bar{\phi}_s \tag{A.5}$$

$$\bar{v}_r' = R_r \bar{i}_r + \frac{d}{dt}\bar{\phi}_r' - \mathrm{j}\omega_r \bar{\phi}_r' \tag{A.6}$$

In Eqs. (A.5) and (A.6), $\bar{v}_s$, $\bar{i}_s$, and $\bar{\phi}_s$ are the space phasor of the stator voltages, stator currents, and stator flux linkages, respectively, and $\bar{v}_r'$, $\bar{i}_r$, and $\bar{\phi}'$ are the space phasor of the rotor voltages, rotor currents, and rotor flux linkages, respectively, and those are expressed as follows:

$$\bar{v}_s = K[v_{su}(t) + a v_{sv}(t) + a^2 v_{sw}(t)] = v_{s\alpha} + \mathrm{j} v_{s\beta} \tag{A.7}$$

$$\bar{i}_s = K[i_{su}(t) + a i_{sv}(t) + a^2 i_{sw}(t)] = i_{s\alpha} + \mathrm{j} i_{s\beta} \tag{A.8}$$

$$\bar{\phi}_s = K[\phi_{su}(t) + a\phi s_v(t) + a^2 \phi s_w(t)] = \phi_{s\alpha} + \mathrm{j}\phi_{s\beta} = L_s \bar{i}_s + L_m \bar{i}_r' \tag{A.9}$$

$$\bar{v}_r' = \bar{v}_r \mathrm{e}^{\mathrm{j}\theta_r} = v_{rd} + \mathrm{j} v_{rq} \tag{A.10}$$

$$\bar{i}_r' = \bar{i}_r \mathrm{e}^{\mathrm{j}\theta_r} = i_{rd} + \mathrm{j} i_{rq} \tag{A.11}$$

$$\bar{\phi}_r' = \bar{\phi}_r \mathrm{e}^{\mathrm{j}\theta_r} = L_r \bar{i}_r' + L_m \bar{i}_s = L_r \bar{i}_r \mathrm{e}^{\mathrm{j}\theta_r} + L_m \bar{i}_s = \phi_{rd} + \mathrm{j}\phi_{rq} \tag{A.12}$$

where a is a spatial operator, $a = \mathrm{e}^{\mathrm{j}2\pi/3} = -\frac{1}{2} + \mathrm{j}\sqrt{\frac{3}{2}}$, and θ_r is the rotor angle. $\bar{v}_r$, $\bar{i}_r$, and $\bar{\phi}_r$ are the space phasor of the rotor voltages, currents, and flux linkages, respectively, expressed in the reference frame fixed to the rotor as follows:

$$\bar{v}_r = K[v_{ru}(t) + a v_{rv}(t) + a^2 v_{rw}(t)] = v_{r\alpha} + \mathrm{j} v_{r\beta} \tag{A.13}$$

$$\bar{v}_r = K[v_{ru}(t) + a v_{rv}(t) + a^2 v_{rw}(t)] = v_{r\alpha} + \mathrm{j} v_{r\beta} \tag{A.14}$$

$$\bar{\phi}_r = K[\phi_{ru}(t) + a\phi_{rv}(t) + a^2 \phi_{rw}(t)] = L_r \bar{i}_r + L_m \bar{i}_s' = L_r \bar{i}_r + L_m \bar{i}_s \mathrm{e}^{-\mathrm{j}\theta_r} = \phi_{r\alpha} + \mathrm{j}\phi_{r\beta} \tag{A.15}$$

Equations (A.5), (A.6), (A.9), and (A.12) are representative equations of the space vector model in the stationary reference frame fixed to the stator. If a general reference frame with direct and quadrature axes x, y, rotating at a general instantaneous speed $\omega_g = \frac{d}{dt}\theta_g$ is used, as shown in Fig. A.2, where θ_g is the angle between the d-axis of the stationary reference frame sD fixed to the stator and the real axis x of the general reference frame, then the following

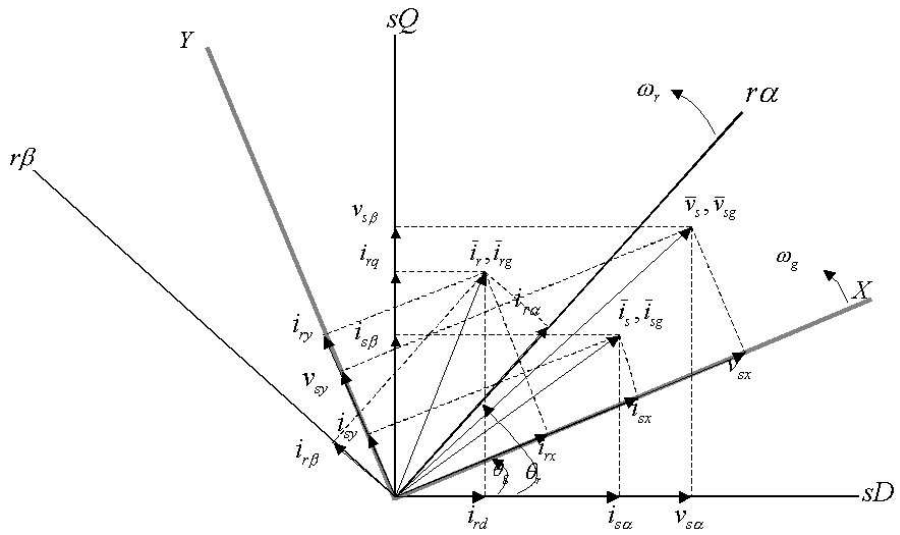

Figure A.2: Space phasor of the general reference frame.

equations define the stator current space phasor, stator voltage space phasor and stator flux linkage space phasor in the general reference frame:

$$\bar{v}_{sg} = \bar{v}_s \mathrm{e}^{-\mathrm{j}\theta_g} = v_{sx} + \mathrm{j}v_{sy} \tag{A.16}$$

$$\bar{i}_{sg} = \bar{i}_s \mathrm{e}^{-\mathrm{j}\theta_g} = i_{sx} + \mathrm{j}i_{sy} \tag{A.17}$$

$$\bar{\phi}_{sg} = \bar{\phi}_s \mathrm{e}^{-\mathrm{j}\theta_g} = \phi_{sx} + \mathrm{j}\phi_{sy} \tag{A.18}$$

The space phasor of the rotor voltages, currents, and flux linkages expressed in the general reference frame are defined as follows:

$$\bar{v}_{rg} = \bar{v}_r \mathrm{e}^{-\mathrm{j}(\theta_g - \theta_r)} = v_{rx} + \mathrm{j}v_{ry} \tag{A.19}$$

$$\bar{i}_{rg} = \bar{i}_r \mathrm{e}^{-\mathrm{j}(\theta_g - \theta_r)} = i_{rx} + \mathrm{j}i_{ry} \tag{A.20}$$

$$\bar{\phi}_{rg} = \bar{\phi}_r \mathrm{e}^{-\mathrm{j}(\theta_g - \theta_r)} = \phi_{rx} + \mathrm{j}\phi_{ry} \tag{A.21}$$

Substitution of Eqs. (A.16)∼(A.21) into Eqs. (A.5), (A.6), (A.9), and (A.12) gives the following stator and rotor space phasor voltage equations in the general reference frame:

$$\bar{v}_{sg} = R_s \bar{i}_{sg} + d\bar{\phi}_{sg}/dt + \mathrm{j}\omega_g \bar{\phi}_{sg} \tag{A.22}$$

$$\bar{v}_{rg} = R_r \bar{i}_{rg} + d\bar{\phi}_{rg}/dt + \mathrm{j}(\omega_g - \omega_r)\bar{\phi}_{rg} \tag{A.23}$$

where the stator and rotor flux linkages in the general reference frame can be expressed in terms of the stator and rotor current space phasor as follows:

$$\bar{\phi}_{sg} = L_s \bar{i}_{sg} + L_m \bar{i}_{rg} \tag{A.24}$$

$$\bar{\phi}_{rg} = L_r \bar{i}_{rg} + L_m \bar{i}_{sg} \tag{A.25}$$

Appendix B

Analysis model used in Chapter 2

B.1 Induction motor model with standard current control and decoupling system

B.1.1 Non-linear system model

$$
\begin{aligned}
\frac{d}{dt}i_{sd} &= [-\tfrac{k_{idp}+R_s}{\sigma L_s} - \tfrac{R_r(1-\sigma)}{\sigma L_r}]i_{sd} + [N\omega_m + \tfrac{R_r}{L_r}\tfrac{i^*_{sq1}}{i^*_{sd2}}]i_{sq} + [\tfrac{MR_r}{\sigma L_s L_r^2}]\phi_{rd} \\
&\quad + [\tfrac{NM}{\sigma L_s L_r}\omega_m]\phi_{rq} + [\tfrac{k_{idi}}{\sigma L_s}]x_{sd} + [\tfrac{k_{idp}}{\sigma L_s}]i^*_{sd} + [-N\omega_m]i^*_{sq1} + [-\tfrac{R_r}{L_r}]\tfrac{i^{*2}_{sq1}}{i^*_{sd2}} \\
\frac{d}{dt}i_{sq} &= [-N\omega_m - \tfrac{R_r i^*_{sq1}}{L_r i^*_{sd2}}]i_{sd} + [-\tfrac{k_{iqp}+R_s}{\sigma L_s} - \tfrac{R_r(1-\sigma)}{\sigma L_r}]i_{sq} + [-\tfrac{NM\omega_m}{\sigma L_s L_r}]\phi_{rd} \\
&\quad + [\tfrac{MR_r}{\sigma L_s L_r^2}]\phi_{rq} + [\tfrac{k_{iqi}}{\sigma L_s}]x_{sq} + [\tfrac{k_{iqp}}{\sigma L_s}]i^*_{sq} + [\tfrac{N\omega_m}{\sigma}]i^*_{sd2} + [\tfrac{R_r}{\sigma L_r}]i^*_{sq1} \\
\frac{d}{dt}\phi_{rd} &= [\tfrac{MR_r}{L_r}]i_{sd} + [-\tfrac{R_r}{L_r}]\phi_{rd} + [\tfrac{R_r}{L_r}\tfrac{i^*_{sq1}}{i^*_{sd2}}]\phi_{rq} \\
\frac{d}{dt}\phi_{rq} &= [\tfrac{MR_r}{L_r}]i_{sq} + [-\tfrac{R_r}{L_r}\tfrac{i^*_{sq1}}{i^*_{sd2}}]\phi_{rd} + [-\tfrac{R_r}{L_r}]\phi_{rq} \\
\frac{d}{dt}\omega_m &= [-\tfrac{NM}{JL_r}\phi_{rq}]i_{sd} + [\tfrac{NM}{JL_r}\phi_{rd}]i_{sq} + [-\tfrac{1}{J}]t_L \\
\frac{d}{dt}x_{sd} &= [-1]i_{sd} + [1]i^*_{sd} \\
\frac{d}{dt}x_{sq} &= [-1]i_{sq} + [1]i^*_{sq} \\
\frac{d}{dt}i^*_{sd1} &= [-\tfrac{1}{T_d}]i^*_{sd1} + [\tfrac{1}{T_d}]i^*_{sd} \\
\frac{d}{dt}i^*_{sq1} &= [-\tfrac{1}{T_d}]i^*_{sq1} + [\tfrac{1}{T_d}]i^*_{sq} \\
\frac{d}{dt}i^*_{sd2} &= [-\tfrac{1}{T_2}]i^*_{sd2} + [\tfrac{1}{T_2}]i^*_{sd1}
\end{aligned}
\tag{B.1}
$$

B.1.2 Linearized system model

$$
\begin{aligned}
\tfrac{d}{dt}\Delta i_{sd} &= [-\tfrac{k_{idp}+R_s}{\sigma L_s} - \tfrac{R_r(1-\sigma)}{\sigma L_r}]\Delta i_{sd} + [N\omega_{m0} + \tfrac{R_r i^*_{sq10}}{L_r i^*_{sd20}}]\Delta i_{sq} + [\tfrac{MR_r}{\sigma L_s L_r^2}]\Delta\phi_{rd} \\
&+ [\tfrac{NM\omega_{m0}}{\sigma L_s L_r}]\Delta\phi_{rq} + [Ni_{sq0} + \tfrac{NM\phi_{rq0}}{\sigma L_s L_r} - Ni^*_{sq10}]\Delta\omega_m + [\tfrac{k_{idi}}{\sigma L_s}]\Delta x_{sd} \\
&+ [-\tfrac{R_r i_{sq0} i^*_{sq10}}{L_r i^{*2}_{sd20}} + \tfrac{R_r i^{*2}_{sq10}}{L_r i^{*2}_{sd20}}]\Delta i^*_{sd2} + [-N\omega_{m0} + \tfrac{R_r i_{sq0}}{L_r i^*_{sd20}} - \tfrac{2R_r i^*_{sq10}}{L_r i^*_{sd20}}]\Delta i^*_{sq1} + [\tfrac{k_{idp}}{\sigma L_s}]\Delta i^*_{sd} \\
\\
\tfrac{d}{dt}\Delta i_{sq} &= [-N\omega_{m0} - \tfrac{R_r i^*_{sq10}}{L_r i^*_{sd20}}]\Delta i_{sd} + [-\tfrac{k_{iqp}+R_s}{\sigma L_s} - \tfrac{R_r(1-\sigma)}{\sigma L_r}]\Delta i_{sq} + [-\tfrac{NM\omega_{m0}}{\sigma L_s L_r}]\Delta\phi_{rd} \\
&+ [\tfrac{MR_r}{\sigma L_s L_r^2}]\Delta\phi_{rq} + [-Ni_{sd0} - \tfrac{NM\phi_{rd0}}{\sigma L_s L_r} + \tfrac{Ni^*_{sd20}}{\sigma}]\Delta\omega_m + [\tfrac{k_{iqi}}{\sigma L_s}]\Delta x_{sq} \\
&+ [\tfrac{N\omega_{m0}}{\sigma} + \tfrac{R_r i_{sd0} i^*_{sq10}}{L_r i^{*2}_{sd20}}]\Delta i^*_{sd2} + [-\tfrac{R_r i_{sd0}}{L_r i^*_{sd20}} + \tfrac{R_r}{\sigma L_r}]\Delta i^*_{sq1} + [\tfrac{k_{iqp}}{\sigma L_s}]\Delta i^*_{sq} \\
\\
\tfrac{d}{dt}\Delta\phi_{rd} &= [\tfrac{MR_r}{L_r}]\Delta i_{sd} + [-\tfrac{R_r}{L_r}]\Delta\phi_{rd} + [\tfrac{R_r i^*_{sq10}}{L_r i^*_{sd20}}]\Delta\phi_{rq} + [\tfrac{R_r\phi_{rq0}}{L_r i^*_{sd20}}]\Delta i^*_{sq1} + [-\tfrac{R_r i^*_{sq10}\phi_{rq0}}{L_r i^{*2}_{sd20}}]\Delta i^*_{sd2} \\
\\
\tfrac{d}{dt}\Delta\phi_{rq} &= [\tfrac{MR_r}{L_r}]\Delta i_{sq} + [-\tfrac{R_r i^*_{sq10}}{L_r i^*_{sd20}}]\Delta\phi_{rd} + [-\tfrac{R_r}{L_r}]\Delta\phi_{rq} + [-\tfrac{R_r\phi_{rd0}}{L_r i^*_{sd20}}]\Delta i^*_{sq1} + [\tfrac{R_r i^*_{sq10}\phi_{rd0}}{L_r i^{*2}_{sd20}}]\Delta i^*_{sd2} \\
\\
\tfrac{d}{dt}\Delta\omega_m &= [-\tfrac{NM\phi_{rq0}}{JL_r}]\Delta i_{sd} + [\tfrac{NM\phi_{rd0}}{JL_r}]\Delta i_{sq} + [\tfrac{NMi_{sq0}}{JL_r}]\Delta\phi_{rd} + [-\tfrac{NMi_{sd0}}{JL_r}]\Delta\phi_{rq} + [-\tfrac{1}{J}]\Delta t_L \\
\\
\tfrac{d}{dt}\Delta x_{sd} &= [-1]\Delta i_{sd} + [1]\Delta i^*_{sd} \\
\\
\tfrac{d}{dt}\Delta x_{sq} &= [-1]\Delta i_{sq} + [1]\Delta i^*_{sq} \\
\\
\tfrac{d}{dt}\Delta i^*_{sd1} &= [-\tfrac{1}{T_d}]\Delta i^*_{sd1} + [\tfrac{1}{T_d}]\Delta i^*_{sd} \\
\\
\tfrac{d}{dt}\Delta i^*_{sq1} &= [-\tfrac{1}{T_d}]\Delta i^*_{sq1} + [\tfrac{1}{T_d}]\Delta i^*_{sq} \\
\\
\tfrac{d}{dt}\Delta i^*_{sd2} &= [-\tfrac{1}{T_2}]\Delta i^*_{sd2} + [\tfrac{1}{T_2}]\Delta i^*_{sd1}
\end{aligned}
\tag{B.2}
$$

B.2 System model of the previous field-weakening scheme

B.2.1 Non-linear system model

$$
\begin{aligned}
\tfrac{d}{dt} i_{sd} &= (-\tfrac{R_s}{\sigma L_s} - \tfrac{R_r(1-\sigma)}{\sigma L_r}) i_{sd} + (N\omega_m + \tfrac{R_r}{L_r}\tfrac{i^*_{sq1}}{i^*_{sd2}}) i_{sq} + \tfrac{1}{\sigma L_s}\tfrac{MR_r}{L_r^2}\phi_{rd} + \tfrac{1}{\sigma L_s}\tfrac{N\omega_m M}{L_r}\phi_{rq} + \tfrac{1}{\sigma L_s} v^*_{sd} \\
\\
v^*_{sd} + k_{idp}k_{vp}v^{*2}_{sd} &= -k_{idp} i_{sd} + k_{idi} x_{sd} + k_{idp}k_{vi}x_v - \sigma L_s N\omega_m i^*_{sq1} - \sigma L_s \tfrac{R_r}{L_r}\tfrac{i^{*2}_{sq1}}{i^*_{sd2}} - k_{idp}k_{vp}v^{*2}_{sq} + k_{idp}k_{vp}v^{*2}_c \\
\\
\tfrac{d}{dt} i_{sq} &= [-N\omega_m - \tfrac{R_r i^*_{sq1}}{L_r i^*_{sd2}}] i_{sd} + [-\tfrac{R_s + k_{iqp}}{\sigma L_s} - \tfrac{R_r(1-\sigma)}{\sigma L_r}] i_{sq} + [-\tfrac{NM\omega_m}{\sigma L_s L_r}]\phi_{rd} + [\tfrac{MR_r}{\sigma L_s L_r^2}]\phi_{rq} \\
&+ [\tfrac{k_{iqi}}{\sigma L_s}] x_{sq} + [N\omega_m] i^*_{sd1} + [\tfrac{(1-\sigma)R_r}{\sigma L_r}] i^*_{sq1} + [\tfrac{R_r}{L_r}]\tfrac{i^*_{sd1} i^*_{sq1}}{i^*_{sd2}} + [\tfrac{(1-\sigma)N\omega_m}{\sigma}] i^*_{sd2} + [\tfrac{k_{iqp}}{\sigma L_s}] i^*_{sq} \\
\\
\tfrac{d}{dt}\phi_{rd} &= [\tfrac{R_r M}{L_r}] i_{sd} + [-\tfrac{R_r}{L_r}]\phi_{rd} + [\tfrac{R_r i^*_{sq1}}{L_r i^*_{sd2}}]\phi_{rq} \\
\\
\tfrac{d}{dt}\phi_{rq} &= [\tfrac{R_r M}{L_r}] i_{sq} + [-\tfrac{R_r i^*_{sq1}}{L_r i^*_{sd2}}]\phi_{rd} + [-\tfrac{R_r}{L_r}]\phi_{rq} \\
\\
\tfrac{d}{dt}\omega_m &= [-\tfrac{NM\phi_{rq}}{JL_r}] i_{sd} + [\tfrac{NM\phi_{rd}}{JL_r}] i_{sq} + [-\tfrac{1}{J}] t_L
\end{aligned}
\tag{B.3}
$$

$$\frac{d}{dt}x_{sd} = [-1]i_{sd} + [k_{vi}]x_v + [-k_{vp}]v_{sd}^{*2} + [-k_{vp}]v_{sq}^{*2} + [k_{vp}](v_c^{*2})$$

$$\frac{d}{dt}x_{sq} = [-1]i_{sq} + [1]i_{sq}^*$$

$$\frac{d}{dt}x_v = [-1]v_{sd}^{*2} + [-1]v_{sq}^{*2} + [1]v_c^{*2}$$

$$\frac{d}{dt}i_{sd1}^* = [\frac{k_{vi}}{T_d}]x_v + [-\frac{1}{T_d}]i_{sd1}^* + [-\frac{k_{vp}}{T_d}]v_{sd}^{*2} + [-\frac{k_{vp}}{T_d}]v_{sq}^{*2} + [\frac{k_{vp}}{T_d}](v_c^{*2})$$

$$\frac{d}{dt}i_{sq1}^* = [\frac{1}{T_d}]i_{sq}^* + [-\frac{1}{T_d}]i_{sq1}^*$$

$$\frac{d}{dt}i_{sd2}^* = [\frac{1}{T_2}]i_{sd1}^* + [-\frac{1}{T_2}]i_{sd2}^*$$

B.2.2 Linearized system model

$$\begin{aligned}
\frac{d}{dt}\Delta i_{sd} = {} & [-\frac{R_s}{\sigma L_s} - \frac{R_r(1-\sigma)}{\sigma L_r} + \frac{-k_{idp}}{\sigma L_s(1+2k_{idp}k_{vp}v_{sd0}^*)}]\Delta i_{sd} + [N\omega_{m0} + \frac{R_r}{L_r}\frac{i_{sq10}^*}{i_{sd20}^*} + \frac{2k_{idp}k_{iqp}k_{vp}v_{sq0}^*}{\sigma L_s(1+2k_{idp}k_{vp}v_{sd0}^*)}]\Delta i_{sq} \\
& + [Ni_{sq0} + \frac{NM\phi_{rq0}}{\sigma L_s L_r} + \frac{-\sigma L_s N i_{sq10}^* - 2k_{idp}k_{vp}v_{sq0}^*(\sigma L_s N i_{sd10}^* + (1-\sigma)L_s N i_{sd20}^*)}{\sigma L_s(1+2k_{idp}k_{vp}v_{sd0}^*)}]\Delta\omega_m \\
& + [\frac{MR_r}{\sigma L_s L_r^2}]\Delta\phi_{rd} + [\frac{N\omega_{m0}M}{\sigma L_s L_r}]\Delta\phi_{rq} + [\frac{-2\sigma L_s N k_{idp}k_{vp}v_{sq0}^*\omega_{m0}}{\sigma L_s(1+2k_{idp}k_{vp}v_{sd0}^*)}]\Delta i_{sd1}^* \\
& + [\frac{R_r}{L_r}\frac{i_{sq0}}{i_{sd20}^*} - \frac{\sigma L_s L_r N\omega_{m0}i_{sd20}^* + 2\sigma L_s R_r i_{sq10}^* + 2k_{idp}k_{vp}v_{sq0}^*\{(1-\sigma)L_s R_r i_{sd20}^* + \sigma L_s R_r i_{sd10}^*\}}{\sigma L_s L_r(1+2k_{idp}k_{vp}v_{sd0}^*)i_{sd20}^*}]\Delta i_{sq1}^* \\
& + [-\frac{R_r}{L_r}\frac{i_{sq0}i_{sq10}^*}{i_{sd20}^{*2}} + \frac{\sigma L_s R_r i_{sq10}^{*2} + 2k_{idp}k_{vp}v_{sq0}^*\{\sigma L_s R_r i_{sd10}^* i_{sq10}^* - (1-\sigma)L_s L_r N\omega_{m0}i_{sd20}^{*2}\}}{\sigma L_s(1+2k_{idp}k_{vp}v_{sd0}^*)L_r i_{sd20}^{*2}}]\Delta i_{sd2}^* \\
& + [\frac{k_{idi}}{\sigma L_s(1+2k_{idp}k_{vp}v_{sd0}^*)}]\Delta x_{sd} + [\frac{-2k_{idp}k_{iqi}k_{vp}v_{sq0}^*}{\sigma L_s(1+2k_{idp}k_{vp}v_{sd0}^*)}]\Delta x_{sq} + [\frac{k_{idp}k_{vi}}{\sigma L_s(1+2k_{idp}k_{vp}v_{sd0}^*)}]\Delta x_v \\
& + [\frac{-2k_{idp}k_{iqp}k_{vp}v_{sq0}^*}{\sigma L_s(1+2k_{idp}k_{vp}v_{sd0}^*)}]\Delta i_{sq}^* + [\frac{k_{idp}k_{vp}}{\sigma L_s(1+2k_{idp}k_{vp}v_{sd0}^*)}]\Delta(v_c^{*2})
\end{aligned}$$

$$\begin{aligned}
\frac{d}{dt}\Delta i_{sq} = {} & [-N\omega_{m0} - \frac{R_r i_{sq10}^*}{L_r i_{sd20}^*}]\Delta i_{sd} + [-\frac{R_s + k_{iqp}}{\sigma L_s} - \frac{R_r(1-\sigma)}{\sigma L_r}]\Delta i_{sq} + [-\frac{NM\omega_{m0}}{\sigma L_s L_r}]\Delta\phi_{rd} \\
& + [\frac{MR_r}{\sigma L_s L_r^2}]\Delta\phi_{rq} + [-Ni_{sd0} - \frac{NM\phi_{rd0}}{\sigma L_s L_r} + Ni_{sd10}^* + \frac{(1-\sigma)Ni_{sd20}^*}{\sigma}]\Delta\omega_m + [\frac{k_{iqi}}{\sigma L_s}]\Delta x_{sq} \\
& + [N\omega_{m0} + \frac{R_r i_{sq10}^*}{L_r i_{sd20}^*}]\Delta i_{sd1}^* + [-\frac{R_r i_{sd0}}{L_r i_{sd20}^*} + \frac{(1-\sigma)R_r}{\sigma L_r} + \frac{R_r i_{sd10}^*}{L_r i_{sd20}^*}]\Delta i_{sq1}^* \\
& + [\frac{R_r i_{sd0} i_{sq10}^*}{L_r i_{sd20}^{*2}} - \frac{R_r i_{sd10}^* i_{sq10}^*}{L_r i_{sd20}^{*2}} + \frac{(1-\sigma)N\omega_{m0}}{\sigma}]\Delta i_{sd2}^* + [\frac{k_{iqp}}{\sigma L_s}]\Delta i_{sq}^*
\end{aligned}$$

$$\begin{aligned}
\frac{d}{dt}\Delta\phi_{rd} = {} & [\frac{R_r M}{L_r}]\Delta i_{sd} + [-\frac{R_r}{L_r}]\Delta\phi_{rd} + [\frac{R_r i_{sq10}^*}{L_r i_{sd20}^*}]\Delta\phi_{rq} + [\frac{R_r\phi_{rq0}}{L_r i_{sd20}^*}]\Delta i_{sq1}^* + [-\frac{R_r\phi_{rq0}i_{sq10}^*}{L_r i_{sd20}^{*2}}]\Delta i_{sd2}^* \\
\frac{d}{dt}\Delta\phi_{rq} = {} & [\frac{R_r M}{L_r}]\Delta i_{sq} + [-\frac{R_r i_{sq10}^*}{L_r i_{sd20}^*}]\Delta\phi_{rd} + [-\frac{R_r}{L_r}]\Delta\phi_{rq} + [-\frac{R_r\phi_{rd0}}{L_r i_{sd20}^*}]\Delta i_{sq1}^* + [\frac{R_r i_{sq10}^*\phi_{rd0}}{L_r i_{sd20}^{*2}}]\Delta i_{sd2}^* \\
\frac{d}{dt}\Delta\omega_m = {} & [-\frac{NM\phi_{rq0}}{JL_r}]\Delta i_{sd} + [\frac{NM\phi_{rd0}}{JL_r}]\Delta i_{sq} + [\frac{NMi_{sq0}}{JL_r}]\Delta\phi_{rd} + [-\frac{NMi_{sd0}}{JL_r}]\Delta\phi_{rq} + [-\frac{1}{J}]\Delta t_L
\end{aligned} \tag{B.4}$$

$$\begin{aligned}
\frac{d}{dt}\Delta x_{sd} = {} & \begin{bmatrix} -1 + \frac{2k_{idp}k_{vp}v_{sd0}^*}{1+2k_{idp}k_{vp}v_{sd0}^*} \end{bmatrix}\Delta i_{sd} + \begin{bmatrix} \frac{-4k_{idp}k_{iqp}k_{vp}^2 v_{sd0}^* v_{sq0}^*}{1+2k_{idp}k_{vp}v_{sd0}^*} + 2k_{iqp}k_{vp}v_{sq0}^* \end{bmatrix}\Delta i_{sq} \\
& + \begin{bmatrix} \frac{2k_{vp}v_{sd0}^*(\sigma L_s N i_{sq10}^* + 2k_{idp}k_{vp}v_{sq0}^*(\sigma L_s N i_{sd10}^* + (1-\sigma)L_s N i_{sd20}^*))}{1+2k_{idp}k_{vp}v_{sd0}^*} \\ -2k_{vp}v_{sq0}^*\{\sigma L_s N i_{sd10}^* + (1-\sigma)L_s N i_{sd20}^*\} \end{bmatrix}\Delta\omega_m \\
& + \begin{bmatrix} \frac{-2k_{idi}k_{vp}v_{sd0}^*}{1+2k_{idp}k_{vp}v_{sd0}^*} \end{bmatrix}\Delta x_{sd} + \begin{bmatrix} \frac{4k_{idp}k_{iqi}k_{vp}^2 v_{sd0}^* v_{sq0}^*}{1+2k_{idp}k_{vp}v_{sd0}^*} - 2k_{iqi}k_{vp}v_{sq0}^* \end{bmatrix}\Delta x_{sq} \\
& + \begin{bmatrix} \frac{-2k_{idp}k_{vp}k_{vi}v_{sd0}^*}{1+2k_{idp}k_{vp}v_{sd0}^*} + k_{vi} \end{bmatrix}\Delta x_v + \begin{bmatrix} \frac{4\sigma L_s N k_{idp}k_{vp}^2\omega_{m0}v_{sd0}^* v_{sq0}^*}{1+2k_{idp}k_{vp}v_{sd0}^*} - 2\sigma L_s N k_{vp}\omega_{m0}v_{sq0}^* \end{bmatrix}\Delta i_{sd1}^* \\
& + \begin{bmatrix} \frac{2k_{vp}v_{sd0}^*\{\sigma L_s L_r N\omega_m i_{sd20}^* + 2\sigma L_s R_r i_{sq10}^* + 2k_{idp}k_{vp}v_{sq0}^*\{(1-\sigma)L_s R_r i_{sd20}^* + \sigma L_s R_r i_{sd10}^*\}\}}{(1+2k_{idp}k_{vp}v_{sd0}^*)L_r i_{sd20}^*} \end{bmatrix}
\end{aligned}$$

$$
\begin{aligned}
&\quad - \frac{2k_{vp}v^*_{sq0}\{(1-\sigma)L_sR_ri^*_{sd20}+\sigma L_sR_ri^*_{sd10}\}}{L_ri^*_{sd20}} \Bigg] \Delta i^*_{sq1} \\
&+ \Bigg[\frac{-2k_{vp}v^*_{sd0}\{\sigma L_sR_ri^{*2}_{sq10}+2k_{idp}k_{vp}v^*_{sq0}\{\sigma L_sR_ri^*_{sd10}i^*_{sq10}-(1-\sigma)L_sL_rN\omega_{m0}i^{*2}_{sd20}\}\}}{(1+2k_{idp}k_{vp}v^*_{sd0})L_ri^{*2}_{sd20}} \\
&\quad + \frac{2k_{vp}v^*_{sq0}\{\sigma L_sR_ri^*_{sd10}i^*_{sq10}-(1-\sigma)L_sL_rN\omega_{m0}i^{*2}_{sd20}\}}{L_ri^{*2}_{sd20}} \Bigg] \Delta i^*_{sd2} \\
&+ \Bigg[\frac{4k_{idp}k_{iqp}k^2_{vp}v^*_{sd0}v^*_{sq0}}{1+2k_{idp}k_{vp}v^*_{sd0}} - 2k_{iqp}k_{vp}v^*_{sq0} \Bigg] \Delta i^*_{sq} \\
&+ \Bigg[\frac{-2k_{idp}k^2_{vp}v^*_{sd0}}{1+2k_{idp}k_{vp}v^*_{sd0}} + k_{vp} \Bigg] \Delta(v_c^{*2})
\end{aligned}
$$

$$
\frac{d}{dt}\Delta x_{sq} = [-1]\Delta i_{sq} + [1]\Delta i^*_{sq}
$$

$$
\begin{aligned}
\frac{d}{dt}\Delta x_v = &\Bigg[\frac{2k_{idp}v^*_{sd0}}{1+2k_{idp}k_{vp}v^*_{sd0}} \Bigg] \Delta i_{sd} + \Bigg[\frac{-4k_{idp}k_{vp}v^*_{sq0}k_{iqp}v^*_{sd0}}{1+2k_{idp}k_{vp}v^*_{sd0}} + 2k_{iqp}v^*_{sq0} \Bigg] \Delta i_{sq} \\
&+ \Bigg[\frac{-2v^*_{sd0}\{-\sigma L_sNi^*_{sq10}-2k_{idp}k_{vp}v^*_{sq0}(\sigma L_sNi^*_{sd10}+(1-\sigma)L_sNi^*_{sd20})\}}{1+2k_{idp}k_{vp}v^*_{sd0}} \\
&\quad - 2v^*_{sq0}\{\sigma L_sNi^*_{sd10}+(1-\sigma)L_sNi^*_{sd20}\} \Bigg] \Delta\omega_m \\
&+ \Bigg[\frac{-2k_{idi}v^*_{sd0}}{1+2k_{idp}k_{vp}v^*_{sd0}} \Bigg] \Delta x_{sd} + \Bigg[\frac{4k_{idp}k_{vp}v^*_{sq0}k_{iqi}v^*_{sd0}}{1+2k_{idp}k_{vp}v^*_{sd0}} - 2k_{iqi}v^*_{sq0} \Bigg] \Delta x_{sq} \\
&+ \Bigg[\frac{-2k_{idp}k_{vi}v^*_{sd0}}{1+2k_{idp}k_{vp}v^*_{sd0}} \Bigg] \Delta x_v + \Bigg[\frac{4k_{idp}k_{vp}v^*_{sq0}\sigma L_sN\omega_{m0}v^*_{sd0}}{1+2k_{idp}k_{vp}v^*_{sd0}} - 2\sigma L_sN\omega_{m0}v^*_{sq0} \Bigg] \Delta i^*_{sd1} \\
&+ \Bigg[\frac{2v^*_{sd0}\{\sigma L_sN\omega_{m0}L_ri^*_{sd20}+2\sigma L_sR_ri^*_{sq10}+2k_{idp}k_{vp}v^*_{sq0}\{(1-\sigma)L_sR_ri^*_{sd20}+\sigma L_sR_ri^*_{sd10}\}\}}{(1+2k_{idp}k_{vp}v^*_{sd0})L_ri^*_{sd20}} \\
&\quad - \frac{2v^*_{sq0}\{(1-\sigma)L_sR_ri^*_{sd20}+\sigma L_sR_ri^*_{sd10}\}}{L_ri^*_{sd20}} \Bigg] \Delta i^*_{sq1} \\
&+ \Bigg[\frac{-2v^*_{sd0}\{\sigma L_sR_ri^{*2}_{sq10}+2k_{idp}k_{vp}v^*_{sq0}\{\sigma L_sR_ri^*_{sd10}i^*_{sq10}-(1-\sigma)L_sN\omega_{m0}L_ri^{*2}_{sd20}\}\}}{(1+2k_{idp}k_{vp}v^*_{sd0})L_ri^{*2}_{sd20}} \\
&\quad + \frac{2v^*_{sq0}\{\sigma L_sR_ri^*_{sd10}i^*_{sq10}-(1-\sigma)L_sN\omega_{m0}L_ri^{*2}_{sd20}\}}{L_ri^{*2}_{sd20}} \Bigg] \Delta i^*_{sd2} \\
&+ \Bigg[\frac{4k_{idp}k_{iqp}k_{vp}v^*_{sd0}v^*_{sq0}}{1+2k_{idp}k_{vp}v^*_{sd0}} - 2k_{iqp}v^*_{sq0} \Bigg] \Delta i^*_{sq} \\
&+ \Bigg[\frac{-2k_{idp}k_{vp}v^*_{sd0}}{1+2k_{idp}k_{vp}v^*_{sd0}} + 1 \Bigg] \Delta(v_c^{*2})
\end{aligned}
$$

$$
\begin{aligned}
\frac{d}{dt}\Delta i^*_{sd1} = &\Bigg[\frac{2k_{idp}k_{vp}v^*_{sd0}}{T_d(1+2k_{idp}k_{vp}v^*_{sd0})} \Bigg] \Delta i_{sd} + \Bigg[-\frac{4k_{idp}k_{iqp}k^2_{vp}v^*_{sd0}v^*_{sq0}}{T_d(1+2k_{idp}k_{vp}v^*_{sd0})} + \frac{2k_{iqp}k_{vp}v^*_{sq0}}{T_d} \Bigg] \Delta i_{sq} \\
&+ \Bigg[\frac{2k_{vp}v^*_{sd0}(\sigma L_sNi^*_{sq10}+2k_{idp}k_{vp}v^*_{sq0}(\sigma L_sNi^*_{sd10}+(1-\sigma)L_sNi^*_{sd20}))}{T_d(1+2k_{idp}k_{vp}v^*_{sd0})} \\
&\quad - \frac{2k_{vp}v^*_{sq0}(\sigma L_sNi^*_{sd10}+(1-\sigma)L_sNi^*_{sd20})}{T_d} \Bigg] \Delta\omega_m \\
&+ \Bigg[-\frac{2k_{idi}k_{vp}v^*_{sd0}}{T_d(1+2k_{idp}k_{vp}v^*_{sd0})} \Bigg] \Delta x_{sd} + \Bigg[\frac{4k_{idp}k_{iqi}k^2_{vp}v^*_{sd0}v^*_{sq0}}{T_d(1+2k_{idp}k_{vp}v^*_{sd0})} - \frac{2k_{iqi}k_{vp}v^*_{sq0}}{T_d} \Bigg] \Delta x_{sq} \\
&+ \Bigg[-\frac{2k_{idp}k_{vp}k_{vi}v^*_{sd0}}{T_d(1+2k_{idp}k_{vp}v^*_{sd0})} + \frac{k_{vi}}{T_d} \Bigg] \Delta x_v \\
&+ \Bigg[-\frac{1}{T_d} + \frac{4\sigma L_sNk_{idp}k^2_{vp}\omega_{m0}v^*_{sd0}v^*_{sq0}}{T_d(1+2k_{idp}k_{vp}v^*_{sd0})} - \frac{2\sigma L_sNk_{vp}v^*_{sq0}\omega_{m0}}{T_d} \Bigg] \Delta i^*_{sd1} \\
&+ \Bigg[\frac{2k_{vp}v^*_{sd0}(\sigma L_sL_rN\omega_{m0}i^*_{sd20}+2\sigma L_sR_ri^*_{sq10}+2k_{idp}k_{vp}v^*_{sq0}((1-\sigma)L_sR_ri^*_{sd20}+\sigma L_sR_ri^*_{sd10}))}{T_d(1+2k_{idp}k_{vp}v^*_{sd0})L_ri^*_{sd20}} \\
&\quad - \frac{2k_{vp}v^*_{sq0}((1-\sigma)L_sR_ri^*_{sd20}+\sigma L_sR_ri^*_{sd10})}{T_dL_ri^*_{sd20}} \Bigg] \Delta i^*_{sq1}
\end{aligned}
$$

$$+\left[\begin{array}{c}\frac{-2k_{vp}v^*_{sd0}(\sigma L_s R_r i^{*2}_{sq10}+2k_{idp}k_{vp}v^*_{sq0}(\sigma L_s R_r i^*_{sd10}i^*_{sq10}-(1-\sigma)L_s L_r N\omega_{m0}i^{*2}_{sd20}))}{T_d(1+2k_{idp}k_{vp}v^*_{sd0})L_r i^{*2}_{sd20}}\\ +\frac{2k_{vp}v^*_{sq0}(\sigma L_s R_r i^*_{sd10}i^*_{sq10}-(1-\sigma)L_s L_r N\omega_{m0}i^{*2}_{sd20})}{T_d L_r i^{*2}_{sd20}}\end{array}\right]\Delta i^*_{sd2}$$

$$+\left[\frac{4k_{idp}k_{iqp}k^2_{vp}v^*_{sd0}v^*_{sq0}}{T_d(1+2k_{idp}k_{vp}v^*_{sd0})}-\frac{2k_{iqp}k_{vp}v^*_{sq0}}{T_d}\right]\Delta i^*_{sq}$$

$$+\left[-\frac{2k_{idp}k^2_{vp}v^*_{sd0}}{T_d(1+2k_{idp}k_{vp}v^*_{sd0})}+\frac{k_{vp}}{T_d}\right]\Delta(v^{*2}_c)$$

$$\frac{d}{dt}\Delta i^*_{sq1}=[-\tfrac{1}{T_d}]\Delta i^*_{sq1}+[\tfrac{1}{T_d}]\Delta i^*_{sq}$$

$$\frac{d}{dt}\Delta i^*_{sd2}=[\tfrac{1}{T_2}]\Delta i^*_{sd1}+[-\tfrac{1}{T_2}]\Delta i^*_{sd2}$$

B.3 System model of the proposed field-weakening scheme (i_{sq} as disturbance)

B.3.1 Non-linear system model

$$\begin{aligned}\frac{d}{dt}i_{sd}&=[-\tfrac{R_s+k_{idp}}{\sigma L_s}-\tfrac{R_r(1-\sigma)}{\sigma L_r}]i_{sd}+[N\omega_m+\tfrac{R_r i^*_{sq1}}{L_r i^*_{sd2}}+\tfrac{sign.k_{dist}k_{idp}}{\sigma L_s}]i_{sq}+[\tfrac{MR_r}{\sigma L_s L_r^2}]\phi_{rd}\\&+[\tfrac{N\omega_m M}{\sigma L_s L_r}]\phi_{rq}+[\tfrac{k_{idi}}{\sigma L_s}]x_{sd}+[-N\omega_m]i^*_{sq1}+[-\tfrac{R_r}{L_r}]\tfrac{i^{*2}_{sq1}}{i^*_{sd2}}+[-\tfrac{k_{idp}k_{vp}}{\sigma L_s}]v^{flt}_s+[\tfrac{k_{idp}k_{vp}}{\sigma L_s}](v^{*2}_c)\end{aligned}$$

$$\begin{aligned}\frac{d}{dt}i_{sq}&=[-N\omega_m-\tfrac{R_r i^*_{sq1}}{L_r i^*_{sd2}}]i_{sd}+[-\tfrac{R_s+k_{iqp}}{\sigma L_s}-\tfrac{R_r(1-\sigma)}{\sigma L_r}]i_{sq}+[-\tfrac{NM\omega_m}{\sigma L_s L_r}]\phi_{rd}+[\tfrac{MR_r}{\sigma L_s L_r^2}]\phi_{rq}\\&+[\tfrac{k_{iqi}}{\sigma L_s}]x_{sq}+[N\omega_m]i^*_{sd1}+[\tfrac{(1-\sigma)R_r}{\sigma L_r}]i^*_{sq1}+[\tfrac{R_r}{L_r}]\tfrac{i^*_{sd1}i^*_{sq1}}{i^*_{sd2}}+[\tfrac{(1-\sigma)N\omega_m}{\sigma}]i^*_{sd2}+[\tfrac{k_{iqp}}{\sigma L_s}]i^*_{sq}\end{aligned}$$

$$\frac{d}{dt}\phi_{rd}=[\tfrac{R_r M}{L_r}]i_{sd}+[-\tfrac{R_r}{L_r}]\phi_{rd}+[\tfrac{R_r i^*_{sq1}}{L_r i^*_{sd2}}]\phi_{rq}$$

$$\frac{d}{dt}\phi_{rq}=[\tfrac{R_r M}{L_r}]i_{sq}+[-\tfrac{R_r i^*_{sq1}}{L_r i^*_{sd2}}]\phi_{rd}+[-\tfrac{R_r}{L_r}]\phi_{rq}$$

$$\frac{d}{dt}\omega_m=[-\tfrac{NM\phi_{rq}}{JL_r}]i_{sd}+[\tfrac{NM\phi_{rd}}{JL_r}]i_{sq}+[-\tfrac{1}{J}]t_L \tag{B.5}$$

$$\frac{d}{dt}x_{sd}=[-1]i_{sd}+[sign.k_{dist}]i_{sq}+[-k_{vp}]v^{flt}_s+[k_{vp}]v^{*2}_c$$

$$\frac{d}{dt}x_{sq}=[-1]i_{sq}+[1]i^*_{sq}$$

$$\frac{d}{dt}i^*_{sd1}=[\tfrac{sign.k_{dist}}{T_d}]i_{sq}+[-\tfrac{1}{T_d}]i^*_{sd1}+[-\tfrac{k_{vp}}{T_d}]v^{flt}_s+[\tfrac{k_{vp}}{T_d}]v^{*2}_c$$

$$\frac{d}{dt}i^*_{sq1}=[\tfrac{1}{T_d}]i^*_{sq}+[-\tfrac{1}{T_d}]i^*_{sq1}$$

$$\frac{d}{dt}i^*_{sd2}=[\tfrac{1}{T_2}]i^*_{sd1}+[-\tfrac{1}{T_2}]i^*_{sd2}$$

$$\frac{d}{dt}v^{flt}_s=[\tfrac{1}{T_{flt}}]v^{*2}_{sd}+[\tfrac{1}{T_{flt}}]v^{*2}_{sq}+[-\tfrac{1}{T_{flt}}]v^{flt}_s$$

B.3.2 Linearized system model

$$
\begin{aligned}
\tfrac{d}{dt}\Delta i_{sd} &= [-\tfrac{R_s+k_{idp}}{\sigma L_s} - \tfrac{R_r(1-\sigma)}{\sigma L_r}]\Delta i_{sd} + [N\omega_{m0} + \tfrac{R_r i^*_{sq10}}{L_r i^*_{sd20}} + \tfrac{sign.k_{dist}k_{idp}}{\sigma L_s}]\Delta i_{sq} + [\tfrac{MR_r}{\sigma L_s L_r^2}]\Delta\phi_{rd} \\
&+ [\tfrac{NM\omega_{m0}}{\sigma L_s L_r}]\Delta\phi_{rq} + [Ni_{sq0} + \tfrac{NM\phi_{rq0}}{\sigma L_s L_r} - Ni^*_{sq10}]\Delta\omega_m + [\tfrac{k_{idi}}{\sigma L_s}]\Delta x_{sd} \\
&+ [\tfrac{R_r i_{sq0}}{L_r i^*_{sd20}} - N\omega_{m0} - \tfrac{2R_r i^*_{sq10}}{L_r i^*_{sd20}}]\Delta i^*_{sq1} + [-\tfrac{R_r i_{sq0} i^*_{sq10}}{L_r i^{*2}_{sd20}} + \tfrac{R_r i^{*2}_{sq10}}{L_r i^{*2}_{sd20}}]\Delta i^*_{sd2} + [-\tfrac{k_{idp}k_{vp}}{\sigma L_s}]\Delta v_s^{flt} \\
&+ [\tfrac{k_{idp}k_{vp}}{\sigma L_s}]\Delta(v_c^{*2})
\end{aligned}
$$

$$
\begin{aligned}
\tfrac{d}{dt}\Delta i_{sq} &= [-N\omega_{m0} - \tfrac{R_r i^*_{sq10}}{L_r i^*_{sd20}}]\Delta i_{sd} + [-\tfrac{R_s+k_{iqp}}{\sigma L_s} - \tfrac{R_r(1-\sigma)}{\sigma L_r}]\Delta i_{sq} + [-\tfrac{NM\omega_{m0}}{\sigma L_s L_r}]\Delta\phi_{rd} \\
&+ [\tfrac{MR_r}{\sigma L_s L_r^2}]\Delta\phi_{rq} + [-Ni_{sd0} - \tfrac{NM\phi_{rd0}}{\sigma L_s L_r} + Ni^*_{sd10} + \tfrac{(1-\sigma)Ni^*_{sd20}}{\sigma}]\Delta\omega_m + [\tfrac{k_{iqi}}{\sigma L_s}]\Delta x_{sq} \\
&+ [N\omega_{m0} + \tfrac{R_r i^*_{sq10}}{L_r i^*_{sd20}}]\Delta i^*_{sd1} + [-\tfrac{R_r i_{sd0}}{L_r i^*_{sd20}} + \tfrac{(1-\sigma)R_r}{\sigma L_r} + \tfrac{R_r i^*_{sd10}}{L_r i^*_{sd20}}]\Delta i^*_{sq1} \\
&+ [\tfrac{R_r i_{sd0} i^*_{sq10}}{L_r i^{*2}_{sd20}} - \tfrac{R_r i^*_{sd10} i^*_{sq10}}{L_r i^{*2}_{sd20}} + \tfrac{(1-\sigma)N\omega_{m0}}{\sigma}]\Delta i^*_{sd2} + [\tfrac{k_{iqp}}{\sigma L_s}]\Delta i^*_{sq}
\end{aligned}
$$

$$
\tfrac{d}{dt}\Delta\phi_{rd} = [\tfrac{R_r M}{L_r}]\Delta i_{sd} + [-\tfrac{R_r}{L_r}]\Delta\phi_{rd} + [\tfrac{R_r i^*_{sq10}}{L_r i^*_{sd20}}]\Delta\phi_{rq} + [\tfrac{R_r\phi_{rq0}}{L_r i^*_{sd20}}]\Delta i^*_{sq1} + [-\tfrac{R_r\phi_{rq0} i^*_{sq10}}{L_r i^{*2}_{sd20}}]\Delta i^*_{sd2}
$$

$$
\tfrac{d}{dt}\Delta\phi_{rq} = [\tfrac{R_r M}{L_r}]\Delta i_{sq} + [-\tfrac{R_r i^*_{sq10}}{L_r i^*_{sd20}}]\Delta\phi_{rd} + [-\tfrac{R_r}{L_r}]\Delta\phi_{rq} + [-\tfrac{R_r\phi_{rd0}}{L_r i^*_{sd20}}]\Delta i^*_{sq1} + [\tfrac{R_r i^*_{sq10}\phi_{rd0}}{L_r i^{*2}_{sd20}}]\Delta i^*_{sd2}
$$

$$
\tfrac{d}{dt}\Delta\omega_m = [-\tfrac{NM\phi_{rq0}}{JL_r}]\Delta i_{sd} + [\tfrac{NM\phi_{rd0}}{JL_r}]\Delta i_{sq} + [\tfrac{NMi_{sq0}}{JL_r}]\Delta\phi_{rd} + [-\tfrac{NMi_{sd0}}{JL_r}]\Delta\phi_{rq} + [-\tfrac{1}{J}]\Delta t_L
$$

$$
\tfrac{d}{dt}\Delta x_{sd} = [-1]\Delta i_{sd} + [sign.k_{dist}]\Delta i_{sq} + [-k_{vp}]\Delta v_s^{flt} + [k_{vp}]\Delta(v_c^{*2})
$$

$$
\tfrac{d}{dt}\Delta x_{sq} = [-1]\Delta i_{sq} + [1]\Delta i^*_{sq}
\tag{B.6}
$$

$$
\tfrac{d}{dt}\Delta i^*_{sd1} = [\tfrac{sign.k_{dist}}{T_d}]\Delta i_{sq} + [-\tfrac{1}{T_d}]\Delta i^*_{sd1} + [-\tfrac{k_{vp}}{T_d}]\Delta v_s^{flt} + [\tfrac{k_{vp}}{T_d}]\Delta(v_c^{*2})
$$

$$
\tfrac{d}{dt}\Delta i^*_{sq1} = [-\tfrac{1}{T_d}]\Delta i^*_{sq1} + [\tfrac{1}{T_d}]\Delta i^*_{sq}
$$

$$
\tfrac{d}{dt}\Delta i^*_{sd2} = [\tfrac{1}{T_2}]\Delta i^*_{sd1} + [-\tfrac{1}{T_2}]\Delta i^*_{sd2}
$$

$$
\begin{aligned}
\tfrac{d}{dt}\Delta v_s^{flt} &= \begin{bmatrix} -\frac{2v^*_{sd0}}{T_{flt}}k_{idp} \end{bmatrix}\Delta i_{sd} + \begin{bmatrix} \frac{2v^*_{sd0}}{T_{flt}}k_{idp}sign.k_{dist} - \frac{2v^*_{sq0}}{T_{flt}}k_{iqp} \end{bmatrix}\Delta i_{sq} \\
&+ \begin{bmatrix} -\frac{2v^*_{sd0}}{T_{flt}}\sigma L_s N i^*_{sq10} + \frac{2v^*_{sq0}}{T_{flt}}\left\{ \sigma L_s N i^*_{sd10} + (1-\sigma)L_s N i^*_{sd20} \right\} \end{bmatrix}\Delta\omega_m \\
&+ \begin{bmatrix} \frac{2v^*_{sd0}}{T_{flt}}k_{idi} \end{bmatrix}\Delta x_{sd} + \begin{bmatrix} \frac{2v^*_{sq0}}{T_{flt}}k_{iqi} \end{bmatrix}\Delta x_{sq} + \begin{bmatrix} \frac{2v^*_{sq0}}{T_{flt}}\left\{ \sigma L_s N\omega_{m0} + \frac{\sigma L_s R_r i^*_{sq10}}{L_r i^*_{sd20}} \right\} \end{bmatrix}\Delta i^*_{sd1} \\
&+ \begin{bmatrix} \frac{2v^*_{sd0}}{T_{flt}}\left\{ -\sigma L_s N\omega_{m0} - \frac{2\sigma L_s R_r i^*_{sq10}}{L_r i^*_{sd20}} \right\} + \frac{2v^*_{sq0}}{T_{flt}}\left\{ \frac{(1-\sigma)L_s R_r}{L_r} + \frac{\sigma L_s R_r i^*_{sd10}}{L_r i^*_{sd20}} \right\} \end{bmatrix}\Delta i^*_{sq1} \\
&+ \begin{bmatrix} \frac{2v^*_{sd0}}{T_{flt}}\frac{\sigma L_s R_r i^{*2}_{sq10}}{L_r i^{*2}_{sd20}} + \frac{2v^*_{sq0}}{T_{flt}}\left\{ \frac{-\sigma L_s R_r i^*_{sd10} i^*_{sq10}}{L_r i^{*2}_{sd20}} + (1-\sigma)L_s N\omega_{m0} \right\} \end{bmatrix}\Delta i^*_{sd2} \\
&+ \begin{bmatrix} -\frac{2v^*_{sd0}}{T_{flt}}k_{idp}k_{vp} - \frac{1}{T_{flt}} \end{bmatrix}\Delta v_s^{flt} + \begin{bmatrix} \frac{2v^*_{sd0}}{T_{flt}}k_{idp}k_{vp} \end{bmatrix}\Delta(v_c^{*2}) + \begin{bmatrix} \frac{2v^*_{sq0}}{T_{flt}}k_{iqp} \end{bmatrix}\Delta i^*_{sq}
\end{aligned}
$$

B.4 System model of the proposed field-weakening scheme (i^*_{sq} as disturbance)

B.4.1 Non-linear system model

$$
\begin{aligned}
\tfrac{d}{dt}i_{sd} &= [-\tfrac{R_s+k_{idp}}{\sigma L_s} - \tfrac{R_r(1-\sigma)}{\sigma L_r}]i_{sd} + [N\omega_m + \tfrac{R_r i^*_{sq1}}{L_r i^*_{sd2}}]i_{sq} + [\tfrac{MR_r}{\sigma L_s L_r^2}]\phi_{rd} + [\tfrac{N\omega_m M}{\sigma L_s L_r}]\phi_{rq} + [\tfrac{k_{idi}}{\sigma L_s}]x_{sd} \\
&\quad + [-N\omega_m]i^*_{sq1} + [-\tfrac{R_r}{L_r}]\tfrac{i^{*2}_{sq1}}{i^*_{sd2}} + [-\tfrac{k_{idp}k_{vp}}{\sigma L_s}]v_s^{flt} + [\tfrac{k_{idp}k_{vp}}{\sigma L_s}](v_c^{*2}) + [\tfrac{sign.k_{dist}k_{idp}}{\sigma L_s}]i^*_{sq} \\
\\
\tfrac{d}{dt}i_{sq} &= [-N\omega_m - \tfrac{R_r i^*_{sq1}}{L_r i^*_{sd2}}]i_{sd} + [-\tfrac{R_s+k_{iqp}}{\sigma L_s} - \tfrac{R_r(1-\sigma)}{\sigma L_r}]i_{sq} + [-\tfrac{NM\omega_m}{\sigma L_s L_r}]\phi_{rd} + [\tfrac{MR_r}{\sigma L_s L_r^2}]\phi_{rq} \\
&\quad + [\tfrac{k_{iqi}}{\sigma L_s}]x_{sq} + [N\omega_m]i^*_{sd1} + [\tfrac{(1-\sigma)R_r}{\sigma L_r}]i^*_{sq1} + [\tfrac{R_r}{L_r}]\tfrac{i^*_{sd1}i^*_{sq1}}{i^*_{sd2}} + [\tfrac{(1-\sigma)N\omega_m}{\sigma}]i^*_{sd2} + [\tfrac{k_{iqp}}{\sigma L_s}]i^*_{sq} \\
\\
\tfrac{d}{dt}\phi_{rd} &= [\tfrac{R_r M}{L_r}]i_{sd} + [-\tfrac{R_r}{L_r}]\phi_{rd} + [\tfrac{R_r i^*_{sq1}}{L_r i^*_{sd2}}]\phi_{rq} \\
\\
\tfrac{d}{dt}\phi_{rq} &= [\tfrac{R_r M}{L_r}]i_{sq} + [-\tfrac{R_r i^*_{sq1}}{L_r i^*_{sd2}}]\phi_{rd} + [-\tfrac{R_r}{L_r}]\phi_{rq} \\
\\
\tfrac{d}{dt}\omega_m &= [-\tfrac{NM\phi_{rq}}{JL_r}]i_{sd} + [\tfrac{NM\phi_{rd}}{JL_r}]i_{sq} + [-\tfrac{1}{J}]t_L \\
\\
\tfrac{d}{dt}x_{sd} &= [-1]i_{sd} + [-k_{vp}]v_s^{flt} + [k_{vp}]v_c^{*2} + [sign.k_{dist}]i^*_{sq} \\
\\
\tfrac{d}{dt}x_{sq} &= [-1]i_{sq} + [1]i^*_{sq} \\
\\
\tfrac{d}{dt}i^*_{sd1} &= [-\tfrac{1}{T_d}]i^*_{sd1} + [-\tfrac{k_{vp}}{T_d}]v_s^{flt} + [\tfrac{k_{vp}}{T_d}]v_c^{*2} + [\tfrac{sign.k_{dist}}{T_d}]i^*_{sq} \\
\\
\tfrac{d}{dt}i^*_{sq1} &= [\tfrac{1}{T_d}]i^*_{sq} + [-\tfrac{1}{T_d}]i^*_{sq1} \\
\\
\tfrac{d}{dt}i^*_{sd2} &= [\tfrac{1}{T_2}]i^*_{sd1} + [-\tfrac{1}{T_2}]i^*_{sd2} \\
\\
\tfrac{d}{dt}v_s^{flt} &= [\tfrac{1}{T_{flt}}]v_{sd}^{*2} + [\tfrac{1}{T_{flt}}]v_{sq}^{*2} + [-\tfrac{1}{T_{flt}}]v_s^{flt}
\end{aligned}
\tag{B.7}
$$

B.4.2 Linearized system model

$$
\begin{aligned}
\tfrac{d}{dt}\Delta i_{sd} &= [-\tfrac{R_s+k_{idp}}{\sigma L_s} - \tfrac{R_r(1-\sigma)}{\sigma L_r}]\Delta i_{sd} + [N\omega_{m0} + \tfrac{R_r i^*_{sq10}}{L_r i^*_{sd20}}]\Delta i_{sq} + [\tfrac{MR_r}{\sigma L_s L_r^2}]\Delta\phi_{rd} + [\tfrac{N\omega_{m0}M}{\sigma L_s L_r}]\Delta\phi_{rq} \\
&+ [Ni_{sq0} + \tfrac{NM\phi_{rq0}}{\sigma L_s L_r} - Ni^*_{sq10}]\Delta\omega_m + [\tfrac{k_{idi}}{\sigma L_s}]\Delta x_{sd} + [\tfrac{R_r i_{sq0}}{L_r i^*_{sd20}} - N\omega_{m0} - \tfrac{2R_r i^*_{sq10}}{L_r i^*_{sd20}}]\Delta i^*_{sq1} \\
&+ [-\tfrac{R_r i_{sq0} i^*_{sq10}}{L_r i^{*2}_{sd20}} + \tfrac{R_r i^{*2}_{sq10}}{L_r i^{*2}_{sd20}}]\Delta i^*_{sd2} + [-\tfrac{k_{idp}k_{vp}}{\sigma L_s}]\Delta v_s^{flt} + [\tfrac{k_{idp}k_{vp}}{\sigma L_s}]\Delta(v_c^{*2}) + [\tfrac{sign.k_{dist}k_{idp}}{\sigma L_s}]\Delta i^*_{sq} \\
\\
\tfrac{d}{dt}\Delta i_{sq} &= [-N\omega_{m0} - \tfrac{R_r i^*_{sq10}}{L_r i^*_{sd20}}]\Delta i_{sd} + [-\tfrac{R_s+k_{iqp}}{\sigma L_s} - \tfrac{R_r(1-\sigma)}{\sigma L_r}]\Delta i_{sq} + [-\tfrac{NM\omega_{m0}}{\sigma L_s L_r}]\Delta\phi_{rd} \\
&+ [\tfrac{MR_r}{\sigma L_s L_r^2}]\Delta\phi_{rq} + [-Ni_{sd0} - \tfrac{NM\phi_{rd0}}{\sigma L_s L_r} + Ni^*_{sd10} + \tfrac{(1-\sigma)Ni^*_{sd20}}{\sigma}]\Delta\omega_m + [\tfrac{k_{iqi}}{\sigma L_s}]\Delta x_{sq} \\
&+ [N\omega_{m0} + \tfrac{R_r i^*_{sq10}}{L_r i^*_{sd20}}]\Delta i^*_{sd1} + [-\tfrac{R_r i_{sd0}}{L_r i^*_{sd20}} + \tfrac{(1-\sigma)R_r}{\sigma L_r} + \tfrac{R_r i^*_{sd10}}{L_r i^*_{sd20}}]\Delta i^*_{sq1} \\
&+ [\tfrac{R_r i_{sd0} i^*_{sq10}}{L_r i^{*2}_{sd20}} - \tfrac{R_r i^*_{sd10} i^*_{sq10}}{L_r i^{*2}_{sd20}} + \tfrac{(1-\sigma)N\omega_{m0}}{\sigma}]\Delta i^*_{sd2} + [\tfrac{k_{iqp}}{\sigma L_s}]\Delta i^*_{sq} \\
\\
\tfrac{d}{dt}\Delta\phi_{rd} &= [\tfrac{R_r M}{L_r}]\Delta i_{sd} + [-\tfrac{R_r}{L_r}]\Delta\phi_{rd} + [\tfrac{R_r i^*_{sq10}}{L_r i^*_{sd20}}]\Delta\phi_{rq} + [\tfrac{R_r\phi_{rq0}}{L_r i^*_{sd20}}]\Delta i^*_{sq1} + [-\tfrac{R_r\phi_{rq0} i^*_{sq10}}{L_r i^{*2}_{sd20}}]\Delta i^*_{sd2} \\
\\
\tfrac{d}{dt}\Delta\phi_{rq} &= [\tfrac{R_r M}{L_r}]\Delta i_{sq} + [-\tfrac{R_r i^*_{sq10}}{L_r i^*_{sd20}}]\Delta\phi_{rd} + [-\tfrac{R_r}{L_r}]\Delta\phi_{rq} + [-\tfrac{R_r\phi_{rd0}}{L_r i^*_{sd20}}]\Delta i^*_{sq1} + [\tfrac{R_r i^*_{sq10}\phi_{rd0}}{L_r i^{*2}_{sd20}}]\Delta i^*_{sd2} \\
\\
\tfrac{d}{dt}\Delta\omega_m &= [-\tfrac{NM\phi_{rq0}}{JL_r}]\Delta i_{sd} + [\tfrac{NM\phi_{rd0}}{JL_r}]\Delta i_{sq} + [\tfrac{NMi_{sq0}}{JL_r}]\Delta\phi_{rd} + [-\tfrac{NMi_{sd0}}{JL_r}]\Delta\phi_{rq} + [-\tfrac{1}{J}]\Delta t_L \\
\\
\tfrac{d}{dt}\Delta x_{sd} &= [-1]\Delta i_{sd} + [-k_{vp}]\Delta v_s^{flt} + [k_{vp}]\Delta(v_c^{*2}) + [sign.k_{dist}]\Delta i^*_{sq} \\
\\
\tfrac{d}{dt}\Delta x_{sq} &= [-1]\Delta i_{sq} + [1]\Delta i^*_{sq} \\
\\
\tfrac{d}{dt}\Delta i^*_{sd1} &= [-\tfrac{1}{T_d}]\Delta i^*_{sd1} + [-\tfrac{k_{vp}}{T_d}]\Delta v_s^{flt} + [\tfrac{k_{vp}}{T_d}]\Delta(v_c^{*2}) + [\tfrac{sign.k_{dist}}{T_d}]\Delta i^*_{sq} \\
\\
\tfrac{d}{dt}\Delta i^*_{sq1} &= [-\tfrac{1}{T_d}]\Delta i^*_{sq1} + [\tfrac{1}{T_d}]\Delta i^*_{sq} \\
\\
\tfrac{d}{dt}\Delta i^*_{sd2} &= [\tfrac{1}{T_2}]\Delta i^*_{sd1} + [-\tfrac{1}{T_2}]\Delta i^*_{sd2} \\
\\
\tfrac{d}{dt}\Delta v_s^{flt} &= \begin{bmatrix} -\frac{2v^*_{sd0}}{T_{flt}}k_{idp} \end{bmatrix}\Delta i_{sd} + \begin{bmatrix} -\frac{2v^*_{sq0}}{T_{flt}}k_{iqp} \end{bmatrix}\Delta i_{sq} \\
&+ \begin{bmatrix} -\frac{2v^*_{sd0}}{T_{flt}}\sigma L_s N i^*_{sq10} + \frac{2v^*_{sq0}}{T_{flt}}\left\{ \sigma L_s N i^*_{sd10} + (1-\sigma)L_s N i^*_{sd20} \right\} \end{bmatrix}\Delta\omega_m \\
&+ \begin{bmatrix} \frac{2v^*_{sd0}}{T_{flt}}k_{idi} \end{bmatrix}\Delta x_{sd} + \begin{bmatrix} \frac{2v^*_{sq0}}{T_{flt}}k_{iqi} \end{bmatrix}\Delta x_{sq} + \begin{bmatrix} \frac{2v^*_{sq0}}{T_{flt}}\left\{ \sigma L_s N\omega_{m0} + \frac{\sigma L_s R_r i^*_{sq10}}{L_r i^*_{sd20}} \right\} \end{bmatrix}\Delta i^*_{sd1} \\
&+ \begin{bmatrix} \frac{2v^*_{sd0}}{T_{flt}}\left\{ -\sigma L_s N\omega_{m0} - \frac{2\sigma L_s R_r i^*_{sq10}}{L_r i^*_{sd20}} \right\} + \frac{2v^*_{sq0}}{T_{flt}}\left\{ \frac{(1-\sigma)L_s R_r}{L_r} + \frac{\sigma L_s R_r i^*_{sd10}}{L_r i^*_{sd20}} \right\} \end{bmatrix}\Delta i^*_{sq1} \\
&+ \begin{bmatrix} \frac{2v^*_{sd0}}{T_{flt}}\frac{\sigma L_s R_r i^{*2}_{sq10}}{L_r i^{*2}_{sd20}} + \frac{2v^*_{sq0}}{T_{flt}}\left\{ \frac{-\sigma L_s R_r i^*_{sd10} i^*_{sq10}}{L_r i^{*2}_{sd20}} + (1-\sigma)L_s N\omega_{m0} \right\} \end{bmatrix}\Delta i^*_{sd2} \\
&+ \begin{bmatrix} -\frac{2v^*_{sd0}}{T_{flt}}k_{idp}k_{vp} - \frac{1}{T_{flt}} \end{bmatrix}\Delta v_s^{flt} + \begin{bmatrix} \frac{2v^*_{sd0}}{T_{flt}}k_{idp}k_{vp} \end{bmatrix}\Delta(v_c^{*2}) \\
&+ \begin{bmatrix} \frac{2v^*_{sd0}}{T_{flt}}k_{idp}sign.k_{dist} + \frac{2v^*_{sq0}}{T_{flt}}k_{iqp} \end{bmatrix}\Delta i^*_{sq}
\end{aligned}
\tag{B.8}
$$

List of Publications

Journal/Transaction/Reviewed Paper:

1. **F. Yusivar**, H. Haratsu, M. Sato, S. Wakao, K. Kondo, K. Matsuoka, and T. Kawamatsu, "The Modeling of Lead-Acid Battery by Frequency-Response Characteristics," **The Transaction of IEE Japan, A Publication of Fundamental and Material Society** , Vol. 122-A, No. 8, pp. 715-721, Aug. 2002.

2. **F. Yusivar**, T. Kihara, M. Sato, S. Wakao, and T. Yamamura, "|Iq| Added Flux Weakening Strategy for the Rotor Flux Oriented Control of a Sinusoidal PWM VSI-fed Induction Motor," **Proc. of The 27th Annual Conference of the IEEE Industrial Electronics Society (IECON'01)**, vol. 2, pp. 1160-1165, Nov. 2001.

3. **F. Yusivar**, K.Uchida, T. Kihara, S. Wakao, K. Kondo, and K. Matsuoka, "An Anti Oscillation Strategy for the Regenerative Braking Control of Permanent Magnet Synchronous Motor with Insufficient Load Power Consumption," **Proc. of The 27th Annual Conference of the IEEE Industrial Electronics Society (IECON'01),** vol. 2, pp. 1457-1462, Nov. 2001.

4. **F. Yusivar**, K. Uchida, T. Kihara, S. Wakao, K. Kondo, and K. Matsuoka, "Stability Analysis of Permanent Magnet Synchronous Motor Traction Main Circuit with Regenerative Braking on Insufficient Load's Power Consuming" **The Transaction of IEE Japan, A Publication of Industry Application Society,** vol. 121-D, no. 6, pp. 651-657, June 2001.

5. **F. Yusivar**, K. Uchida, H. Haratsu, S. Wakao, and T. Onuki, "Speed Adaptive Observer for Sensorless IM Drive using Combined Reference Frames," **Proc. of The 15th IEEE Applied Power Electronics Conference and Exposition (APEC'00)**, vol. 1, pp. 127-132, Feb. 2000.

International Conferences:

1. **F. Yusivar**, and S. Wakao, "Minimum Requirements of Motor Vector Control Modeling and Simulation Utilizing C MEX S-function in MATLAB/SIMULINK," The 4th IEEE International Conference on Power Electronics and Drive Systems (PEDS'01), pp. 315-321 , Oct. 2001, Bali, Indonesia.

2. **F. Yusivar**, H. Haratsu, T. Kihara, S. Wakao, and T. Onuki, "Performance Comparison of the Controller Configurations for the Sensorless IM Drive using the Modified Speed Adaptive Observer," The eighth International Conference on Power Electronics and Variable Speed Drives (PEVD'00), Conf. Pub. No. 475, pp. 194-200, Sept. 2000, London, England.

3. D. Hamada, K. Uchida, **F. Yusivar**, H. Haratsu, S. Wakao, and T. Onuki, "Sensorless Control of Permanent Magnet Synchronous Motor Drive using Linear Reduced Order Observer including Disturbance Torque Estimation," The 8th European Conference on Power Electronics and Applications (EPE'99), Sept. 1999, Lausanne, Switzerland.

4. D. Hamada, K. Uchida, **F. Yusivar**, H. Haratsu, S. Wakao, and T. Onuki, "Stability Analysis of Sensorless Permanent Magnet Synchronous Motor Drive with Reduced Order Observer," The 1999 IEEE International Electric Machines and Drives Conference (IEMDC'99), pp. 95-97, May 1999, Seattle, USA.

5. **F. Yusivar**, D. Hamada, K. Uchida, S. Wakao, and T. Onuki, "A New Method of Motor Speed Estimation Using Fuzzy Logic Algorithm," The 1999 IEEE International Electric Machines and Drives Conference (IEMDC'99), pp. 278-280, May 1999, Seattle, USA.

Domestic Conferences:

1. M. Sato, **F. Yusivar**, S. Wakao, and K. Kondo, "Stability Analysis of Induction Motor in Regenerative Brake by Means of Block Diagram," The 2002 Papers of Joint Technical Meeting on Semiconductor Power Converter and Industry Electric and Electronic Application, IEE Japan, SPC-02-99, IEA-02-40, Nov. 2002, Japan.

2. **F. Yusivar**, K. Uchida, T. Kihara, S. Wakao, K. Kondo, and K. Matsuoka,"Stability Analysis of PMSM Traction Main Circuit with Regenerative Braking on Insufficient Load's Power Consuming," The 2001 National Convention Record IEE Japan, No.259, March 2001, Japan.

3. S. Wakao, **F. Yusivar**, H. Haratsu, K. Kondo, H. Hasegawa, and K. Matsuoka, "The Modeling Method for Transient Characteristics of Storage Battery based on Frequency-Response Characteristics," SEV/Society of Electric vehicle, The 6th National Technical Meeting Record, July 2000, Japan.

4. D. Hamada, K. Uchida, **F. Yusivar**, H. Haratsu, S. Wakao, and T. Onuki, "Characteristic Evaluation of Sensorless Permanent Magnet Synchronous Motor Drive with Reduced Order Observer," The 1998 Papers of Technical Meeting on Rotating Machinery, IEE Japan, RM-98-125, Oct. 1998, Japan.

List of Publications (in Japanese)

研究業績

種類別	題名	発表・発行掲載誌名	発表・発行年月	連名者
○論文	The Modeling of Lead-Acid Battery by Frequency-Response Characteristics	The Transaction of IEEJ, A Publication of Fundamental and Material Society (電気学会論文誌、基礎・材料・共通部門誌) Vol. 122-A, No. 8, pp. 715-721 (in Japanese)	Aug. 2002	Yusivar, F. Haratsu, H. Sato, M. Wakao, S. Kondo, K. Matsuoka, K. Kawamatsu, T.
○論文	|Iq| Added Flux Weakening Strategy for the Rotor Flux Oriented Control of a Sinusoidal PWM VSI-fed Induction Motor	Proc. of 27th Annual Conference of the IEEE Industrial Electronics Society (IECON'01), pp. 1160-1165 (in English)	Nov. 2001	Yusivar, F. Kihara, T. Sato, M. Wakao, S. Yamamura, T.
○論文	An Anti Oscillation Strategy for the Regenerative Braking Control of Permanent Magnet Synchronous Motor with Insufficient Load Power Consumption	Proc. of 27th Annual Conference of the IEEE Industrial Electronics Society (IECON'01), pp. 1457-1462 (in English)	Nov. 2001	Yusivar, F. Uchida, K. Kihara, T. Wakao, S. Kondo, K. Matsuoka, K.
○論文	Stability Analysis of Permanent Magnet Synchronous Motor Traction Main Circuit with Regenerative Braking on Insufficient Load's Power Consuming	The Transaction of IEEJ, A Publication of Industry Application Society (電気学会論文誌、産業応用部門誌) Vol. 121-D, No. 6, pp. 651-657 (in Japanese)	June 2001	Yusivar, F. Uchida, K. Kihara, T. Wakao, S. Kondo, K. Matsuoka, K.
○論文	Speed Adaptive Observer for Sensorless IM Drive using Combined Reference Frames	Proc. of 15th IEEE Applied Power Electronics Conference and Exposition (APEC'00), pp. 127-132 (in English)	Feb. 2000	Yusivar, F. Uchida, K. Haratsu, H. Wakao, S. Onuki, T.

研究業績

種類別	題名	発表・発行掲載誌名	発表・発行年月	連名者
講演	Stability Analysis of Induction Motor in Regenerative Brake by Means of Block Diagram	The 2002 Papers of Joint Technical Meeting on Semiconductor Power Converter and Industry Electric and Electronic Application, IEE Japan (平成 14 年電気学会半導体電力変換・産業電力電気応用合同研究会資料)SPC-02-99, IEA-02-40 (in Japanese)	Nov. 2002	Sato, M. Yusivar, F. Wakao, S. Kondo, K.
講演	Minimum Requirements of Motor Vector Control Modeling and Simulation Utilizing C MEX S-function in MATLAB/SIMULINK	Proc. of The 4th IEEE International Conference on Power Electronics and Drive Systems (PEDS'01), pp. 315-321 (in English)	Oct. 2001	Yusivar, F. Wakao, S.
講演	Stability Analysis of PMSM Traction Main Circuit with Regenerative Braking on Insufficient Load's Power Consuming	2001 National Convention Record I.E.E. Japan (平成 13 年電気学会全国大会講演論文集 5) No.259 (in Japanese)	March 2001	Yusivar, F. Uchida, K. Kihara, T. Wakao, S. Kondo, K. Matsuoka, K.
講演	Performance Comparison of the Controller Configurations for the Sensorless IM Drive using the Modified Speed Adaptive Observer	Proc. of eighth International Conference on Power Electronics and Variable Speed Drives (PEVD'00) Conf. Pub. No. 475, pp. 194-200 (in English)	Sept. 2000	Yusivar, F. Haratsu, H. Kihara, T. Wakao, S. Onuki, T.
講演	The Modeling Method for Transient Characteristics of Storage Battery based on Frequency-Response Characteristics	SEV/Society of Electric vehicle, The 6th National Technical Meeting Record (SEV/電気自動車研究会第 6 回研究発表会全国大会概要集) (in Japanese)	July 2000	Wakao, S. Yusivar, F. Haratsu, H. Kondo, K. Hasegawa, H. Matsuoka, K.

研究業績

種類別	題名	発表・発行掲載誌名	発表・発行年月	連名者
講演	Sensorless Control of Permanent Magnet Synchronous Motor Drive using Linear Reduced Order Observer including Disturbance Torque Estimation	Proc. of 8th European Conference on Power Electronics and Applications (EPE'99), Recorded in CD-ROM (6 pages) (in English)	Sept. 1999	Hamada, D. Uchida, K. Yusivar, F. Haratsu, H. Wakao, S. Onuki, T.
講演	Stability Analysis of Sensorless Permanent Magnet Synchronous Motor Drive with Reduced Order Observer	Proc. of IEEE International Electric Machines and Drives Conference (IEMDC'99), pp. 95-97 (in English)	May 1999	Hamada, D. Uchida, K. Yusivar, F. Haratsu, H. Wakao, S. Onuki, T.
講演	A New Method of Motor Speed Estimation Using Fuzzy Logic Algorithm	Proc. of IEEE International Electric Machines and Drives Conference (IEMDC'99), pp. 278-280 (in English)	May 1999	Yusivar, F. Hamada, D. Uchida, K. Wakao, S. Onuki, T.
講演	Characteristic Evaluation of Sensorless Permanent Magnet Synchronous Motor Drive with Reduced Order Observer	The 1998 Papers of Technical Meeting on Rotating Machinery, IEE Japan (平成 10 年電気学会回転機研究会資料) RM-98-125 (in Japanese)	Oct. 1998	Hamada, D. Uchida, K. Yusivar, F. Haratsu, H. Wakao, S. Onuki, T.